

**A Thesis Submitted for the Degree of PhD at the University of Warwick**

**Permanent WRAP URL:**

<http://wrap.warwick.ac.uk/145794>

**Copyright and reuse:**

This thesis is made available online and is protected by original copyright.

Please scroll down to view the document itself.

Please refer to the repository record for this item for information to help you to cite it.

Our policy information is available from the repository home page.

For more information, please contact the WRAP Team at: [wrap@warwick.ac.uk](mailto:wrap@warwick.ac.uk)



**Synthesis and Application of Some Ag<sup>+</sup>-selective  
Ligands and Iron Oxide/Ag<sup>+</sup>-selective Composite  
Nanoparticles**

**by**

**Abiodun Daniel Aderibigbe**

A thesis submitted in partial fulfilment of the requirements for  
the degree of  
Doctor of Philosophy in Chemistry

University of Warwick, Department of Chemistry

July 2019

# Contents

List of Figures .....	vi
List of Tables .....	xi
Acknowledgements .....	xv
Declaration .....	xvi
Abstract .....	xvii
Abbreviations .....	xviii
Chapter 1: Introduction .....	1
1.1 Introduction .....	2
1.2 Methods of metal recovery .....	2
1.2.1 Chemical precipitation .....	2
1.2.2 Membrane filtration .....	4
1.2.3 Ion exchange .....	5
1.2.4 Electrochemical treatment .....	6
1.3 Adsorption .....	9
1.4 Iron oxide nanoparticles (IONPs) .....	15
1.4.1 Methods of iron oxide nanoparticles synthesis .....	16
1.4.2 Surface functionalization of IONPs for metal uptake .....	23
1.5 Problem statement .....	35
Chapter 2: Synthesis and application of novel Ag <sup>+</sup> selective ligands .....	37
2.1 Introduction .....	38
2.1.1 Extraction efficiency of some reported Ag <sup>+</sup> -selective ligands .....	41
2.2 Aims and objectives .....	41

2.3 Result and discussion .....	43
2.3.1 Synthesis of <i>S</i> -benzylcysteamine <b>2.20</b> .....	43
2.3.2 Synthesis of <i>S</i> -benzylcysteamine derivatives <b>2.25-2.28</b> .....	45
2.3.3 Synthesis of gem disubstituted <i>S</i> -benzylcysteamine <b>2.29</b> <sup>215</sup> .....	46
2.3.4 Synthesis of <i>N,N'</i> malonamide derivative <b>2.10</b> .....	46
2.3.5 Summary of structures prepared. ....	52
2.3.6 Efficiency and selectivity of Ag <sup>+</sup> extraction from aqueous solutions .....	53
2.4 Summary of results. ....	60
Chapter 3: Ag <sup>+</sup> -ligand/Ag <sup>+</sup> binding studies: investigation of complex stoichiometry .....	61
3.1 Introduction.....	62
3.2 Aim and objectives .....	64
3.3 Results and discussion .....	65
3.3.1 Synthesis of Ag <sup>+</sup> complexes of <b>2.10</b> and <b>2.38</b> and attempted crystal growth .....	65
3.3.2 Mass spectrometry studies of Ag <sup>+</sup> - <b>2.10</b> and Ag <sup>+</sup> - <b>2.38</b> complexes.....	66
3.3.3 Job's and mole ratio plots for Ag <sup>+</sup> - <b>2.10</b> and Ag <sup>+</sup> - <b>2.38</b> complexes.....	70
3.4 Summary of results .....	74
Chapter 4: Synthesis and application of Fe <sub>3</sub> O <sub>4</sub> /amide Ag <sup>+</sup> selective ligand composite nanoparticles .....	76
4.1 Introduction.....	77
4.2 Aims and objectives.....	79
4.3 Result and discussion.....	80
4.3.1 Synthesis of Fe <sub>3</sub> O <sub>4</sub> @initiator <b>4.12 (4.7)</b> .....	80
4.3.2 Attempted surface initiated ATRP (SI-ATRP) of amide <b>2.38</b> .....	87

4.3.3 AIBN-mediated free radical polymerization of amide <b>2.38</b> .....	94
4.3.4 AIBN-mediated free radical coupling of amide <b>2.38</b> and Fe <sub>3</sub> O <sub>4</sub> @initiator <b>4.12</b> ( <b>4.7</b> ).....	95
4.3.5 Selective Ag <sup>+</sup> extraction using Fe <sub>3</sub> O <sub>4</sub> @oleate ( <b>4.9</b> ), Fe <sub>3</sub> O <sub>4</sub> @initiator <b>4.12</b> ( <b>4.7</b> ), and Fe <sub>3</sub> O <sub>4</sub> @initiator@amide 2.38 ( <b>4.8</b> ).....	98
4.4 Summary of results. ....	101
Chapter 5: Synthesis and application of core-shell Fe <sub>3</sub> O <sub>4</sub> /imidazolium chloride Ag <sup>+</sup> ligand nanoparticle.....	102
5.1 Introduction.....	103
5.2 Aims and objectives.....	103
5.3 Results and discussion .....	104
5.3.1 Synthesis of core-shell iron oxide/imidazolium-based Ag <sup>+</sup> extractant nanoparticle (Fe <sub>3</sub> O <sub>4</sub> @SiO <sub>2</sub> @SIC) <b>5.2</b> .....	104
5.3.2 Ag <sup>+</sup> extraction studies .....	111
5.3.3 Optimization studies for the selective extraction of Ag <sup>+</sup> by the Fe <sub>3</sub> O <sub>4</sub> @SiO <sub>2</sub> @SIC <b>5.2</b> (pH, contact time, nanoparticle extractant dose).....	113
5.3.4 Effect of type of stripping agents.....	119
5.4 Summary of results .....	121
Chapter 6: Conclusion and Future work .....	122
6.1 Conclusion .....	123
6.2 Future work.....	124
Chapter 7 : Experimental .....	125
7.1 Materials and Instrumentation .....	126
7.2 Experimental for chapter two.....	127

7.2.1	General method for synthesis of benzyl cysteamines ( <b>2.20</b> and <b>2.25 – 2.28</b> ).....	127
7.2.2	Synthesis of 2,2-dimethyl-2-benzylthioethyl amine ( <b>2.29</b> ).....	129
7.2.3	Attempted syntheses of <i>N</i> <sup>1</sup> , <i>N</i> <sup>3</sup> -bis(2(benzylthio)ethyl)malonamide derivative <b>2.10</b> .....	130
7.2.4	General method for synthesis of malonamide derivatives ( <b>2.10</b> and <b>2.14 – 2.18</b> ).....	131
7.2.5	General method for synthesis of gem-diethyl malonamide ( <b>2.33 – 2.37</b> )....	134
7.2.6	Attempted synthesis of <i>N</i> <sup>1</sup> -(2-benzylthio)ethyl)- <i>N</i> <sup>3</sup> -(2-((4-vinylbenzyl)thio)ethyl)malonamide ( <b>2.13</b> ).....	137
7.2.7	Synthesis of <i>N</i> -(2-((4-Vinylbenzyl)thio)ethyl)acetamide ( <b>2.38</b> ).....	137
7.2.8	Competitive metal extraction .....	138
7.3	Experimental for chapter three.....	142
7.3.1	Synthesis of Ag <sup>+</sup> complexes of <b>2.10</b> and <b>2.38</b> and attempted crystal growth.....	142
7.3.2	Mass spectrometry studies of Ag <sup>+</sup> - <b>2.10</b> and Ag <sup>+</sup> - <b>2.38</b> complexes.....	143
7.3.3	Job's plot for the interaction of AgClO <sub>4</sub> with <b>2.10</b> or <b>2.38</b> .....	144
7.3.4	Mole ratio plot for the interaction of AgClO <sub>4</sub> with <b>2.10</b> or <b>2.38</b> .....	145
7.4	Experimental for chapter four.....	146
7.4.1	Synthesis of Fe <sub>3</sub> O <sub>4</sub> @oleate ( <b>4.9</b> ).....	146
7.4.2	Synthesis of 2-Bromo-2-methyl- <i>N</i> -(3-(triethoxysilyl)propyl)propenamide (BMTP) ( <b>4.12</b> ) .....	148
7.4.3	Synthesis of Fe <sub>3</sub> O <sub>4</sub> @initiator <b>4.12</b> ( <b>4.7</b> ).....	149
7.4.4	Attempted linkage of amide <b>2.38</b> to Fe <sub>3</sub> O <sub>4</sub> @initiator <b>4.12</b> ( <b>4.7</b> ).....	149

7.4.5	Synthesis of Cu- <i>N</i> -(2-(4-vinylbenzylthio)ethyl)-acetamide ( <b>4.16</b> ).....	150
7.4.6	Synthesis of poly(amide <b>2.38</b> ) ( <b>4.17</b> ) by the solution ATRP of amide <b>2.38</b> .....	150
7.4.7	Synthesis of poly(amide <b>2.38</b> ) ( <b>4.17</b> ) by free radical polymerization.....	151
7.4.8	Free radical-mediated linkage of amide <b>2.38</b> to Fe <sub>3</sub> O <sub>4</sub> @initiator <b>4.12</b> ( <b>4.7</b> ).....	151
7.4.9	Competitive metal extraction .....	152
7.5	Experimental for chapter five .....	154
7.5.1	Synthesis of Fe <sub>3</sub> O <sub>4</sub> <b>5.4</b> .....	154
7.5.2	Synthesis of Fe <sub>3</sub> O <sub>4</sub> @SiO <sub>2</sub> <b>5.6</b> .....	156
7.5.3	Synthesis of Triethoxysilylpropylimidazolium chloride <b>5.9</b> .....	156
7.5.4	Synthesis of Fe <sub>3</sub> O <sub>4</sub> @SiO <sub>2</sub> @siloxylimidazolium chloride <b>5.2</b> .....	157
7.5.5	Competitive metal extraction .....	157
	References.....	166

## List of Figures

Figure 1.1: Chemical precipitation method schematic.....	3
Figure 1.2: Membrane filtration method schematic <sup>15</sup> .....	4
Figure 1.3: Ion exchange method schematic.....	5
Figure 1.4: Schematic of a typical electrocoagulation setup <sup>23</sup> .....	6
Figure 1.5: Typical electrofloatation setup for heavy metal removal <sup>24</sup> .....	7
Figure 1.6: Typical electrodeposition setup for metal removal .....	8
Figure 1.7: Various adsorption mechanisms in metal recovery .....	9
Figure 1.8: Single and multiwalled carbon nanotubes .....	12
Figure 1.9: Schematic for the hot injection thermal decomposition method .....	17
Figure 1.10: Typical schematic for the microemulsion method for synthesis of iron oxide nanoparticles <sup>122</sup> .....	19
Figure 1.11: Schematic for a typical co-precipitation method for iron oxide nanoparticles synthesis.....	20
Figure 1.12: Some chelating agents employed for controlling the size of iron oxide nanoparticles .....	23
Figure 1.13: Some organic ligands component of some magnetic metal-organic framework extractant employed for metal recovery.....	24
Figure 1.14: Structure of humic acid <sup>152</sup> .....	26
Figure 1.15: Some ligands with silane handle employed for metal recovery purposes .....	28
Figure 1.16: Some pyridine-based ligands previously linked to multiwalled carbon nanotubes-Fe <sub>3</sub> O <sub>4</sub> composite and employed for metal recovery .....	29
Figure 1.17: Some amine-based ligands previously utilized for metal recovery .....	29
Figure 1.18: Structure of 3-mercaptopropyltrimethoxysilane and illustration of the Fe <sub>3</sub> O <sub>4</sub> @SiO <sub>2</sub> -SH adsorbent .....	30
Figure 1.19: Structure of ionic liquids: Compound <b>1.22</b> was the first synthesized ionic liquid <sup>171,172</sup> while compound <b>1.23</b> was linked to Fe <sub>3</sub> O <sub>4</sub> for the recovery of cadmium. <sup>173</sup> .....	31

Figure 1.20: Approaches for linking polymers to iron oxide nanoparticles.....	32
Figure 1.21: Some synthetic polymeric ligands previously employed for metal recovery....	33
Figure 1.22: Structure of chitosan.....	35
Figure 1.23: Overall aim of this thesis.....	35
Figure 2.1: Some Ag <sup>+</sup> -selective ligands reported in the literature.....	38
Figure 2.2: Some tripodal Ag <sup>+</sup> ligands <sup>197</sup> .....	40
Figure 2.3: Generic approach to making nanoparticle/polymer composite.....	42
Figure 2.4: Potential scaffolds for selective Ag <sup>+</sup> recovery.....	42
Figure 2.5: Malonamide derivatives prepared and tested in this chapter.....	43
Figure 2.6: A styryl malonamide derivative <b>2.13</b> .....	48
Figure 2.7: Malonamide derivative target ligands <b>2.14-2.18</b> .....	49
Figure 2.8: Structures of two acid chlorides that can provide the acyl moiety of the target malonamide derivatives.....	50
Figure 2.9: Structures of malonamides derivatives with vinyl handles.....	51
Figure 2.10: Summary of successfully prepared potential Ag <sup>+</sup> selective ligands.....	53
Figure 2.11: Structures of malonamide derivative <b>2.10</b> and amide <b>2.38</b> .....	55
Figure 2.12: ICP-OES data showing metal extraction efficiencies by neat chloroform (control), malonamide derivative <b>2.10</b> and amide <b>2.38</b> .....	56
Figure 2.13: ICP-OES data showing metal extraction efficiencies by malonamide derivatives <b>2.10, 2.14-2.17</b> .....	57
Figure 2.14: ICP-OES data showing metal extraction efficiencies by malonamide derivatives <b>2.10, 2.18</b> and <b>2.33</b> .....	59
Figure 3.1: Some Ag <sup>+</sup> complexes investigated by means x-ray diffraction towards the determination of their stoichiometry.....	63

Figure 3.2: Some Ag <sup>+</sup> ligands and complexes studied by means mass spectrometry towards the determination of their stoichiometry.....	64
Figure 3.3: Stoichiometry of the Ag <sup>+</sup> complexes formed by these ligands were investigated by Job's and mole ratio plots.....	64
Figure 3.4: Partial low-resolution ESI mass spectra of Ag <sup>+</sup> - <b>2.10</b> complexes from treatment of <b>2.10</b> with (a) one (b) two and (c) three equivalents of AgOSO <sub>2</sub> CF <sub>3</sub> .....	68
Figure 3.5: Partial low-resolution ESI mass spectra of Ag <sup>+</sup> - <b>2.38</b> complexes from treatment of <b>2.38</b> with (a) one equivalent (0-500 <i>m/z</i> ), (b) one equivalent (500-1000 <i>m/z</i> ), (c) two equivalents (0-500 <i>m/z</i> ), (d) two equivalents (500-1000 <i>m/z</i> ), (e) three equivalents (0-500 <i>m/z</i> ), (f) three equivalents (500-1000 <i>m/z</i> ) of AgOSO <sub>2</sub> CF <sub>3</sub> .....	69
Figure 3.6: (a and b) <sup>1</sup> H NMR (300 MHz) spectra of the interaction of Ag <sup>+</sup> with (a) <b>2.10</b> and (b) <b>2.38</b> respectively; (c and d) Job's plots of the interaction of 0.005 M Ag <sup>+</sup> with (c) 0.005 M malonamide derivative <b>2.10</b> and (d) 0.005 M amide <b>2.38</b> at room temperature.....	71
Figure 3.7: (a and b) <sup>1</sup> H NMR (300 MHz) spectra of the interaction of Ag <sup>+</sup> with (a) malonamide derivative <b>2.10</b> and (b) amide <b>2.38</b> and (b and d) mole ratio plots of the interaction of Ag <sup>+</sup> with (a) malonamide derivative <b>2.10</b> and (b) amide <b>2.38</b> .....	73
Figure 3.8: Proposed structures for (a) [Ag( <b>2.10</b> )] <sup>+</sup> , (b) [Ag( <b>2.38</b> )] <sup>+</sup> and (c) [Ag( <b>2.38</b> ) <sub>2</sub> ] <sup>+</sup> based on stoichiometry results observed from mass spectrometry and <sup>1</sup> H NMR titrations (leading to Job's and mole ratio plots).	74
Figure 4.1: Structure of Fe <sub>3</sub> O <sub>4</sub> @SiO <sub>2</sub> @TiO <sub>2</sub> @ Ag <sup>+</sup> -imprinted triazine.....	78
Figure 4.2: Examples of thio-based Ag <sup>+</sup> ligands employed for metal recovery in literature.....	78
Figure 4.3: Ag <sup>+</sup> ligands with trimethoxysilane handles previously utilized for metal recovery in literature.....	79
Figure 4.4: X-ray diffractogram of Fe <sub>3</sub> O <sub>4</sub> @oleate <b>4.9</b> (Co K $\alpha$ source wavelength = 1.79 Å, voltage = 40 kV, current = 40 mA).....	82

Figure 4.5: FTIR spectra of (a) Fe <sub>3</sub> O <sub>4</sub> @oleate <b>4.9</b> (b) Fe <sub>3</sub> O <sub>4</sub> @initiator <b>4.12 (4.7)</b> .....	83
Figure 4.6: XPS survey spectra of (a) Fe <sub>3</sub> O <sub>4</sub> @oleate <b>4.9</b> (black) and (b) Fe <sub>3</sub> O <sub>4</sub> @initiator <b>4.12 (4.7)</b> (blue) (X-ray source: Mono (Al), 150 W, 90°, Slot).....	84
Figure 4.7: XPS spectra of core level scans of C 1s in (a) Fe <sub>3</sub> O <sub>4</sub> @oleate <b>4.9</b> and (b) Fe <sub>3</sub> O <sub>4</sub> @initiator <b>4.7</b> .....	84
Figure 4.8: (a,c) Transmission electron micrographs of (a) Fe <sub>3</sub> O <sub>4</sub> @oleate <b>4.9</b> and (c) Fe <sub>3</sub> O <sub>4</sub> @initiator <b>4.12 (4.7)</b> , (b,d) Histograms for the size distributions of (b) Fe <sub>3</sub> O <sub>4</sub> @oleate <b>4.9</b> and (d) Fe <sub>3</sub> O <sub>4</sub> @initiator <b>4.12 (4.7)</b>	85
Figure 4.9: Magnetization curves for (a) Fe <sub>3</sub> O <sub>4</sub> @oleate <b>4.9</b> (black) and (b) Fe <sub>3</sub> O <sub>4</sub> @initiator <b>4.12 (4.7)</b> (blue), (Temperature: 300 K)	86
Figure 4.10: Thermogravimetry analysis curves of (a) Fe <sub>3</sub> O <sub>4</sub> @oleate <b>4.9</b> and (b) Fe <sub>3</sub> O <sub>4</sub> @initiator <b>4.7</b> (red) and Fe <sub>3</sub> O <sub>4</sub> @oleate <b>4.9</b> (dashed black), (Atmosphere: nitrogen, heating rate: 10 °C/min)	87
Figure 4.11: FTIR spectra of (a) Fe <sub>3</sub> O <sub>4</sub> @initiator <b>4.12 (4.7)</b> (black) and (b) brown solid <b>4.15</b> (red).....	89
Figure 4.12: XPS S 2p core level scans of (a) Fe <sub>3</sub> O <sub>4</sub> @initiator <b>4.12 (4.7)</b> (blue), (b) brown solid <b>4.15</b> (green).....	89
Figure 4.13: TGA thermograms of (a) brown solid <b>4.15</b> (black) (b) Fe <sub>3</sub> O <sub>4</sub> @initiator <b>4.12 (4.7)</b> (red) and (c) amide <b>2.38</b> (blue).....	90
Figure 4.14: <sup>1</sup> H NMR (300 MHz, CDCl <sub>3</sub> ) spectra of amide <b>2.38</b> and complex <b>4.16</b> .....	91
Figure 4.15: Low resolution mass spectrum of Cu <sup>+</sup> complex <b>4.16</b> .....	92
Figure 4.16: A section of <sup>1</sup> H NMR (d <sub>6</sub> -DMSO, 300 MHz) spectra of reaction mixture from the attempted solution ATRP of amide <b>2.38</b> at (a) t = 0 h and (b) t = 16 h. (x = phenyl protons of <i>p</i> -DMB internal standard).....	93
Figure 4.17: A section of <sup>1</sup> H NMR (d <sub>6</sub> -DMSO, 300 MHz) spectra of reaction mixture from the attempted polymerization of amide <b>2.38</b> at (a) t = 0 h and (b) t = 17 h.....	95
Figure 4.18: FTIR spectra of (a) Fe <sub>3</sub> O <sub>4</sub> @initiator <b>4.12 (4.7)</b> (black) (b) Fe <sub>3</sub> O <sub>4</sub> @initiator@amide <b>2.38 (4.8)</b> (red).....	97

Figure 4.19: XPS spectra of core level scans for S 2p in (a) Fe <sub>3</sub> O <sub>4</sub> @initiator <b>4.12 (4.7)</b> (red) and (b) Fe <sub>3</sub> O <sub>4</sub> @initiator@amide <b>2.38 (4.8)</b> (green).....	97
Figure 4.20: TGA thermogram of (a) Fe <sub>3</sub> O <sub>4</sub> @initiator <b>4.12 (4.7)</b> (black dashed) and (b) Fe <sub>3</sub> O <sub>4</sub> @initiator@amide <b>2.38 (4.8)</b> (red) (c) amide <b>2.38</b> (blue dashed) (Atmosphere: Nitrogen, Heating rate: 10 °C/min).....	98
Figure 4.21: Structures of nanoparticles <b>4.7 - 4.9</b> .....	100
Figure 4.22: ICP-OES data showing metal extraction efficiencies by magnetic nanoparticles <b>4.7 - 4.9</b> .....	100
Figure 5.1: Core-shell magnetic/imidazolium Ag <sup>+</sup> ligand nanoparticles.....	103
Figure 5.2: Core-shell iron oxide/imidazolium-based Ag <sup>+</sup> extractant composite nanoparticle (Fe <sub>3</sub> O <sub>4</sub> @SiO <sub>2</sub> @SIC) <b>5.2</b> .....	104
Figure 5. 3: X-ray diffractogram of bare Fe <sub>3</sub> O <sub>4</sub> (Co K $\alpha$ source wavelength = 1.79 Å, voltage = 40 kV, current = 40 mA).....	106
Figure 5.4: (a,c,e) Transmission electron micrographs of (a) Bare Fe <sub>3</sub> O <sub>4</sub> <b>5.4</b> (b) Fe <sub>3</sub> O <sub>4</sub> @SiO <sub>2</sub> <b>5.6</b> and (c) Fe <sub>3</sub> O <sub>4</sub> @SiO <sub>2</sub> @SIC <b>5.2</b> , (b,d,f) Histograms showing size distribution of (b) Bare Fe <sub>3</sub> O <sub>4</sub> <b>5.4</b> (d) Fe <sub>3</sub> O <sub>4</sub> @SiO <sub>2</sub> <b>5.6</b> and (f) Fe <sub>3</sub> O <sub>4</sub> @SiO <sub>2</sub> @SIC <b>5.2</b> .....	107
Figure 5.5: Magnetization curves for (a) Bare Fe <sub>3</sub> O <sub>4</sub> <b>5.4</b> (b) Fe <sub>3</sub> O <sub>4</sub> @SiO <sub>2</sub> <b>5.6</b> and (c) Fe <sub>3</sub> O <sub>4</sub> @SiO <sub>2</sub> @SIC <b>5.2</b> (Inset: Expanded magnetization curve showing coercivities of bare Fe <sub>3</sub> O <sub>4</sub> <b>5.4</b> (black), Fe <sub>3</sub> O <sub>4</sub> @SiO <sub>2</sub> <b>5.6</b> (red), Fe <sub>3</sub> O <sub>4</sub> @SiO <sub>2</sub> @SIC <b>5.2</b> (blue), separation of <b>5.2</b> from an aqueous solution using a magnet).....	108
Figure 5.6: FTIR spectra of (a) Bare Fe <sub>3</sub> O <sub>4</sub> <b>5.4</b> (black) (b) Fe <sub>3</sub> O <sub>4</sub> @SiO <sub>2</sub> <b>5.6</b> (red) and (c) Fe <sub>3</sub> O <sub>4</sub> @SiO <sub>2</sub> @SIC <b>5.2</b> (green).....	109
Figure 5.7: XPS survey spectra of (a) Bare Fe <sub>3</sub> O <sub>4</sub> <b>5.4</b> (black) (b) Fe <sub>3</sub> O <sub>4</sub> @SiO <sub>2</sub> <b>5.6</b> (red) and (c) Fe <sub>3</sub> O <sub>4</sub> @SiO <sub>2</sub> @SIC <b>5.2</b> (green).....	110

Figure 5.8: TGA thermograms for (a) Bare Fe <sub>3</sub> O <sub>4</sub> <b>5.4</b> (black) (b) Fe <sub>3</sub> O <sub>4</sub> @SiO <sub>2</sub> <b>5.6</b> (red) and (c) Fe <sub>3</sub> O <sub>4</sub> @SiO <sub>2</sub> @SIC <b>5.2</b> (blue) (Atmosphere: nitrogen, heating rate: 10 °C/min).....	111
Figure 5.9: Extraction efficiencies of bare Fe <sub>3</sub> O <sub>4</sub> <b>5.4</b> , Fe <sub>3</sub> O <sub>4</sub> @SiO <sub>2</sub> <b>5.6</b> and Fe <sub>3</sub> O <sub>4</sub> @SiO <sub>2</sub> @SIC <b>5.2</b> for Ag <sup>+</sup> extraction from aqueous solution. (conditions: [Ag <sup>+</sup> ] <sub>0</sub> = 1 ppm, volume = 10 mL, pH = 1.30, contact time = 45 min, temperature = RT, extractant dose = 20 mg).....	112
Figure 5.10: Effect of pH in the selective extraction of Ag <sup>+</sup> from simulated mixed metal aqueous solution by the Fe <sub>3</sub> O <sub>4</sub> @SiO <sub>2</sub> @SIC <b>5.2</b> (Conditions: [M <sup>n+</sup> ] = 2 ppm, volume = 10 mL, contact time = 2 h, temperature = RT, extractant dose = 10 mg).....	115
Figure 5.11: Effect of contact time in the selective extraction of Ag <sup>+</sup> from simulated mixed metal aqueous solution by the Fe <sub>3</sub> O <sub>4</sub> @SiO <sub>2</sub> @SIC <b>5.2</b> (Conditions: [M <sup>n+</sup> ] = 2 ppm, volume = 10 mL, pH = 1.30, temperature = RT, extractant dose = 10 mg).....	116
Figure 5.12: Effect of extractant dose in the selective extraction of Ag <sup>+</sup> from simulated mixed metal aqueous solution by the Fe <sub>3</sub> O <sub>4</sub> @SiO <sub>2</sub> @SIC <b>5.2</b> (conditions: [M <sup>n+</sup> ] = 2 ppm, volume = 10 mL, pH = 1.30, contact time = 45 min, temperature = RT).....	118
Figure 5.13: Effect of stripping agent type and concentration in the stripping of Ag <sup>+</sup> from impregnated Fe <sub>3</sub> O <sub>4</sub> @SiO <sub>2</sub> @SIC <b>5.2</b> (volume of acid = 5 mL, contact time = 1 h, temperature = RT).....	120

## List of Tables

Table 1.1: Surface area of some nanosized metal oxides.....	13
Table 2.1: Classification of Lewis bases into Hard, Soft or Borderline <sup>204</sup> .....	39
Table 2.2: Classification of Lewis acids into Hard, Soft or Borderline <sup>204</sup> .....	39
Table 2.3: Extraction efficiencies of some proven Ag <sup>+</sup> -selective ligands for Ag <sup>+</sup> extraction	41

Table 2.4: Effect of reaction time on synthesis of <b>2.20</b> at room temperature .....	44
Table 2.5: Attempted synthesis of malonamide derivative <b>2.10</b> by microwave assisted method .....	47
Table 2.6: Synthesis of malonamide derivatives <b>2.10</b> , <b>2.14</b> – <b>2.18</b> .....	49
Table 2.7: Efficiency and selectivity of <b>2.10</b> and <b>2.14-2.17</b> for Ag <sup>+</sup> relative to Cu <sup>2+</sup> and Pb <sup>2+</sup> .....	58
Table 3.1: Ag <sup>+</sup> complexes <b>3.21</b> – <b>3.24</b> .....	66
Table 3.2: Effect of Ag <sup>+</sup> equivalent on stoichiometry of Ag <sup>+</sup> complexes of <b>2.10</b> and <b>2.38</b> ...	67
Table 4.1: Conversion of amide <b>2.38</b> after solution ATRP (concentration of protons was represented by their integrals in the <sup>1</sup> H NMR spectrum) .....	93
Table 4.2: Conversion of amide <b>2.38</b> (concentration of protons was represented by their integrals in the <sup>1</sup> H NMR spectrum).....	95
Table 4.3: Efficiency and selectivity of nanoparticles <b>4.7</b> - <b>4.9</b> for Ag <sup>+</sup> extraction.....	100
Table 5.1: Effect of pH on selectivity of the Fe <sub>3</sub> O <sub>4</sub> @SiO <sub>2</sub> @SIC <b>5.2</b> for Ag <sup>+</sup> over Cu <sup>2+</sup> and Pb <sup>2+</sup> .....	115
Table 5.2: Effect of contact time on selectivity of the Fe <sub>3</sub> O <sub>4</sub> @SiO <sub>2</sub> @SIC <b>5.2</b> for Ag <sup>+</sup> over Cu <sup>2+</sup> & Pb <sup>2+</sup> .....	117
Table 5.3: Effect of extractant dose on selectivity by the Fe <sub>3</sub> O <sub>4</sub> @SiO <sub>2</sub> @SIC <b>5.2</b> for Ag <sup>+</sup> over Cu <sup>2+</sup> and Pb <sup>2+</sup> .....	119
Table 7.1: Calibration data for the ICP-OES analysis .....	139
Table 7.2: ICP-OES extraction analysis data for neat chloroform (control).....	139
Table 7.3: ICP-OES extraction analysis data for <b>2.10</b> .....	139

Table 7.4: ICP-OES extraction analysis data for <b>2.38</b> .....	140
Table 7.5: ICP-OES extraction analysis data for <b>2.14</b> .....	140
Table 7.6: ICP-OES extraction analysis data for <b>2.15</b> .....	140
Table 7.7: ICP-OES extraction analysis data for <b>2.16</b> .....	141
Table 7.8: ICP-OES extraction analysis data for <b>2.17</b> .....	141
Table 7.9: ICP-OES extraction analysis data for <b>2.18</b> .....	141
Table 7.10: ICP-OES extraction analysis data for <b>2.33</b> .....	142
Table 7.11: <sup>1</sup> H NMR titration data for the Job's plot of the interaction of <b>2.10</b> and AgClO <sub>4</sub> .....	144
Table 7.12: <sup>1</sup> H NMR titration data for the Job's plot of the interaction of <b>2.38</b> and AgClO <sub>4</sub> .....	145
Table 7.13: <sup>1</sup> H NMR titration data for the mole ratio plot of the interaction of <b>2.10</b> and AgClO <sub>4</sub> .....	146
Table 7.14: <sup>1</sup> H NMR titration data for the mole ratio plot of the interaction of <b>2.38</b> and AgClO <sub>4</sub> .....	146
Table 7.15: ICP-OES calibration data for the metal extraction experiment by Fe <sub>3</sub> O <sub>4</sub> @oleate ( <b>4.9</b> ), Fe <sub>3</sub> O <sub>4</sub> @initiator <b>4.12</b> ( <b>4.7</b> ) and Fe <sub>3</sub> O <sub>4</sub> @initiator@amide <b>2.38</b> ( <b>4.8</b> ) .....	153
Table 7.16: ICP-OES extraction analysis data for Fe <sub>3</sub> O <sub>4</sub> @oleate ( <b>4.9</b> ) .....	153
Table 7.17: ICP-OES extraction analysis data for Fe <sub>3</sub> O <sub>4</sub> @initiator <b>4.12</b> ( <b>4.7</b> ).....	153
Table 7.18: ICP-OES extraction analysis data for Fe <sub>3</sub> O <sub>4</sub> @initiator@amide <b>2.38</b> ( <b>4.8</b> ) .....	154
Table 7.19: ICP-OES calibration data for the metal extraction experiment by Fe <sub>3</sub> O <sub>4</sub> @SiO <sub>2</sub> @siloxymidazolium chloride <b>5.2</b> and Ag <sup>+</sup> stripping studies different stripping agents .....	159
Table 7.20 (a-e): ICP-OES extraction analysis data by Fe <sub>3</sub> O <sub>4</sub> @SiO <sub>2</sub> @siloxymidazolium chloride <b>5.2</b> at pH 1.03 – 4.97.....	160
Table 7.21 (a-g): ICP-OES extraction analysis data by Fe <sub>3</sub> O <sub>4</sub> @SiO <sub>2</sub> @siloxymidazolium chloride <b>5.2</b> from 0 to 90 min .....	161

Table 7.22 (a-e): ICP-OES extraction analysis data by Fe <sub>3</sub> O <sub>4</sub> @SiO <sub>2</sub> @siloxymidazolium chloride <b>5.2</b> using 5 – 80 mg.....	164
Table 7.23: ICP-OES extraction analysis data of the stripping of Ag <sup>+</sup> by different stripping agents .....	165

## Acknowledgements

I will like to start by expressing my gratitude to Prof. Andrew J. Clark and Prof. Stefan A.F. Bon as they trusted and expertly guided me to undertake a rather difficult project. And a thank you to The Commonwealth Scholarship Commission and The University of Warwick for funding this research.

On a personal note, I will like to thank Dave, Phillip and Andy 3 for advice on laboratory work and techniques and the several lunches we had together on campus. Past and present members of the Clark, Chan, Rourke and Bon groups including Jess, Paul, Stuart, Nyle, Jivan, Brooke, Ross, Andrea and the MChems made my time enjoyable with the get-togethers and education about life in the UK.

Now, I can confidently operate several analytical instruments and I have the following people to thank for that; Dr. Marc Walker (XPS), Dr. Daniel Lester (TGA), Dr. Amari Houari (TEM), Dr. Lijiang Song, Mr. Phillip Aston & Mr. Jim Morrey (ICP-OES), Dr David Walker (XRD). I am grateful to Dr. Ivan Prokes & Mr. Rob Perry for training on the open access NMR facilities and running high resolution NMR experiments. Magnetic susceptibility results provided in chapters 4 and 5 were possible thanks to Dr. Lees Martin of the Physics department. I have enjoyed support from collaborators including Dr. Devin Saspford (Cardiff) & Dr. Richard Crane (Exeter).

Away from school, my family – Dad, mom, Abigail, Segun, and Bosun have provided the much-needed moral support. During my PhD I met my fiancée – Tumilara and I am grateful for all her support and understanding. Also, I appreciate the chats I had with my previous and present flatmates during my PhD.

Finally, I am grateful to my best friend ever; Jesus Christ!

## **Declaration**

The work presented in this thesis is the original work of the author. Reference to previous related results and ideas has been fully acknowledged. All work has been performed in the Department of Chemistry at the University of Warwick between October 2015 and May 2019 and has not been submitted for a degree at any other institution.

Abiodun Daniel Aderibigbe

## Abstract

The work presented in this thesis reports the synthesis and application of some novel Ag<sup>+</sup>-selective ligands and magnetic iron oxide /Ag<sup>+</sup>-ligand nanocomposites for Ag<sup>+</sup> recovery from aqueous solutions. Also investigated is the Ag<sup>+</sup>-selective ligand binding studies using traditional methods including mass spectrometry and proton NMR titrations. Chapter 1 provides a detailed introduction to methods of metal recovery leading to discussion of adsorption technology and ending with a detail review of types of iron oxide/ligand composites for metal recovery.

Chapter 2 reports on a novel room temperature route to accessing a range of novel *N,N'*-malonamide derivatives and styrylamide Ag<sup>+</sup>-selective ligands, and the measurement of their efficiency and selectivity for Ag<sup>+</sup> extraction from aqueous solution.

Chapter 3 presents a detailed investigation of the binding stoichiometries of two Ag<sup>+</sup> selective ligands (*N,N'*-malonamide derivatives and styrylamide) with Ag<sup>+</sup>, using mass spectrometry and proton NMR titrations (leading to Job's and mole ratio plots).

Chapter 4 focuses on the synthesis of iron oxide nanoparticle and its linkage to a novel styrylamide Ag<sup>+</sup>-selective ligand by means of atom transfer radical polymerization (ATRP) and free radical polymerization (FRP) and ending with testing of the iron oxide/styryl amide nanocomposite obtained for Ag<sup>+</sup> recovery from aqueous solution.

Chapter 5 describes the synthesis of iron oxide/imidazolium-based Ag<sup>+</sup>-ligand nanocomposite and the optimization of parameters (pH, time, dosage and stripping agent) for efficient and selective Ag<sup>+</sup> recovery from aqueous solutions.

Chapter 6 details the experimental procedures and chemical analyses undertaken in this thesis.

## Abbreviations

1-EtImSH	1-Ethylimidazoline-2-thione
AC	Activated carbon
AIBN	Azobisisobutyronitrile
APTES	3-Aminopropyltriethoxysilane
BET	Brunauer-Emmett-Teller
CD <sub>3</sub> OD	Deuterated methanol
CM- $\beta$ -BD	Carboxymethyl- $\beta$ -cyclodextrin
CNTs	Carbon nanotubes
CTAB	Cetyl trimethylammonium bromide
DETA	Diethylenetriamine
DMF	Dimethylformamide
DMSO-d <sub>6</sub>	Deuterated dimethylsulfoxide
DPA	Diphenylamine
EC	Electrocoagulation
ED	Electrodeposition
EDTA	Ethylenediaminetetraacetic acid
EE	Extraction efficiency
EF	Electrofloatation
ESI-MS	Electrospray ionization-mass spectrometry
EtOAc	Ethylacetate
FAAS	Flame atomic absorption spectrophotometry
FAB-MS	Fast atom bombardment-mass spectrometry
FRP	Free radical polymerization
FTIR/IR	Fourier transform infrared spectroscopy
gly-ppy	glycine doped polypyrrole
GO	Graphene oxide
HP	Hydroxide precipitation
HPLC	High performance liquid chromatography
HRMS	High resolution mass spectrometry
HSAB	Hard soft acid and base
ICP-OES	Inductively coupled plasma optical emission spectroscopy
IL	Ionic liquid

IONPs	Iron oxide nanoparticles
LRMS	Low resolution mass spectrometry
MF	Membrane filtration
MIEs	Magnetic inorganic extractants
MMOF	Magnetic metal organic framework
MOEs	Magnetic organic extractants
MOFs	Magnetic organic frameworks
MPEs	Magnetic polymeric extractants
MRI	Magnetic resonance imaging
MWCNTs	Multiwalled carbon nanotubes
NMOs	Nanosized metal oxides
<i>p</i> -DMB	<i>para</i> -dimethoxybenzene
PEI	Polyethyleneimine
PILs	polyionic liquids
PMDETA	Pentamethyldiethylenetriamine
RTIL	Room temperature ionic liquid
SE	Stripping efficiency
SEM	Scanning electron microscopy/microscope
SI-ATRP	Surface initiated atom transfer radical polymerization
SILM	Supported ionic liquid membranes
SP	Sulfide precipitation
SQUID	Superconducting quantum interference device
SWCNTs	Single walled carbon nanotubes
TD	Thermal decomposition
TEM	Transmission electron microscopy/microscope
TEOS	Tetraethoxysilane
TGA	Thermogravimetric analysis
THF	Tetrahydrofuran
TLC	Thin layer chromatography
TPI	Triethoxysilylpropylisocyanate
TSIL	Task specific ionic liquid
UV/Visible	ultraviolet/visible spectroscopy
XPS	X-ray photoelectron spectroscopy
XRD	X-ray diffraction

# **Chapter 1: Introduction**

## 1.1 Introduction

Metals are an important part of our everyday life. They are found in homes (e.g. in kitchen utensils), cars and in public infrastructure (e.g. bridges) etc. A very important class of metals are the precious metals including gold, platinum, rhodium, iridium, osmium, palladium, rhenium, ruthenium and silver.<sup>1</sup> Silver stands out from this group due to its outstanding thermal, electrical and antimicrobial properties.<sup>2</sup> In fact, silver has the greatest thermal and electrical conductivity of any metal.<sup>3</sup> Consequently, silver is found in phones<sup>4</sup>, batteries<sup>5</sup>, jewellery<sup>6</sup> and in dressings for wounds<sup>7</sup> to mention a few.

As the world population increases, the demand for products containing silver is certain to increase as well. Unfortunately, silver just like other metals are non-renewable resources. Therefore, in order to meet the increasing demand, the supply of silver must be guaranteed. Two major options that have been explored to guarantee the supply of silver and indeed other metals is the search for new primary sources<sup>8</sup> (i.e. new metal ore deposits) and the secondary sources or urban mining (in other words, recycling of metals)<sup>9</sup>. Therefore, a review of known methods of metal recovery, highlighting where possible examples involving silver recovery, will be undertaken in the following sections.

## 1.2 Methods of metal recovery

### 1.2.1 Chemical precipitation

The chemical precipitation method involves the conversion of soluble metal ions into insoluble precipitates using precipitants (see Figure 1.1 below).<sup>10,11</sup> Perhaps due to its simplicity, the method is very popular in industrial scale metal removal processes.<sup>12</sup> However, some shortcomings of the method includes the need for large amounts of precipitating agents, the generation of large amount of waste which require appropriate disposal and the inefficiency of the method in media with low metal concentration.<sup>12</sup> The chemical precipitation method has been achieved by the sulfide and hydroxide precipitation techniques.<sup>10-12</sup>

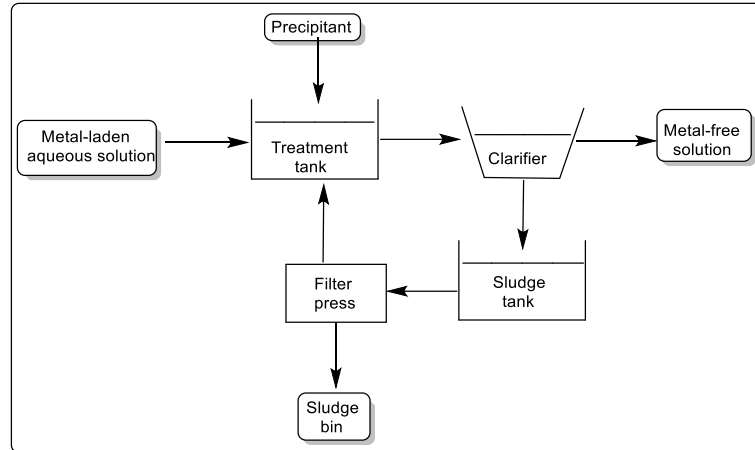
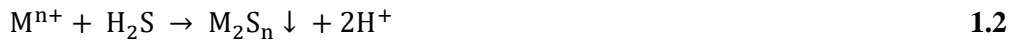


**Figure 1.1: Chemical precipitation method schematic**

### 1.2.1.1 Sulfide precipitation



The sulfide precipitation (SP) technique is based on the reaction between  $\text{H}_2\text{S}$  and soluble metal ions to form insoluble metal sulfides (Equations 1.1 and 1.2).<sup>10</sup> The sulfides;  $\text{FeS}$ ,  $\text{CaS}$ ,  $\text{Na}_2\text{S}$ , are some examples of precipitants used in this method. In 2016, Ahlatci *et al*<sup>13</sup> reported the quantitative precipitation (>99 %) of  $\text{Ag}^+$  as  $\text{AgS}$  using  $\text{Na}_2\text{S}$  as precipitant. It was also observed that increasing the  $\text{Na}_2\text{S}$  concentration increased the amount of  $\text{AgS}$  precipitated.

Some advantages of the SP technique include high degree of metal removal over a broad pH range, selective metal recovery and generation of high density sludge which is easy to remove.<sup>10-12</sup> However the most common drawback of the method is the generation of  $\text{H}_2\text{S}$  gas due to the acidic conditions involved in the process. Therefore, it has been advised that the process be undertaken under neutral or basic conditions.<sup>10-12</sup>

### 1.2.1.2 Hydroxide precipitation



The hydroxide precipitation (HP) method involves the appropriate tuning of the pH of the metal-laden aqueous solution, by the addition of specific precipitating agents, with the aim of

generating insoluble metal hydroxides (Equation 1.3).<sup>10</sup> The removal of metals like  $\text{Cd}^{2+}$ ,  $\text{Zn}^{2+}$ ,  $\text{Cu}^{2+}$  and  $\text{Mn}^{2+}$  by the addition of precipitants like lime ( $\text{CaO}$ ), slaked lime ( $\text{Ca}(\text{OH})_2$ ), caustic soda ( $\text{NaOH}$ ), magnesia ( $\text{MgO}$ ) and limestone have been reported.<sup>11,12</sup> In 2001, Ratanamskul and coworkers<sup>14</sup> reported the investigation of the performances of the chemical precipitation and metallic replacement methods for  $\text{Ag}^+$  removal from photographic waste solution. They found out that the chemical precipitation method (using  $\text{NaOH}$  as precipitant) was slightly less efficient as a lower  $\text{Ag}^+$  extraction efficiency of 95.9 % was observed compared to the >99 % observed for the metallic replacement method.

Despite the simplicity of the hydroxide precipitation process, some problems like the need to use coagulants to increase the sludge density and the associated increase in cost and the inhibition of the precipitants by complexing agents have been reported.<sup>10-12</sup>

## 1.2.2 Membrane filtration

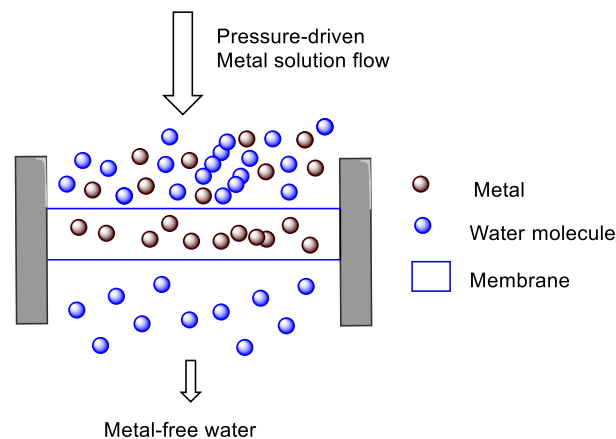


**Figure 1.2: Membrane filtration method schematic<sup>15</sup>**

In the membrane filtration (MF) method, metals are recovered by pushing the aqueous solution through membranes made up of specific-sized porous materials under pressure (see Figure 1.2 above)<sup>15</sup>. The removal of metals can be enhanced by the treatment of the membranes with appropriate chemical substances.<sup>16,17</sup> Some benefits enjoyed by employing the MF method include high efficiency of metal removal and easy operation.<sup>10,11</sup> Notwithstanding the method is fraught with problems such as high cost associated with the periodic replacement of the

membranes.<sup>12</sup> Based on the size of particles that can be retained on the membrane, the MF method has been classified into reverse osmosis (1–2 nm), nanofiltration (2–10 nm), ultrafiltration (10–100 nm) and microfiltration (100–1000).<sup>10,12</sup> The effect of the flow rate of wastewater sample containing  $\text{Ag}^+$  on the recovery of the metal by means of the microfiltration technique was examined by Zanain and Lovitt<sup>18</sup>. They discovered that halving the initial flow rate of 5 L/h increased the amount of  $\text{Ag}^+$  recovered by 50 %.

### 1.2.3 Ion exchange

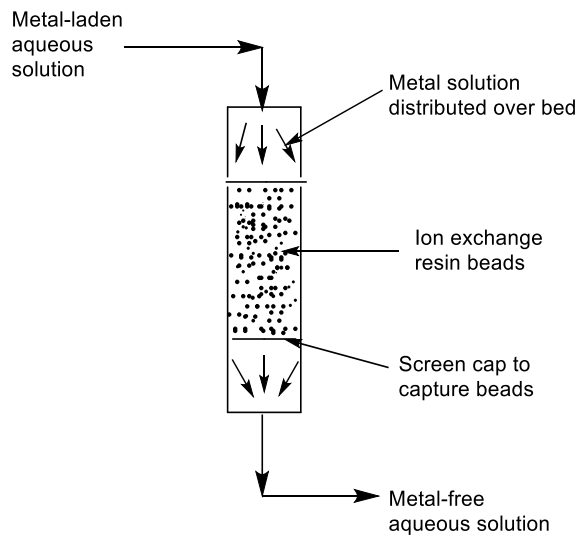
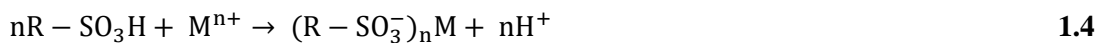


**Figure 1.3: Ion exchange method schematic**

The ion exchange method of metal removal is based on the substitution of exchangeable ions on the surface of a resin for the metal ions in solution (as in cationic ion exchangers, Equation 1.4)<sup>12</sup> or the adsorption of metal ions (as in anionic ion exchangers)<sup>19</sup> as an aqueous solution containing the metal ion is contacted with the resin (see Figure 1.3 above).



Seventy-two percent  $\text{Ag}^+$  was recovered from a concentrated base metal-chloride solution by means of the ion exchange technique using a weak anion exchange resin with polyamine functionality. The recovered  $\text{Ag}^+$  was eluted quantitatively using either thiourea or thiosulfate solution.<sup>20</sup> Some merits of the ion exchange method for metal removal include high metal removal efficiencies and ability to treat large volumes of metal-laden wastewater.<sup>21</sup> Some

demerits of the process include the high cost associated with regular rejuvenation of the resin and creation of secondary wastes after the resin rejuvenation.<sup>22</sup>

## 1.2.4 Electrochemical treatment

Electrochemical treatment involves the use of electrical energy for the removal of metals from aqueous solutions and is subdivided into electrocoagulation, electrofloatation and electrodeposition techniques.<sup>10-12</sup>

### 1.2.4.1 Electrocoagulation (EC) technique

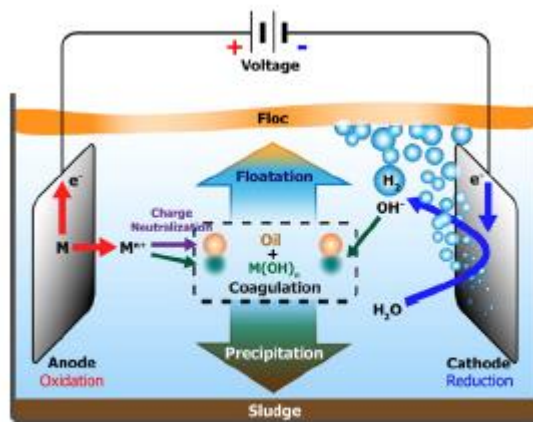


Figure 1.4: Schematic of a typical electrocoagulation setup<sup>23</sup>

Electrocoagulation basically involves the *in situ* production of coagulants by the oxidation of a sacrificial anode.<sup>29</sup> Taking a sacrificial anode made of metal  $M$  as an example, the electrocoagulation technique proceeds as follows;<sup>25</sup>

- Oxidation of the sacrificial anode occurs to form a positively charged ionic coagulant;  $M^{n+}$  (Equation 1.5 and Figure 1.4 above):



- Water molecules are reduced at the cathode to give  $OH^{-}$  ions (Equation 1.6 and Figure 1.4):



- The migration of the formed ions ( $\text{OH}^-$ ) from the cathode to the anode results in the destabilization of pollutants and particulate suspensions.
- Ultimately, the  $\text{OH}^-$  ions reach the anode and interacts with the metal ion ( $\text{M}^{n+}$ ) to form hydroxides with good adsorption property (Equation 1.7 and Figure 1.4).



The EC technique has been reported to be effective for heavy metal removal from aqueous solutions. For example, in 2012, the removal rates and removal mechanism of some heavy metals and  $\text{Ag}^+$  by the EC process was studied. It was observed that the removal rate for these metals reduced in the order  $\text{Cu}^{2+} > \text{Ni}^{2+} > \text{Zn}^{2+} > \text{Ag}^+$ . The removal mechanism of  $\text{Ag}^+$  was by reduction at the cathode surface and combination with the  $\text{OH}^-$  released from the cathode to form hydroxides and co-precipitation with  $\text{Al}(\text{OH})_3$  formed during the coagulation procedure.<sup>26</sup>

Earlier in 2009, the performance of the electrocoagulation technique for  $\text{Cr}^{6+}$  removal was investigated by Ölmöz<sup>27</sup>. About >99 % of the initial  $\text{Cr}^{6+}$  concentration of 1470 mg/L was removed by the EC technique operated at optimum conditions of applied current of 7.4 A, NaCl electrolyte concentration of 33.6 mM and current application time of 70 min. Other metals including  $\text{As}^{3+}$ ,<sup>28</sup>  $\text{Mn}^{2+}$ <sup>29</sup> and  $\text{Ni}^{2+}$ <sup>30</sup> have been recovered using the EC method with excellent efficiencies of >99, 78 and >99 % respectively.

#### 1.2.4.2 Electrofloatation (EF) technique

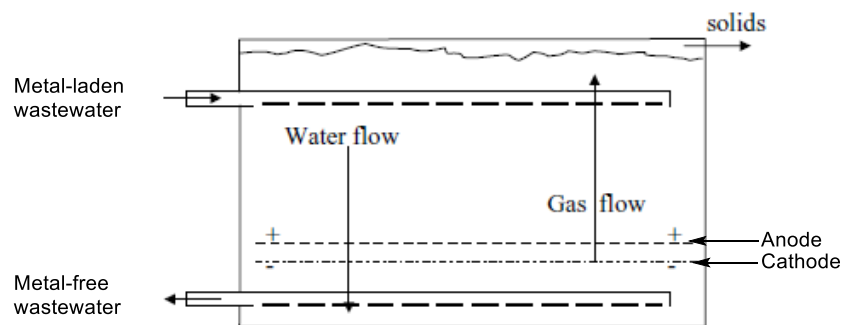
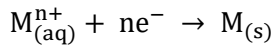


Figure 1.5: Typical electrofloatation setup for heavy metal removal<sup>24</sup>

Electrofloatation involves the hydrogen and oxygen gas-assisted floatation of heavy metal pollutants to the top of the wastewater or aqueous solution (Figure 1.5).<sup>11,12</sup> The hydrogen and oxygen gases are produced by the electrolytic process. The EF process can be employed for the separation of not only heavy metals, but also organic compounds from wastewater.<sup>31</sup> For example, Selim *et al*<sup>32</sup> investigated the kinetics and removal efficiency of the precious metals;  $\text{Ag}^+$  and  $\text{Au}^{3+}$  from wastewater samples by means of the EF technique. They observed that the metal removal proceeded by pseudo first order kinetics, indicating a physical adsorption of the metals and that removal efficiency was at least 99 % for each metal. In a different study, da Mota *et al*<sup>33</sup> disclosed that the removal efficiencies of some heavy metals;  $\text{Zn}^{2+}$ ,  $\text{Pb}^{2+}$  and  $\text{Ba}^{2+}$  by the EF technique were approximately 92, 95 and 97 % respectively at optimum pH of 10 using stainless steel electrodes.

#### 1.2.4.3 Electrodeposition (ED) technique

Electrodeposition involves the reduction of heavy metal ions and their deposition as elemental metal on the surface of a cathode (see Figure 1.6 below and Equation 1.8). The cathode is usually a pure strip of the metal to be recovered, allowing for selective metal recovery.



1.8

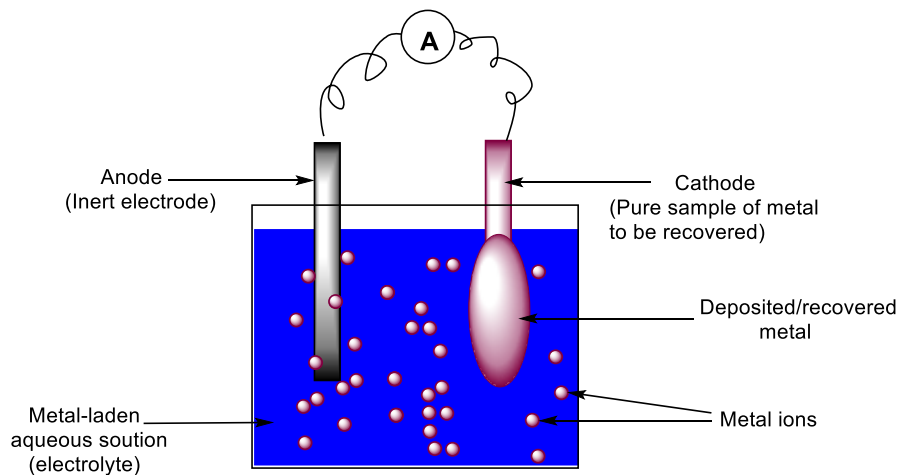


Figure 1.6: Typical electrodeposition setup for metal removal

The concentration of  $\text{Cu}^{2+}$  in a mining residue leachate was decreased by about 86 % by means of the ED technique using Ti/RuO<sub>2</sub> as anode and copper as cathode, at optimum conditions of current intensity of 1.3 A and treatment time of 80 min.<sup>34</sup> Furthermore, the electrochemical performance for the recovery of EDTA-copper complex by a combination of the integrated ultrasound-ED technique was studied by Chang *et al*<sup>35</sup>. They observed that the combined technique was effective for removal of the Cu complex as 96 % of the Cu-EDTA complex was removed at pH 3.

The ED technique provides benefits such as relative low cost, high selectivity of metals removed, no sludge generated and no need for the use of further reagents.<sup>36,37</sup> However, some drawbacks of the ED technique like the low thermal stability, narrow electrochemical window and effervescence of H<sub>2</sub> gas and the need contain the gas have raised some concerns.

### 1.3 Adsorption

Adsorption is a mass conversion method where the metal ions are transferred to the surface of adsorbents and held in place by various means including electrostatic attraction, cation exchange and complexation<sup>38</sup>(see Figure 1.7 below).

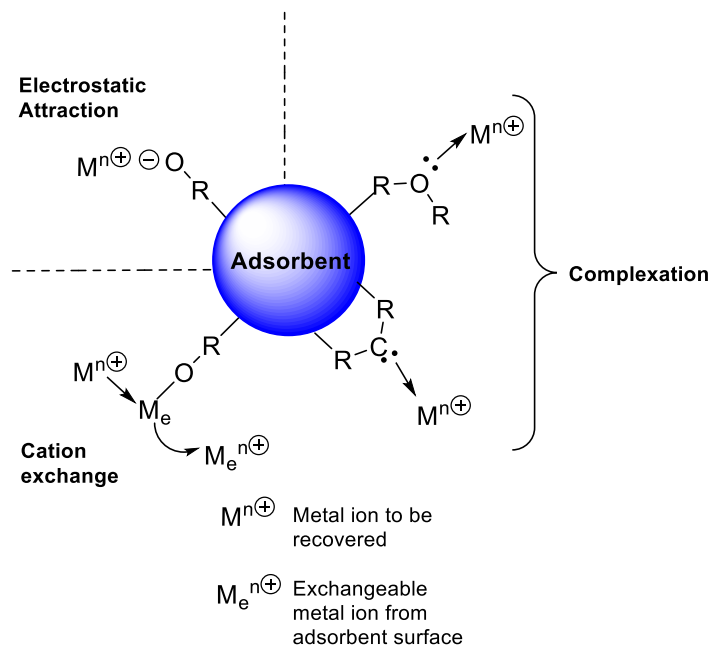


Figure 1.7: Various adsorption mechanisms in metal recovery

The efficiency of an adsorption process depends greatly on properties of the adsorbent including surface area, pore size distribution and available functional groups.<sup>39</sup> Adsorption is highly patronised because it is generally efficient, relatively cheap to undertake, involves simple experimental design and set-up, does not create toxic pollutants and is sustainable (since adsorbents can be regenerated after appropriate treatment).<sup>40</sup> Adsorbents for metal removal can be classified into bio-based and non-bio-based.

### 1.3.1.1 Bio-based adsorbents

Bio-based adsorbents are obtained from living organisms. They are renewable, relatively cheap, biodegradable and non-toxic. However, sourcing large amounts for industrial applications may be expensive. Also, most bio-based adsorbents need to be pretreated or chemically modified prior to use which adds to the cost of the process. Examples of bio-based adsorbents include agricultural wastes, algae, microbes and biopolymers.

Examples of agricultural wastes adsorbents employed for metal removal include rice husk,<sup>41</sup> moringa pod, bamboo leaf powder, cashew nut,<sup>42</sup> palm oil fruit shell,<sup>43</sup> plantain peel,<sup>44</sup> barley straw,<sup>45</sup> orange peel,<sup>46</sup> etc.

Researchers have employed algae as a metal adsorbent owing to its outstanding properties including the presence of multiple cell layers (which provides, the sorbent with high surface area), , low-cost, high metal sorption capacity and wide availability.<sup>47</sup> Algae has been employed for the removal of  $\text{Cu}^{2+}$ ,<sup>48,49</sup> and  $\text{Zn}^{2+}$  and  $\text{Pb}^{2+}$ <sup>50,51</sup>.

Microbial derived adsorbents, which can be further divided into fungi (including yeasts) and bacterial have demonstrated reasonable sorption capacities for metal removal.<sup>52,53</sup> For instance, Chen and Wang<sup>54</sup> utilized brewery-sourced yeast powder for the uptake of  $\text{Ag}^+$  and some heavy metals following a batch process. The maximum  $\text{Ag}^+$  uptake capacity of the yeast powder adsorbent was found to be 42.7 mg/g. Recently, Tekin *et al*<sup>55</sup> reported that white rot fungi (*Trametes versicolor*) removed  $\text{Cu}^{2+}$  with an adsorption capacity of 39.9 mg/g at optimum conditions of pH 5.5, temperature of 20.1 °C and initial  $\text{Cu}^{2+}$  concentration of 61

mg/L. Chitosan is an example of a biopolymer that has been extensively employed for  $\text{Ag}^+$  with reported maximum adsorption capacities for  $\text{Ag}^+$  ranging from 121.9 to 510 mg/g.<sup>56-58</sup>

### 1.3.1.2 Non-bio-based adsorbents

Non-bio-based adsorbents are adsorbents derived from all other sources apart from living organisms. These adsorbents can be subdivided into activated carbon (AC), carbon nanotubes (CNTs), industrial by-products and nanosized metal oxides (NMOs).

Activated carbons (AC) are processed carbon-based adsorbents usually with high surface area, arising from their large micropore size and volumes. While coal has been the major source of AC, the decline in supply of this sedimentary rock has led to the search for alternative sources for AC. Therefore, plant materials like eucalyptus bark,<sup>59</sup> cassava peel,<sup>60</sup> olive cake,<sup>61</sup> European black pine<sup>62</sup> etc have been processed into AC. For example, in 2013, El-shafey and Al-kindy<sup>63</sup> prepared activated carbon from date palm leaflets and employed the adsorbent for the recovery of  $\text{Ag}^+$  and  $\text{Cu}^{2+}$ . They found out that the adsorbent demonstrated a slower sorption rate but higher sorption capacity for  $\text{Ag}^+$  than  $\text{Cu}^{2+}$  at 45 °C ( $\text{Ag}^+$ ; 53 mg/g and  $\text{Cu}^{2+}$ ; 23 mg/g). The  $\text{Ag}^+$  sorption mechanism was found to be a reduction as the presence of elemental Ag was detected on the surface of the adsorbent by SEM and XRD analyses. Kongsuwan *et al*<sup>59</sup> observed that AC sourced from Eucaplytus bark removed  $\text{Cu}^{2+}$  and  $\text{Pb}^{2+}$  with adsorption capacities of 0.45 and 0.53 mg/g respectively. Also, oxidized AC was found to remove  $\text{Pb}^{2+}$  with an adsorption capacity of 559 mg/g.<sup>64</sup> AC has also been employed for the removal of  $\text{Cd}^{2+}$  and  $\text{Co}^{2+}$ <sup>65</sup> and  $\text{Pb}^{2+}$ <sup>62,64</sup> as well.

Carbon nanotubes (CNTs), discovered in 1991 by Iijima,<sup>66</sup> are cylindrical graphite sheets enveloped into a tubular structure. Types of CNTs include single walled carbon nanotubes (SWCNTs) and multi-walled carbon nanotubes (MWCNTs), with one and multiple graphite sheets respectively (Figure 1.8). Properties that make CNTs attractive for metal removal include their high surface area, high chemical stability and excellent mechanical properties. CNTs have been chemically modified with the aim of increasing their metal sorption capacities. For example, poly(amidoamine) functionalized CNT demonstrated remarkably

high adsorption capacities of 3900, 3800, 3650 and 3350 mg/g for  $\text{Ni}^{2+}$ ,  $\text{Co}^{2+}$ ,  $\text{Zn}^{2+}$  and  $\text{As}^{3+}$  recoveries respectively.<sup>67</sup> Other heavy metals including  $\text{Pb}^{2+}$ ,<sup>68</sup>  $\text{Cr}^{6+}$ ,<sup>69</sup>  $\text{Cu}^{2+}$ ,<sup>70</sup> have been removed using acidified MWCNTs, raw CNTs and alginate-modified CNTs respectively with excellent adsorption efficiencies and capacities. The mechanism of metal uptake depends on the active site on the CNT surface and includes electrostatic attraction, complexation, sorption-precipitation etc.<sup>20</sup>

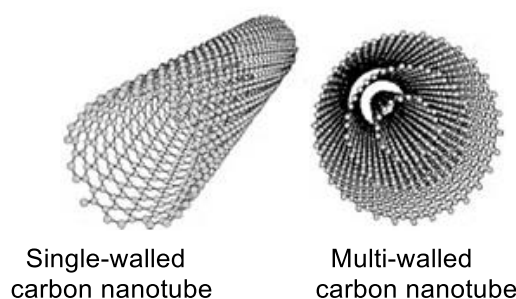


**Figure 1.8: Single and multiwalled carbon nanotubes**

Industrial by-products are an attractive option as metal sorbents because they can be diverted from landfills. Examples of industrial by-products previously employed for metal removal includes furnace sludge, textile cellulose fibres, fly ash, metal sludge etc. For example, modified basic oxygen furnace sludge was employed for the removal of  $\text{Cu}^{2+}$ <sup>71</sup> and  $\text{Pb}^{2+}$ <sup>72</sup> with excellent extraction efficiency of 99 % and maximum adsorption capacity of 92.5 mg/g respectively. Furthermore, modified waste textile cellulose fibres,<sup>73</sup> fly ash geopolymer,<sup>74</sup> and coal ash,<sup>75</sup> have been employed for the recovery of  $\text{Cd}^{2+}$ ,  $\text{Cu}^{2+}$  and  $\text{Hg}^{2+}$  respectively. Finally, metal sludge obtained from the electroplating industry was observed to be very efficient for the removal of  $\text{Cd}^{2+}$  with an adsorption capacity of 40 mg/g.<sup>76</sup>

Nanosized metal oxides (NMOs) are oxides of metals with at least one dimension with length less than 100 nm. Examples of NMOs that have been employed for metal removal include magnesium oxides,<sup>10</sup> cerium oxides,<sup>10</sup> manganese oxides,<sup>77</sup> titanium oxides,<sup>10</sup> aluminium oxides,<sup>10</sup> copper oxides<sup>78</sup> and iron oxides<sup>79</sup>. NMOs have large surface areas which are

important for metal removal purposes. The surface area of some metal oxides is provided in Table 1.1.

**Table 1.1: Surface area of some nanosized metal oxides**

Nanosized metal oxide	Diameter (nm)	Surface area (m <sup>2</sup> /g)
CuO <sup>78</sup>	33 – 160	220
Manganese nodule (mixture of manganese and iron oxides) <sup>77</sup>	-	125
TiO <sub>2</sub> <sup>80</sup>	5	288
MnO <sup>81</sup>	8	145

Magnesium oxides have outstanding properties including low cost, relative abundance, low toxicity<sup>82</sup> and are potent antibacterial agents.<sup>83</sup> These oxides have been employed for removal of heavy metals from aqueous matrices. For instance, Madhavi<sup>84</sup> reported that the adsorption capacities by MgO nanoparticles for Cd<sup>2+</sup>, Cu<sup>2+</sup>, Ni<sup>2+</sup>, and Pb<sup>2+</sup> were 135, 149.1, 149.9, and 148.6 mg/g respectively. The removal mechanism was attributed to adsorption and precipitation. Furthermore, MgO nanoparticles prepared by the combustion method were observed to demonstrate high extraction efficiency of 96 % for Cu<sup>2+</sup> removal from aqueous solution with initial Cu<sup>2+</sup> concentration of 10 mg/L.<sup>85</sup> Remarkably high adsorption capacities of 2614 and 2294 mg/g (as calculated from the Langmuir isotherm) for Pb<sup>2+</sup> and Cd<sup>2+</sup> removal by mesoporous MgO nanoparticles) were disclosed by Xiong *et al*<sup>86</sup>. Finally, Feng *et al*<sup>87</sup> reported the preparation of MgO nanosheets and their Ni<sup>2+</sup> uptake capacity was determined. They were pleased to observe that the MgO nanosheets showed high uptake capacity of 1684.25 mg/g for Ni<sup>2+</sup> following the Langmuir isotherm in a batch adsorption experiment. The high uptake capacity was attributed primarily to the precipitation of the Ni<sup>2+</sup> afforded by the generated OH<sup>-</sup> from Mg(OH)<sub>2</sub> and secondarily to adsorption effects afforded by the high BET surface area of 182 m<sup>2</sup>/g. These Ni<sup>2+</sup> removal mechanisms were supported by FTIR and XPS characterization of the Ni<sup>2+</sup>-impregnated MgO adsorbents.

Titanium oxide can photodegrade organic pollutants and remove metals from aqueous matrices with relative high efficiency.<sup>88</sup> In 2014, Youseff and Malhat<sup>89</sup> found out that the

removal efficiencies by TiO<sub>2</sub> nanowires (with average diameter of 40 nm) for Fe<sup>3+</sup> and Pb<sup>2+</sup> are 80 and 97 % respectively. Meanwhile, Nabi and coresearchers<sup>90</sup> prepared TiO<sub>2</sub> by the sol-gel method and employed the TiO<sub>2</sub> for As<sup>5+</sup> removal. It was observed that when the adsorbent dose was kept constant, the adsorption capacity increased slightly with increasing initial As<sup>5+</sup> concentration from 4.9 mg/g to 20.4 mg/g for initial As<sup>5+</sup> concentrations of 5 and 90 mg/L respectively. Madhavi *et al*<sup>84</sup> discovered that TiO<sub>2</sub> showed preference in the removal of some heavy metals, with respect to the maximum removal capacities, in the order; Pb<sup>2+</sup><Ni<sup>2+</sup><Cu<sup>2+</sup><Cd<sup>2+</sup> (Pb<sup>2+</sup>; 21.7, Ni<sup>2+</sup>; 39.3, Cu<sup>2+</sup>;50.2 and Cd<sup>2+</sup>;120.1 mg/g). The removal of these metals was explained to have proceeded by adsorption. Mesoporous TiO<sub>2</sub> prepared by the thermohydrolytic approach and with large BET determined surface area of 278 m<sup>2</sup>/g exhibited removal capacity of 25.8 mg/g for Cr<sup>6+</sup> from aqueous solution.<sup>91</sup> Unfortunately, the titanium oxide preparation process can be complex and the separation from aqueous solutions can be difficult.<sup>92</sup> These problems may have discouraged the use of the oxide for metal removal purposes.

Aluminium oxides are cheap to produce and the oxide has high decontamination efficiency.<sup>93</sup> Of all the crystalline forms (including  $\alpha$ ,  $\gamma$ ,  $\theta$ ,  $\eta$ -)  $\gamma$ -alumina is the most widely used. This crystalline form has excellent metal uptake capacity and reasonable mechanical strength.<sup>94</sup> For example,  $\gamma$ -Al<sub>2</sub>O<sub>3</sub> nanoparticles prepared via the sol-gel method removed Pb<sup>2+</sup> and Cd<sup>2+</sup> with adsorption capacities of 47.1 and 17.2 mg/g respectively. The metal removal process was observed to follow the Freundlich isotherm, indicating a physisorption.<sup>95</sup> Finally, the maximum removal capacities of Al<sub>2</sub>O<sub>3</sub> nanoparticles towards Cd<sup>2+</sup>, Cu<sup>2+</sup>, Ni<sup>2+</sup>, and Pb<sup>2+</sup> were 118.9, 47.9, 35.9, and 41.2 mg/g respectively. The removal mechanism was attributed to adsorption.<sup>84</sup>

Cerium oxide is non-toxic<sup>96</sup> and has also been employed for the removal of heavy metals<sup>97</sup>. In 2010, Recillas *et al*<sup>98</sup> determined the size and surface area of CeO<sub>2</sub> nanoparticles and the adsorption capacity of the oxide for Cr<sup>6+</sup> removal. The size and surface area of the CeO<sub>2</sub> nanoparticles were 12 nm and 65 m<sup>2</sup>/g respectively and the maximum adsorption capacity of

the oxide was 122 mg/g for  $\text{Cr}^{6+}$ . In a separate study,  $\text{CeO}_2$  nanoparticles with a surface area of  $257 \text{ m}^2/\text{g}$  were employed for the removal of arsenic ions -  $\text{As}^{3+}$  and  $\text{As}^{5+}$  from water in a batch method by Mishra *et al*<sup>99</sup>. The metal removal process was found to fit the Langmuir isotherm best with adsorption capacities of 71.9 and 36.8 mg/g for  $\text{As}^{3+}$  and  $\text{As}^{5+}$  respectively. Unfortunately, the presence of the anions;  $\text{H}_2\text{PO}_4^-$ ,  $\text{SO}_4^{2-}$ , and  $\text{HCO}_3^-$  reduced the adsorption capacities of the adsorbent for the arsenic ions.

Manganese and zinc oxides have also been reported to demonstrate high metal removal capacities.<sup>81,100</sup> For example, nanoscale  $\text{MnO}$  was observed to remove  $\text{Tl}^+$  rapidly (in 15 min) from aqueous solution with a high adsorption capacity of 672 mg/g.<sup>101</sup> Furthermore,  $\text{ZnO}$  removed  $\text{Zn}^{2+}$ ,  $\text{Hg}^{2+}$  and  $\text{Cd}^{2+}$  with adsorption capacities of 357, 714 and 387 mg/g respectively following the Langmuir isotherm.<sup>102</sup> Other nanosized metal oxides like  $\text{ZrO}_2$ ,  $\text{HfO}_2$ ,  $\text{Nb}_2\text{O}_5$  and  $\text{Ta}_2\text{O}_5$  have been employed for metal removal.<sup>91</sup>

Amongst all nanosized metal oxides, functionalized iron oxide is perhaps the most widely employed for heavy metal removal purposes and this may be due to the magnetic property of iron oxide. Therefore, the synthesis and application (for metal recovery) of nanosized functionalized iron oxide will be exhaustively discussed in the following sections.

## 1.4 Iron oxide nanoparticles (IONPs)

There are six iron oxides known, amongst which  $\text{Fe}_2\text{O}_3$  (haematite;  $\alpha\text{-Fe}_2\text{O}_3$  and maghemite;  $\gamma\text{-Fe}_2\text{O}_3$ ) and  $\text{Fe}_3\text{O}_4$  (magnetite) are the most common.<sup>103</sup> In addition to metal recovery applications<sup>104,105</sup>, IONPs have also found applications in medicine,<sup>106,107</sup> catalysis,<sup>108</sup> and as contrast agents in magnetic resonance imaging (MRI)<sup>109,110</sup>. As stated earlier, the key to their importance is the ability to respond, by attraction to an external magnetic field which makes their separation with the aid of a magnet relatively easy.

### **1.4.1 Methods of iron oxide nanoparticles synthesis**

Iron oxide nanoparticles have been synthesized by a variety of methods broadly classified into physical (or mechanical), biological and chemical, differing in how the IONPs characteristics (including size, polydispersity, morphology, crystallinity and porosity) are controlled, the cost of the process and simplicity of undertaking the synthesis.

#### **1.4.1.1 Physical methods**

Physical methods of IONPs synthesis include electron beam lithography, gas phase deposition, laser induced pyrolysis, aerosol, powder ball milling and pulsed laser ablation.<sup>111</sup>

While some physical methods like powder ball milling produce IONPs with broad size distribution, others like the newly developed laser ablation method have been reported to produce IONPs with low polydispersity.<sup>112</sup> Notwithstanding, the relative high cost and complexity of physical methods of IONPs synthesis may have forced researchers to embrace other methods including biological and chemical.<sup>113</sup>

#### **1.4.1.2 Biological methods**

The biological method of IONPs synthesis, which can also be referred to as biomineralization, is mediated usually by microbes giving IONPs with low polydispersity. For example, magnetotactic bacteria has been reported to generate magnetosomes (protein-coated nanosized crystals of iron oxide) with narrow size distribution.<sup>114</sup> On the down side, biological methods can be complex and difficult to scale up. Consequently, chemical methods are usually employed for IONP synthesis.

#### **1.4.1.3 Chemical methods**

Amongst the chemical methods of IONP synthesis, only the popular methods including high temperature thermal decomposition, hydro/solvothermal, microemulsion, sonochemical and co-precipitation methods will be discussed here.

#### 1.4.1.3.1 High temperature thermal decomposition

The thermal decomposition (TD) method for formation of IONPs proceeds by two different protocols namely “hot injection” and “heating up”.<sup>115</sup>

In the hot injection method, reagent solution (typically an iron salt) is introduced into a hot surfactant solution (e.g. oleic acid and octyl ether) followed by the stirring of the iron salt/surfactant solution and the alteration of reaction conditions (mainly temperature) (Figure 1.9). The introduction of the iron salt into a hot surfactant solution induces a fast and homogenous nucleation and the alteration of the reaction temperature helps control the growth of the IONPs, resulting in the production of monodisperse IONPs.

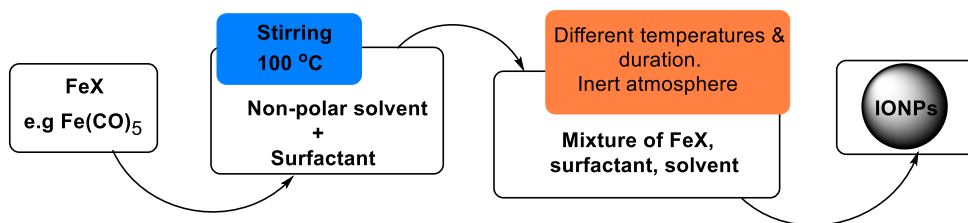


**Figure 1.9: Schematic for the hot injection thermal decomposition method**

The second type of thermal decomposition method for IONP synthesis is the heating up method which involves the steady heating of a pre-mixed solution of precursor compounds, solvent and surfactant up to a specified temperature at which IONPs nucleation and growth begins.<sup>116,117</sup>

Usually undertaken at high temperatures (up to 300 °C), researchers have been attracted to the thermal decomposition method because of its potential to give monodisperse and highly crystalline IONPs. For instance, Hyeon and coworkers<sup>118</sup> successfully prepared monodisperse (as evidence from the low resolution TEM micrographs) and highly crystalline (evidenced by high resolution TEM)  $\gamma$ -Fe<sub>2</sub>O<sub>3</sub> NPs after the high temperature (300 °C) aging of the Fe-oleate complex obtained from the thermal decomposition of iron pentacarbonyl (Fe(CO)<sub>5</sub>) and oleic acid at 100 °C. Interestingly, the particle size was regulated by varying the molar ratios of Fe(CO)<sub>5</sub> and oleic acid. From a different study, monodisperse (20.00±0.15 nm) and pure

(evidenced from x-ray diffractogram) Fe<sub>3</sub>O<sub>4</sub> NPs were accessed after the thermal decomposition of goethite (FeOOH).<sup>119</sup> Notwithstanding the advantages of the TD process, problems of IONP accurate shape reproducibility and the high temperatures involved have raised concerns about the large-scale application of the method.

#### ***1.4.1.3.2 Hydrothermal and solvothermal methods***

Hydrothermal and solvothermal methods of IONPs synthesis generally involve heating either mixed hydroxides or oxides of iron and other chosen metals at elevated temperature (between 130 – 250 °C) and elevated pressure (typically between 0.3 – 14 MPa) in a sealed vessel in aqueous (hydrothermal) or non-aqueous (solvothermal) solution.<sup>113</sup> Both methods have the advantages of producing IONPs (including  $\gamma$ -Fe<sub>2</sub>O<sub>3</sub>,  $\alpha$ -Fe<sub>2</sub>O<sub>3</sub> and Fe<sub>3</sub>O<sub>4</sub>) of very high crystallinity and narrow size distribution with good control over size. For example, Sun *et al*<sup>120</sup> obtained monodisperse Fe<sub>3</sub>O<sub>4</sub> nanoparticles (4.0±0.6 nm) after the hydrothermal reduction of FeCl<sub>3</sub> in the presence of sucrose. Indeed, the Fe<sub>3</sub>O<sub>4</sub> particle size could be tuned by varying the sucrose to FeCl<sub>3</sub> molar ratio. In another study, Gao and coworkers<sup>121</sup> undertook the solvothermal synthesis in diethylene glycol (as solvent) and were pleased to report the synthesis of highly crystalline and monodisperse Fe<sub>3</sub>O<sub>4</sub> nanoparticles (6.5±1.5 nm). Despite these positives, the hydrothermal synthesis process can be experimentally demanding and risky due to the extreme conditions of heightened temperature and pressure, leading to its low popularity for large scale IONPs synthesis. Consequently, less experimentally demanding methods requiring milder conditions have been investigated.

## 1.4.1.3.3 Microemulsion

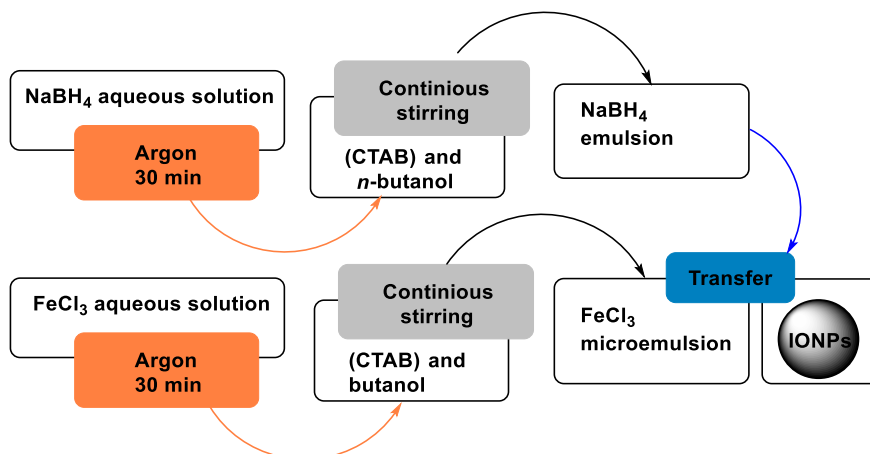


**Figure 1.10: Typical schematic for the microemulsion method for synthesis of iron oxide nanoparticles<sup>122</sup>**

The microemulsion method for IONPs synthesis involves the vigorous mixing of two separate emulsions one containing a reducing agent (e.g.  $\text{NaBH}_4$ ) and the other containing an iron salt (e.g.  $\text{FeCl}_3$ ) to form a microemulsion (Figure 1.10). The microemulsion is a thermodynamically stable mixture of immiscible liquids (for example oil and water) in the presence of a surfactant (e.g. Cetyltrimethylammonium bromide) and usually a co-surfactant (e.g. *n*-butanol).<sup>115</sup> IONPs with good size and shape control have been prepared by the microemulsion method. For instance, with the aim of investigating the effect of particle size on the magnetic structure, monodisperse IONPs with varying sizes of  $3.2 \pm 0.5$ ,  $6.3 \pm 0.9$  and  $9.1 \pm 1.4$  nm were separately prepared following the microemulsion method at room temperature. After Mössbauer spectroscopy characterization, it was observed that the Fe spins reduce with increasing IONP size.<sup>123</sup> In a separate study, Okoli *et al*<sup>124</sup> prepared roughly spherical monodisperse IONPs (size ranged from 7 – 10 nm) by a water-in-oil microemulsion process and the IONPs were employed for protein purification. Notwithstanding the attractive features of the microemulsion process, IONPs prepared by the microemulsion method usually require repeated washings and extensive stabilization treatments.

#### 1.4.1.3.4 Sonolysis or sonochemical method

By taking advantage of the chemical effect of ultrasound irradiation, various types of bare and surface functionalized IONPs have been prepared. Typically, sonolysis involves exposure of an aqueous ferrous salt solution to high intensity ultrasound irradiation under ambient conditions, often in the presence of air.<sup>125</sup> For example, Wang *et al*<sup>126</sup> prepared amorphous Fe<sub>3</sub>O<sub>4</sub> nanoparticles by the sonolysis of Fe(CO)<sub>5</sub> in the presence of sodium dodecyl sulfate. The particles were very stable (no precipitation observed after 6 months) but with broad size distribution from 3.3 to 13.8 nm. With the purpose of narrowing the size distribution of the Fe<sub>3</sub>O<sub>4</sub> prepared, they undertook the Fe<sub>3</sub>O<sub>4</sub> preparation in the presence of 3-aminopropyltriethoxysilane (APTES). Therefore, APTES-coated Fe<sub>3</sub>O<sub>4</sub> nanoparticles with narrower size distribution (5.5 to 11 nm) were obtained. Their study revealed that the APTES coated Fe<sub>3</sub>O<sub>4</sub> nanoparticles had high magnetization saturation of 70.5 emu/g and exhibited typical magnetorheological effects expected of a ferrofluid. Some shortcomings of the sonolysis process are the requirement of specialized equipment and the poor control over IONP shape.<sup>125</sup>

#### 1.4.1.3.5 Co-precipitation method

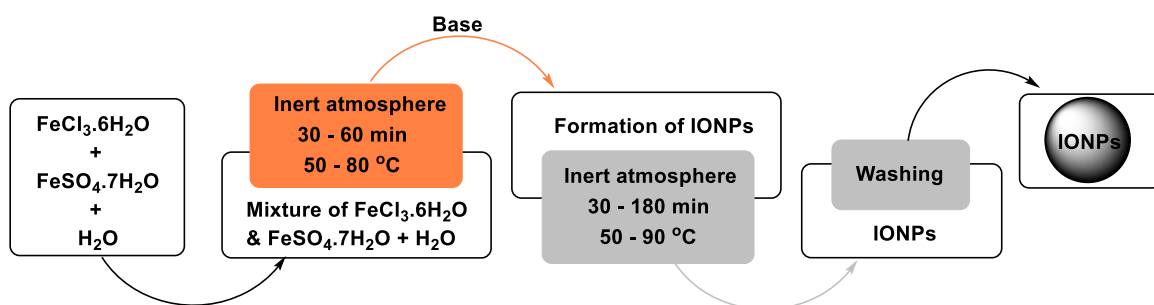


**Figure 1.11: Schematic for a typical co-precipitation method for iron oxide nanoparticles synthesis**

Amongst the chemical methods for IONP synthesis, co-precipitation is perhaps the most commonly employed. The co-precipitation method involves the precipitation of Fe<sup>3+</sup> and Fe<sup>2+</sup> salts (obtained from chlorides and/or sulfates) first to their hydroxides by a base and finally to Fe<sub>3</sub>O<sub>4</sub> under an inert atmosphere at high temperatures between 50 and 90°C (Figure 1.11 and

Equation 1.9). The co-precipitation process is comprised of two stages namely the nucleation and the particle growth stages.<sup>127</sup> In order to obtain monodisperse IONPs, these stages should be separated; this means that particle growth should not happen simultaneously as nucleation is taking place.<sup>127</sup>



Despite the advantages of low cost, easy implementation and ease of scaling up, the co-precipitation method suffers from limited control of IONPs size distribution. Therefore, with the hope of achieving better control of size distribution, the adjustment of some IONPs synthesis parameters have been studied. One of these factors is the solution pH of the reaction mixture.

Studies reveal that the average particle size of IONPs decrease with increase in pH of the reaction mixture. For example, Yusoff *et al*<sup>128</sup> was able to reduce the average particle size of Fe<sub>3</sub>O<sub>4</sub> from 17.7 to 10.6 nm by increasing the pH of the reaction media from 11.3 to 12.2. Furthermore, Ahmadi *et al*<sup>129</sup> observed that by increasing the solution pH from 11 to 12, the average size of the Fe<sub>3</sub>O<sub>4</sub> was halved (from 20 to 10 nm).

The average particle size of IONPs can be increased by increasing the reaction temperature. For instance, by increasing the reaction temperature from 25 to 80 °C, Saragi and coworkers<sup>130</sup> managed to increase the average particle size of the spherical Fe<sub>3</sub>O<sub>4</sub> nanoparticles from 10 to 12 nm. Furthermore, Chia and coworkers<sup>131</sup> were pleased to observe the increase in the average size of the Fe<sub>3</sub>O<sub>4</sub> nanoparticles from 11 to 14 nm by increasing the reaction temperature from room temperature to the boiling point of water. Finally, Niu and Zheng<sup>132</sup> revealed that by increasing the reaction temperature by only 30 °C, they were able to double the initial Fe<sub>3</sub>O<sub>4</sub> average size. The direct relationship between IONP mean particle size and reaction temperature has been attributed to the suppression of nucleation and promotion of particle growth due to the increase in the volume of the reaction mixture, which is a consequence of increase in temperature.<sup>133</sup>

A direct relationship was found between the  $\text{Fe}^{2+}/\text{Fe}^{3+}$  ratio and the mean particle size of  $\text{Fe}_3\text{O}_4$  synthesized. To start with, in 1999, Babes *et al*<sup>134</sup> controlled the particle size of uncoated IONPs by altering the  $\text{Fe}^{2+}/\text{Fe}^{3+}$  ratio. They achieved the increase of the IONPs mean size from 3 to 5 nm by increasing the  $\text{Fe}^{2+}/\text{Fe}^{3+}$  ratio from 0.4 to 0.6. In another study, Jolivet *et al*<sup>135</sup>, were able to increase the mean particle size of the IONPs by almost 40 % (from 3.5 to 5.5 nm) by increasing the  $\text{Fe}^{2+}/\text{Fe}^{3+}$  ratio by only 0.05 units (0.15 – 0.20). By increasing the  $\text{Fe}^{2+}/\text{Fe}^{3+}$  ratio to 0.5, IONPs particles with average size of 10 nm were obtained.

An inverse relationship between IONP mean particle size and stirring speed has been observed. For example, in 2013, Mahdavi *et al*<sup>136</sup> revealed that a 100 % increase in stirring speed (from 400 to 800 rpm) resulted in lowering of the average particle size from 9.4 to 7.8 nm. Above 800 rpm, the mean particle size increased. Similarly, Sunaryono *et al*<sup>137</sup> were pleased to observe that the mean size of  $\text{Fe}_3\text{O}_4$  could be reduced from 12.5 to 9.7 nm by increasing the stirring speed from 1250 to 1375 rpm. However, the stirring speed of 1375 rpm represented the limit above which the mean particle size remained as 9.7 nm. It has been rationalized that increase in stirring speed increases the energy transferred to the reaction mixture with the result that the reaction suspension is dispersed into smaller droplets, leading to the production of smaller particle sizes.<sup>138</sup>

In addition to solution pH, reaction temperature,  $\text{Fe}^{2+}/\text{Fe}^{3+}$  ratio and stirring speed, the use of chelating organic ligands has also been noticed to influence the magnitude and distribution of IONPs sizes.<sup>127</sup> For example, use of the ligand - mercaptoethanol **1.1** (see Figure 1.12 below) in the synthesis of  $\text{Fe}_3\text{O}_4$  helped access the  $\text{Fe}_3\text{O}_4$  with lower average particle size (8 nm) than the  $\text{Fe}_3\text{O}_4$  prepared without the ligand (15 nm).<sup>139</sup> Tan and Abu Bakar<sup>140</sup> observed a clear difference in the magnitude and distribution of the size of the  $\text{Fe}_3\text{O}_4$  prepared in the absence and presence of surfactants. Higher size and broader size distribution of  $\text{Fe}_3\text{O}_4$  particles were observed when  $\text{Fe}_3\text{O}_4$  was prepared without the surfactant; stearic acid **1.2** (Figure 1.12) than in the presence of the surfactant ( $\text{Fe}_3\text{O}_4$  average sizes: without stearic acid;  $57.2 \pm 74.9$  nm, with stearic acid;  $33.9 \pm 11.6$  nm). In fact, other surfactants tested in the same study afforded similar

sizes and narrow distribution as the stearic acid (CTAB **1.3**:  $35.3 \pm 15.8$  nm, sodium dodecyl sulfate **1.4**:  $43.4 \pm 15.8$  nm). Finally, chelating organic ligands have not only been used to control the magnitude and distribution of IONPs sizes, but also, they have been linked to IONPs for metal recovery purposes.

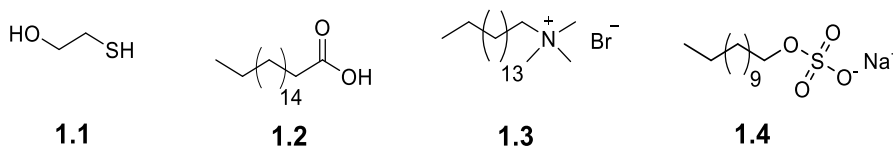


**Figure 1.12:** Some chelating agents employed for controlling the size of iron oxide nanoparticles

### 1.4.2 Surface functionalization of IONPs for metal uptake

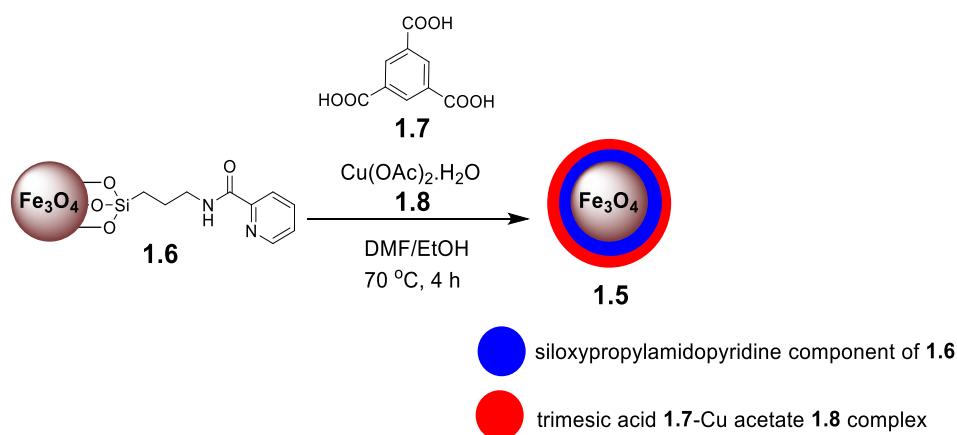
Though unfunctionalized IONPs have been observed to demonstrate high metal extraction efficiencies,<sup>141–144</sup> yet problems like poor metal selectivity and physical and chemical instability of these IONPs may have discouraged continuous applications for metal recovery. Fortunately, surface functionalization of these IONPs has helped overcome these problems by providing specific functional groups for the selective detection and recovery of targeted metal ions and protection of the IONP surface.<sup>79,145</sup> The surface of IONPs have been functionalized for metal uptake using inorganic, organic and polymeric ligands.

#### 1.4.2.1 Magnetic inorganic extractants (MIEs)

Magnetic inorganic extractants (MIEs) are made by the linkage of inorganic compounds to IONPs. Types of inorganic compounds linked to IONPs for the purpose of metal removal include alumina, aluminosilicates and metal-organic frameworks (MOFs).<sup>145</sup> The high surface area of these inorganic compounds make them capable of removing metals from aqueous solutions. For example, in 2015, Amjadi and coworkers<sup>146</sup> linked the aluminosilicate mineral (Halloysite) to  $\text{Fe}_3\text{O}_4$  by the co-precipitation method and the resulting composite extractant was employed for the preconcentration of  $\text{Cd}^{2+}$  prior to its determination by flame atomic absorption spectrophotometry (FAAS). Satisfied with the adsorption capacity of 11.4 mg/g and detection limit of 0.27 ng/mL obtained, the investigators employed the composite

extractant for the preconcentration of trace concentrations (of about 2 ng/mL) of  $\text{Cd}^{2+}$  from real life samples from which excellent recovery efficiencies (at least 96 %) were observed.

Another sub-class of magnetic inorganic extractant commonly employed for metal recovery is magnetic metal-organic frameworks (MMOF's). In 2013, a magnetic metal-organic framework (MMOF) **1.5** extractant prepared from the  $\text{Fe}_3\text{O}_4$ -pyridine conjugate **1.6**, trimesic acid **1.7** and copper acetate **1.8** (Scheme 1.1) was employed for the preconcentration of the heavy metals;  $\text{Cd}^{2+}$  and  $\text{Pb}^{2+}$  from water and soil samples prior to the quantification by FAAS. After adsorption capacities of 186 mg/g and 198 mg/g for  $\text{Cd}^{2+}$  and  $\text{Pb}^{2+}$  respectively were observed, the investigators proceeded to measure the  $\text{Cd}^{2+}$  and  $\text{Pb}^{2+}$  recovery efficiencies from real water and soil samples. Fortunately, quantitative recoveries (at least 96 %) of trace levels of the heavy metals in seawater and sediment samples by the trimesic acid based MMOF extractant was observed.<sup>147</sup>



**Scheme 1.1: Synthesis of the trimesic acid-based magnetic metal-organic framework extractant<sup>147</sup>**

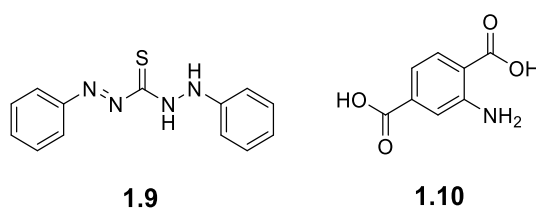


**Figure 1.13: Some organic ligands component of some magnetic metal-organic framework extractant employed for metal recovery**

Later in 2013, magnetic metal organic framework (MMOF) extractant (resembling **1.5** in Scheme 1.1 above) was prepared from dithiozone **1.9** (see Figure 1.13 above)-modified Fe<sub>3</sub>O<sub>4</sub> NPs and Cu(II)-trimesic acid complex. This MMOF extractant was employed for the preconcentration of some heavy metals namely Cd<sup>2+</sup>, Pb<sup>2+</sup>, Zn<sup>2+</sup> and Ni<sup>2+</sup>. Based on the adsorption capacity values obtained, the extractant was observed to show slight preference for the metals in the order Zn<sup>2+</sup>>Cd<sup>2+</sup>>Pb<sup>2+</sup>>Ni<sup>2+</sup>. Detection limits observed were 0.39, 0.12, 1.2 and 0.98 ng/mL for Zn<sup>2+</sup>, Cd<sup>2+</sup>, Pb<sup>2+</sup> and Ni<sup>2+</sup> respectively. Finally, quantitative recovery efficiencies (Zn<sup>2+</sup>; 90 % Cd<sup>2+</sup>; 90 %, Pb<sup>2+</sup>; 92 % and Ni<sup>2+</sup>; 90 %) of trace amounts (5 ng/mL) were observed.<sup>148</sup>

Recently, another MMOF extractant prepared using Fe<sub>3</sub>O<sub>4</sub>, Zn<sup>2+</sup> and 2-aminoterephthalic acid **1.10** (see Figure 1.13 above) and identified as Fe<sub>3</sub>O<sub>4</sub>/IRMOF-3 was employed for the preconcentration and quantification of trace levels of Cu<sup>2+</sup> from simulated aqueous metal solutions and from real life samples. Adsorption capacity and detection limit of 2.4 mg/g and 73 ng/mL respectively were obtained when Cu<sup>2+</sup> removal studies from simulated aqueous metal-laden solution was undertaken. From real life samples, excellent recoveries (at least 98 %) of trace levels of Cu<sup>2+</sup> (1 ng/mL) were observed. The magnetization saturation ( $M_s$ ) was significantly reduced from 80.9 emu/g for the bare Fe<sub>3</sub>O<sub>4</sub> to 20.3 emu/g for the MMOF extractant.<sup>149</sup>

More recently, Moradi *et al*<sup>150</sup> undertook the preconcentration of Cd<sup>2+</sup> using a sulfonated metal organic framework linked to Fe<sub>3</sub>O<sub>4</sub> to give the extractant identified as; Fe<sub>3</sub>O<sub>4</sub>@MOF-235(Fe-OSO<sub>3</sub>H). High adsorption capacity of 163.9 mg/g and low detection limit of 0.04 ng/mL were observed. Excellent recovery efficiency (>98.5 %) of trace levels of Cd<sup>2+</sup> (2 ng/mL) from tap water samples were also observed. The adsorption mechanism was attributed to chemisorption because the adsorption isotherm fitted the Langmuir model best. It was also found that the extractant could be reused for at least ten times without significant loss of Cd<sup>2+</sup> removal efficiency.

### 1.4.2.2 Magnetic organic extractants (MOEs)

Some organic ligands have been linked to iron oxide magnetic nanoparticles (IONPs) to give MOEs for the purposes of metal recovery and/or preconcentration prior to quantification. Examples of such ligands include carboxylic acid-based, amine/pyridine-based, thiol-based ligands and ionic liquids.

#### 1.4.2.2.1 Carboxylic acid-based MOEs

A few examples of metal recovery by these composite nanoparticles will be discussed. In 2008, Liu and coworkers<sup>151</sup> linked humic acid **1.11** (Figure 1.14) to Fe<sub>3</sub>O<sub>4</sub> to give Fe<sub>3</sub>O<sub>4</sub>@humic acid extractant by the simple co-precipitation method. They were pleased to observe that the humic acid surface functionalization did not significantly reduce the magnetization saturation, (79 emu/g for bare Fe<sub>3</sub>O<sub>4</sub> and 68.1 emu/g for Fe<sub>3</sub>O<sub>4</sub>@humic acid), attributable to the thin humic acid layer. Also, the extractant, Fe<sub>3</sub>O<sub>4</sub>@humic acid was observed to demonstrate excellent efficiencies in the removal of some heavy metals from aqueous solution (Pb<sup>2+</sup> and Hg<sup>2+</sup>; >99 % each; Cd<sup>2+</sup> and Cu<sup>2+</sup>; 95 % each). Another parameter used to measure the efficiency of a metal extractant is the adsorption capacity. The adsorption capacities (in mg/g) observed by the extractant Fe<sub>3</sub>O<sub>4</sub>@humic acid for the heavy metals decreased in the order Hg<sup>2+</sup>>Pb<sup>2+</sup>>Cd<sup>2+</sup>>Cu<sup>2+</sup>. The heavy metal removal was thought to have been achieved by complexation between the *O*- donors in humic acid **1.11** and the heavy metals.

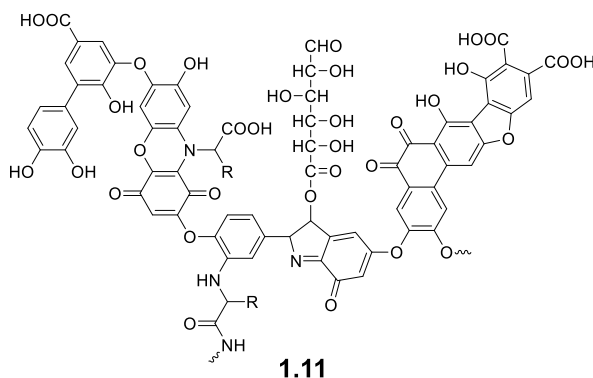
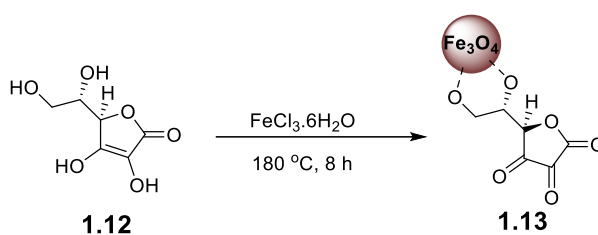


Figure 1.14: Structure of humic acid<sup>152</sup>

In 2012, ascorbic acid **1.12** functionalized  $\text{Fe}_3\text{O}_4$  extractant was prepared by the hydrothermal method to give  $\text{Fe}_3\text{O}_4$ @dehydroascorbic acid **1.13** (Scheme 1.2) as the ascorbic acid was observed from IR analysis to have been oxidized to dehydroascorbic acid) (Scheme 1.2). The  $\text{Fe}_3\text{O}_4$ @dehydroascorbic acid **1.13** extractant with a high surface area of  $179 \text{ m}^2/\text{g}$ , was employed for the recovery of two arsenic species namely;  $\text{As}^{3+}$  and  $\text{As}^{5+}$  and was observed to show higher adsorption capacity for the former ( $\text{As}^{3+}$ ;  $46.06 \text{ mg/g}$ ) than the latter ( $\text{As}^{5+}$ ;  $16.56 \text{ mg/g}$ ), attributable to the lower free energy of adsorption of  $\text{As}^{3+}$  than for  $\text{As}^{5+}$ .<sup>153</sup> The mechanism of metal uptake was determined to be chemisorption.<sup>154</sup>



**Scheme 1.2: Synthesis of  $\text{Fe}_3\text{O}_4$ @dehydroascorbic acid extractant**

#### 1.4.2.2.2 Amine/pyridine-based MOEs

Various *N*-donor ligands linked to IONPs have employed for metal recovery and some interesting results have been reported. In 2010, amino-functionalized  $\text{Fe}_3\text{O}_4$ @ $\text{SiO}_2$  nanoparticles prepared using 3-aminopropyltrimethoxysilane **1.14** (see Figure 1.15 below) as the silylation agent was observed to demonstrate adsorption capacities of 43.8, 111.9 and  $37.1 \text{ mg/g}$  for  $\text{Cu}^{2+}$ ,  $\text{Pb}^{2+}$  and  $\text{Cd}^{2+}$  respectively. Unfortunately, the magnetization saturation ( $M_s$ ) was significantly reduced after the silica ( $\text{SiO}_2$ ) coating and  $M_s$  determined for the  $\text{Fe}_3\text{O}_4$ ,  $\text{Fe}_3\text{O}_4$ @ $\text{SiO}_2$  and the amino-functionalized  $\text{Fe}_3\text{O}_4$ @ $\text{SiO}_2$  were 68.0, 36.2 and  $34.0 \text{ emu/g}$  respectively.<sup>104</sup>

In 2014, Behbahani *et al*<sup>155</sup> linked a pyridine functionalizing agent, *N*-(3-(triethoxysilyl)propyl)isonicotinamide (TPI) **1.15** (see Figure 1.15 below) to  $\text{Fe}_3\text{O}_4$ @ $\text{SiO}_2$  by a condensation of the hydroxyl group (from the surface of  $\text{Fe}_3\text{O}_4$ @ $\text{SiO}_2$ ) and ethoxy groups (from TPI) to form the nanocomposite extractant;  $\text{Fe}_3\text{O}_4$ @ $\text{SiO}_2$ @TPI which was employed for

the preconcentration of trace levels of  $\text{Pb}^{2+}$  and  $\text{Cu}^{2+}$ . The extractant demonstrated relatively high adsorption capacities of 287 and 194 mg/g for  $\text{Pb}^{2+}$  and  $\text{Cu}^{2+}$  respectively. Low detection limits of 0.1 and 0.08 ng/mL for  $\text{Pb}^{2+}$  and  $\text{Cu}^{2+}$  respectively were also obtained. Even in the presence of interfering ions like  $\text{Al}^{3+}$ ,  $\text{Cr}^{3+}$ ,  $\text{Mg}^{2+}$  and  $\text{Fe}^{3+}$ , excellent extraction efficiencies (of at least 96 % each) of both metals were observed.

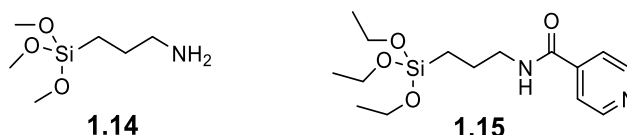


**Figure 1.15: Some ligands with silane handle employed for metal recovery purposes**

Later in 2014, Taghizadeh *et al*<sup>156</sup> anchored 8-aminoquinoline (8-AQ) **1.16** (Figure 1.16) on a multi-walled CNT (MWCNT)- $\text{Fe}_3\text{O}_4$  support and employed the resulting nanocomposite extractant (MWCNT- $\text{Fe}_3\text{O}_4$ @8-AQ) (Figure 1.16) for the preconcentration of trace levels of some heavy metals including  $\text{Cd}^{2+}$ ,  $\text{Pb}^{2+}$  and  $\text{Ni}^{2+}$  respectively. The MWCNT- $\text{Fe}_3\text{O}_4$ @8-AQ extractant was observed to demonstrate relatively high adsorption capacities of 201, 172 and 150 mg/g for  $\text{Cd}^{2+}$ ,  $\text{Ni}^{2+}$  and  $\text{Pb}^{2+}$ . These high adsorption capacities observed may have been achieved due to the high surface area of the MWCNT.

In 2015, the preparation of the MWCNT- $\text{Fe}_3\text{O}_4$ @ $\text{SiO}_2$ -diphenylamine (DPA) extractant was achieved over three steps, with the last step involving the nucleophilic substitution reaction between diphenylamine **1.17** (Figure 1.16) and 3-chloropropyltriethoxysilane on the surface of MWCNT- $\text{Fe}_3\text{O}_4$ @ $\text{SiO}_2$  to form MWCNT- $\text{Fe}_3\text{O}_4$ @ $\text{SiO}_2$ @DPA (see Figure 1.16 below). While the investigators observed a significant reduction in magnetization saturation of the MWCNT- $\text{Fe}_3\text{O}_4$ @ $\text{SiO}_2$ @DPA extractant (22 emu/g) compared to that of the precursor; MWCNT- $\text{Fe}_3\text{O}_4$  (55 emu/g), they will have been pleased to observe that the extractant demonstrated relatively high adsorption capacities for the removal of the heavy metals analytes studied ( $\text{Cr}^{3+}$ , 190 mg/g;  $\text{Cu}^{2+}$ , 180 mg/g and  $\text{Pb}^{2+}$ , 215 mg/g).<sup>157</sup>

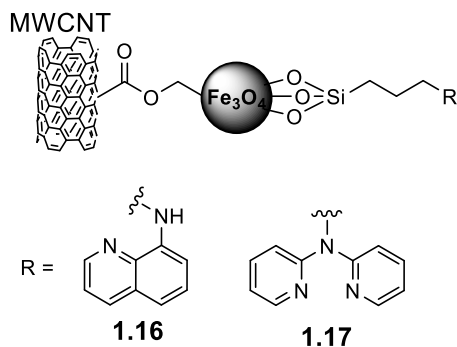


**Figure 1.16: Some pyridine-based ligands previously linked to multiwalled carbon nanotubes-Fe<sub>3</sub>O<sub>4</sub> composite and employed for metal recovery**

With the hope of developing a novel analytical method for the preconcentration and quantification of trace amounts of Cu<sup>2+</sup>, the limit of detection of Cu<sup>2+</sup> by the extractant; Fe<sub>3</sub>O<sub>4</sub>/GO@1,6-hexadiazine (prepared by functionalizing Fe<sub>3</sub>O<sub>4</sub>/GO with 1,6-hexadiazine **1.18** (Figure 1.17) following the solvothermal method in ethylene glycol) was determined. The extractant was observed to have low detection limit and precision of 0.9 ng/mL and 1.23 % respectively. Satisfied with these results, the investigators attempted the recovery of trace levels (0.5 µg/g) of Cu<sup>2+</sup> from some real samples including mushroom and eggplant and were pleased to observe quantitative recoveries of 98 and 97 % respectively.<sup>158</sup>



**Figure 1.17: Some amine-based ligands previously utilized for metal recovery**

Recently, the diethylenetriamine **1.19** (Figure 1.17) functionalized magnetic-GO nanocomposite extractant was prepared by the amidation reaction between diethylenetriamine and Fe<sub>3</sub>O<sub>4</sub>-GO to form the extractant nanoparticle, GO-Fe<sub>3</sub>O<sub>4</sub>-DETA. After employing the extractant for the preconcentration of trace levels (50 ng/mL) of Pb<sup>2+</sup> and Cd<sup>2+</sup>, relatively high adsorption capacities of 172.41 and 59.88 mg/g respectively were observed. The adsorbed metals were subsequently desorbed using HNO<sub>3</sub> (1 M, 3 mL) prior to their quantification by FAAS.<sup>159</sup>

### 1.4.2.2.3 Thiol-based MOEs

Thiol-based ligands/IONPs composites have been employed for  $\text{Au}^{3+}$  and  $\text{Hg}^{2+}$  recoveries. For example, in 2013, Zhang *et al*<sup>160</sup> linked 3-mercaptopropyltrimethoxysilane **1.20** (Figure 1.18) to  $\text{Fe}_3\text{O}_4@ \text{SiO}_2$  and observed that the resulting adsorbent (identified as  $\text{Fe}_3\text{O}_4@ \text{SiO}_2\text{-SH}$  **1.21**) recovered  $\text{Hg}^{2+}$  with a relatively high adsorption capacity of 148.8 mg/g at neutral pH. Using the same adsorbent ( $\text{Fe}_3\text{O}_4@ \text{SiO}_2\text{-SH}$ ), Roto and coinvestigators<sup>161</sup> recovered the precious metal; Au (as  $\text{AuCl}^-$ ) with a lower adsorption capacity of 115 mg/g and the process was governed by the Langmuir isotherm, indicating possible complexation between the thiol groups and the  $\text{AuCl}^-$  complex. Finally, Peng *et al*<sup>162</sup> reported that the  $\text{Fe}_3\text{O}_4@ \text{SiO}_2\text{-SH}$  adsorbent selectively removed  $\text{Au}^{3+}$  from aqueous solution containing  $\text{Cu}^{2+}$ , with an adsorption capacity of 43.7 mg/g.

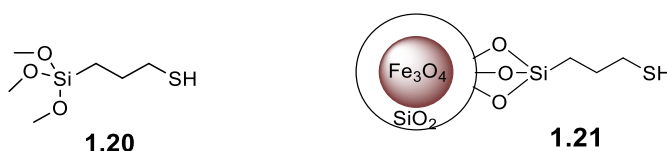


**Figure 1.18: Structure of 3-mercaptopropyltrimethoxysilane and illustration of the  $\text{Fe}_3\text{O}_4@ \text{SiO}_2\text{-SH}$  adsorbent**

### 1.4.2.2.4 Ionic liquid-based MOEs

Ionic liquids (ILs) are another example of organic ligands that have been linked to IONPs for metal recovery purposes.<sup>163,164</sup> ILs have been defined as compounds consisting only of ions and are liquids at or near room temperature. ILs have been classified into polyionic liquids (PILs)<sup>165</sup>, task specific ionic liquids (TSILs)<sup>166</sup>, room temperature ionic liquids (RTILs)<sup>167,168</sup>, and supported IL membranes (SILMs)<sup>169,170</sup>. Following the synthesis of the first ionic liquid – ethylammonium nitrate **1.22** (see Figure 1.19 below), in 1914, ionic liquids have been attracted huge research interest mainly due to their attractive features including their thermal stability, near-zero vapour pressure, adjustable polarity, hydrophobicity and solvent miscibility attributes following suitable modification of the anion and cation moieties.<sup>171,172</sup>



grafting density of polymers attached is usually low. This is due to steric hindrance on the nanoparticle surface by already adsorbed polymers.<sup>176</sup>

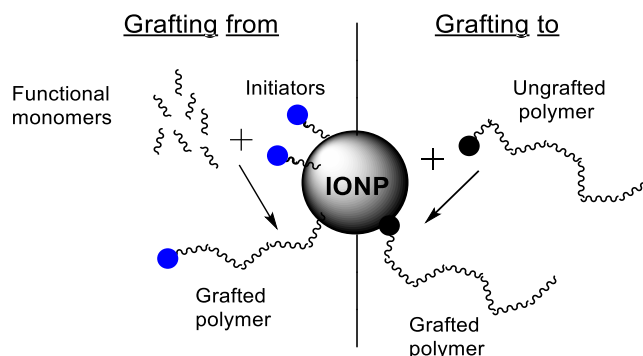


**Figure 1.20: Approaches for linking polymers to iron oxide nanoparticles**

In the grafting from technique, monomers are grown as polymers off the surface of the IONP through initiators that have been pre-attached to the IONP surface (Figure 1.20). The grafting from method has proceeded by free radical<sup>177</sup>, oxidative/chemical<sup>178,179</sup> and Cu(I)-mediated<sup>180,181</sup> polymerizations to mention a few. An attractive feature of this method is that polymer grafting density is arguably higher than for the grafting to method.<sup>125</sup> This is because steric hindrance is much lower since only a small amount of initiator is grafted onto the nanoparticle surface prior to polymerization.<sup>125</sup>

Different types of polymeric ligands including synthetic<sup>177,182</sup> and bio-based<sup>183,184</sup> types have been linked to IONPs for metal detection and recovery.

#### ***1.4.2.3.1 Synthetic magnetic polymeric extractants***

Synthetic magnetic polymeric extractants have been prepared by grafting synthetic polymeric ligands like polypyrrole and polythiophene from IONPs for metal recovery purposes. For example, in 2017, Mehdina and coinvestigators<sup>178</sup> linked polypyrrole **1.24** (see Figure 1.21 below), via oxidative polymerization to the Fe<sub>3</sub>O<sub>4</sub>-TiO<sub>2</sub> composite to give the core shell nanoparticle extractant; Fe<sub>3</sub>O<sub>4</sub>@TiO<sub>2</sub>@polypyrrole. The magnetization saturations of the Fe<sub>3</sub>O<sub>4</sub>@SiO<sub>2</sub>@polypyrrole extractant and its precursor Fe<sub>3</sub>O<sub>4</sub>/TiO<sub>2</sub> composite were found to be 65 and 28 emu/g respectively, indicating that the polypyrrole functionalization significantly

reduced the magnetization saturation. Fortunately, the  $\text{Fe}_3\text{O}_4@\text{TiO}_2@\text{polypyrrole}$  extractant demonstrated good adsorption capacity and low limit of detection of 126 mg/g and 0.28 ng/mL respectively in the recovery of trace amounts of  $\text{Pb}^{2+}$ . In fact, the extractant showed good recyclability property by retaining the initial  $\text{Pb}^{2+}$  adsorption efficiency after 8 cycles of  $\text{Pb}^{2+}$  adsorption and desorption.

$\text{Fe}_3\text{O}_4$  was functionalized with glycine doped polypyrrole (gly-ppy) via *in situ* oxidative polymerization to give  $\text{Fe}_3\text{O}_4@\text{gly-ppy}$  nanocomposite extractant which was found to have a much lower magnetization saturation than its precursor  $\text{Fe}_3\text{O}_4$  ( $\text{Fe}_3\text{O}_4$ ; 60 emu/g vs  $\text{Fe}_3\text{O}_4@\text{gly-ppy}$ ; 2.2 emu/g). Using optimum conditions of pH 2 and temperature of 45 °C, an adsorption capacity of 303 mg/g in the recovery of  $\text{Cr}^{6+}$  was observed. Electrostatic attraction between the positively charged surface of the extractant and the chromium complex  $\text{HCrO}_4^-$  (the preferred form of chromium at low pH) was put forward as the mechanism for the  $\text{Cr}^{6+}$  removal.<sup>185</sup>

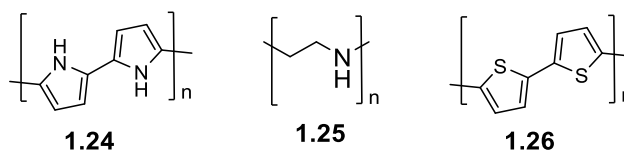


**Figure 1.21: Some synthetic polymeric ligands previously employed for metal recovery.**

In 2011 Pang *et al*<sup>186</sup> grafted polyethylenimine (PEI) **1.25** (Figure 1.21) off  $\text{Fe}_3\text{O}_4@\text{SiO}_2$  particles to give the extractant;  $\text{Fe}_3\text{O}_4@\text{SiO}_2@\text{PEI}$  which, based on extraction efficiency data, showed some selectivity for  $\text{Cu}^{2+}$  from a ternary aqueous solution containing  $\text{Cu}^{2+}$ ,  $\text{Zn}^{2+}$  and  $\text{Cd}^{2+}$  (extraction efficiencies in %;  $\text{Cu}^{2+}$ ; 96,  $\text{Zn}^{2+}$ ; 37 and  $\text{Cd}^{2+}$ ; 34). The selectivity by the extractant,  $\text{Fe}_3\text{O}_4@\text{SiO}_2@\text{PEI}$  for  $\text{Cu}^{2+}$  was attributed to the fit between the atomic radius of  $\text{Cu}^{2+}$  and the pore spaces in the extractant. The extractant could be regenerated by washing in 15 mL 0.02 M EDTA without significant loss of adsorption capacity.

In 2014, Tahmasebi and Yamini<sup>187</sup> claimed that polythiophene (Pth) **1.26** (Figure 1.21) functionalized  $\text{Fe}_3\text{O}_4$  nanoparticles prepared via the oxidative polymerization of thiophene to

give Fe<sub>3</sub>O<sub>4</sub>@Pth extractant, selectively recovered a mixture of the precious metals – Ag<sup>+</sup>, Au<sup>3+</sup> and Pd<sup>2+</sup> from aqueous solution containing these precious metals and the heavy metals – Fe<sup>3+</sup>, Co<sup>2+</sup>, Zn<sup>2+</sup>, Cr<sup>3+</sup> and Pb<sup>2+</sup>. The selectivity of the Fe<sub>3</sub>O<sub>4</sub>@Pth extractant for the precious metals was attributed to the HSAB principle where the soft S- donor in the extractant preferentially complexed the soft acceptors – Ag<sup>+</sup>, Au<sup>3+</sup> and Pd<sup>2+</sup>. Twenty milligrams of the extractant could be rapidly regenerated (in 1 min) by eluting the adsorbed metals using a 0.2 mL mixture of 1 M thiourea (to elute Ag<sup>+</sup> and Au<sup>3+</sup>) and 0.01 M HNO<sub>3</sub> (to elute Pd<sup>2+</sup>).

#### **1.4.2.3.2 Bio-based magnetic polymeric extractants**

Bio-based magnetic polymeric extractants have been made by linking bio-based polymeric ligands to IONPs and good metal recovery efficiencies and relatively high adsorption capacities have been reported. For example, carboxymethyl-β-cyclodextrin (CM-β-BD) was linked to a Fe<sub>3</sub>O<sub>4</sub> magnetic nanoparticle by a one pot co-precipitation procedure and was found to preferentially extract some heavy metals in the order Pb<sup>2+</sup>>>Cd<sup>2+</sup>>Ni<sup>2+</sup> from ternary aqueous solutions. The extraction efficiencies achieved after an optimum contact time of 45 min were 94.9 %, 10.3 % and 7.3 % for Pb<sup>2+</sup>, Cd<sup>2+</sup> and Ni<sup>2+</sup> respectively. The preference of the carboxymethyl-β-cyclodextrin for Pb<sup>2+</sup> was explained by the HSAB principle. The extractant could be regenerated by sequential elution using 0.01 M HNO<sub>3</sub> (for Pb<sup>2+</sup>), 0.02 M H<sub>3</sub>PO<sub>4</sub> (for Cd<sup>2+</sup> and Ni<sup>2+</sup>).<sup>188</sup>

Furthermore, Fe<sub>3</sub>O<sub>4</sub> nanoparticles were modified using the bio-based polymer, chitosan **1.27** (see Figure 1.22 below) by the co-precipitation method to give Fe<sub>3</sub>O<sub>4</sub>@chitosan extractant. It was observed that the higher the chitosan amount employed for the surface modification of Fe<sub>3</sub>O<sub>4</sub> nanoparticles, the lower the magnetization saturation ( $M_s$ ) value of the Fe<sub>3</sub>O<sub>4</sub>@chitosan extractant obtained. Starting with a  $M_s$  value of 70.1 emu/g for the bare Fe<sub>3</sub>O<sub>4</sub>, chitosan contents of 0.125, 0.250 and 0.500 w/v % gave Fe<sub>3</sub>O<sub>4</sub>@chitosan extractant with  $M_s$  values of 66.4, 61.6 and 45.1 emu/g respectively. The investigators were surprised to find that the higher the chitosan content on the surface of the extractant, the lesser the amount of Pb<sup>2+</sup> recovered. They hypothesized that the high chitosan content may have occasioned a higher degree of

aggregation of the extractant, leading to lower surface area and ultimately lower extraction efficiencies. The best extraction efficiency observed was 54 % at chitosan content of 0.125 w/v %.<sup>189</sup>

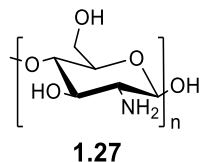


Figure 1.22: Structure of chitosan

Finally, a magnetic solid phase extraction method for the preconcentration of trace levels of  $\text{Cr}^{3+}$  and  $\text{Cr}^{6+}$ , based on the chitosan **1.27** (Figure 1.22) functionalized  $\text{Fe}_3\text{O}_4@\text{SiO}_2$  nanoparticle was developed and found to be selective for  $\text{Cr}^{3+}$  at pH 9 (extraction efficiencies in %;  $\text{Cr}^{3+}$ , 90 and  $\text{Cr}^{6+}$ , 10).<sup>190</sup>

## 1.5 Problem statement

From the literature surveyed, it appears that attention has not been paid to the selective and efficient recovery of  $\text{Ag}^+$  from ternary aqueous solutions using  $\text{Fe}_3\text{O}_4$  nanoparticles coated with selective organic ligands. Therefore, in this work, a method based on adsorption for the selective recovery of  $\text{Ag}^+$  from ternary aqueous solutions will be investigated which allows concentration of silver via extraction of  $\text{Fe}_3\text{O}_4$  nanoparticles from solution by a magnetic process (Figure 1.23).

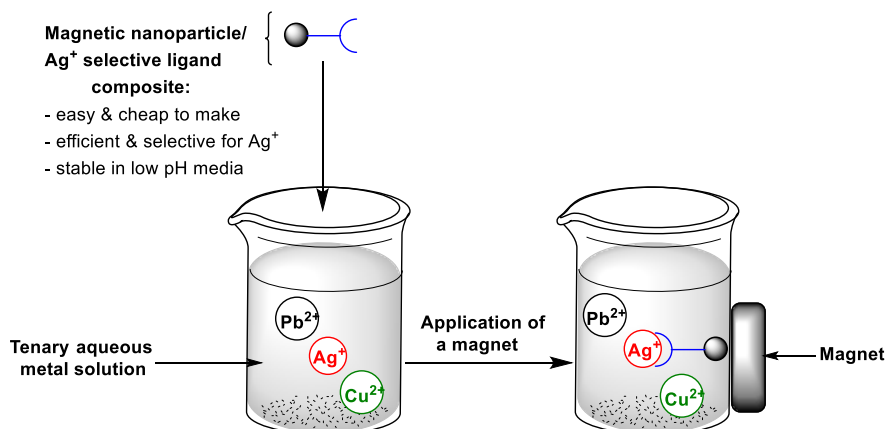


Figure 1.23: Overall aim of this thesis

The investigation will begin with the synthesis and testing of selective  $\text{Ag}^+$  ligands for the selective  $\text{Ag}^+$  recovery from ternary aqueous solutions. This will be followed by a thorough investigation of the binding studies of these ligands with  $\text{Ag}^+$ . Upon satisfaction with the selectivity and efficiency of the synthesized  $\text{Ag}^+$  ligands, their linkage to magnetic iron oxide nanoparticles via a 'grafting on' approach to form  $\text{Ag}^+$ -ligand/magnetic composite nanoparticles will be undertaken (without significant loss of magnetisation). Upon successful synthesis of the  $\text{Ag}^+$ /ligand-magnetic composite nanoparticles, selective  $\text{Ag}^+$  recovery studies will be undertaken.

It is hoped that the knowledge gained from this study can be applied for selective  $\text{Ag}^+$  recovery from real life samples like metallurgical slag heaps and mining tailings containing  $\text{Ag}^+$ .

## **Chapter 2: Synthesis and application of novel Ag<sup>+</sup> selective ligands**



for Ag<sup>+</sup> by these ligands are numerous, and not one principle perfectly explains the theoretical basis for their Ag<sup>+</sup> selectivity and efficiency. Notwithstanding, a range of factors have been put forward for the preferential binding of Ag<sup>+</sup> by almost all the ligands **2.1-2.10** from Figure 2.1. The Ag<sup>+</sup> selectivity of cyclophosphagenes **2.1**, carboxylic acid **2.2**, thioamide **2.4** and imidazolium **2.6** was explained by the Hard Soft Acid Base rule (HSAB). The HSAB rule states that hard acids will prefer to bind to hard bases, while soft acids will prefer to bind to soft bases.<sup>204</sup> According to Pearson<sup>204</sup>, the Ag<sup>+</sup> ion is a soft acid while *S*-, or *N*-atoms, are soft bases (Table 2.1 and Table 2.2).

**Table 2.1: Classification of Lewis bases into Hard, Soft or Borderline<sup>204</sup>**

Hard	Soft
H <sub>2</sub> O, OH <sup>-</sup> , F <sup>-</sup> , CH <sub>3</sub> CO <sub>2</sub> <sup>-</sup> , SO <sub>4</sub> <sup>2-</sup> , ClO <sub>4</sub> <sup>-</sup> , NO <sub>3</sub> <sup>-</sup> , ROH, R <sub>2</sub> O, RNH <sub>2</sub> , N <sub>2</sub> H <sub>4</sub> , PO <sub>4</sub> <sup>3-</sup> , Cl <sup>-</sup> , CO <sub>3</sub> <sup>2-</sup> , RO <sup>-</sup> , NH <sub>3</sub>	R <sub>2</sub> S, RSH, RS <sup>-</sup> , I <sup>-</sup> , SCN <sup>-</sup> , S <sub>2</sub> O <sub>3</sub> <sup>2-</sup> , R <sub>3</sub> P, (RO) <sub>3</sub> P, CN <sup>-</sup> , R <sub>3</sub> As, RNC, CO, C <sub>2</sub> H <sub>4</sub> , C <sub>6</sub> H <sub>6</sub> , H <sup>-</sup> , R <sup>-</sup>
<b>Borderline</b> C <sub>6</sub> H <sub>5</sub> NH <sub>2</sub> , C <sub>5</sub> H <sub>5</sub> N, N <sup>3-</sup> , Br <sup>-</sup> , SO <sub>3</sub> <sup>2-</sup> , N <sub>2</sub>	
R = alkyl or aryl group	

**Table 2.2: Classification of Lewis acids into Hard, Soft or Borderline<sup>204</sup>**

Hard	Soft
H <sup>+</sup> , Li <sup>+</sup> , Na <sup>+</sup> , K <sup>+</sup> , Mg <sup>2+</sup> , Ca <sup>2+</sup> , Sr <sup>2+</sup> , Al <sup>3+</sup> , Cr <sup>3+</sup> , Co <sup>3+</sup> , Fe <sup>3+</sup> , Si <sup>4+</sup> , Ti <sup>4+</sup> , Zr <sup>4+</sup> , U <sup>4+</sup>	Cu <sup>+</sup> , Ag <sup>+</sup> , Au <sup>+</sup> , Hg <sup>+</sup> , Pd <sup>2+</sup> , Cd <sup>2+</sup> , Pt <sup>2+</sup> , Hg <sup>2+</sup> , CH <sub>3</sub> Hg <sup>+</sup> , Pt <sup>4+</sup> , Te <sup>4+</sup>
<b>Borderline</b> Fe <sup>2+</sup> , Co <sup>2+</sup> , Ni <sup>2+</sup> , Cu <sup>2+</sup> , Zn <sup>2+</sup> , Pb <sup>2+</sup> , Sn <sup>2+</sup>	

For the cyclophosphagene ligand **2.1** and the imidazolium **2.6** the presence of the soft *N*-donor atom was associated with their selectivity for Ag<sup>+</sup>. Further, for cyclophosphagene **2.1** it was reported that irrespective of the nature of the side arm group (R = -C<sub>2</sub>H<sub>5</sub>, or -C<sub>2</sub>H<sub>4</sub>OCH<sub>3</sub>), selectivity of **2.1** for Ag<sup>+</sup> was roughly the same.<sup>195</sup> This confirmed that the *N*-donor, not the *O*-donor in the ether arm was probably responsible for Ag<sup>+</sup> binding. Similarly, it was claimed that the *N*- and *S*-donor centres are responsible for the selectivity of the Ag<sup>+</sup> ion by the carboxylic acid group in ligand **2.2**.<sup>196</sup> The possibility of *O*-coordination by the carboxylic moiety was eliminated on the basis that best extraction efficiency for Ag<sup>+</sup> was observed at a lower pH (pH = 4) than the p*K*<sub>a</sub> of the ligand, (p*K*<sub>a</sub> ~ 4.8). In the solvent extraction of Ag<sup>+</sup>

from water into chloroform the high selectivity and efficiency of the thioether **2.3** for Ag<sup>+</sup> was attributed to the greater lipophilicity of its Ag<sup>+</sup> complex compared with the corresponding Ag<sup>+</sup> complexes formed by the similar tripodal ligands **2.11** and **2.12**. The Ag<sup>+</sup>-thioether **2.3** complex was considered more lipophilic owing to the presence of an extra aryl group. While this explanation may seem satisfactory, perhaps a better explanation could be that the S-donor is softer than the O-donor.<sup>204,205</sup> A similar selectivity was observed for the S-, N-donors in thioamide **2.4**.

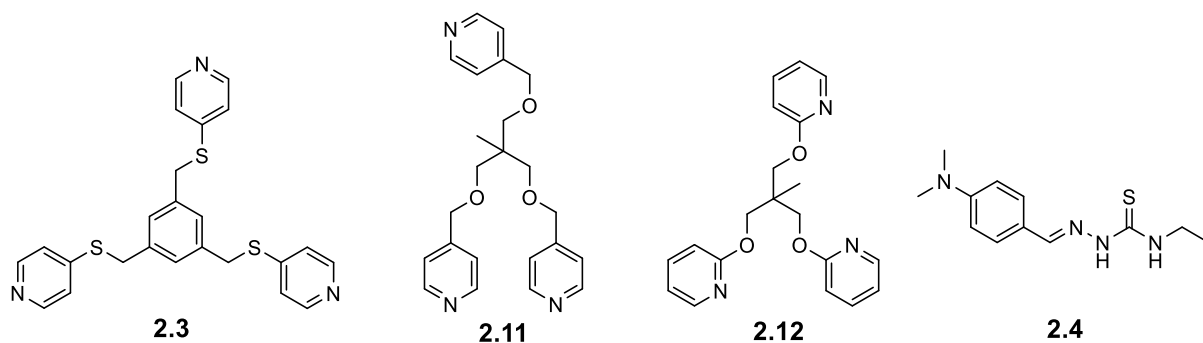


Figure 2.2: Some tripodal Ag<sup>+</sup> ligands<sup>197</sup>

Imprinted molecules such as **2.7** and **2.8** are selective due to “molecule memory”.<sup>200</sup> For ligand **2.7**, a Ag<sup>+</sup> complex of the ligand was first synthesized, then the Ag<sup>+</sup> was leached from this complex. After leaching, the metal free ligand was then used to extract Ag<sup>+</sup> selectively from an aqueous solution containing other interfering ions.<sup>200</sup> In contrast to the HSAB, lipophilicity and molecule memory factors, selectivity of calix[n]arene **2.9** for the Ag<sup>+</sup> ion has been attributed to the formation of “ $\pi$ -coordination” between the electron cloud in the benzene ring and Ag<sup>+</sup>.<sup>206</sup> In addition to these factors, other general characteristics such as the hydration energy of the Ag<sup>+</sup>-ligand complex<sup>195</sup>, the polarity or dielectricity of the organic solvent<sup>207</sup>, and the size of ligand (such as whether it is monomeric or polymeric)<sup>195</sup> are all influential in determining the selectivity and efficiency of ligands for extraction of Ag<sup>+</sup>. That said, the most adopted principle to explain the selectivity of these ligands is the HSAB rule.

### 2.1.1 Extraction efficiency of some reported Ag<sup>+</sup>-selective ligands

Interest has been paid to the efficiency of Ag<sup>+</sup> selective ligands to recover Ag<sup>+</sup> from very dilute aqueous solutions (as dilute as 20 ng/mL). Solvent extraction and pre-concentration studies (prior to analysis) have been undertaken to investigate efficiency.<sup>200,203,208</sup> Several of the ligands already described have demonstrated excellent efficiencies and selectivities for Ag<sup>+</sup> extraction from aqueous matrices (Table 2.3).

**Table 2.3: Extraction efficiencies of some proven Ag<sup>+</sup>-selective ligands for Ag<sup>+</sup> extraction**

Ligand	Interfering ions	Extraction efficiency (%)
2.1 <sup>195</sup>	Cu <sup>2+</sup> , Na <sup>+</sup> , K <sup>+</sup> , Mg <sup>2+</sup> , Ca <sup>2+</sup> , Rb <sup>+</sup> , Cs <sup>+</sup> , Sr <sup>2+</sup> , Ba <sup>2+</sup> & Co <sup>2+</sup>	90
2.2 <sup>196</sup>	Cu <sup>2+</sup> , Pb <sup>2+</sup> , Na <sup>+</sup>	99 89 99
2.4 <sup>198</sup>	Cu <sup>2+</sup> Pb <sup>2+</sup> Zn <sup>2+</sup>	96 98 98
2.5 <sup>199</sup>	Co <sup>2+</sup> , Ni <sup>2+</sup> , Cu <sup>2+</sup> , Zn <sup>2+</sup> , Cd <sup>2+</sup> & Pb <sup>2+</sup>	73
2.6 <sup>164</sup>	Cu <sup>2+</sup> & Pb <sup>2+</sup>	96
2.7 <sup>200</sup>	Cu <sup>2+</sup> , Ni <sup>2+</sup> , Fe <sup>2+</sup> , Fe <sup>3+</sup> , Mg <sup>2+</sup> & Ca <sup>2+</sup>	98
2.9 <sup>202</sup>	Pd <sup>2+</sup>	99

Studies have considered the effect of the ligand structure, the effect of interfering metals, the extraction pH, the extraction time and the effect of the type of organic solvent in the selective extraction of Ag<sup>+</sup>.

## 2.2 Aims and objectives

The main aim described in this chapter is to prepare a Ag<sup>+</sup> selective ligand bearing a vinyl handle. The vinyl handle will be required to tether Ag<sup>+</sup> selective ligands along with other vinyl monomers, via a polymerization technique, to a magnetic nanoparticle to form a core-shell nanoparticle/polymer composite containing Ag<sup>+</sup> selective ligands (see Figure 2.3 below). The tethering of the vinyl functionalized ligand will be the focus in chapter 4.

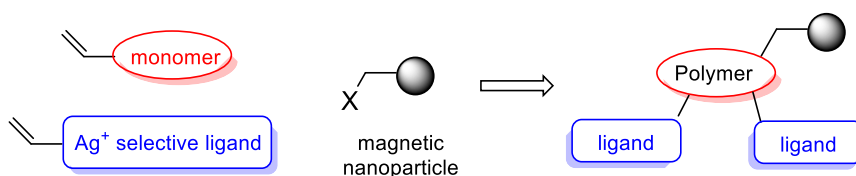


**Figure 2.3: Generic approach to making nanoparticle/polymer composite**

In addition, any selective ligand prepared must have the following characteristics;

- A simple synthesis and requiring cheap/readily available reagents,
- Easily functionalizable with a vinyl group,
- Have a high stability in low and high pH environments

The ligands chosen are needed to possess these features because of the nature of the potentially low pH environment of landfills, mine tailings and metallurgical slag heaps where they may be applied.<sup>209</sup> Additionally, as Ag<sup>+</sup> is usually present in very low concentrations in these sources, large amounts of the ligands will be required. Therefore, to minimize cost, cheap and readily available reagents are needed. After a literature search guided by the criteria above, malonamide derivative **2.10** (and consequently the vinyl derivative **2.13**) (Figure 2.4) were chosen to be initial targets.

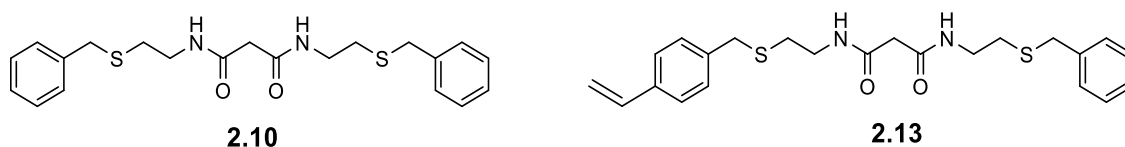


**Figure 2.4: Potential scaffolds for selective Ag<sup>+</sup> recovery**

In addition, it was also decided to investigate the effects of electronic (**2.14-2.17**) and steric (**2.18-2.19**) changes of ligand structure to the efficiency of Ag<sup>+</sup> extraction (see Figure 2.5 below).

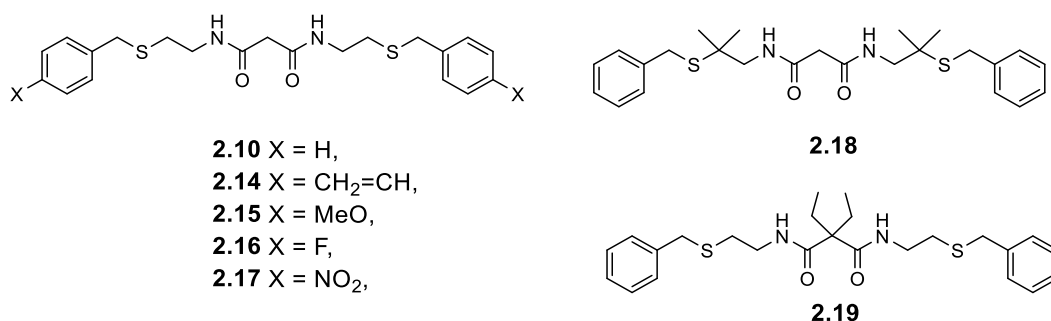
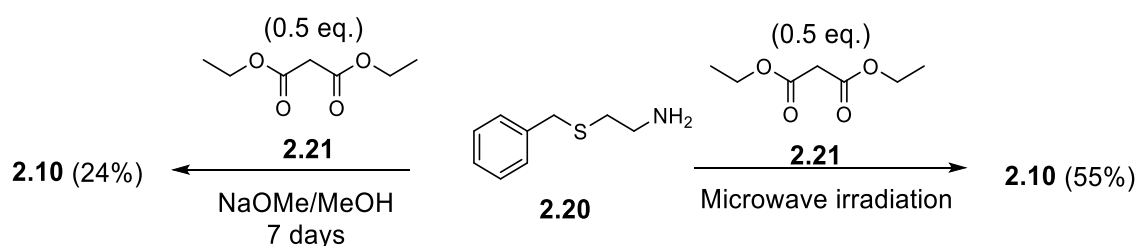


Figure 2.5: Malonamide derivatives prepared and tested in this chapter

## 2.3 Result and discussion

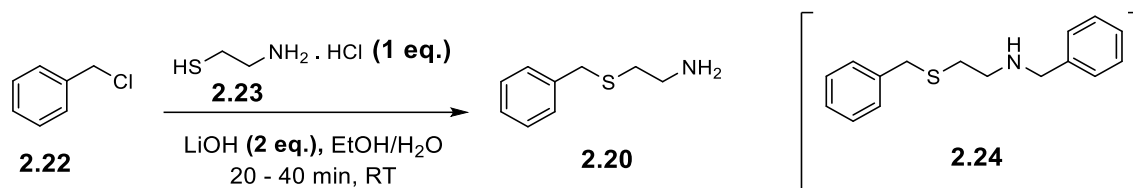
The Ag<sup>+</sup> ligand **2.10** has been reported to demonstrate excellent selectivity and efficiency (97%) for the major isotopes of Ag<sup>+</sup> - <sup>107</sup>Ag and <sup>109</sup>Ag from an aqueous solution also containing Cu<sup>2+</sup> and Pb<sup>2+</sup>.<sup>203</sup> Furthermore, because the **2.10** scaffold possesses no easily hydrolysable or basic nitrogen/pyridyl groups it should be very stable in low and high pH environments. Indeed, it was reported that extraction efficiency of the ligand **2.10** for Ag<sup>+</sup> was almost constant in the pH range of 2–9.<sup>203</sup> This suggests that the ligand is quite stable and efficient at both low and slightly high pH. Malonamide derivative **2.10** was previously prepared by amidation of diethylmalonate by *S*-benzylcysteamine **2.20** or its hydrochloride salt either via microwave irradiation or thermally (Scheme 2.1).<sup>203</sup>

Scheme 2.1: Previous synthesis of malonamide derivative **2.10**<sup>203</sup>

### 2.3.1 Synthesis of *S*-benzylcysteamine **2.20**

Pleasingly, several reported protocols<sup>210–214</sup> for the synthesis of **2.20** – a precursor to the target ligand **2.10** were found. Among the protocols found for the preparation of **2.20**, that reported by Ghosh and Tochtrop<sup>214</sup> appeared the simplest (see Scheme 2.2 below). From the published

experimental procedure, it became apparent that the temperature and time of the reaction was very specific and so both parameters were investigated in detail.



**Scheme 2.2. Synthesis of amine 2.20**<sup>214</sup>

Therefore, a solution of benzyl chloride **2.22** was added in a dropwise manner for 5 min to a stirred mixture of hydrochloride salt **2.23** and LiOH in a water/EtOH (3:1) mixture and the whole mixture was stirred at room temperature for 40 minutes (Scheme 2.2). The crude product was extracted with DCM and concentrated *in vacuo* to furnish a slightly yellow oil. The target compound **2.20** was then isolated from the crude product by flash chromatography providing pure **2.20** in a yield of 61 % (Table 2.4, entry 1). Two products were obtained both at 40 minutes (entry 1) and 30 minutes (entry 2) and identified as the desired product **2.20** and the dibenzylated by-product **2.24** in a 17:1 ratio respectively.

**Table 2.4: Effect of reaction time on synthesis of 2.20 at room temperature**

Entry	Reaction time (min)	2.20: 2.24	Isolated Yield
1	40	17:1	61 %
2	30	17:1	60 %
3	20	45:1	57 %

Two possible factors could have encouraged the formation of **2.24**.

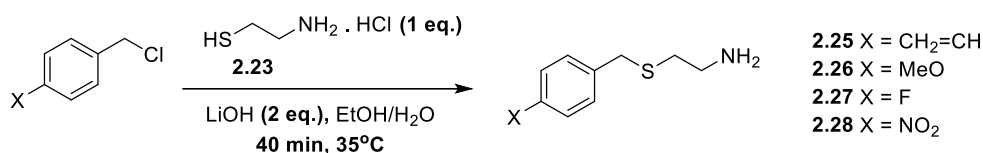
- Nucleophilic displacement of a second molecule of benzyl chloride **2.22** by amine **2.20**.
- Initial *N*-alkylation of **2.23** by benzyl chloride **2.22** followed by a second *S*-alkylation.

The known increased nucleophilicity of the thiol group over the amine group suggest the former explanation. One method for testing this hypothesis is to limit the interaction of **2.22**

and **2.20**. A practical way of doing this is to reduce the reaction time further. The reaction time was reduced to 20 min with the hope of obtaining higher selectivity for **2.20**. Pleasingly, a higher selectivity of 45:1 was obtained (entry 3). Monitoring the reaction by TLC indicated that the reaction was complete after 20 minutes at room temperature.

The effect of temperature was next determined by repeating the reaction for a duration of 20 and 40 minutes but at 35 °C instead of room temperature. The higher temperature led to lower selectivity for the desired product **2.20** (20 minutes; **2.20:2.24** = 40:1, 40 minutes; **2.20:2.24** = 10:1) but the highest isolated yield of **2.20** was obtained after 20 minutes at 35 °C (90%).

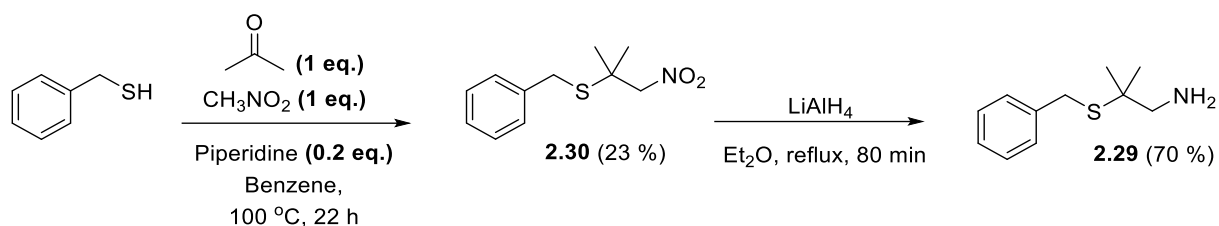
### 2.3.2 Synthesis of S-benzylcysteamine derivatives 2.25-2.28



**Scheme 2.3: Synthesis of amines 2.25-2.28**

The optimum conditions (time; 20 min and temperature; 35° C) were next applied to prepare the novel styryl analogue **2.25** (Scheme 2.3). For the styryl derivative **2.25** it was necessary to extend the reaction time to 40 minutes to give an acceptable isolated yield (20 mins = 16%, 40 mins = 77%). Having successfully prepared the styryl derivative **2.25**, the synthesis of a range of related ligands **2.26-2.28** containing electron withdrawing F-, and -NO<sub>2</sub> groups and the electron donating -OMe group using the same protocol as used for the preparation of **2.25** (time: 40 mins, temperature; 35 °C) were briefly investigated. Good selectivity (negligible dibenzylated products were detected <3%) and yields were observed for all three compounds (**2.26** = 88%, **2.27** = 85%, **2.28** = 85%). In fact, only the crude product obtained from the synthesis of the fluoro analogue **2.27** needed purification.

### 2.3.3 Synthesis of gem disubstituted *S*-benzylcysteamine **2.29**<sup>215</sup>

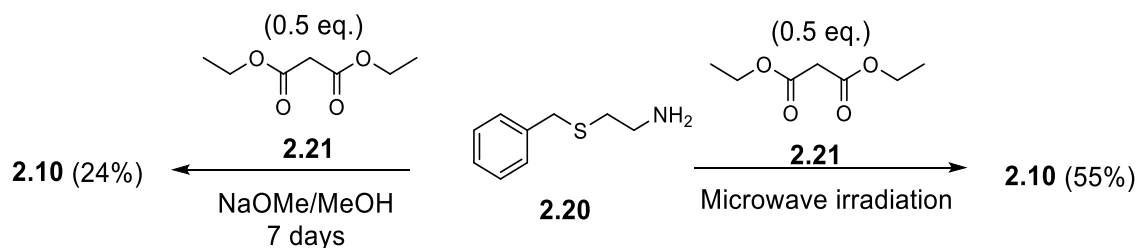


**Scheme 2.4:** Synthesis of gem-disubstituted *S*-benzylcysteamine **2.29**<sup>215</sup>

In order to assess the effect of sterics on potential novel ligands the substituted *S*-benzylcysteamine **2.29** was synthesized by a modification of a method reported by Carroll and coresearchers.<sup>215</sup> Briefly, a mixture of benzylmercaptan (1 eq.), piperidine (0.2 eq.), nitromethane (1 eq.) and acetone (1 eq.) in benzene was heated at 100 °C for 22h. The crude product obtained was purified by flash chromatography to furnish **2.30** as a yellow oil in a 23 % yield. The nitro derivative **2.30** was then reduced with an ethereal solution of LiAlH<sub>4</sub>. The crude product obtained was then purified by flash chromatography to furnish as a yellow oil **2.29** in a 70 % yield (Scheme 2.4).

### 2.3.4 Synthesis of *N,N'* malonamide derivative **2.10**

*N,N'*-Malonamide derivatives have interesting applications in medicinal<sup>216</sup> and environmental chemistry<sup>217–219</sup>. Therefore, their synthesis has been extensively studied. It was stated earlier that Daubinet and Kaye<sup>203</sup> accessed malonamide derivative **2.10** *via* two different routes; a microwave assisted method and a thermal one (Scheme 2.5).



**Scheme 2.5:** Previous synthesis of malonamide derivative **2.10**<sup>203</sup>

### 2.3.4.1 Attempted synthesis of 2.10 by the microwave assisted method

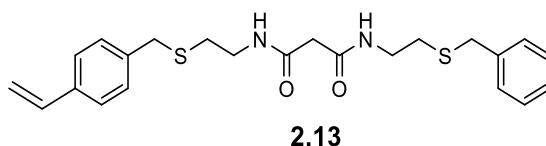
It was decided to adopt the microwave assisted method because it requires a shorter reaction time. Therefore, to confirm the reproducibility of this approach (which used a different microwave set-up), initial work focused on accessing **2.10** by reacting a mixture of amine **2.20** and malonate **2.21** at 300 W, 100 °C and 3.5 min in a microwave reactor. Unfortunately, only starting materials were recovered (Table 2.5, entry 1). Increasing the reaction time to 20 minutes or increasing the temperature to 200 °C furnished the same result (entries 2-6). It is believed that attempts at accessing **2.10** via the microwave assisted method were unsuccessful because the exact conditions employed by Daubinet and Kaye<sup>203</sup> in their paper could not be replicated. Daubinet and Kaye<sup>203</sup> reported that the microwave reactor they used was set to “defrost setting”. The defrost setting mode employed by Daubinet and Kaye<sup>203</sup> could only be achieved using a regular kitchen microwave, which was deemed not acceptable for laboratory work due to safety implications (typically kitchen microwaves are not spark proof).

**Table 2.5: Attempted synthesis of malonamide derivative 2.10 by microwave assisted method**

Entry	Temperature (°C)	Time (min)	Result
1	100	3.5	No reaction
2	100	10	No reaction
3	120	5	No reaction
4	150	5	No reaction
5	180	5	No reaction
6	200	5	No reaction

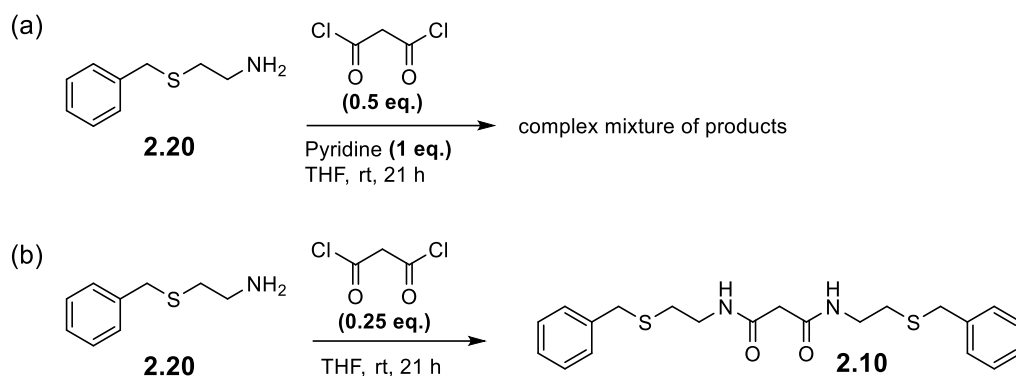
### 2.3.4.2 Approaches towards malonamide derivatives using malonyl chloride

After failing to access **2.10** by the microwave assisted method, the reaction of *S*-benzylcysteamine **2.20** with malonyl chloride at room temperature was next explored. The reactive acid chloride should facilitate amide formation and reduce the reaction time from the reported 7 days at elevated temperatures. The malonyl chloride route at room temperature would be important when preparing malonate derivatives with styryl groups (e.g. **2.13**, see Figure 2.6 below) potentially minimizing any undesired polymerization during preparation.



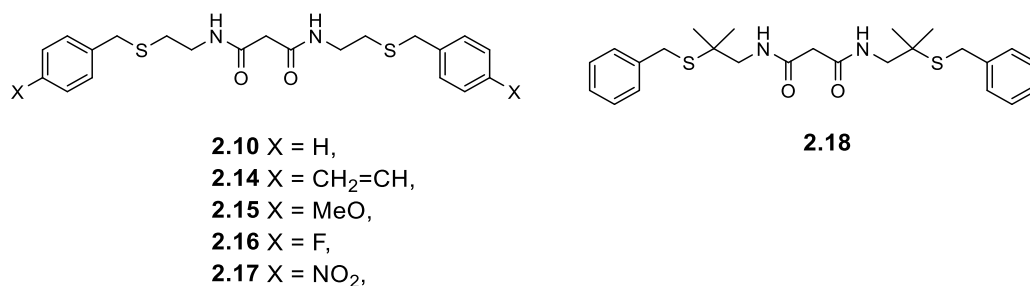
**Figure 2.6: A styryl malonamide derivative 2.13**

The new approach to accessing the malonamide derivative **2.10** which is a modification of that reported by Daubinet and Kaye<sup>203</sup>, was attempted by adding a THF solution of malonyl chloride in a dropwise manner to a stirred solution of amine **2.20** (1 eq.) and pyridine (1 eq.) in dry THF at room temperature (Scheme 2.6a). As the first few drops of the malonyl chloride solution were added to **2.20**, the reaction mixture turned bright red. Later as the addition continued, the reaction mixture turned brown. After the complete addition the reaction was left to stir overnight. The crude mixture obtained was extracted with EtOAc to obtain a crude material, which upon TLC contained many products. Unfortunately, attempts at isolating **2.10** were unsuccessful. In case the base pyridine was causing problems, it was removed and malonyl chloride was treated with 4 equivalents of *S*-benzylcysteamine **2.20** (it acting as its own sacrificial base). Hence, a THF solution of malonyl chloride (0.25 eq.) was added in a dropwise manner to a stirred THF solution of **2.20** (1 eq.) (Scheme 2.6b). As the first few drops of malonyl chloride were added to **2.20**, formation of a white precipitate was observed in the reaction mixture. Later as the addition continued, the reaction mixture turned yellow. The reaction was left overnight. The crude product was purified by flash chromatography providing **2.10** as a yellow solid in a 33 % yield (Table 2.6, entry 1). This yield is slightly greater than that reported by Daubinet and Kaye<sup>203</sup> (24%) using diethylmalonate.

Scheme 2.6: Synthesis of **2.10** using malonyl chloride

### 2.3.4.2.1 Synthesis of aryl substituted malonamide derivatives **2.14–2.17**

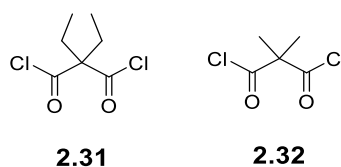
As stated in section 2.2, the initial aims were to prepare a range of derivatives of **2.10** altering electronic and steric parameters to determine structure activity relationships for Ag<sup>+</sup> selectivity and efficiency of extraction from aqueous solutions. Satisfied with the new route to accessing **2.10**, it decided to apply it to the formation of **2.14–2.18** using the amine derivatives **2.25–2.29** prepared in the previous section (see section 2.3.2). Consequently, it was observed that all target malonamide derivatives **2.14–2.18**, (Table 2.6, entries 2–6) were accessed.

Figure 2.7: Malonamide derivative target ligands **2.14–2.18**Table 2.6: Synthesis of malonamide derivatives **2.10**, **2.14 – 2.18**.

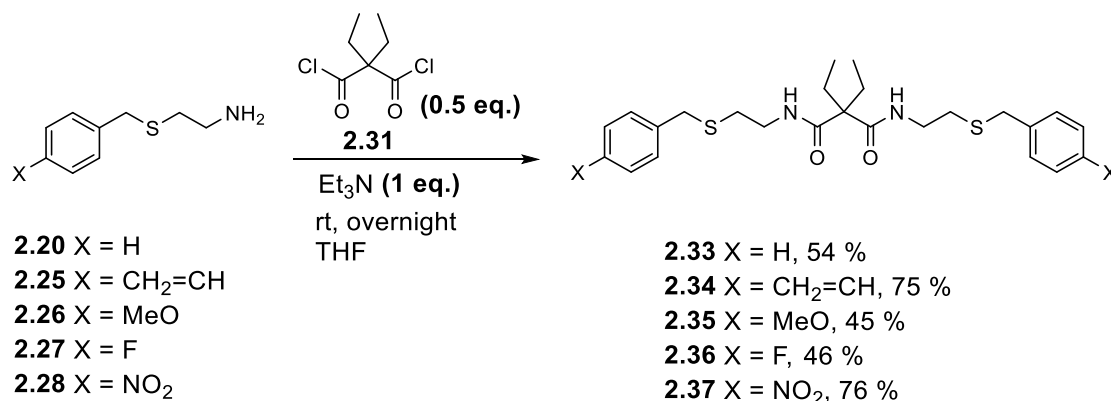
Entry	Substrate	X	Product	Yield
1	<b>2.20</b>	H	<b>2.10</b>	33 %
2	<b>2.25</b>	CH <sub>2</sub> =CH	<b>2.14</b>	33 %
3	<b>2.26</b>	MeO	<b>2.15</b>	12 %
4	<b>2.27</b>	F	<b>2.16</b>	31 %
5	<b>2.28</b>	NO <sub>2</sub>	<b>2.17</b>	34 %
6	<b>2.29</b>	-	<b>2.18</b>	89 %

### 2.3.4.3 Synthesis of aryl substituted gem-diethyl malonamide derivatives of **2.10** and **2.14–2.17**

Hypothesizing that the poor yields of the malonamide derivatives **2.14–2.17** maybe due to the readily enolizable protons adjacent to the carbonyls of the malonate functionality, the reaction with C-disubstitution at the malonyl group (Scheme 2.7). This would also allow us to study the effect of steric hindrance at this position in Ag<sup>+</sup> extraction. The gem-diethyl analogue **2.31** was chosen because it was cheaper than the gem-dimethyl analogue **2.32** (see Figure 2.8 below).



**Figure 2.8: Structures of two acid chlorides that can provide the acyl moiety of the target malonamide derivatives**

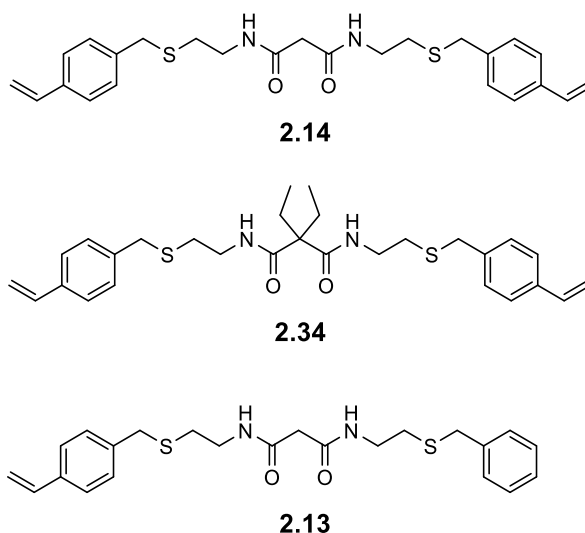


**Scheme 2.7: Structures of gem-diethyl malonamide derivatives 2.33-2.37**

Adding a dry ether solution of acid chloride **2.31** to a stirred solution of 2 equivalents of amine **2.20** and 1 equivalent of triethylamine in dry ether at room temperature allowed for the preparation of **2.33** in 54% isolated yield. The other derivatives **2.34–2.37** were accessed using the same procedure in moderate to good yields (45–76%).

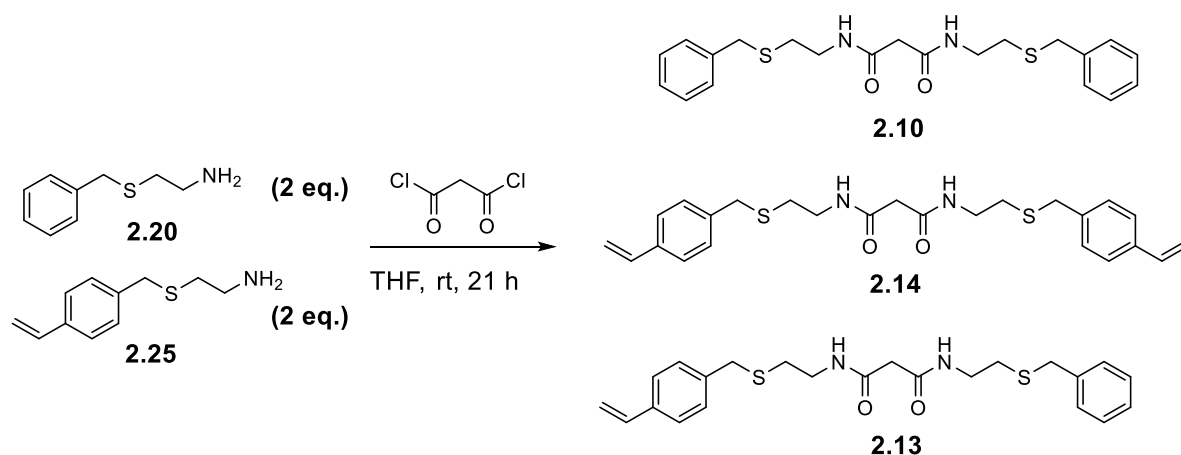
### 2.3.4.4 Synthesis of malonamide derivatives suitable for attaching to a magnetic nanoparticle

As stated in section 2.2, a styryl derived Ag<sup>+</sup> selective ligand is required to be attached (by a radical polymerization processes) to a magnetic nanoparticle. At this point the two symmetric malonamide derivatives **2.14** and **2.34** (Figure 2.9) which can be potentially tethered to a nanoparticle by a polymerization technique have been accessed. However, the potential for these ligands to cross-link nanoparticles would not be desirable. In order to minimize this complication, the preparation of the unsymmetrical ligand **2.13** containing only one polymerizable group was attempted.

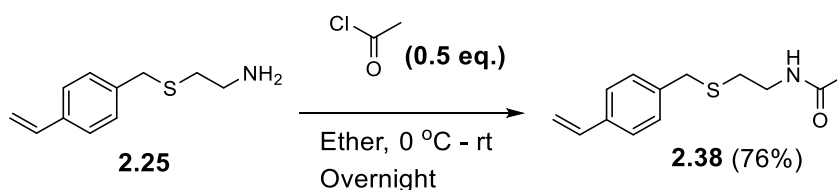


**Figure 2.9: Structures of malonamides derivatives with vinyl handles**

Hence 1 equivalent of malonyl chloride was added in a dropwise fashion to a stirred solution containing 2 equivalents each of amines **2.20** and **2.25** (Scheme 2.8). The crude product obtained contained a statistical mixture of the products **2.10**, **2.14** and **2.13** as expected. However, it wasn't possible to separate the three components either by standard flash column chromatography or by means of preparatory HPLC using an acetonitrile/water (70:30) eluent mixture.

Scheme 2.8. Attempted synthesis of **2.13**

Although the literature reports the symmetrical parent malonamide derivative **2.10** is a selective ligand for Ag<sup>+</sup>, there is less data on ligands containing only one amide group. The difficulty in isolation of pure **2.13** suggested the study of the simpler styryl ligand **2.38** (Scheme 2.9).

Scheme 2.9: Synthesis of amide **2.38**; a potential Ag<sup>+</sup> selective extraction ligand.

Therefore, acetyl chloride (0.5 eq.) was added in a dropwise manner to an ice cold and stirred solution of amine **2.25** (1 eq.) in dry ether. The reaction mixture was left to warm up to room temperature overnight after which it was extracted with ether and concentrated *in vacuo* to give a white solid in a 76 % yield. This novel, potential Ag<sup>+</sup> selective ligand was accessed in two steps and with good yield.

### 2.3.5 Summary of structures prepared.

In summary, in sections 2.3.4, twelve (12) potential ligands have been prepared and isolated (Figure 2.10) for selective Ag<sup>+</sup> extraction. In the next section and Chapter 3 preliminary studies will be undertaken on these ligands to assess their binding to metals.

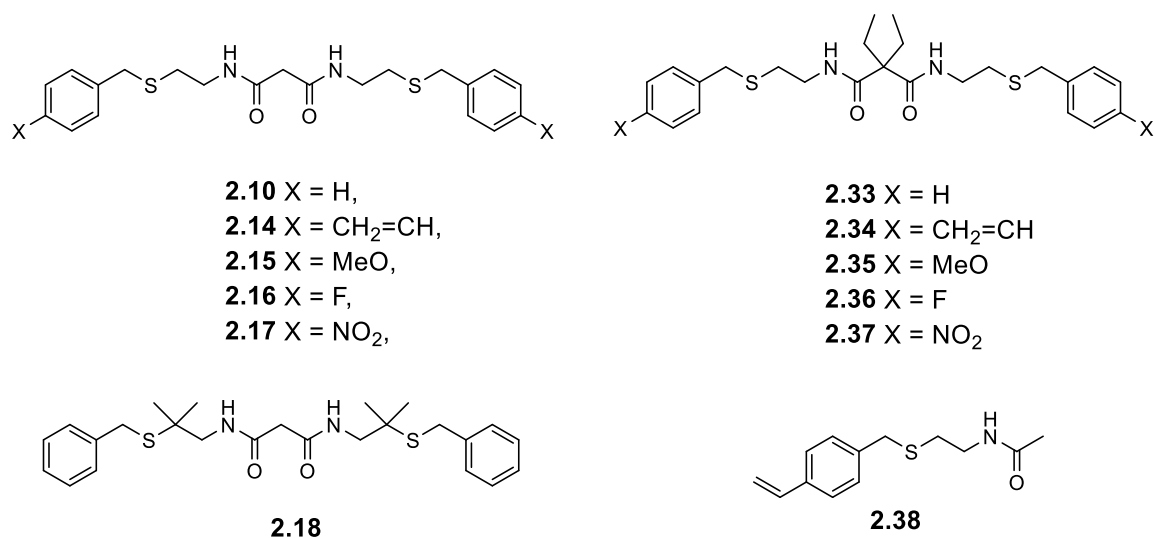


Figure 2.10: Summary of successfully prepared potential Ag<sup>+</sup> selective ligands.

### 2.3.6 Efficiency and selectivity of Ag<sup>+</sup> extraction from aqueous solutions

The initial aim was to measure the efficiency of the novel ligands in selective Ag<sup>+</sup> extraction from aqueous solutions. It is important to measure both the efficiency and selectivity of the ligands before committing time and resources to attempts at tethering the most appropriate to a nanoparticle. The previously published solvent extraction method was employed to investigate the efficiency of the ligands for Ag<sup>+</sup> extraction.<sup>203,205</sup> This approach was also used in the original publication for the synthesis of **2.10**<sup>203</sup> and thus was useful for comparative purposes. The ligand solutions were prepared by dissolving the appropriate amount of ligand in chloroform (see Section 7.2.8). Prior to its use in preparation of ligands solutions, the chloroform solvent was presaturated with twice its volume of acidified deionized water to remove any water-soluble components in order to minimize volume changes during the liquid/liquid metal extraction process. A 500 ppm stock solution of Ag<sup>+</sup>, Cu<sup>2+</sup> and Pb<sup>2+</sup> was prepared by dissolving appropriate amounts of AgNO<sub>3</sub>, Pb(NO<sub>3</sub>)<sub>2</sub>, and CuSO<sub>4</sub> in deionized water. The desired metal concentration (4 ppm each of Ag<sup>+</sup>, Cu<sup>2+</sup> and Pb<sup>2+</sup>) was ensured by dilution of the stock solution. The choice of Cu<sup>2+</sup> and Pb<sup>2+</sup> as competing ions is borne out of the knowledge that these metals usually coexist with Ag<sup>+</sup> in ores and mine tailings, for instance.<sup>209</sup> It was decided to prepare mixed metal aqueous solutions with very low

concentrations (4 ppm) of Ag<sup>+</sup>, Cu<sup>2+</sup> and Pb<sup>2+</sup> because Ag<sup>+</sup> typically exists in very low concentrations in Ag<sup>+</sup> repositories where the novel ligands may be applied.<sup>209</sup>

For sensible comparisons to be made, each solvent extraction experiment was undertaken in duplicate and with vigorous stirring using a stir bar with equal volumes of ligand and metal solutions for 15 mins. A control experiment was also undertaken with the metal solution using chloroform without any ligands present. This would determine any extraction efficiency of the solvent itself (the background extraction). After stirring, the organic and aqueous layers were left to separate. The aqueous layer (the raffinate) containing the metal was then collected into a beaker and the residual organic solvent in it was removed by slow evaporation on a steam bath for about 15 min. The aqueous sample was then diluted to the initial volume of the experiment (to ensure appropriate concentration comparisons because some water was lost during the evaporation process). The concentration of the metals in the raffinate was measured by means of ICP-OES. Each metal concentration value from the ICP-OES was the average of three analytic runs. Finally, the extraction efficiency was determined by the equation below;

$$\% EE = \frac{C_i - C_f}{C_i} \times 100 \quad \mathbf{2.1}$$

Where % EE is percentage extraction efficiency, C<sub>i</sub> and C<sub>f</sub> are the initial and final metal ion concentrations respectively.

The selectivity of the malonamide derivatives for Ag<sup>+</sup> relative to Cu<sup>2+</sup> and Pb<sup>2+</sup> was determined as follows<sup>220</sup>;

$$K_{Ag^+/M^{n+}} = \frac{D_{Ag^+}}{D_{M^{n+}}} \quad \mathbf{2.2}$$

Where  $K_{Ag^+/M^{n+}}$  represents selectivity coefficient of Ag<sup>+</sup> relative to M<sup>n+</sup> (M<sup>n+</sup> = Cu<sup>2+</sup> or Pb<sup>2+</sup>),

$D$  is the distribution coefficient of the metal ions between the aqueous and organic phases defined as;

$$D_{M^{n+}} = \frac{C_i - C_f}{C_f} \times \frac{V_{aq}}{V_{org}} \quad \mathbf{2.3}$$

$D_{Mn^+}$  represents the distribution factor for the metal ion  $M^{n+}$ ,  $C_i$  and  $C_f$  are the initial and final metal ion concentrations,  $V_{aq}$  and  $V_{org}$  are the volumes of the aqueous (metal) and organic (ligand) solutions respectively.

Since equal volumes of aqueous and organic solutions were used, the distribution factor formula is simplified into;

$$D_{M^{n+}} = \frac{C_i - C_f}{C_f} \quad 2.4$$

### 2.3.6.1 The Ag<sup>+</sup> extraction efficiency of malonamide derivative 2.10 verses amide 2.38

The requirement for the approach to Ag<sup>+</sup> extraction was to identify a ligand with a styryl group that could be attached to a nanoparticle. A secondary requirement was that the ligand should only have one styryl group. Thus, it became important to identify whether 2.38 was a suitable ligand early in this study. The efficiency of potential Ag<sup>+</sup> ligand 2.38 (Figure 2.11) was measured and compared to that for the known ligand 2.10. Daubinet and Kaye<sup>203</sup> had reported that 2.10 demonstrated excellent selectivity and efficiency (97 %) for Ag<sup>+</sup> in the presence of Cu<sup>2+</sup> and Pb<sup>2+</sup>. Structures of malonamide derivative 2.10 and amide 2.38 has been presented in (Figure 2.11) for easy reference.

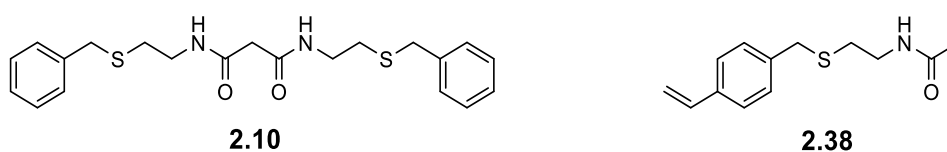
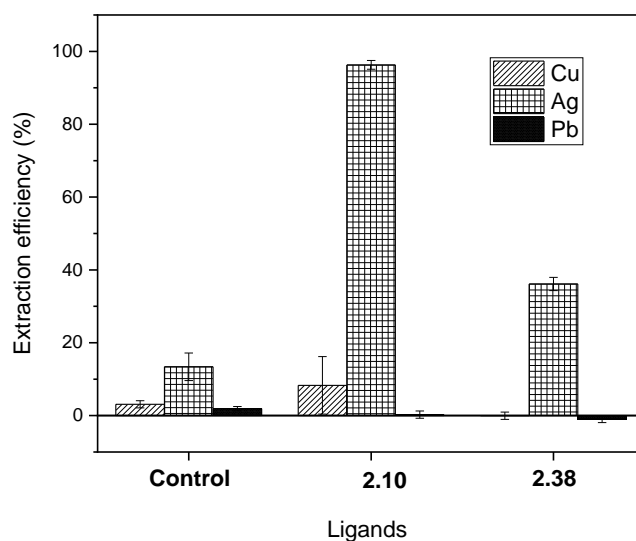


Figure 2.11: Structures of malonamide derivative 2.10 and amide 2.38



**Figure 2.12: ICP-OES data showing metal extraction efficiencies by neat chloroform (control), malonamide derivative 2.10 and amide 2.38**

It was observed that neat chloroform itself (the control) was able to extract some metals with a slight preference for Ag<sup>+</sup> (Figure 2.12). This is likely due to the differential partial solubility of these metals in chloroform. For the ligands, the extraction efficiencies observed were 96.3±1.2 % and 36.1±1.9 % by **2.10** and **2.38** respectively. The difference in extraction efficiencies may be attributed to the presence of extra *S*- and *N*- donors in **2.10** compared to **2.38**. If efficiencies are compared per ligand unit, then **2.10** is still slightly more efficient at extraction (**2.10**; 48.2 % vs **2.43**; 36.1 %). This may be due to **2.10** acting as a tetradentate ligand or with some other sort of cooperativity. However, the simplicity in preparation of **2.38** versus the difficulty in preparation of **2.10** suggested that **2.38** should be targeted as a ligand for attachment to magnetic nanoparticles. Interestingly, the selectivity of Ag<sup>+</sup> over Cu<sup>2+</sup> was significantly better for the amide ligand **2.38** (selectivity Ag<sup>+</sup>: Cu<sup>2+</sup>, **2.10** = 11.6, **2.38** = 36.0).

### 2.3.6.2 Electronic effects on efficiency and selectivity of Ag<sup>+</sup> extraction in malonamides.

The effect of electronic differences in ligands on the efficiency of Ag<sup>+</sup> recovery was studied by comparing extraction efficiencies and selectivity's exhibited by the malonamide

derivatives **2.10** and **2.14-2.17**. The observed extraction efficiencies are presented in Figure 2.13.

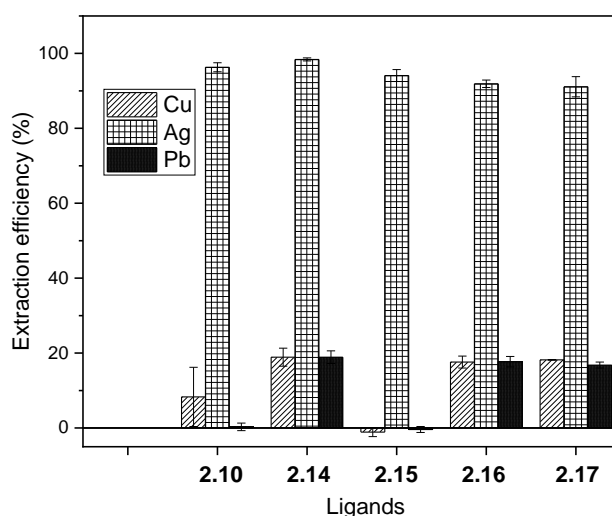
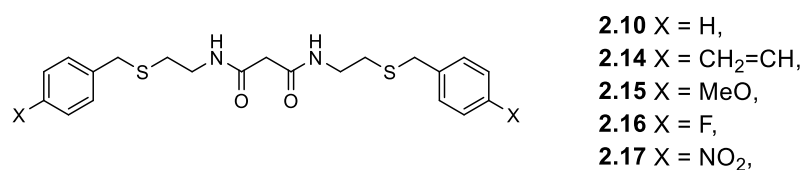


**Figure 2.13: ICP-OES data showing metal extraction efficiencies by malonamide derivatives 2.10, 2.14-2.17**

While the efficiencies for Ag<sup>+</sup> extraction by these ligands differ only slightly (**2.10** = 96.3±1.2 %, **2.14** = 98.4±0.4 %, **2.15** = 94.1±1.6 %, **2.16** = 91.1±1.0 %, **2.17** = 91.1±2.7 %), extraction efficiencies for those with electron withdrawing substituents **2.16-2.17** are the lowest (extraction efficiency order **2.17** = **2.16** < **2.15** < **2.10** < **2.14**) (see Table 2.7 below). The highest extraction efficiency observed for **2.14** could be because it would give the least polar Ag<sup>+</sup> complex and thus have the highest solubility in chloroform.<sup>207</sup> Correspondingly, the least extraction efficiencies were observed for **2.16** (X = F) and **2.17** (X = NO<sub>2</sub>) because (a) the Ag<sup>+</sup> complexes are the most polar and so least soluble in chloroform.<sup>207</sup> and (b) the electron withdrawing nature of the aryl groups will make the sulfur atom lone pairs less available for binding Ag<sup>+</sup> (the soft sulfur atom being crucial in efficiency and selectivity following the HSAB rule). For the methoxy derivative **2.15** a combination of the polar nature of its Ag<sup>+</sup>

complex lowering extraction efficiency with the more electron rich nature of the sulfur atom increasing binding leads to an intermediate extraction efficacy. The latter explanation (b), if true, would also explain the poorer selectivity's for the ligands with electron withdrawing groups (**2.14**, **2.16**, **2.17**), noting that in the styryl ligand **2.14** the inductive electron withdrawing nature of the vinyl group will be the dominant effect. A greater selectivity would be predicated and is in fact observed for the strongly electron donating methoxy substituent in **2.15**, where selectivity of Ag<sup>+</sup> verses Cu<sup>2+</sup> is approximately nine times better than **2.10**. The results observed here suggest that electronics have only a small influence on the efficiency of Ag<sup>+</sup> extraction by these ligands but a significant effect on selectivity.

**Table 2.7: Efficiency and selectivity of 2.10 and 2.14-2.17 for Ag<sup>+</sup> relative to Cu<sup>2+</sup> and Pb<sup>2+</sup>**

Ligand	Efficiency (%)	K <sub>Ag<sup>+</sup>}/Cu<sup>2+</sup></sub>	K <sub>Ag<sup>+</sup>}/Pb<sup>2+</sup></sub>
<b>2.10</b>	96.3±1.2	11.6	321
<b>2.14</b>	98.4±0.4	5.2	5.2
<b>2.15</b>	94.1±1.6	85.5	235.3
<b>2.16</b>	91.1±1.0	5.2	5.2
<b>2.17</b>	91.1±2.7	5.0	5.4

### 2.3.6.3 Effect of steric hindrance adjacent to the S- donor and at the acyl methylene

Finally, the effect of steric hindrance at various sites in the ligand (**2.10**) was investigated. Steric hindrance around the crucial sulphur atom required for binding in ligand **2.18** might be predicted to lead to lower efficiencies in extraction while placing steric hindrance further away at the malonamide central carbon **2.33** might be predicted to have less effect (Figure 2.14). Structures of malonamide derivatives **2.10**, **2.18** and **2.33** have been presented below for easy reference.

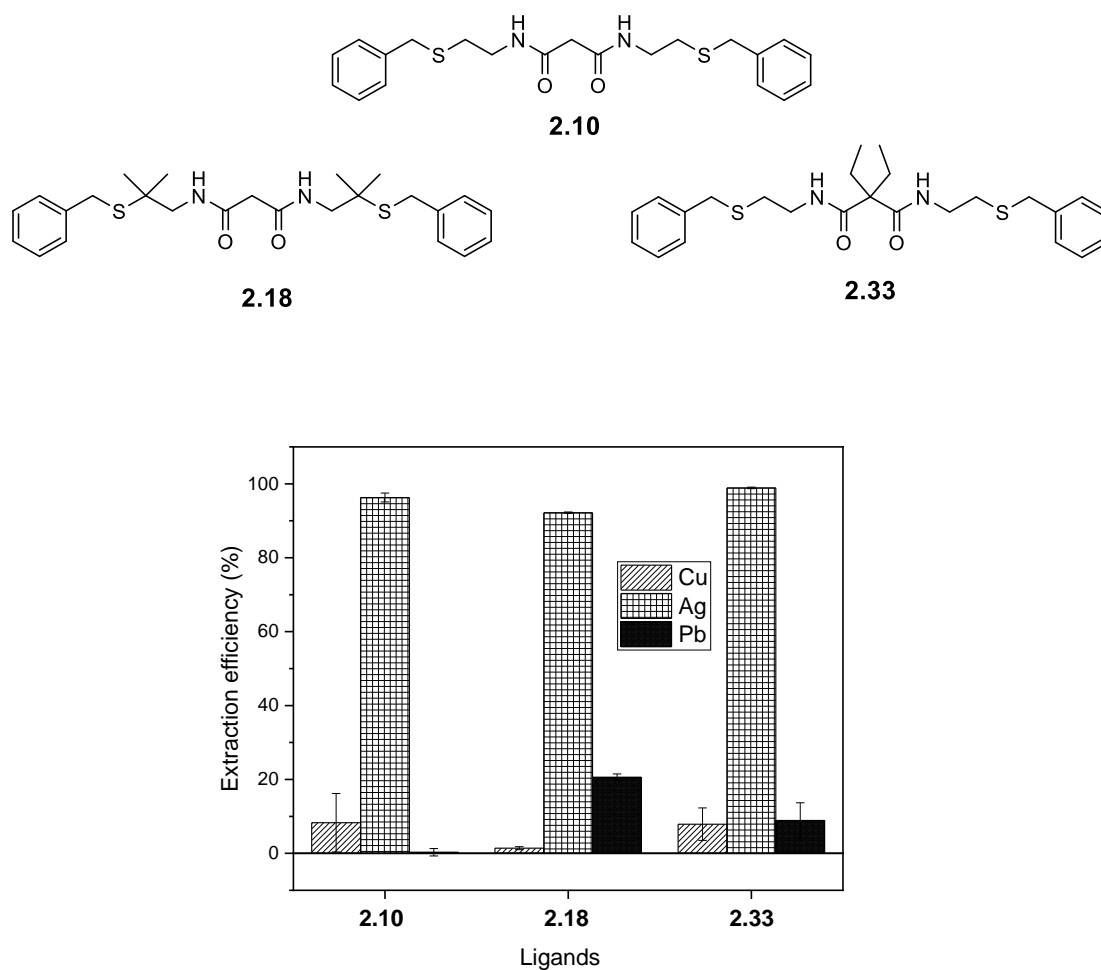


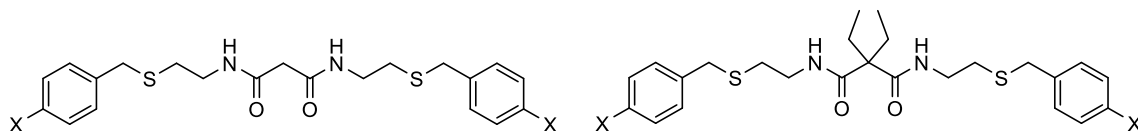
**Figure 2.14: ICP-OES data showing metal extraction efficiencies by malonamide derivatives **2.10**, **2.18** and **2.33****

Malonamide **2.18**, sterically hindered near the sulfur atom, extracted with less efficiency (~4 %) for Ag<sup>+</sup> (92.2±0.2 %) than the analogue without such steric hindrance **2.10** (96.3±1.2 %) (Figure 2.14) as predicted. This is attributed to the slightly greater difficulty of **2.18** in assuming the right conformation needed to bind Ag<sup>+</sup> because of the presence of the dimethyl substitution.<sup>221</sup> On the other hand, malonamide derivative **2.33**, sterically hindered at the acyl region extracted slightly higher amounts of Ag<sup>+</sup> compared to **2.10** (**2.10** = 96.3±1.2 % versus **2.33** = 98.9±0.2 %) attributed to the higher solubility of the Ag<sup>+</sup> complex of the former in chloroform than that of the latter. Interestingly both **2.18** and **2.33** were less selective than **2.10** for binding with Pb<sup>2+</sup> (**2.18**;  $K_{Ag^+/Pb^{2+}} = 4.5$ , **2.33**;  $K_{Ag^+/Pb^{2+}} = 11.1$ , **2.10**;  $K_{Ag^+/Pb^{2+}} = 321$ )

and this could be attributed to the higher solubility of the Pb<sup>2+</sup> complexes of **2.18** and **2.33** in chloroform due to the gem dialkyl groupings.<sup>207</sup>

## 2.4 Summary of results.

- A range of novel symmetrical and unsymmetrical Ag<sup>+</sup> ligands were prepared.



**2.10** X = H,

**2.14** X = CH<sub>2</sub>=CH,

**2.15** X = MeO,

**2.16** X = F,

**2.17** X = NO<sub>2</sub>,

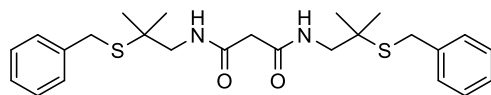
**2.33** X = H

**2.34** X = CH<sub>2</sub>=CH

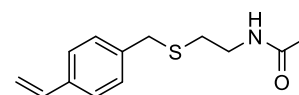
**2.35** X = MeO

**2.36** X = F

**2.37** X = NO<sub>2</sub>



**2.18**



**2.38**

- Electronic effects at the 4-position of the aromatic groups in malonamide ligands **2.14-2.17** had little effect on Ag<sup>+</sup> extraction efficiency but a greater effect on metal selectivity, with the electron rich ligand **2.15** being the most selective for Ag<sup>+</sup>.
- Increased steric hindrance near the sulphur atom has a small negative effect on Ag<sup>+</sup> extraction efficiency, while hindrance at the central carbon atom lowers selectivity
- The novel styryl ligand **2.38** was easy to prepare (yield 76%, over two steps) and showed acceptable selectivity's for extraction of Ag<sup>+</sup> over Cu<sup>2+</sup> and Pb<sup>2+</sup> even though metal extraction efficiency was low (36 %).
- Going forward, ligands **2.10** and **2.38** were chosen for more detailed binding studies (Chapter 3) and **2.38** was chosen to be attached to a magnetic nanoparticle (Chapter 4).

**Chapter 3: Ag<sup>+</sup>-ligand/Ag<sup>+</sup> binding studies:  
investigation of complex stoichiometry**

### 3.1 Introduction

Silver(I) complexes have been reported to be potent antimicrobial<sup>222,223</sup> and anti-cancer agents<sup>224</sup>. Therefore, synthesis and binding stoichiometries of Ag<sup>+</sup> complexes have been extensively studied. Binding stoichiometries of Ag<sup>+</sup> complexes have been investigated by several methods including x-ray diffraction, mass spectrometry, Job's and mole ratio plots (from NMR, UV/Visible or potentiometric titrations).

X-ray diffraction analysis is a popular method for investigating binding stoichiometries. For example, in 1993, Rosser and co-workers<sup>225</sup> observed after x-ray diffraction analysis that the Ag<sup>+</sup>-thiourea **3.1** complex (**3.2**) (see Figure 3.1 below) has a 3:1 (Ag<sup>+</sup>:**3.1**) stoichiometry. In a separate study, another group of researchers investigating the anticancer activity of an heteroleptic complex **3.3** (Figure 3.1) observed after x-ray diffraction analysis that the complex **3.3** has a binding stoichiometry of 1:1:2 (Ag<sup>+</sup>:benzimidazolurea:triphenylphosphine) with a tetrahedral geometry. Interestingly, they also discovered that the complex **3.3** was four times more potent than the popular anticancer drug – cisplatin, against some cancerous cells.<sup>226</sup> Finally, the Meijboom group<sup>227</sup> determined the stoichiometry of the anti-cancer agent complex **3.4** (Figure 3.1), by means of x-ray diffraction. The complex **3.4** was observed to crystallize as a dimeric unit and had a 1:1:2 (Ag<sup>+</sup>:thiocyanato:triphenylphosphine) stoichiometry.

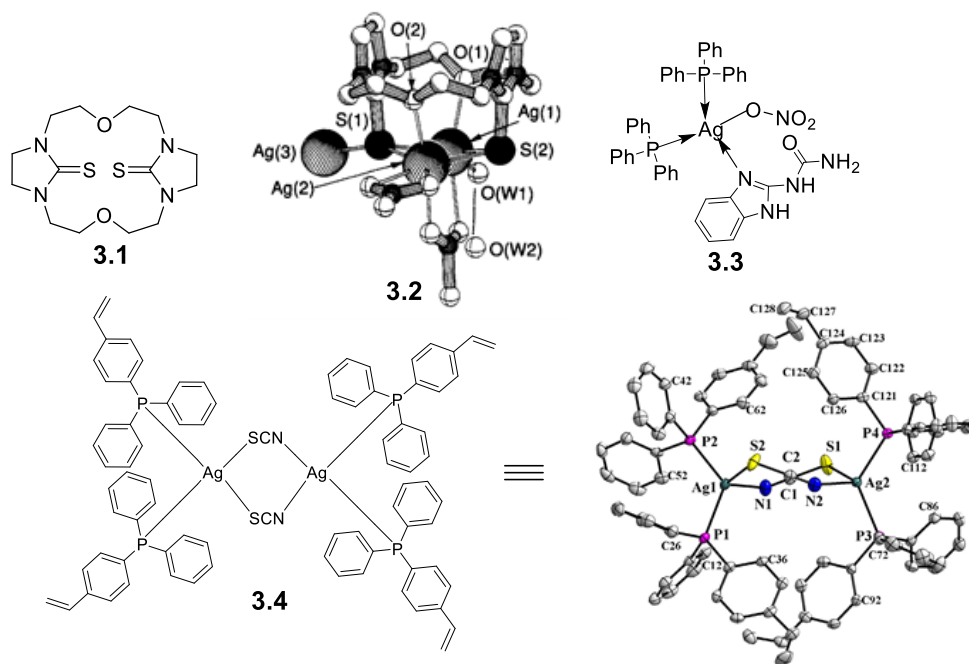


**Figure 3.1:** Some Ag<sup>+</sup> complexes investigated by means x-ray diffraction towards the determination of their stoichiometry

Fast atom bombardment mass spectrometry (FAB-MS) has been employed to determine the stoichiometry of Ag<sup>+</sup> complexes. By means of FAB-MS, Rosser and co-workers<sup>225</sup> discovered that the novel Ag<sup>+</sup>-macrocyclic thiourea **3.5** (see Figure 3.2 below) adopts a 1:1 (Ag<sup>+</sup>:thiourea **3.5**) stoichiometry. Based on the observed stoichiometry, they hypothesized that **3.5** binds Ag<sup>+</sup> in a linear fashion through the soft *S*-donors. Also, by means of FAB-MS, José and coinvestigators<sup>228</sup> as part of their work on heterocyclic thiones observed that Ag<sup>+</sup> binds to 1-EtImSH **3.6** (Figure 3.2) in a 4:5 (Ag<sup>+</sup>-**3.6**) fashion. Stoichiometry of Ag<sup>+</sup> complexes have been investigated not only by FAB-MS, but also by electrospray ionization mass spectrometry (ESI-MS). Perhaps the attraction to ESI-MS is that it is a softer ionization technique than FAB-MS.<sup>229</sup> Intrigued by the excellent Ag<sup>+</sup> selectivity and efficiency properties of crownophane **3.7** (Figure 3.2), Inokuma and coworkers<sup>230</sup> investigated the Ag<sup>+</sup>-**3.7** binding stoichiometry by means of ESI-mass spectrometry. They observed that Ag<sup>+</sup> forms a 1:1 complex with the crownophane **3.7** and claimed that all five *O*- and two *N*-donors partake in complexing Ag<sup>+</sup>. Finally, stoichiometry of heteroleptic complexes formed by diazaperylenes **3.8** – **3.11** (Figure 3.2) with Ag<sup>+</sup> were determined by ESI-MS and were all found to be 1:1.

Based on data from density functional theory calculations, it was reported that the *N*- donors in the diazaperylenes **3.8** – **3.11** bind to Ag<sup>+</sup> to form a distorted tetrahedral complex (**3.12**) (Figure 3.2).<sup>231</sup>

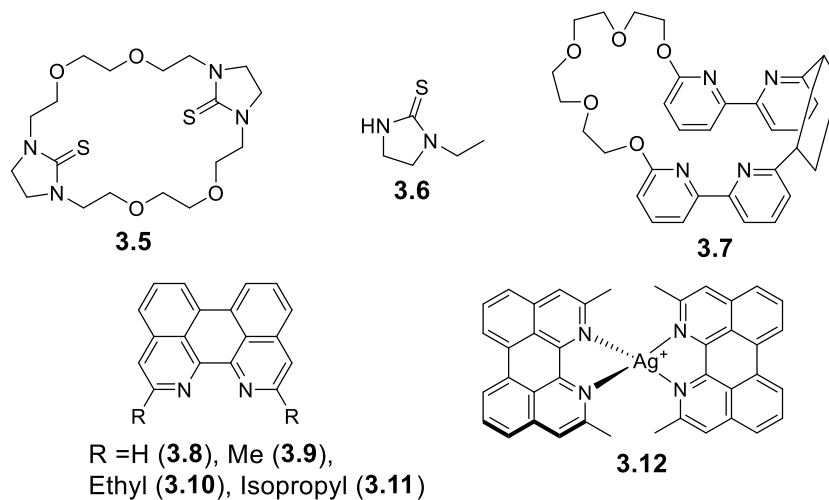


**Figure 3.2: Some Ag<sup>+</sup> ligands and complexes studied by means mass spectrometry towards the determination of their stoichiometry**

Finally, the Job's plot (also known as the method of continuous variation) and the mole ratio plot have been employed to determine binding stoichiometries of Ag<sup>+</sup> complexes of pyrimidine **3.13**<sup>232</sup>, podand **3.14**<sup>232</sup> and dicarbonyls **3.15** – **3.17**<sup>233</sup> (Figure 3.3).

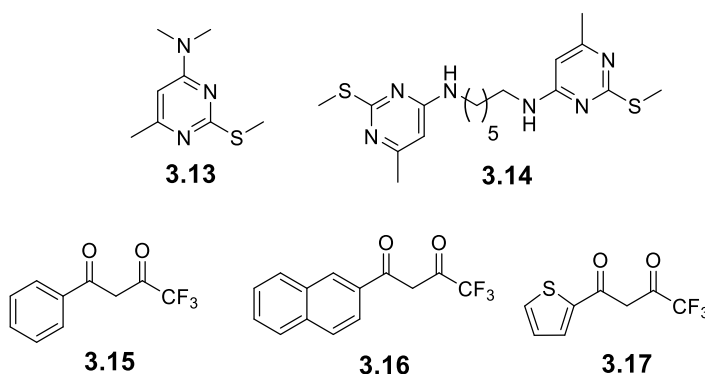
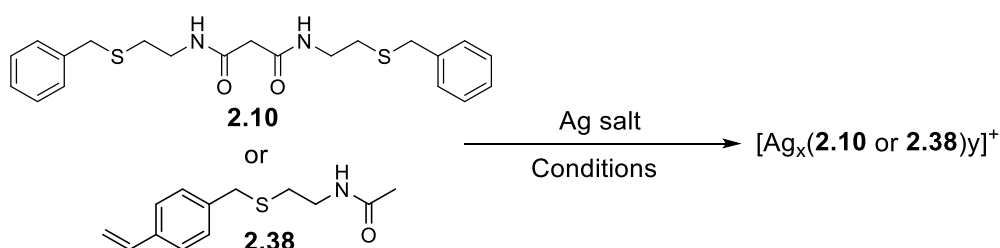


**Figure 3.3: Stoichiometry of the Ag<sup>+</sup> complexes formed by these ligands were investigated by Job's and mole ratio plots.**

## 3.2 Aim and objectives

The main aim discussed in this chapter is the investigation of the binding stoichiometries of the Ag<sup>+</sup> complexes of the malonamide derivative **2.10** and the amide **2.38**. To achieve this

aim, a series of Ag<sup>+</sup> complexes of **2.10** and **2.38** will be synthesized using different Ag salts (see Scheme 3.1 below). Subject to successfully growing x-ray diffraction-worthy crystals, structural elucidation and stoichiometry determination by means of x-ray diffraction will be undertaken. In addition, the stoichiometries of these Ag<sup>+</sup> complexes in solution will be determined by means of mass spectrometry, Job's and mole ratio plots (from <sup>1</sup>H NMR titrations).

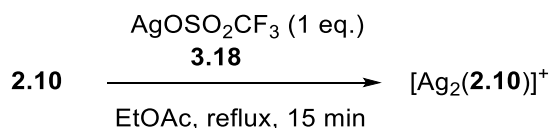
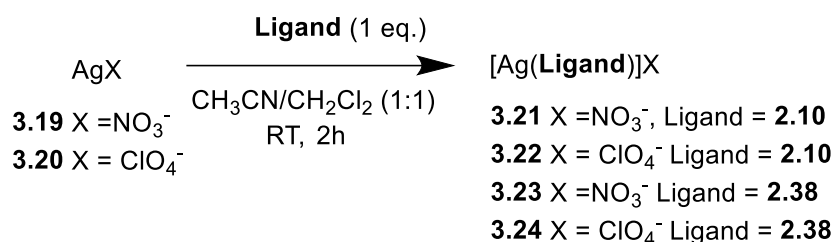


**Scheme 3.1: Generic scheme for the syntheses of Ag<sup>+</sup> complexes of malonamide derivative **2.10** and amide **2.38****

### 3.3 Results and discussion

#### 3.3.1 Synthesis of Ag<sup>+</sup> complexes of **2.10** and **2.38** and attempted crystal growth

Daubinet<sup>234</sup> synthesized the Ag<sup>+</sup>-**2.10** complex using Ag triflate **3.18** (Scheme 3.2) and tried to determine its binding stoichiometry by means of x-ray diffraction. Unfortunately, his attempts at growing x-ray diffraction-worthy crystals of the Ag<sup>+</sup>-**2.10** complex failed as the Ag<sup>+</sup>-**2.10** was obtained as a yellow paste. Suspecting that the triflate counterion might be responsible for the failure of the Ag<sup>+</sup>-**2.10** complex to aggregate into appropriate crystals, initial work focused on synthesis of the Ag<sup>+</sup>-**2.10** complex using other Ag salts (in this study; AgNO<sub>3</sub> and AgClO<sub>4</sub>) followed by attempted crystal growth. The choice of AgNO<sub>3</sub>, for example, was inspired by the work of Soliman and co-workers<sup>235</sup> where x-ray diffraction-worthy crystals were grown from a Ag<sup>+</sup>-malonamide complex prepared using AgNO<sub>3</sub> as source of Ag<sup>+</sup>.

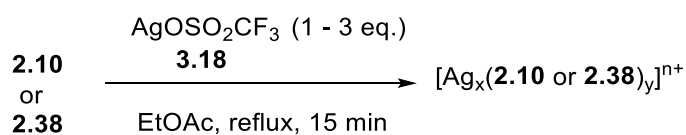
Scheme 3.2: Synthesis of Ag<sup>+</sup>-2.10 complex<sup>234</sup>Scheme 3.3: Syntheses of Ag<sup>+</sup> complexes of 2.10 and 2.38 using AgNO<sub>3</sub> and AgClO<sub>4</sub>

The Ag<sup>+</sup> complexes of ligands **2.10** and **2.38** were synthesized by stirring equal amounts of **2.10** or **2.38** with AgNO<sub>3</sub> **3.19** or AgClO<sub>4</sub> **3.20** for 2 h at room temperature in the dark (Scheme 3.3 and Table 3.1). Unfortunately, attempted crystal growth of all the complexes by the methods of either vapour diffusion or slow evaporation failed. Both complexes from malonamide derivative **2.10** were obtained as golden yellow pastes (**3.21** and **3.22**) while those derived from **2.38** were obtained as a cream-coloured solid (**3.23**) or a colourless paste (**3.24**).

Table 3.1: Ag<sup>+</sup> complexes 3.21 – 3.24

Entry	AgX	Ligand	Product	Yield
1	NO <sub>3</sub> <sup>-</sup> , <b>3.19</b>	<b>2.10</b>	<b>3.21</b>	70 %
2	ClO <sub>4</sub> <sup>-</sup> , <b>3.20</b>	<b>2.10</b>	<b>3.22</b>	66 %
3	NO <sub>3</sub> <sup>-</sup> , <b>3.19</b>	<b>2.38</b>	<b>3.23</b>	77 %
4	ClO <sub>4</sub> <sup>-</sup> , <b>3.20</b>	<b>2.38</b>	<b>3.24</b>	98 %

### 3.3.2 Mass spectrometry studies of Ag<sup>+</sup>-2.10 and Ag<sup>+</sup>-2.38 complexes

Scheme 3.4: Syntheses of Ag<sup>+</sup> complexes of 2.10 and 2.38 using AgOSO<sub>2</sub>CF<sub>3</sub>

Following the method employed by Daubinet<sup>234</sup> (Scheme 3.1), equal amount of malonamide derivative **2.10** and Ag triflate **3.18** were refluxed in EtOAc in the dark (Scheme 3.4). After 15 mins, the crude product was concentrated *in vacuo* to give **3.25** as a brown paste in a 91 % yield (see Table 3.2, Entry 1 below). In the wide scan ( $m/z$  0 – 2400) low resolution mass spectrum (LRMS) of **3.25**, the only pair of peaks with ratio of ~1:1 (indicative of a Ag<sup>+</sup> complex) were observed at  $m/z$  509/511 (see Figure 3.4a on page 68). Indeed, the  $m/z$  509 was confirmed by high resolution mass spectrometry (HRMS) as the complex - [<sup>107</sup>Ag(**2.10**)]<sup>+</sup> (see experimental). Interestingly, reacting malonamide ligand **2.10** with 2 and 3 equivalents of Ag<sup>+</sup> to give complexes **3.26** and **3.27** respectively (Table 3.2, Entries 2 and 3) were also found to give complexes with a 1:1 (Ag<sup>+</sup>:**2.10**) stoichiometry. On the other hand, repeating the protocol with ligand **2.38** with one, two and three equivalents of AgOSO<sub>2</sub>CF<sub>3</sub> **3.17** gave excellent yields of the Ag<sup>+</sup> complexes, **3.28** – **3.30**. (Table 3.2, Entries 4 – 6). This time, LRMS-ESI data (see Figure 3.5 on page 69) of the complexes **3.28** – **3.30** indicated that both the 1:1 and 1:2 (Ag<sup>+</sup>:**2.38**) complexes are formed. HRMS-ESI analysis of all the complexes confirmed the identification of the complexes (see experimental). These results indicate that the stoichiometry of the Ag<sup>+</sup> complex with ligand **2.10** is 1:1, while those for **2.38** are both 1:1 and 1:2 (Ag<sup>+</sup>-**2.38**).

**Table 3.2: Effect of Ag<sup>+</sup> equivalent on stoichiometry of Ag<sup>+</sup> complexes of 2.10 and 2.38**

Entry	Ligand	AgOSO <sub>2</sub> CF <sub>3</sub> eq.	Product	x:y	Yield
1	<b>2.10</b>	1	<b>3.25</b>	1:1	91 %
2	<b>2.10</b>	2	<b>3.26</b>	1:1	65 %
3	<b>2.10</b>	3	<b>3.27</b>	1:1	85 %
4	<b>2.38</b>	1	<b>3.28</b>	1:1 and 1:2	94%
5	<b>2.38</b>	2	<b>3.29</b>	1:1 and 1:2	75%
6	<b>2.38</b>	3	<b>3.30</b>	1:1 and 1:2	85%

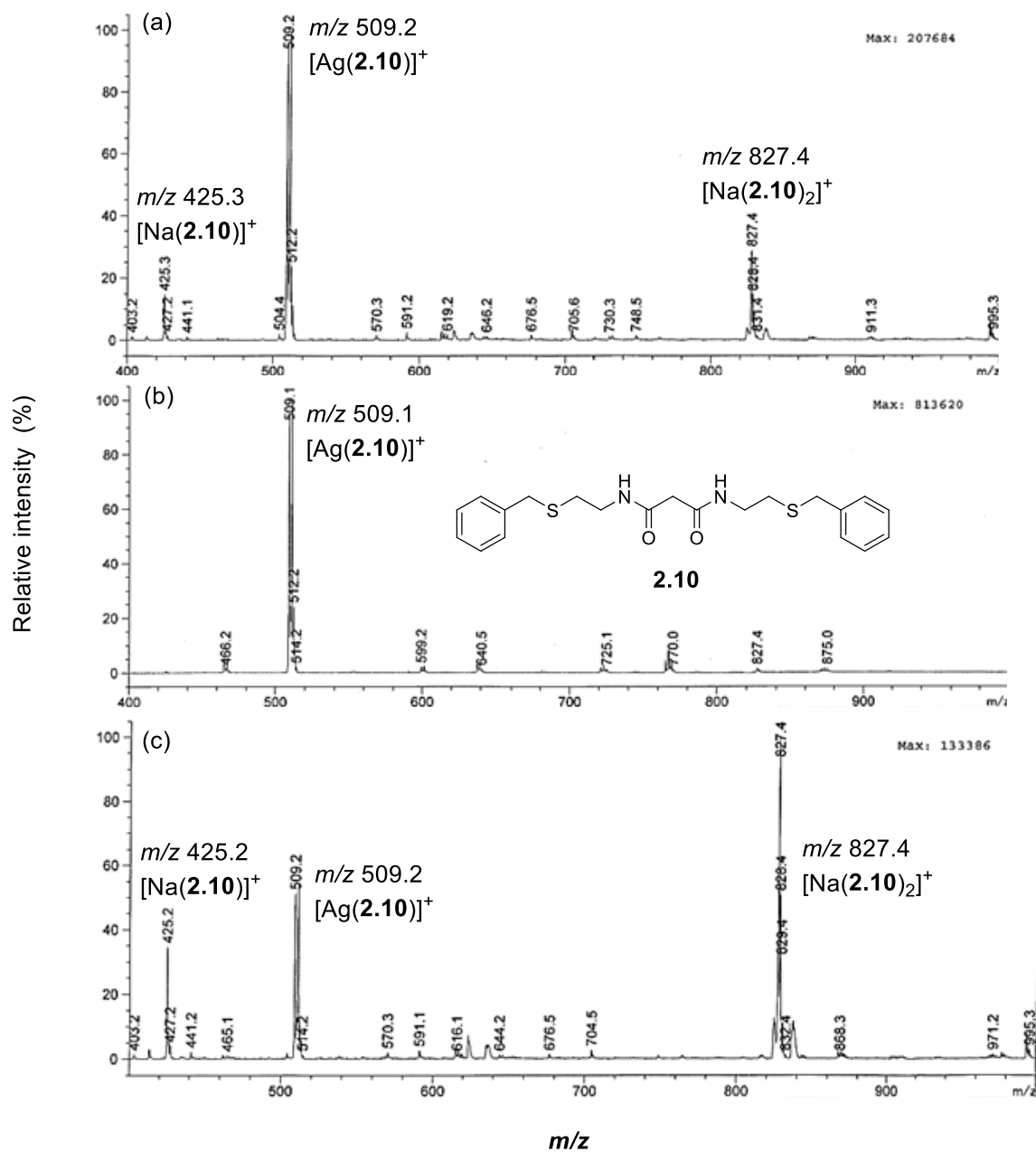
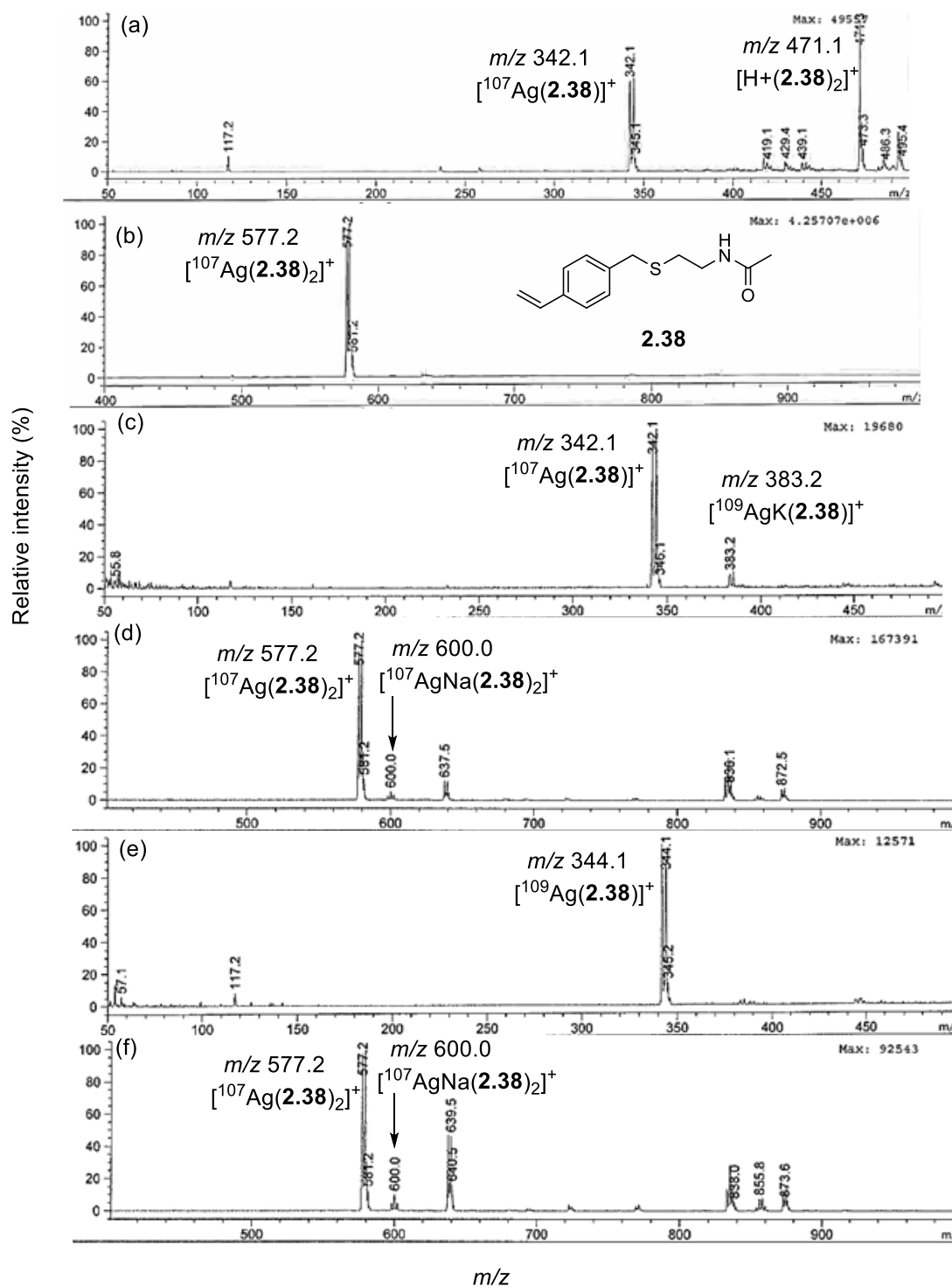


Figure 3.4: Partial low-resolution ESI mass spectra of Ag<sup>+</sup>-2.10 complexes from treatment of 2.10 with (a) one (b) two and (c) three equivalents of AgOSO<sub>2</sub>CF<sub>3</sub>



**Figure 3.5: Partial low-resolution ESI mass spectra of Ag<sup>+</sup>·2.38 complexes from treatment of 2.38 with (a) one equivalent (0-500  $m/z$ ), (b) one equivalent (500-1000  $m/z$ ), (c) two equivalents (0-500  $m/z$ ), (d) two equivalents (500-1000  $m/z$ ), (e) three equivalents (0-500  $m/z$ ), (f) three equivalents (500-1000  $m/z$ ) of AgOSO<sub>2</sub>CF<sub>3</sub>**

### 3.3.3 Job's and mole ratio plots for Ag<sup>+</sup>-**2.10** and Ag<sup>+</sup>-**2.38** complexes

Attention was turned to undertaking <sup>1</sup>H NMR titrations and construction of Job's and mole ratio plots from these titrations to confirm stoichiometries of Ag<sup>+</sup> complexes of **2.10** and **2.38** determined from the LRMS-ESI studies. The Job's plot for the Ag<sup>+</sup>-**2.10** complex was constructed from <sup>1</sup>H NMR titration of a 0.005 M **2.10** solution against an equal concentration (0.005 M) of AgClO<sub>4</sub>. Similarly, the Job's plot for the Ag<sup>+</sup>-**2.38** complex was constructed from <sup>1</sup>H NMR titration using the same ligand and Ag<sup>+</sup> concentrations (0.005 M) as above. The <sup>1</sup>H NMR titration of the Ag<sup>+</sup> against the malonamide derivative **2.10** was undertaken in DMSO-d<sub>6</sub> after initial solvent screening experiments revealed the unsuitability of other common NMR solvents tested (due to poor solubility of ligand **2.10** in these solvents). On the other hand, the <sup>1</sup>H NMR titration of the Ag<sup>+</sup> against amide **2.38** was undertaken in CD<sub>3</sub>OD.

In a typical <sup>1</sup>H NMR titration experiment, ten samples representing ten different Ag<sup>+</sup> mole fractions ( $\chi_{\text{Ag}^+} = 0.0 - 1.0$ ) were prepared inside ten separate NMR tubes by mixing appropriate volumes of the 0.005 M solution of **2.10** or **2.38** with the 0.005 M solution of AgClO<sub>4</sub> **3.19**. For example, a sample representing  $\chi_{\text{Ag}^+} = 0.0$  is a 0.5 mL, 0.005 M solution of ligand (**2.10** or **2.38**) on its own. Furthermore, a sample representing  $\chi_{\text{Ag}^+} = 0.1$  is a mixture prepared by mixing 0.05 mL of 0.005 M AgClO<sub>4</sub> **3.19** solution and 0.45 mL of 0.005 M ligand solution. Proton NMR spectra of all ten samples were obtained at room temperature. The <sup>1</sup>H NMR titrations of Ag<sup>+</sup> separately against **2.10** and **2.38** did not lead to the appearance of new peaks (see Figures 3.6a and b below) but caused distinct changes in chemical shifts, indicating a fast rate of exchange between the complexed (Ag<sup>+</sup>-**2.10** or **2.38**) and uncomplexed (free **2.10** or **2.38**) states. The Job's plots for the Ag<sup>+</sup>-**2.10** (Figure 3.6c) and Ag<sup>+</sup>-**2.38** (Figure 3.6d) interactions were constructed after appropriate calculations (detailed in Section 7.3.3) had been undertaken.

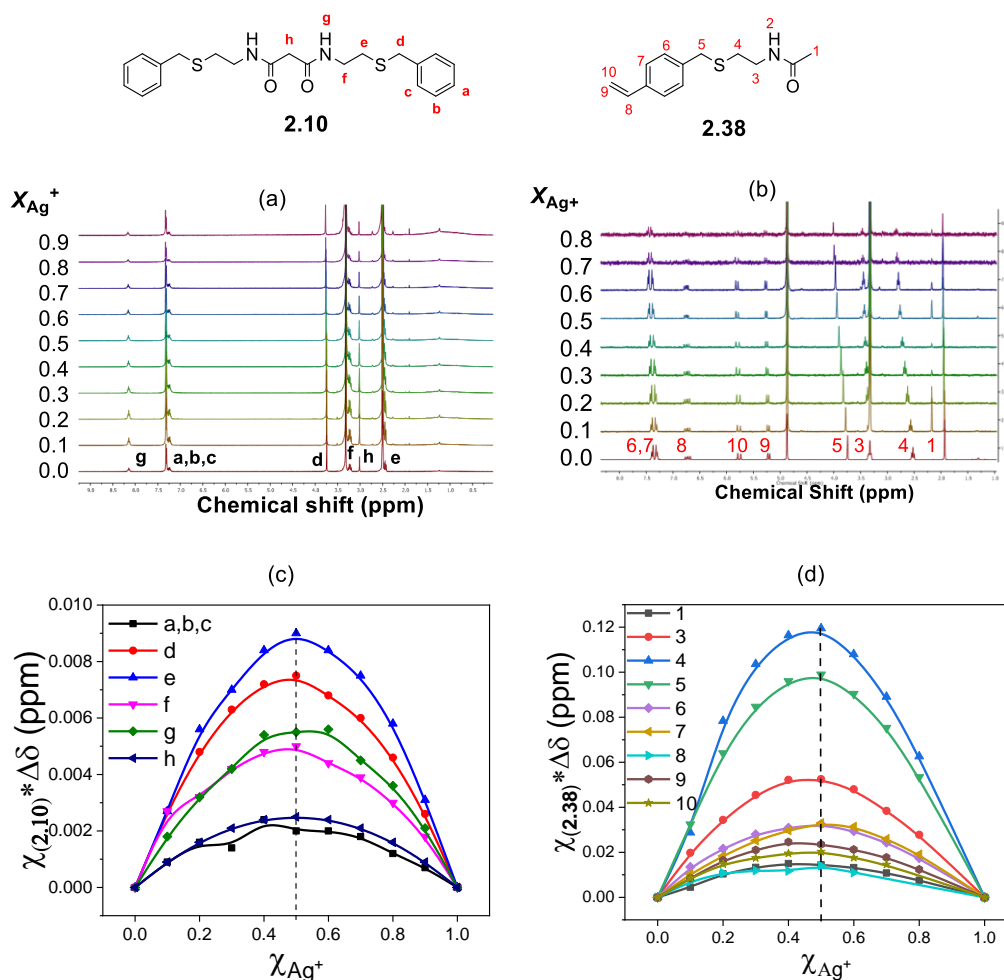


**Figure 3.6:** (a and b) <sup>1</sup>H NMR (300 MHz) spectra of the interaction of Ag<sup>+</sup> with (a) **2.10** and (b) **2.38** respectively; (c and d) Job's plots of the interaction of 0.005 M Ag<sup>+</sup> with (c) 0.005 M malonamide derivative **2.10** and (d) 0.005 M amide **2.38** at room temperature

The gentle curvature of the curves in both Job's plots (Figures 3.6c and d) indicates the binding between the ligands and Ag<sup>+</sup> is weak<sup>236</sup> and may explain the unsuccessful attempts at obtaining x-ray suitable crystals of these complexes. Furthermore, it can be observed that the coefficient on the x-axis of the maxima of all curves in both Job's plots (Figures 3.6c and d) is at χ<sub>Ag<sup>+</sup></sub> = 0.5, indicating that the ligands **2.10** and **2.38** may bind Ag<sup>+</sup> in any of the 1:1, 2:2 or any other *n:n* fashion. To confirm the actual stoichiometry, mole ratio plots of the interactions of the **2.10** and the **2.38**, separately with Ag<sup>+</sup> were constructed.

The mole ratio plots of Ag<sup>+</sup>-**2.10** and Ag<sup>+</sup>-**2.38** were constructed from <sup>1</sup>H NMR titrations different from that employed for the Job's plots. Here, a constant amount of a 0.539 M or

0.419 M Ag<sup>+</sup> solution is successively added to the ligands **2.10** or **2.38** solutions respectively to prepare Ag<sup>+</sup>/ligand mole ratios ( $n_{\text{Ag}^+}/n_{\text{ligand}}$ ) ranging from 0.5 to 4.0. Proton NMR spectra after successive addition of the Ag<sup>+</sup> solution was recorded (see Figures 3.7a and b below), and the mole ratio plots are constructed from the change in chemical shift values obtained from these spectra (Figures 3.7c and d).

In a typical mole ratio plot, the stoichiometry of a complex is the coefficient on the x-axis where the curve changes shape for example from concave to convex or vice versa. The point of inflection is the point on a curve where the direction of the curve changes. In the case of the Ag<sup>+</sup>-**2.10** complex (Figure 3.7c), it was very difficult to get a distinct point of inflection for any of the curves. This indicates a weak binding between the Ag<sup>+</sup> and **2.10**.<sup>236</sup> It also suggests that the Ag<sup>+</sup>-**2.10** complex can adopt more than one type of stoichiometry in solution including the 1:1 observed from mass spectrometry and the Job's plot.<sup>236</sup> Fortunately, for the Ag<sup>+</sup>-**2.38** mole ratio plot (Figure 3.7d), a tentative point of inflection could be identified (for example using the curve representing proton '4') and it corresponds to a  $n_{\text{Ag}^+}/n_{\text{2.38}} = 1.0$ , indicating that the **2.38** binds to Ag<sup>+</sup> in a 1:1 fashion and confirms mass spectrometry and Job's plot results. The observation of a distinct point of inflection only at  $n_{\text{Ag}^+}/n_{\text{2.38}} = 1.0$  and not also at  $n_{\text{Ag}^+}/n_{\text{2.38}} = 2.0$ , may be due to that fact that the 1:1 (Ag<sup>+</sup>:**2.38**) complex is more stable in solution than the 1:2 (Ag<sup>+</sup>:**2.38**) complex. This claim is backed by the observation of a continuous increase in the  $\Delta\delta$  (Figure 3.7d) indicating that other types of stoichiometries (perhaps including the observed 1:2 – Ag<sup>+</sup>:**2.38** from the LRMS-ESI spectra) may exist for the Ag<sup>+</sup>-**2.38** complex.

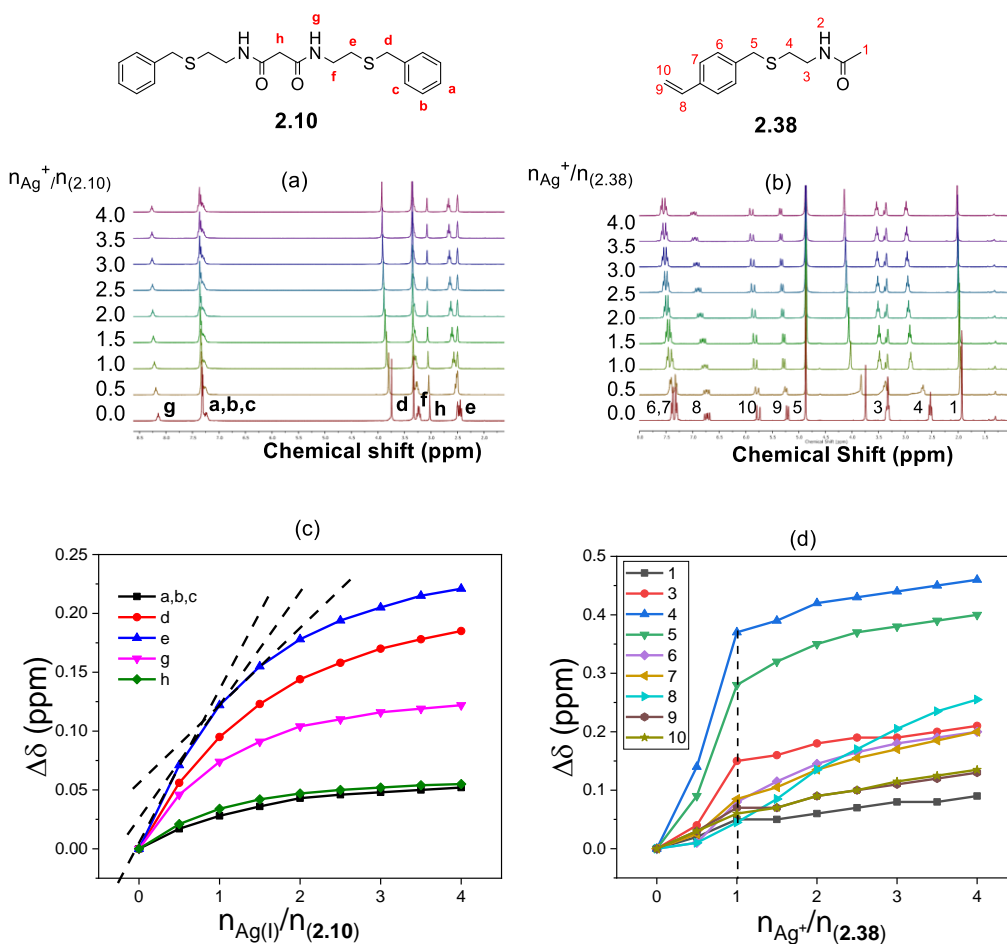


**Figure 3.7:** (a and b) <sup>1</sup>H NMR (300 MHz) spectra of the interaction of Ag<sup>+</sup> with (a) malonamide derivative 2.10 and (b) amide 2.38 and (b and d) mole ratio plots of the interaction of Ag<sup>+</sup> with (a) malonamide derivative 2.10 and (b) amide 2.38

The highest  $\Delta\delta$  values were observed for protons 'e' and 'd' in 2.10, and '4' and '5' in 2.38 (the protons on carbons alpha to the S- donor atoms). The next highest  $\Delta\delta$  values were observed for protons 'g' in 2.10, and '3' in 2.38 (the protons on the carbons alpha to the amide N- donor, Figures 3.7c and d). The observed high  $\Delta\delta$ 's may be due to deshielding effects experienced by these protons as the S- and N- donors participate in binding Ag<sup>+</sup>. Unsurprisingly, lower  $\Delta\delta$  values were observed for phenyl protons ('a', 'b' and 'c' in 2.10, '6' and '7' in 2.38) since they are not in the neighbourhood of the S- and N- donors. The continuous increase in  $\Delta\delta$  for vinyl proton '8' (Figure 3.7d) may be attributed to the participation of the  $\pi$  electrons in binding Ag<sup>+</sup> after the S- and N- donor sites are saturated.

Based on these observations, it was hypothesized that malonamide derivative **2.10** binds Ag<sup>+</sup> using its two *S*- and *N*- donor centres to form a tetrahedral complex (Figure 3.8a). Amide **2.38** may bind Ag<sup>+</sup> also using its *S*- and *N*- donors to form linear and tetrahedral complexes (Figures 3.8b and c).

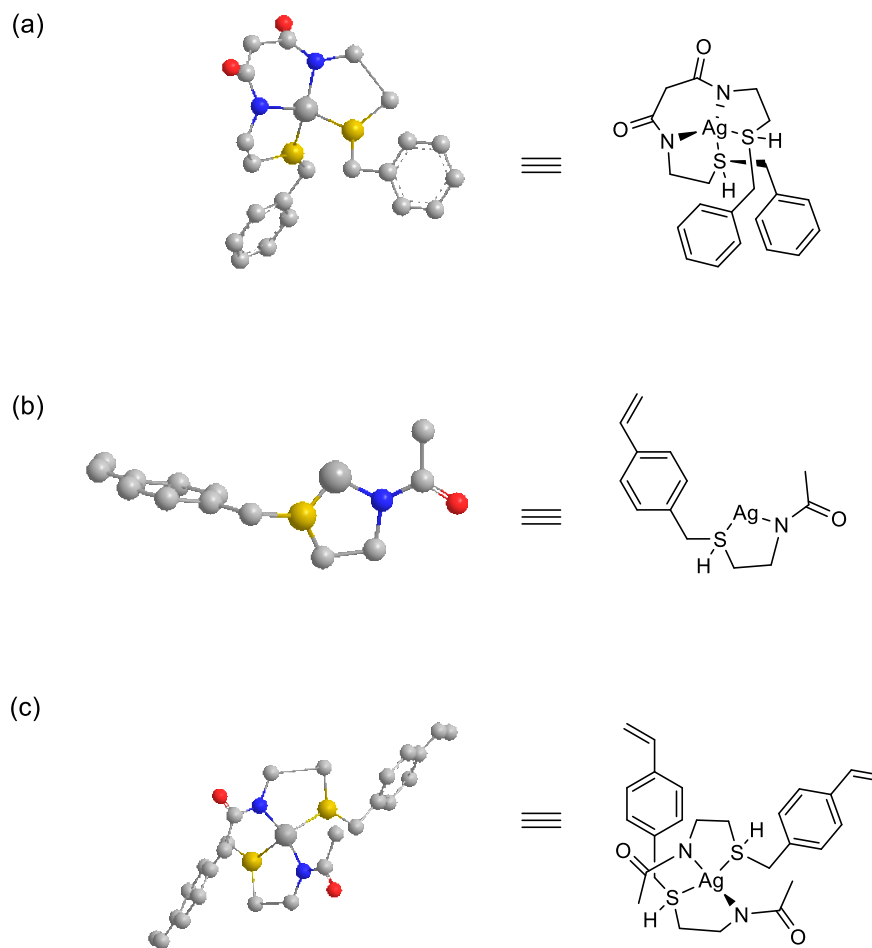


**Figure 3.8:** Proposed structures for (a) [Ag(2.10)]<sup>+</sup>, (b) [Ag(2.38)]<sup>+</sup> and (c) [Ag(2.38)<sub>2</sub>]<sup>+</sup> based on stoichiometry results observed from mass spectrometry and <sup>1</sup>H NMR titrations (leading to Job's and mole ratio plots).

### 3.4 Summary of results

- Two Ag<sup>+</sup>-**2.10** and two Ag<sup>+</sup>-**2.38** complexes were synthesized in excellent yields. However, it was not possible to investigate their binding stoichiometries by means of x-ray diffraction because attempts at growing appropriate crystals were unsuccessful

- The binding stoichiometries of the Ag<sup>+</sup> complexes of malonamide derivative **2.10** and amide **2.38** were determined by mass spectrometry, Job's and mole ratio plots (from <sup>1</sup>H NMR titrations). The malonamide derivative **2.10** binds to Ag<sup>+</sup> in a 1:1 fashion, while the amide **2.38** binds to Ag<sup>+</sup> with both the 1:1 and 1:2 (Ag<sup>+</sup>-**2.38**) stoichiometries.
- The next chapter will focus on attachment of amide **2.38** to a magnetic nanoparticle and trial Ag<sup>+</sup> extraction experiment using the synthesized magnetic nanoparticle/amide **2.38** composite.

**Chapter 4: Synthesis and application of Fe<sub>3</sub>O<sub>4</sub>/amide  
Ag<sup>+</sup> selective ligand composite  
nanoparticles**

## 4.1 Introduction

Silver (Ag) is a precious metal that has found applications in medicine, electronics and synthetic chemistry.<sup>164,237</sup> Unfortunately, owing to causes like improper disposal methods, silver in products can end up in water bodies. Once in water bodies, it can be bioaccumulated and biomagnified in aquatic organisms. The metal can then be passed on to humans through consumption of aquatic organisms. Exposure by humans to high levels of silver have been implicated in respiratory problems, skin colour changes, abdominal discomfort and lung irritation.<sup>164</sup> To prevent these, it is necessary to develop efficient methods for Ag extraction from water bodies. In addition to the environmental and health benefits of silver removal, there is the potential economic benefit as well. Extracted silver can be recycled and reused. In water, like most other sources of silver, the metal is usually present alongside other metals in trace amounts. Therefore, selective and efficient methods for Ag extraction are needed.

Silver has been extracted from aqueous matrices using methods including solvent extraction,<sup>203</sup> ion exchange,<sup>20</sup> chemical precipitation<sup>13</sup> and solid phase extraction<sup>164,238</sup>. The solid phase extraction method has recently become very popular. This is due to its simplicity, lowering of disposal costs, and potential for achieving elevated recoveries.<sup>164</sup>

In solid phase extraction, preparation of the extractant is an important consideration. Some properties desired in extractants are; stability across a wide pH range, easy recovery, high extraction efficiencies, low extraction times, very low extractant mass to sample volumes and simple preparation procedures. Extractants possessing some of these desired properties have been reported. For example, in 2018, Jalilian and Taheri<sup>239</sup> reported that nanoparticle **4.1** (Fe<sub>3</sub>O<sub>4</sub>@SiO<sub>2</sub>@TiO<sub>2</sub>@ Ag<sup>+</sup>-imprinted triazine **4.2**) (Figure 4.1 below) demonstrated a higher distribution ratio and selectivity coefficient than the non-imprinted analogue in the selective extraction and preconcentration of Ag<sup>+</sup>. The extractant could also be easily separated by a magnet and recycled (eight times without significant loss of extraction efficiency). On the downside, extraction efficiency was low at low pH. This is probably due to poor stability of the extractant at low pH.



**Figure 4.1: Structure of Fe<sub>3</sub>O<sub>4</sub>@SiO<sub>2</sub>@TiO<sub>2</sub>@ Ag<sup>+</sup>-imprinted triazine**

In the same year, Yin *et al*<sup>237</sup> reported the synthesis of a Ag<sup>+</sup> imprinted thiol **4.3** (Figure 4.2) tethered to Fe<sub>3</sub>O<sub>4</sub>@SiO<sub>2</sub>@TiO<sub>2</sub>. They revealed that the extractant showed high selectivity, at room temperature, for Ag<sup>+</sup> from aqueous solutions also containing Li<sup>+</sup>, Co<sup>2+</sup>, Cu<sup>2+</sup> and Ni<sup>2+</sup>. However, the extractant synthesis protocol was rather complex, achieved over four steps.

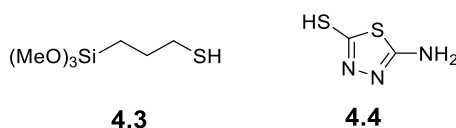


**Figure 4.2: Examples of thio-based Ag<sup>+</sup> ligands employed for metal recovery in literature**

Extractants prepared via relatively simple methods and with excellent efficiencies for selective extraction and preconcentration of trace amounts of Ag<sup>+</sup> have been documented. For instance, in 2012, a combination of thiadiazole **4.4** (Figure 4.2) and sodium dodecyl sulphate tethered by a facile condensation reaction to Fe<sub>3</sub>O<sub>4</sub>/Al<sub>2</sub>O<sub>3</sub>, was reported to extract Ag<sup>+</sup> selectively and quantitatively even in the presence of 100 folds of Zn<sup>2+</sup>, Bi<sup>3+</sup> and Pd<sup>2+</sup>. A remarkable discovery from this work is that Ag<sup>+</sup> extraction was rapid (> 98% Ag<sup>+</sup> was extracted in just 15 min!). Notwithstanding, extraction efficiency was relatively low at low pH.<sup>238</sup>

In just 5 min, a Fe<sub>3</sub>O<sub>4</sub>@SiO<sub>2</sub>@Schiff base **4.5** (Figure 4.3) nanocomposite prepared using facile methods removed about 95 %, 30 % and 22 % of Ag<sup>+</sup>, Pb<sup>2+</sup> and Cu<sup>2+</sup> respectively. Despite the very short extraction duration, amounts of interfering metal ions (Cu<sup>2+</sup> and Pb<sup>2+</sup>) are relatively high from an economic point of view.<sup>240</sup> In 2015, an extractant prepared by a well-established condensation reaction of imidazolium **4.6** (Figure 4.3 below) onto Mn<sub>3</sub>O<sub>4</sub>@SiO<sub>2</sub> was reported to demonstrate high selectivity and efficiency for extraction and preconcentration of ultratrace amounts of Ag<sup>+</sup> (60 ng/mL). Perhaps the most interesting

finding from this study is that the extractant could be reused for up to 300 times. Despite this outstanding result, relatively high extractant mass to sample volume ratio was required. Also, the extractant could not be easily separated, with the aid of a magnet for example, because Mn<sub>3</sub>O<sub>4</sub> has low magnetization saturation.<sup>164</sup>

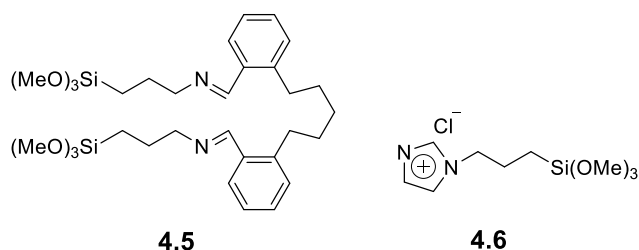
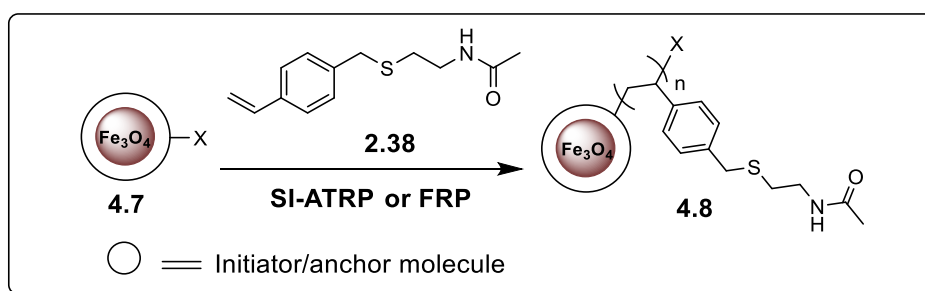


**Figure 4.3:** Ag<sup>+</sup> ligands with trimethoxysilane handles previously utilized for metal recovery in literature

## 4.2 Aims and objectives

The main aim described in this chapter is the attempted tethering of the low pH stable styryl amide **2.38** to an initiator-functionalized iron oxide magnetic nanoparticle **4.7** via two different routes; surface-initiated atom transfer radical polymerization (SI-ATRP) and free radical polymerization (FRP) techniques to afford the extractant nanoparticle **4.8** (Scheme 4.1). The extractant nanoparticle **4.8** represents the approach adopted in this study to addressing some of the shortfalls highlighted in section 4.1 above including the difficulty in recovering the extractant particle, the low extraction efficiency at low pH and the poor selectivity for Ag<sup>+</sup>.



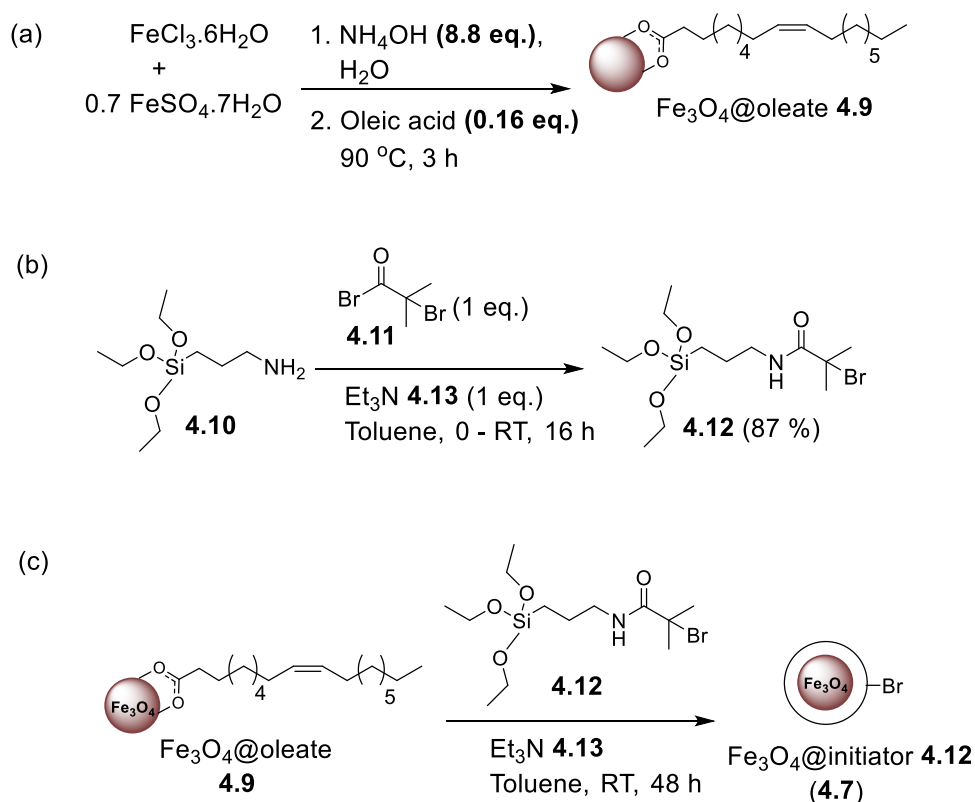
**Scheme 4.1:** Generic scheme for synthesis of a novel Ag<sup>+</sup> selective extractant nanoparticle **4.8**

The amide **2.38** which was previously observed to be highly selective and moderately efficient for Ag<sup>+</sup> extraction at low pH (Chapter 2) will be grown off the Fe<sub>3</sub>O<sub>4</sub>@initiator **4.7** scaffold

as a polymer with the hope of improving on the moderate (36 %) efficiency observed for the monomer ligand in chapter 2. To protect the Fe<sub>3</sub>O<sub>4</sub> core, for example, from degradation in low pH media and more importantly to tether the Ag<sup>+</sup> selective ligand (amide **2.38**), the Fe<sub>3</sub>O<sub>4</sub> will be functionalized with an initiator/anchor molecule (Scheme 4.1) to provide the nanoparticle Fe<sub>3</sub>O<sub>4</sub>@initiator **4.7**. Finally, to achieve good dispersion of the extractant particle **4.8** (in an aqueous media) and easy recovery after Ag<sup>+</sup> extraction, a core of nano-sized Fe<sub>3</sub>O<sub>4</sub> was chosen to be synthesized.

## 4.3 Result and discussion

### 4.3.1 Synthesis of Fe<sub>3</sub>O<sub>4</sub>@initiator **4.12** (**4.7**)



**Scheme 4.2: Overall synthesis steps for Fe<sub>3</sub>O<sub>4</sub>@initiator **4.12** (**4.7**) nanoparticle**

The synthesis of Fe<sub>3</sub>O<sub>4</sub>@initiator **4.12** (**4.7**) nanoparticle was achieved over three steps (Scheme 4.2). The first step involved synthesis of Fe<sub>3</sub>O<sub>4</sub>@oleate **4.9** undertaken following the method reported by Puig and coworkers.<sup>241</sup> This method was chosen amongst others mainly because it involved a simple workup procedure. Briefly, FeCl<sub>3</sub> and FeSO<sub>4</sub> were dissolved in

water and heated at 90 °C for 30 mins. This was followed by the quick addition of aqueous ammonia and oleic acid in succession leading to change in the colour of the reaction mixture from orange to black. After 3 hours, the black solid obtained was washed, dried and dispersed in toluene to achieve a concentration of 26 mg/mL (Scheme 4.2a). An aliquot of the toluene dispersion of the Fe<sub>3</sub>O<sub>4</sub>@oleate **4.9** was oven-dried to obtain a black solid which was subjected to XRD characterization and its identity was confirmed using the XRD diffraction pattern (Figure 4.4 below) as Fe<sub>3</sub>O<sub>4</sub>. The XRD diffraction pattern was employed alongside the Scherrer equation<sup>241</sup> in the determination of the particle diameter of **4.9** (see experimental section) and found out that **4.9** was nano-sized (9.9±0.2 nm).

In the second step, initiator **4.12** was accessed following the method reported by Sun *et al*<sup>242</sup>. Succinctly, aminosilane **4.10** was treated with acid bromide **4.11** in toluene in the presence of triethylamine **4.13** (needed to mop up the HBr formed during the reaction, Scheme 4.2b). After about 16 h reaction time, the crude product was filtered and the filtrate was concentrated *in vacuo* to give, as a yellow oil, initiator **4.12** in a 87 % yield. The amide linkage of the initiator portion of this molecule should be stable to the low pH requirements of potential applications. In the final step, the target particle; Fe<sub>3</sub>O<sub>4</sub>@initiator **4.12** (**4.7**) was accessed following the method reported by Sun *et al*<sup>242</sup>. Hence, initiator **4.12** was tethered to the Fe<sub>3</sub>O<sub>4</sub> core of Fe<sub>3</sub>O<sub>4</sub>@oleate **4.9** by a ligand exchange process achieved by stirring a mixture of Fe<sub>3</sub>O<sub>4</sub>@oleate **4.9**, initiator **4.12** and triethylamine **4.13** (employed as the catalyst) at room temperature in toluene for 2 days (Scheme 4.2c).

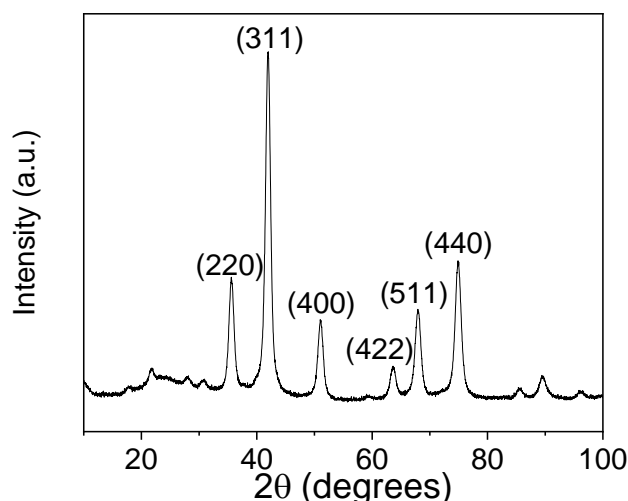


**Figure 4.4: X-ray diffractogram of Fe<sub>3</sub>O<sub>4</sub>@oleate **4.9** (Co K $\alpha$  source wavelength = 1.79 Å, voltage = 40 kV, current = 40 mA)**

The particles Fe<sub>3</sub>O<sub>4</sub>@oleate **4.9** and Fe<sub>3</sub>O<sub>4</sub>@initiator **4.12** (**4.7**) were characterized by FTIR and X-ray photoelectron spectroscopy (XPS) in order to determine their chemical composition and act as a reference for comparison to later steps in the synthetic pathway to the subsequent functionalization of **4.7** with amide **2.38** as stated earlier. As expected, the FTIR spectrum of Fe<sub>3</sub>O<sub>4</sub>@oleate **4.9** (Figure 4.5a below) contained bands at 557 cm<sup>-1</sup>, characteristic of the Fe-O bending vibration, and at 1515 and 1411 cm<sup>-1</sup>, representing the C-O asymmetric and symmetric stretching frequencies respectively in oleate ligand.<sup>242</sup> The FTIR spectra of the Fe<sub>3</sub>O<sub>4</sub>@initiator **4.12** (**4.7**) (Figure 4.5b) contains absorption bands at 1641 and 1530, representing the N-C=O bending vibration. Furthermore, bands at 1107 and 1034 cm<sup>-1</sup> in **4.7** characteristic of the Si-O-Si stretch in initiator **4.12** are absent in the spectrum of precursor Fe<sub>3</sub>O<sub>4</sub>@oleate **4.9** (Figure 4.5a), suggesting the successful ligand exchange of initiator **4.12** for the oleate<sup>242</sup>

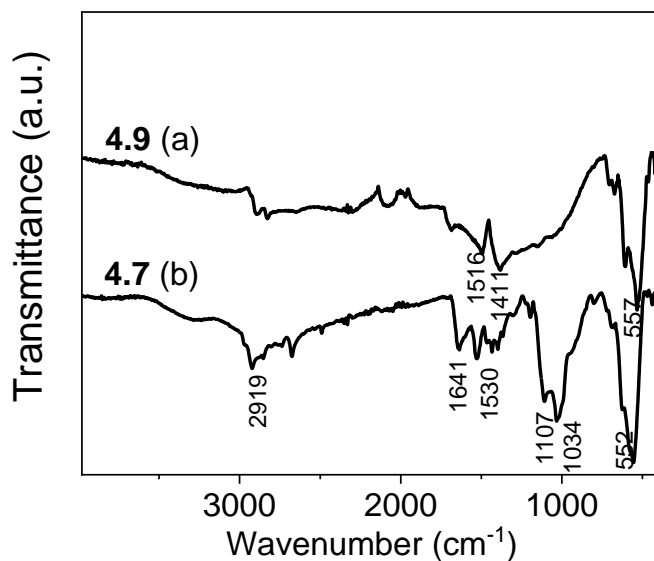


**Figure 4.5:** FTIR spectra of (a) Fe<sub>3</sub>O<sub>4</sub>@oleate **4.9** (b) Fe<sub>3</sub>O<sub>4</sub>@initiator **4.12** (**4.7**)

The XPS survey (Figure 4.6a & b below) and high-resolution (Figure 4.7a & b) spectra of the particles Fe<sub>3</sub>O<sub>4</sub>@oleate **4.9** and Fe<sub>3</sub>O<sub>4</sub>@initiator **4.12** (**4.7**) corroborate the FTIR data suggesting that **4.9** and **4.7** have been synthesized. First, the survey spectrum of Fe<sub>3</sub>O<sub>4</sub>@oleate **4.9** (Figure 4.6a) contains photoelectron lines at 725/710, 284.8 and 533 eV indicating the presence of Fe 2p (in Fe<sub>3</sub>O<sub>4</sub>), C 1s and O 1s (in oleate ligand) respectively.<sup>242</sup> In addition, a peak at 288.8 eV can be observed in the high-resolution spectra of Fe<sub>3</sub>O<sub>4</sub>@oleate **4.9** (Figure 4.7a) which is attributed to the C 1s of a carboxylic acid group of oleate ligand.<sup>242</sup> These observations indicate that oleic acid has been chemisorbed onto Fe<sub>3</sub>O<sub>4</sub>. The XPS survey spectrum of Fe<sub>3</sub>O<sub>4</sub>@initiator **4.12** (**4.7**) (Figure 4.6b) contain the photoelectron lines characteristic of N, Si and Br not present in the spectrum of the Fe<sub>3</sub>O<sub>4</sub>@oleate **4.9** (Figure 4.6a). Furthermore, the C 1s high resolution (better known as core level) scan of Fe<sub>3</sub>O<sub>4</sub>@initiator **4.12** (**4.7**) (Figure 4.7b) contains peaks at 284.1, 286.5 and 288.4 eV not found in the corresponding core level spectrum of the Fe<sub>3</sub>O<sub>4</sub>@oleate **4.9** (see Figure 4.7a). The peak at 284.1 eV was attributed to the sp<sup>3</sup> C in the Si-C bond from the Fe<sub>3</sub>O<sub>4</sub>@initiator **4.7**.<sup>242</sup> The peak at 286.5 eV was attributed to C 1s in C-N and C-Br bonds on the surface of Fe<sub>3</sub>O<sub>4</sub>@initiator **4.7**. Finally, the peak at 288.4 eV was attributed to the carbonyl carbon in the

amide moiety of **4.7**. These observations confirm that the oleate ligand has been exchanged for initiator **4.12** to give  $Fe_3O_4$ @initiator **4.12** (**4.7**).

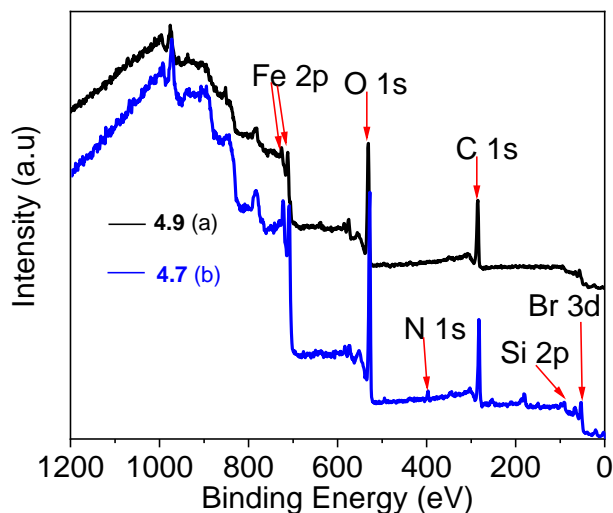


**Figure 4.6:** XPS survey spectra of (a)  $Fe_3O_4$ @oleate **4.9** (black) and (b)  $Fe_3O_4$ @initiator **4.12** (**4.7**) (blue) (X-ray source: Mono (Al), 150 W, 90°, Slot).

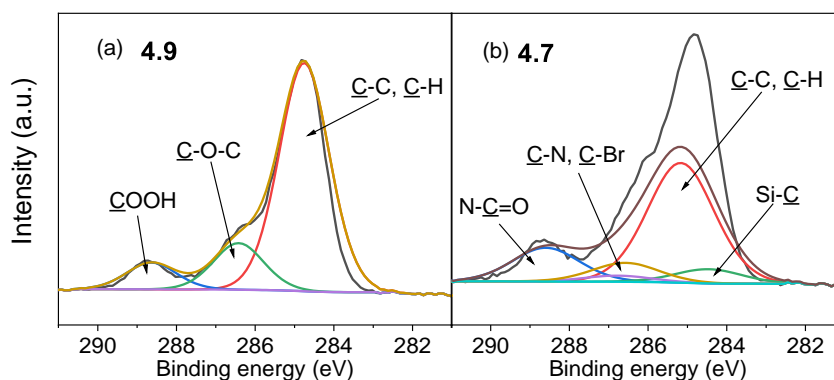


**Figure 4.7:** XPS spectra of core level scans of C 1s in (a)  $Fe_3O_4$ @oleate **4.9** and (b)  $Fe_3O_4$ @initiator **4.7**.

Under the electron microscope, the  $Fe_3O_4$ @oleate **4.9** (Figure 4.8a below) appear as dispersed spherical particles and their average size was determined after analysis of the TEM micrograph of **4.9** as  $10 \pm 2.4$  nm (Figure 4.8b). This size ( $10 \pm 2.4$  nm) is in good agreement with that obtained ( $9.9 \pm 0.2$  nm) after analysis of XRD diffraction pattern of the particle **4.9**. Unlike  $Fe_3O_4$ @oleate **4.9**, the  $Fe_3O_4$ @initiator **4.12** (**4.7**) particles appear aggregated (Figure 4.8c),

an observation attributed to the hydrolysis and condensation of the siloxy groups in the **4.12**. The average size of **4.7**; 10.0±1.94 nm (Figure 4.8d) determined after analysis of its micrograph was found to be identical to that of its precursor Fe<sub>3</sub>O<sub>4</sub>@oleate **4.9** (10.0±2.4 nm) with the implication that the particle **4.7** is still in the nano-size range and superparamagnetic just like **4.9**.

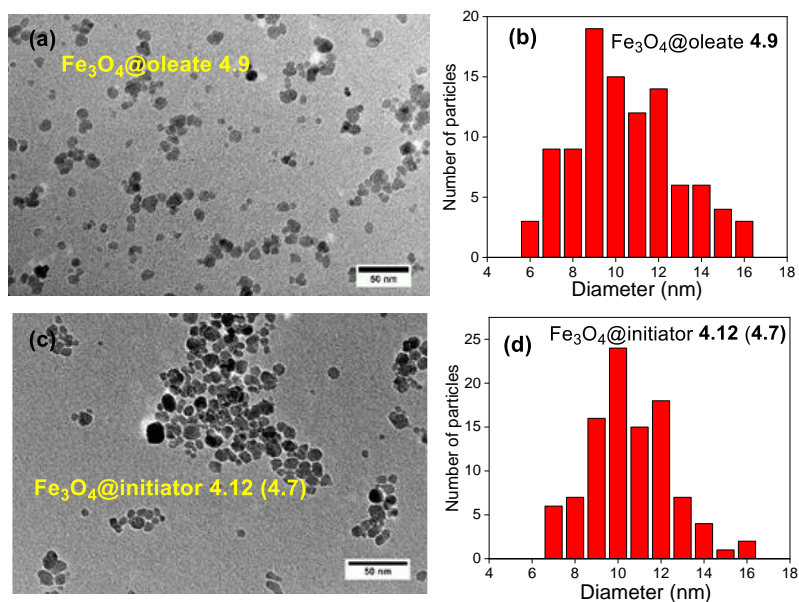


**Figure 4.8:** (a,c) Transmission electron micrographs of (a) Fe<sub>3</sub>O<sub>4</sub>@oleate **4.9** and (c) Fe<sub>3</sub>O<sub>4</sub>@initiator **4.12 (4.7)**, (b,d) Histograms for the size distributions of (b) Fe<sub>3</sub>O<sub>4</sub>@oleate **4.9** and (d) Fe<sub>3</sub>O<sub>4</sub>@initiator **4.12 (4.7)**

Indeed, the superparamagnetic behaviours of the nanoparticles; Fe<sub>3</sub>O<sub>4</sub>@oleate **4.9** and Fe<sub>3</sub>O<sub>4</sub>@initiator **4.12 (4.7)** were confirmed from the shape of their magnetization curves and low coercivities observed (**4.9** = 10.5 and **4.7** = 11.6 Oe) (Figure 4.9a & b below).<sup>243,244</sup> Unfortunately, the magnetization saturation ( $M_s$ ) of Fe<sub>3</sub>O<sub>4</sub>@initiator **4.12 (4.7)** was found to be lower (48.73±0.14 emu/g) (Figure 4.8b) than that of its precursor - Fe<sub>3</sub>O<sub>4</sub>@initiator **4.7** (64.90±0.05 emu/g) at room temperature (Figure 4.9a). The lower  $M_s$  in the Fe<sub>3</sub>O<sub>4</sub>@initiator **4.7** compared to the Fe<sub>3</sub>O<sub>4</sub>@oleate **4.9** was attributed to the presence of the non-magnetic initiator **4.12** coating on Fe<sub>3</sub>O<sub>4</sub>.

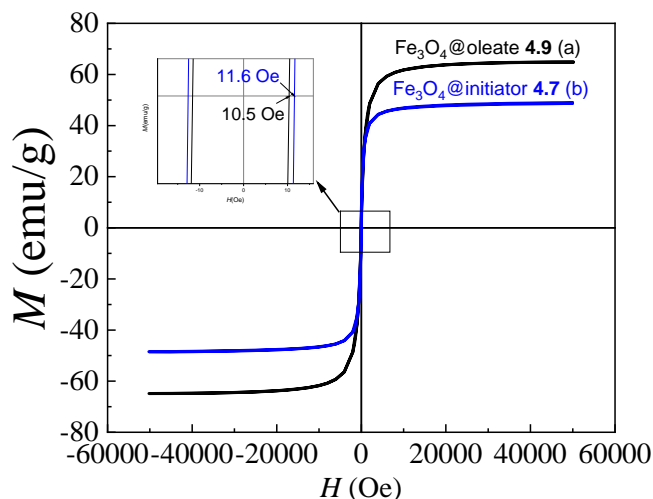


**Figure 4.9: Magnetization curves for (a) Fe<sub>3</sub>O<sub>4</sub>@oleate 4.9 (black) and (b) Fe<sub>3</sub>O<sub>4</sub>@initiator 4.12 (4.7) (blue), (Temperature: 300 K)**

The surface coverage by the oleate ligand and initiator **4.12** on the Fe<sub>3</sub>O<sub>4</sub> in Fe<sub>3</sub>O<sub>4</sub>@oleate **4.9** and Fe<sub>3</sub>O<sub>4</sub>@initiator **4.12** (**4.7**) respectively were determined after analysis of their thermogravimetry analysis (TGA) curves. The surface coverage was calculated using the formula<sup>242</sup>;

$$\text{No of molecules per nm}^2 = \frac{W \times d_{\text{Fe}_3\text{O}_4} \times r \times N_A}{M(1-W) \times 3 \times 10^{21}} \quad (4.1)$$

Where W is weight loss of the sample (determined from a TGA curve),  $d_{\text{Fe}_3\text{O}_4}$  is the density of Fe<sub>3</sub>O<sub>4</sub>, r is the radius of the particle,  $N_A$  is Avogadro's constant and M is the molecular weight of the surface coating of the Fe<sub>3</sub>O<sub>4</sub>.

The surface coverage of the oleate ligand on Fe<sub>3</sub>O<sub>4</sub> in **4.9** was determined to be 4 molecules/nm<sup>2</sup> from the combined observed weight losses of 4.5 % (between 164 and 272 °C) and 14.6 % (between 272 and 461 °C) attributed to decomposition of free and bound oleic acid respectively (see Figure 4.10a below). This surface coverage is lower than that reported by Sun *et al*<sup>242</sup> (~ 8%) due to the lower amount of oleic acid used in the synthesis of the Fe<sub>3</sub>O<sub>4</sub>@oleate **4.9** in this work. Further analysis of the TGA curve of **4.9** revealed a weight loss of 23.9 % (between 461-803 °C) attributed to the phase change from Fe<sub>3</sub>O<sub>4</sub> to FeO and deoxidation of FeO (since the TG characterization was undertaken under N<sub>2</sub>).<sup>245</sup> The surface

coverage of the Fe<sub>3</sub>O<sub>4</sub> by initiator **4.12** in Fe<sub>3</sub>O<sub>4</sub>@initiator **4.12** (**4.7**) was determined, from its weight loss of 14.9 % (between 260-480 °C) to be approximately 3 molecules/nm<sup>2</sup> (Figure 4.10b). The observed weight loss pattern above 480 °C for the Fe<sub>3</sub>O<sub>4</sub>@initiator **4.7** is identical to related structures.<sup>246</sup>

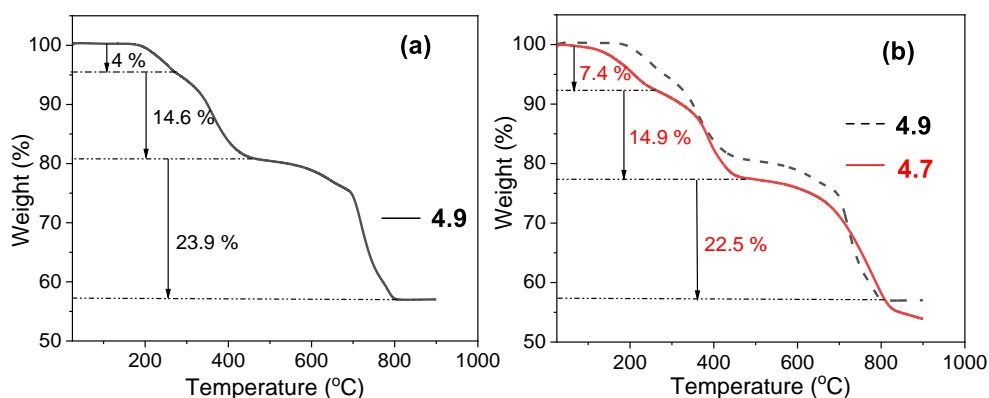
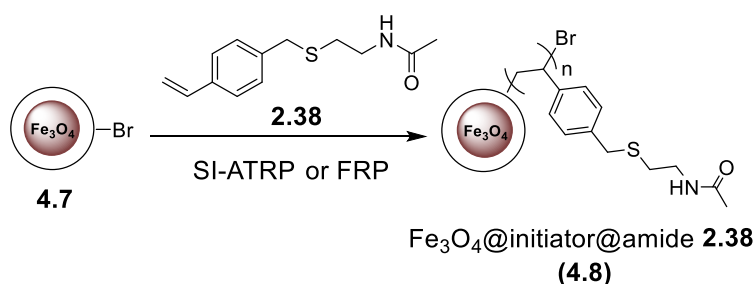


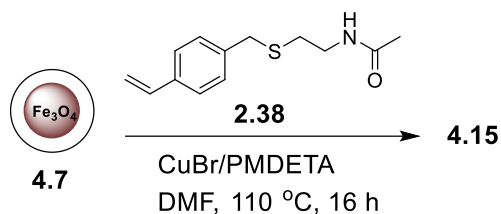
**Figure 4.10:** Thermogravimetry analysis curves of (a) Fe<sub>3</sub>O<sub>4</sub>@oleate **4.9** and (b) Fe<sub>3</sub>O<sub>4</sub>@initiator **4.7** (red) and Fe<sub>3</sub>O<sub>4</sub>@oleate **4.9** (dashed black), (Atmosphere: nitrogen, heating rate: 10 °C/min)

### 4.3.2 Attempted surface initiated ATRP (SI-ATRP) of amide **2.38**

As stated above, the aim of this chapter is the synthesis of a novel extractant nanoparticle by growing amide **2.38** as a polymer off the Fe<sub>3</sub>O<sub>4</sub>@initiator **4.12** (**4.7**) scaffold (Scheme 4.3) via both the surface-initiated atom transfer radical polymerization (SI-ATRP) and free radical polymerization (FRP) processes. In this section, the SI-ATRP procedure is described.



**Scheme 4.3:** Generic scheme for the synthesis of Fe<sub>3</sub>O<sub>4</sub>@initiator@amide **2.38** (**4.8**)



**Scheme 4.4: Attempted SI-ATRP of amide 2.38**

The SI-ATRP of amide **2.38** was attempted by adapting the method described by Sun *et al*<sup>242</sup>. Briefly, a mixture of amide **2.38**, CuBr, PMDETA and Fe<sub>3</sub>O<sub>4</sub>@initiator **4.12** (**4.7**) were heated at 110° C (Scheme 4.4). The crude product obtained after heating for 16 h was diluted with THF and precipitated using petroleum ether to afford a brown solid **4.15** which after FTIR, XPS and TGA analysis was determined not to be the desired compound indicating that the SI-ATRP of amide **2.38** was most likely unsuccessful. Had the SI-ATRP of amide **2.38** been successful, the intensities of the peaks at 1645 cm<sup>-1</sup> and 3300 cm<sup>-1</sup>, indicative of the C=O and N-H stretches in amide **2.38** should have been higher in the spectrum of solid **4.15** (Figure 4.11b below) than in the spectrum of its precursor **4.7** (Figure 4.11a) since both spectra were plotted on the same scale with normalisation. Furthermore, the absence of the photoelectron line at 163.5 eV characteristic of the organic (C-S) S 2p peak in the XPS core level scans of **4.15** (Figure 4.12b) was highly indicative that the attempted the SI-ATRP of amide **2.38** had failed.

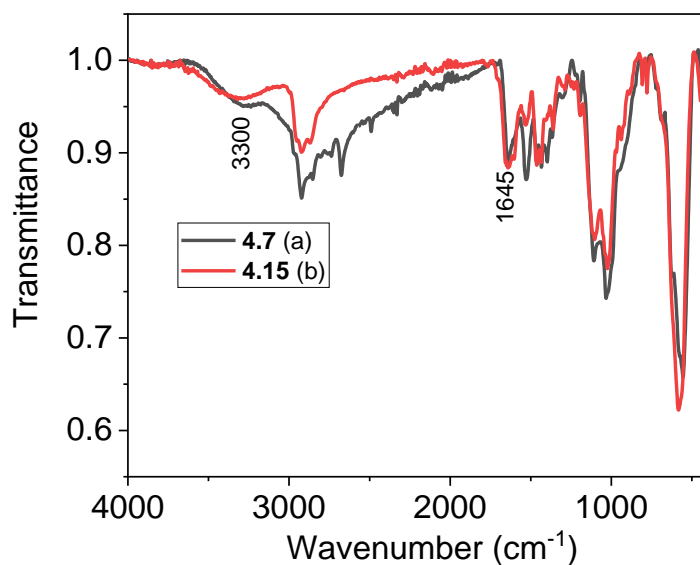


Figure 4.11: FTIR spectra of (a)  $Fe_3O_4$ @initiator 4.12 (4.7) (black) and (b) brown solid 4.15 (red)

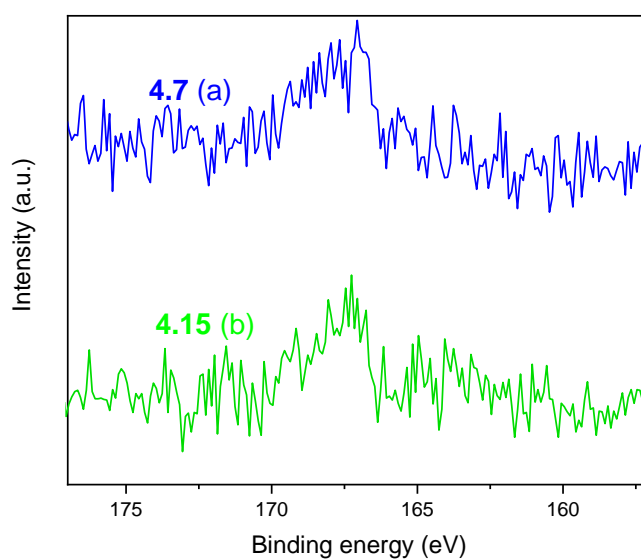
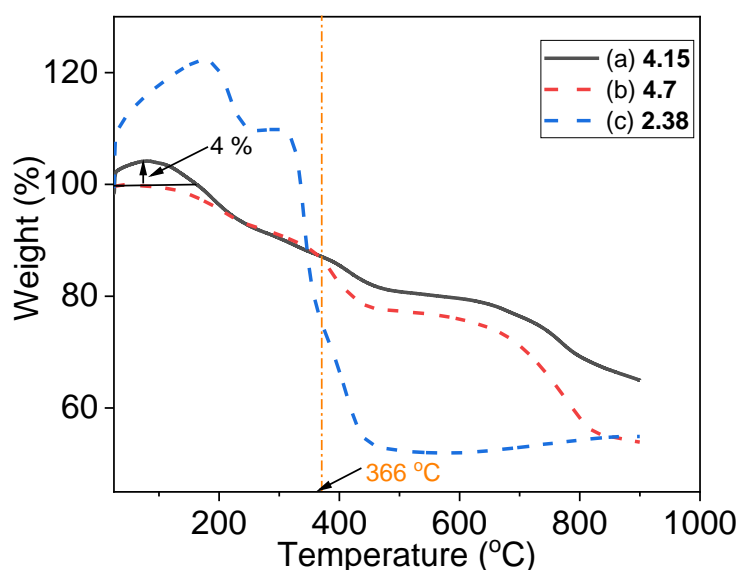


Figure 4.12: XPS S 2p core level scans of (a)  $Fe_3O_4$ @initiator 4.12 (4.7) (blue), (b) brown solid 4.15 (green)

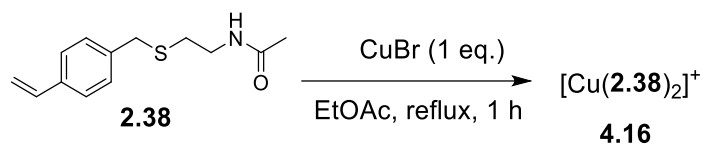
However, the TGA thermograms of the precursor nanoparticle **4.7** (Figure 4.13b below) and the prepared brown solid **4.15** (Figure 4.13a) were slightly different. The free amide **2.38** (blue) shows a weight increase in the TGA curve (Figure 4.13c) which is mirrored in the brown

solid **4.15** suggesting weakly absorbed amide **2.38**. Between the 200 - 366 °C region, similar weight loss patterns can be observed between **4.7** & **4.15**, attributed to the decomposition of the initiator **4.12** portion. Beyond 366 °C, the weight loss for both **4.7** and **4.15** are different again, however, it does not suggest that amide **2.38** was attached to **4.7** since the particle **4.15** experienced lower weight loss than its precursor **4.7**. Also, had the SI-ATRP of amide **2.38** been successful, a step loss, by the solid **4.15**, identical to that of the free amide **2.38** (Figure 4.13c) should have been observed.



**Figure 4.13:** TGA thermograms of (a) brown solid **4.15** (black) (b)  $Fe_3O_4$ @initiator **4.12** (**4.7**) (red) and (c) amide **2.38** (blue)

It was hypothesized that the attempted SI-ATRP of amide **2.38** failed because the amide **2.38** itself may have chelated  $Cu^+$  from  $CuBr$  in competition with the ligand (PMDETA) required for the SI-ATRP, thereby making the metal ion unavailable for the activation of the macroinitiator –  $Fe_3O_4$ @initiator **4.12** (**4.7**). This reasoning was inspired by the HSAB principle where  $Cu^+$  is classed as a soft acceptor and  $S^-$  in amide **2.38** is classed as a soft donor.<sup>204</sup> Indeed,  $^1H$  NMR and mass spectrometry data of the product (**4.16**) obtained after refluxing equal amounts of amide **2.38** and  $CuBr$  in ethylacetate (Scheme 4.5 below) suggests that the formulated hypothesis has merit.



**Scheme 4.5: Synthesis of Cu-amide 2.38 complex**

In the <sup>1</sup>H NMR spectrum of the complex **4.16** (Figure 4.14), downfield shifts of 0.04, 0.04, 0.06 and 0.05 ppm were observed for protons ‘b’, ‘c’, ‘d’, and ‘e’ respectively compared to the <sup>1</sup>H NMR of neat **2.38**. Furthermore, the *m/z* peak at 533 representative of [Cu(**2.38**)<sub>2</sub>]<sup>+</sup> was observed in the low resolution mass spectrum of complex **4.16** (Figure 4.15) which was subsequently confirmed by high resolution mass spectrometry (see experimental).

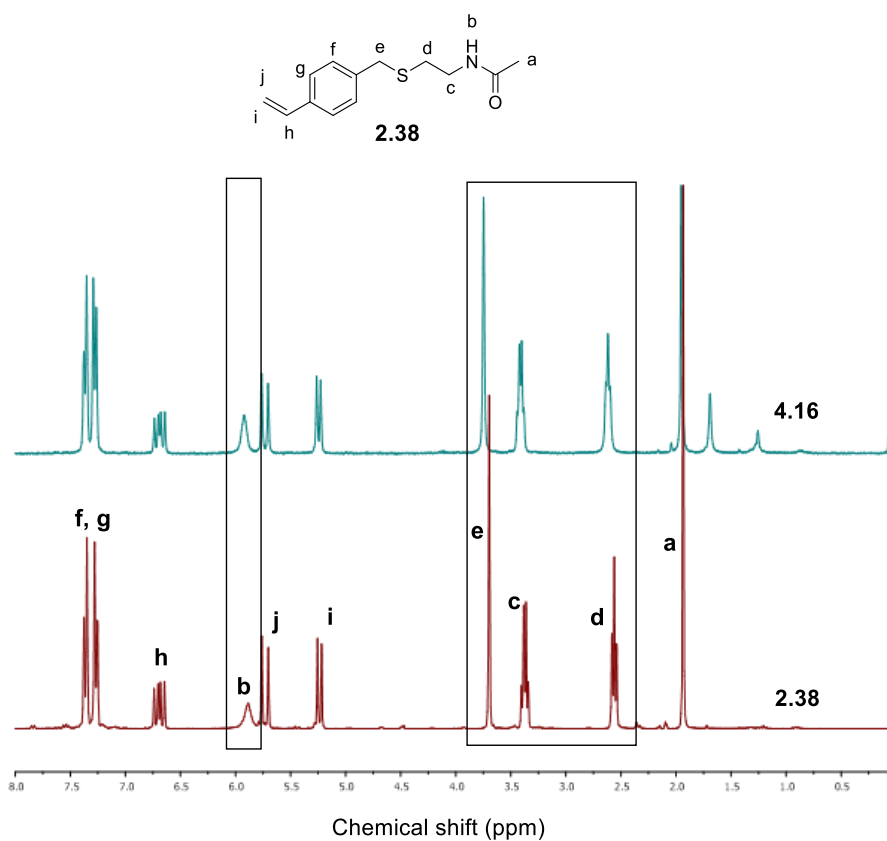


**Figure 4.14: <sup>1</sup>H NMR (300 MHz, CDCl<sub>3</sub>) spectra of amide 2.38 and complex 4.16**

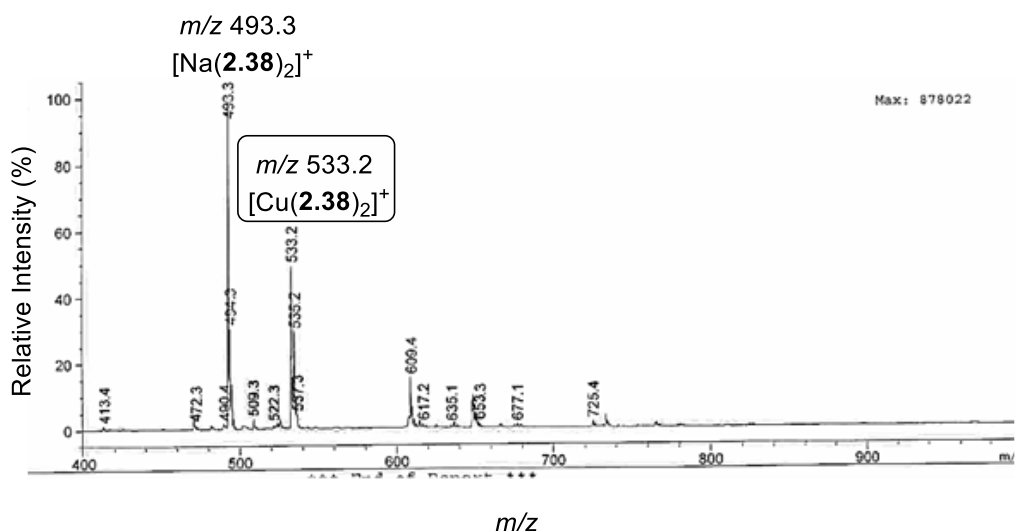
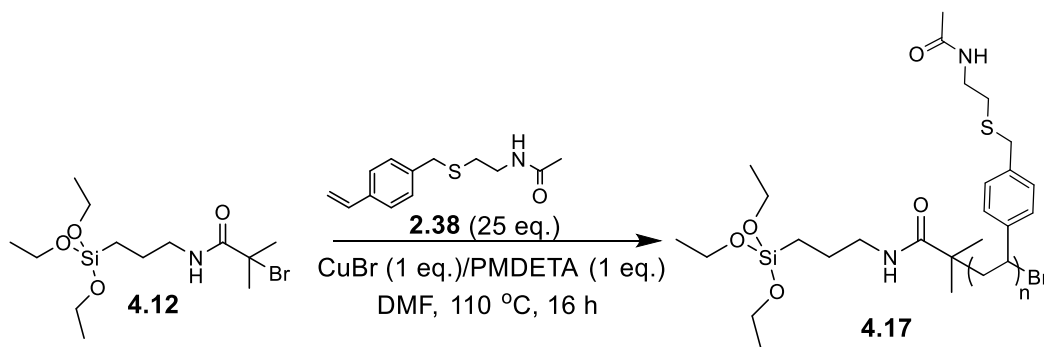


Figure 4.15: Low resolution mass spectrum of Cu<sup>+</sup> complex 4.16

In order to confirm that complexation of the CuBr by the ligand **2.38** was stopping the desired ATRP process, a solution ATRP study of amide **2.38** was undertaken. Therefore, the reaction of the initiator **4.12** (1 eq.) with **2.38** (25 eq.), CuBr (1 eq.), PMDETA (1. eq) and *p*-DMB (12 mg, *ca.* 3 % relative to **2.38** as internal <sup>1</sup>H NMR standard to estimate conversion of **2.38**) in DMF at 110 °C for 16 hr was attempted (Scheme 4.6).



Scheme 4.6: Attempted synthesis of poly(**2.38**) by solution ATRP of amide **2.38**

The conversion of **2.38** to poly(**2.38**) or **4.17** was monitored by <sup>1</sup>H NMR by taking samples of the reaction mixture at the start and end of the reaction. Subsequently, the conversion was then determined by formula provided by Colombani and coworkers<sup>247</sup> shown below;

$$\alpha = 1 - \frac{[M]_t}{[M]_o} \quad 4.2$$

Where  $\alpha$  = conversion,  $[M]_t$  = monomer concentration at time  $t$  and  $[M]_0$  = monomer concentration at the start of the reaction.

The concentrations of the geminal protons – ‘i’ and ‘j’ of the vinyl group in amide **2.38** were represented by their integrals and these integrals were referenced to the phenyl protons of the internal standard (*p*-DMB, depicted as ‘x’ in the <sup>1</sup>H NMR spectra) and which was set as 1.00 (Figure 4.16a and b).

Even after 16 hours, conversion of amide **2.38** to any polymer (**4.17**) was very low (0.02 or 2 %) (Table 4.1) and this indicated that the ATRP reaction in the presence of **2.38** was not possible to high conversion. Attention was turned to other free radical processes that did not require a metal for mediation such as AIBN initiated processes.

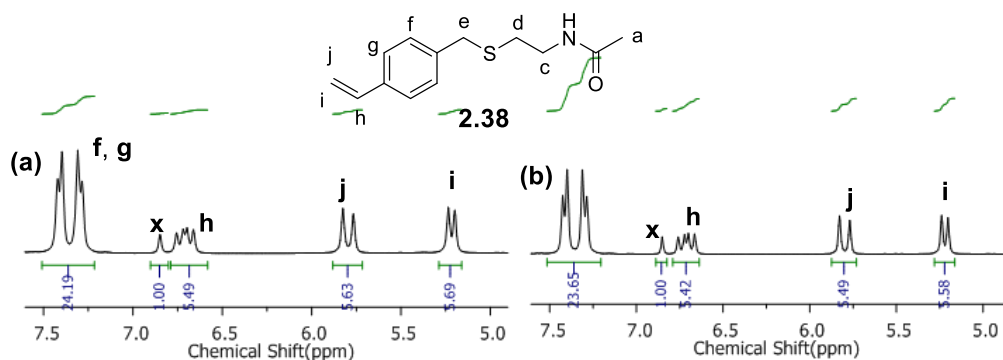


**Figure 4.16:** A section of <sup>1</sup>H NMR (d<sub>6</sub>-DMSO, 300 MHz) spectra of reaction mixture from the attempted solution ATRP of amide **2.38** at (a)  $t = 0$  h and (b)  $t = 16$  h. (x = phenyl protons of *p*-DMB internal standard).

**Table 4.1:** Conversion of amide **2.38** after solution ATRP (concentration of protons was represented by their integrals in the <sup>1</sup>H NMR spectrum)

Protons		
Time (h)	i	j
0	5.69	5.63
16	5.58	5.49
Conversion	0.02	0.02

### 4.3.3 AIBN-mediated free radical polymerization of amide **2.38**



**Scheme 4.7: Free radical polymerization of amide **2.38****

Prior to the linkage of the amide **2.38** to the Fe<sub>3</sub>O<sub>4</sub>@initiator **4.7** by the free radical process mediated by AIBN, the free radical polymerization of the neat amide **2.38** was attempted in solution by warming a mixture of the amide **2.38** and AIBN in THF for 17 h (Scheme 4.7). The conversion of the amide **2.38** as monitored by <sup>1</sup>H NMR as described for the solution ATRP of amide **2.38** above. Monomer conversion was calculated by employing the formula in equation 4.2 above. Only that this time, the concentrations of the geminal protons – ‘i’ and ‘j’ of the vinyl group in amide **2.38** represented by their integrals were compared those of the phenyl group which were set as 1.00 (see Figure 4.17a and b below). The conversion of the amide **2.38** to **4.17** was average (for proton i; 0.56 or 56 % or proton j; 0.48 or 48 %) (see Table 4.2 below). This could be because hydrogen atoms at positions ‘e’ ‘d’ and ‘c’ in the molecule **2.38** are readily abstractable by radicals which would either terminate polymerisation or retard initiation. Notwithstanding the average conversion observed, the linkage of the amide **2.38** to the Fe<sub>3</sub>O<sub>4</sub>@initiator **4.7** by employing the AIBN-mediated polymerization process was attempted.

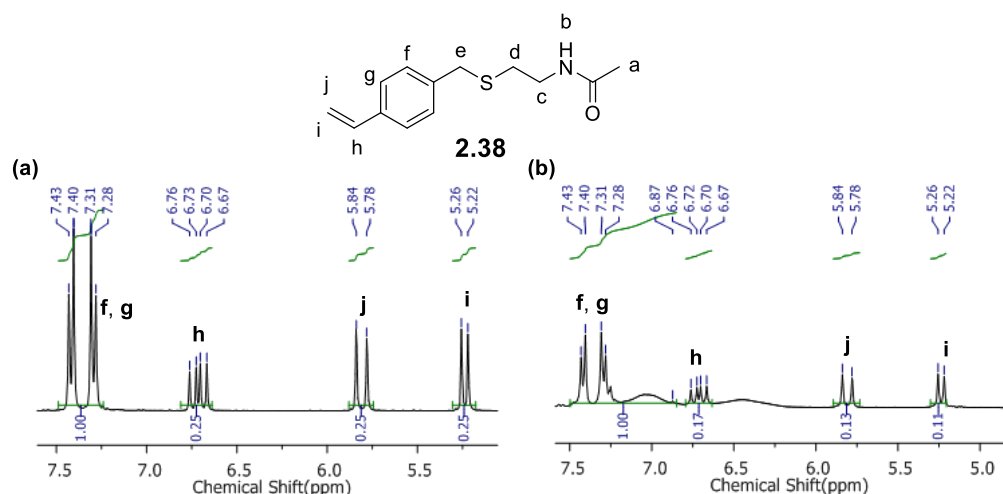


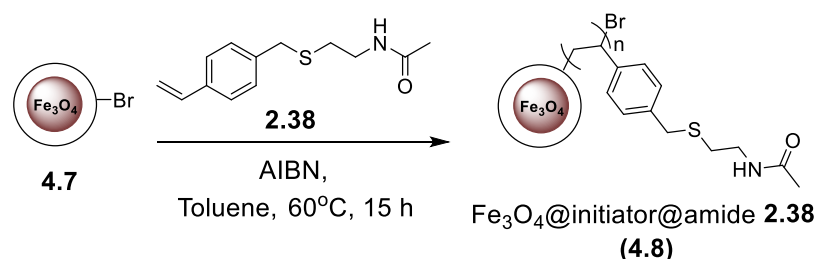
Figure 4.17: A section of  $^1\text{H}$  NMR ( $\text{d}_6\text{-DMSO}$ , 300 MHz) spectra of reaction mixture from the attempted polymerization of amide **2.38** at (a)  $t = 0$  h and (b)  $t = 17$  h.

Table 4.2: Conversion of amide **2.38** (concentration of protons was represented by their integrals in the  $^1\text{H}$  NMR spectrum)

Time (h)	Protons	
	i	j
0	0.25	0.25
17	0.11	0.13
Conversion	0.56	0.48

#### 4.3.4 AIBN-mediated free radical coupling of amide **2.38** and $\text{Fe}_3\text{O}_4$ @initiator **4.12** (**4.7**)

Attention was next turned to tethering the amide **2.38** to the  $\text{Fe}_3\text{O}_4$ @initiator **4.12** (**4.7**) scaffold via a free radical polymerization process initiated by AIBN.



Scheme 4.8: AIBN-mediated coupling of amide **2.38** to  $\text{Fe}_3\text{O}_4$ @initiator **4.12** (**4.7**)

Therefore, the toluene solution of AIBN was slowly added to a stirred toluene solution of scaffold **4.7**, amide **2.38** and AIBN at 60 °C (see Scheme 4.8 above). After 15 h, the crude product obtained was left to cool to room temperature and subsequently washed with THF, magnetically separated and dried *in vacuo* to furnish a brown solid **4.8**. Pleasingly, results from the characterizations (FTIR, XPS and TGA) undertaken indicated that the amide **2.38** has been successfully linked to the scaffold **4.7**. After FTIR analysis, it was observed that the intensities of the characteristic absorptions at 3268 cm<sup>-1</sup> (amide N-H stretch), 2919 cm<sup>-1</sup> (alkyl C-H stretch), 1641 cm<sup>-1</sup> (amide C-O, asymmetric) and 1544 cm<sup>-1</sup> (amide C-O symmetric) are higher in the spectrum of **4.8** (Figure 4.18b below) compared to that of its precursor **4.7** (Figure 4.18a), after the IR spectrum had been plotted on the same scale and normalized, indicating that amide **2.38** may have been attached to **4.7**. Furthermore, the characteristic binding energy (163.5 eV) for organic sulfur (C-S) can be observed in the deconvoluted S 2p XPS core level scan of the **4.8** (Figure 4.19b below) but absent in that of its precursor **4.7** (Figure 4.19a). Finally, the weight loss patterns and % weight losses observed from the TGA thermograms of **4.8** (Figure 4.20b below) and that of **4.7** (Figure 4.20a) are clearly different. The total weight loss of 41 % by **4.8** observed between 200 and 480 °C is attributed to decomposition of covalently bound amide **2.38** and initiator **4.12** from the surface of the Fe<sub>3</sub>O<sub>4</sub> (Figure 4.20b).

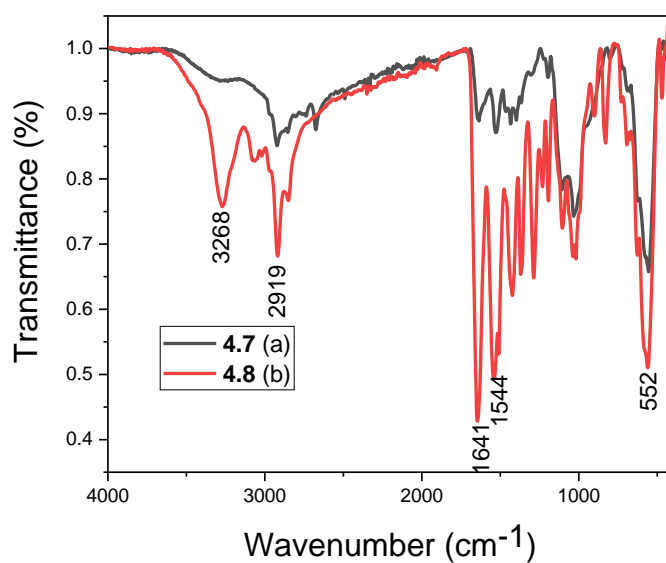


**Figure 4.18:** FTIR spectra of (a)  $Fe_3O_4$ @initiator 4.12 (4.7) (black) (b)  $Fe_3O_4$ @initiator@amide 2.38 (4.8) (red)

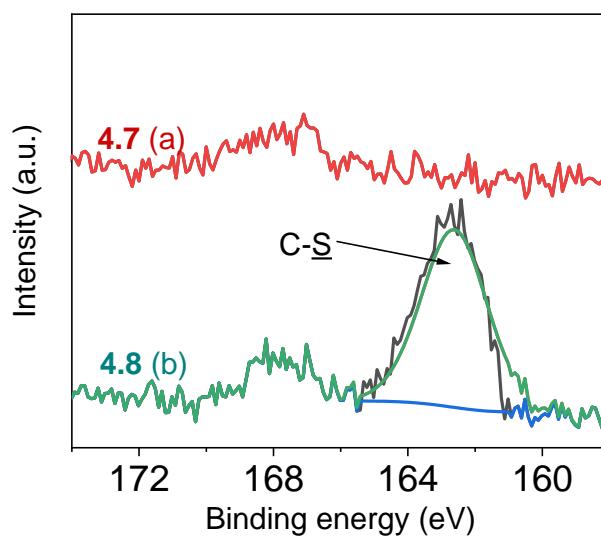


**Figure 4.19:** XPS spectra of core level scans for S 2p in (a)  $Fe_3O_4$ @initiator 4.12 (4.7) (red) and (b)  $Fe_3O_4$ @initiator@amide 2.38 (4.8) (green)

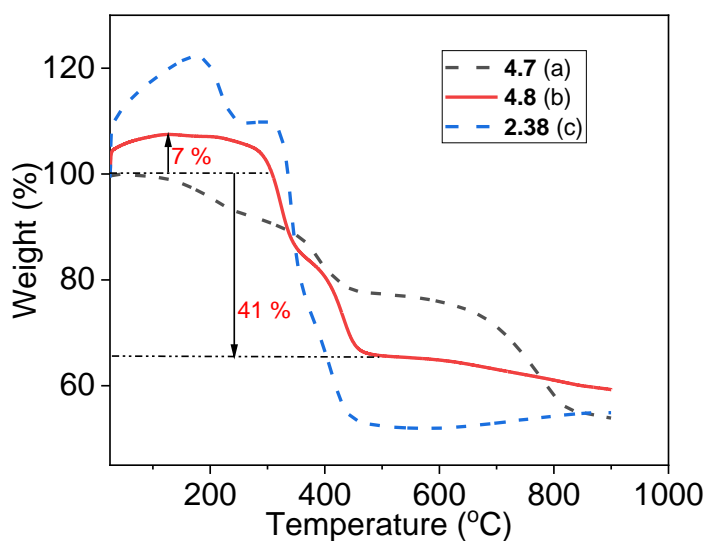


**Figure 4.20:** TGA thermogram of (a) Fe<sub>3</sub>O<sub>4</sub>@initiator 4.12 (4.7) (black dashed) and (b) Fe<sub>3</sub>O<sub>4</sub>@initiator@amide 2.38 (4.8) (red) (c) amide 2.38 (blue dashed) (Atmosphere: Nitrogen, Heating rate: 10 °C/min)

### 4.3.5 Selective Ag<sup>+</sup> extraction using Fe<sub>3</sub>O<sub>4</sub>@oleate (4.9), Fe<sub>3</sub>O<sub>4</sub>@initiator 4.12 (4.7), and Fe<sub>3</sub>O<sub>4</sub>@initiator@amide 2.38 (4.8)

The initial aim was to prepare a novel magnetic extractant nanoparticle with high efficiency and selectivity for Ag<sup>+</sup> extraction in low pH media. The novel extractant nanoparticle **4.8** (Figure 4.21) was designed with this aim in mind and was tested for its Ag<sup>+</sup> extraction efficiency and selectivity. This was undertaken by introducing 10 mg of the nanoparticle **4.8** into a 10 mL tenary metal solution containing *ca.* 5 ppm each of Cu<sup>2+</sup>, Ag<sup>+</sup> and Pb<sup>2+</sup>. As a control, the efficiencies of the precursors - **4.9** and **4.7** were also measured (see experimental section for detailed protocol).

The extraction efficiency was determined by the following equation;

$$\% EE = \frac{C_i - C_f}{C_i} \times 100 \quad 2.1$$

Where % *EE* is percentage extraction efficiency, *C<sub>i</sub>* and *C<sub>f</sub>* in ppm are initial and final Ag<sup>+</sup> concentration respectively.

The extraction efficiency was determined by the equation 4.3 above. The selectivity factor was determined by the following equation<sup>208</sup>;

$$K_{\text{Ag}^+/\text{M}^{n+}} = \frac{K_{\text{d}}^{\text{Ag}^+}}{K_{\text{d}}^{\text{M}^{n+}}} \quad 4.3$$

$$K_{\text{d}} = \frac{(C_i - C_f)v}{mC_f} \quad 4.4$$

$K_{\text{d}}$  = distribution ratio,  $C_i$  and  $C_f$  are initial and final metal ion concentration (in ppm),  $v$  is volume of aqueous solution in mL,  $m$  is mass of extractant (in mg).

As expected, the oleate-coated nanoparticle **4.9** demonstrated very poor efficiency ( $0.9 \pm 1.3$  %) and selectivity ( $K_{\text{Ag}^+/\text{Cu}^{2+}} = 1.8$ ,  $K_{\text{Ag}^+/\text{Pb}^{2+}} = 1.8$ ) for Ag<sup>+</sup> extraction, attributed to the absence of appropriate donor groups on its surface (see Figure 4.22 and Table 4.3 below). Surprisingly, the initiator coated nanoparticle **4.7** was observed to demonstrate the same excellent efficiency (100 %) and in fact better selectivity for Ag<sup>+</sup> extraction than the ‘designed’ Ag<sup>+</sup> ligand **2.38** functionalized extractant nanoparticle **4.8** ( $K_{\text{Ag}^+/\text{Cu}^{2+}}$ , **4.7** = 333.3 vs **4.8** = 62.5 and  $K_{\text{Ag}^+/\text{Pb}^{2+}}$ , **4.7** = 625 vs **4.8** = 125) (Figure 4.22 and Table 4.3). The efficiencies of **4.7** and **4.8** nanoparticles for Ag<sup>+</sup> extraction may be attributed to the presence of the *N*- donor of the amides in both and the *Br*- and *S*- donors respectively.<sup>204</sup> It is unclear why amide **4.7** is more selective for Ag<sup>+</sup> than **4.8**. In terms of the HSAB principle, *S*- is a softer donor than *Br*-, with the implication that **4.8** should be more selective for Ag<sup>+</sup> than **4.7**. Apparently, this was not observed, leading to the conclusion that other factors in addition to the hard/soft principle may be responsible for the results observed.

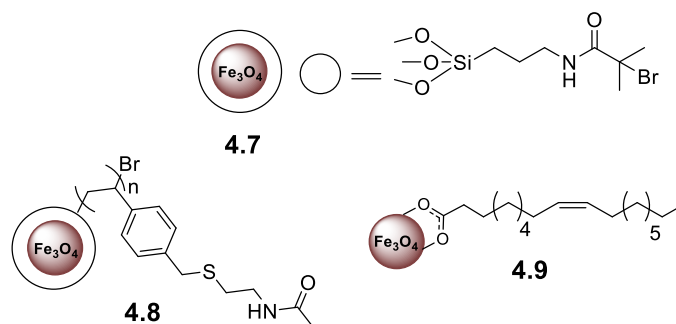


Figure 4.21: Structures of nanoparticles 4.7 - 4.9

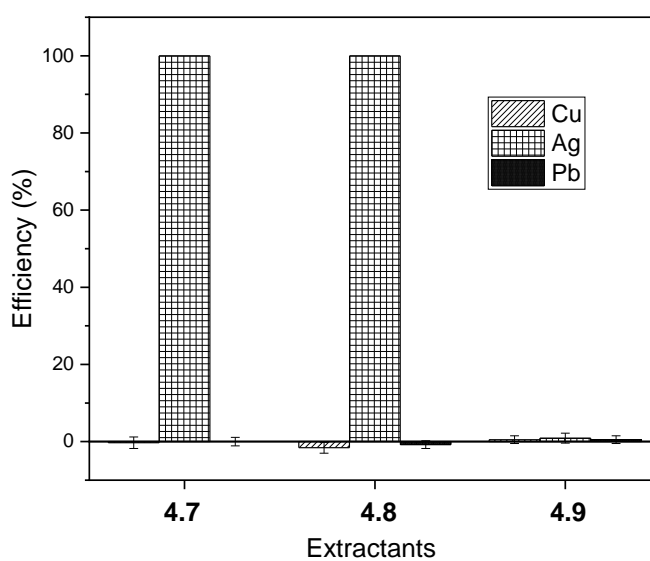


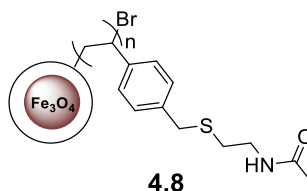
Figure 4.22: ICP-OES data showing metal extraction efficiencies by magnetic nanoparticles 4.7 - 4.9.

Table 4.3: Efficiency and selectivity of nanoparticles 4.7 - 4.9 for  $Ag^+$  extraction

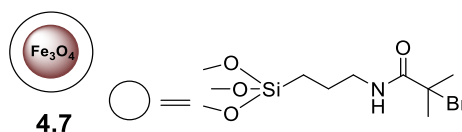
Nanoparticle	Efficiency (%)	$K_{Ag^+}/Cu^{2+}$	$K_{Ag^+}/Pb^{2+}$
4.7	100±0.0	333.3	625
4.8	100±0.0	62.5	125
4.9	0.9±1.3	1.8	1.8

## 4.4 Summary of results.

- The novel Ag<sup>+</sup> selective nanoparticle **4.8** was prepared by a free radical process after a surface-initiated atom transfer radical polymerization (SI-ATRP) route failed.



- The failure of the attempted SI-ATRP route was found to be due to the trapping by chelation of the Cu<sup>+</sup> by the amide **2.38**
- The nanoparticle - Fe<sub>3</sub>O<sub>4</sub>@initiator **4.12** (**4.7**) was found to be similarly efficient, but more selective than the Fe<sub>3</sub>O<sub>4</sub>@initiator@amide **2.38** (**4.8**) in the extraction of Ag<sup>+</sup>.



**Chapter 5: Synthesis and application of core-shell  
Fe<sub>3</sub>O<sub>4</sub>/imidazolium chloride Ag<sup>+</sup> ligand  
nanoparticle**

## 5.1 Introduction

After initial unsuccessful attempts to link amide **2.38** to a magnetic nanoparticle by the SI-ATRP route (see Chapter 4), alternative core-shell magnetic nanoparticles bearing Ag<sup>+</sup> selective ligands were sought. This led us back to the work by Abdolmohammad-Zadeh and Javan<sup>164</sup> (discussed in section 4.1) where the core-shell Mn<sub>3</sub>O<sub>4</sub>@SiO<sub>2</sub>@siloxymidazolium chloride (Mn<sub>3</sub>O<sub>4</sub>@SiO<sub>2</sub>@SIC) nanoparticle **5.1** (Figure 5.1) was observed to demonstrate excellent efficiency (at least 96 %) for Ag<sup>+</sup> in the presence of interfering metal ions like K<sup>+</sup>, Ca<sup>2+</sup>, Pb<sup>2+</sup> and Cu<sup>2+</sup>. Noticing that Abdolmohammad-Zadeh and Javan<sup>164</sup> undertook optimization studies only for the pH parameter in the extraction of Ag<sup>+</sup> from a unary solution (solution containing only one metal ion) and because understanding the pH extraction profile is important for potential applications, an opportunity was seen to extend this pH study to a ternary solution containing Cu<sup>2+</sup>, Pb<sup>2+</sup> and the metal of interest – Ag<sup>+</sup>. Also, while they employed Mn<sub>3</sub>O<sub>4</sub> as the core of nanoparticle **5.1**, an opportunity was seen to improve on the magnetic response of the nanoparticle by having a Fe<sub>3</sub>O<sub>4</sub> core.<sup>248</sup> While the nanoparticle Fe<sub>3</sub>O<sub>4</sub>@SiO<sub>2</sub>@siloxymidazolium chloride (Fe<sub>3</sub>O<sub>4</sub>@SiO<sub>2</sub>@SIC) **5.2**<sup>249–255</sup> (Figure 5.1) had been previously synthesized by different researchers, no study was found where optimum conditions for the selective extraction of Ag<sup>+</sup> from a ternary aqueous metal solution by the nanoparticle **5.2** was undertaken.

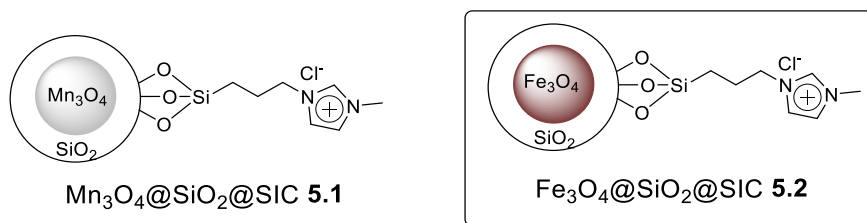


**Figure 5.1: Core-shell magnetic/imidazolium Ag<sup>+</sup> ligand nanoparticles**

## 5.2 Aims and objectives

The main aim described in this chapter is the synthesis of the core-shell iron oxide/imidazolium-based Ag<sup>+</sup> ligand extractant nanoparticle (Fe<sub>3</sub>O<sub>4</sub>@SiO<sub>2</sub>@SIC) **5.2** (Figure

5.2) and the investigation of optimum conditions (pH, contact time, extractant dose and stripping agent) for the extraction of  $\text{Ag}^+$  by the nanoparticle 5.2.

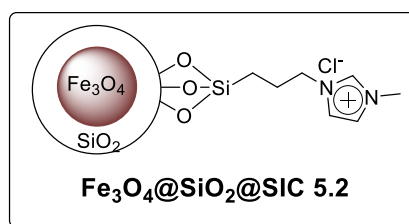
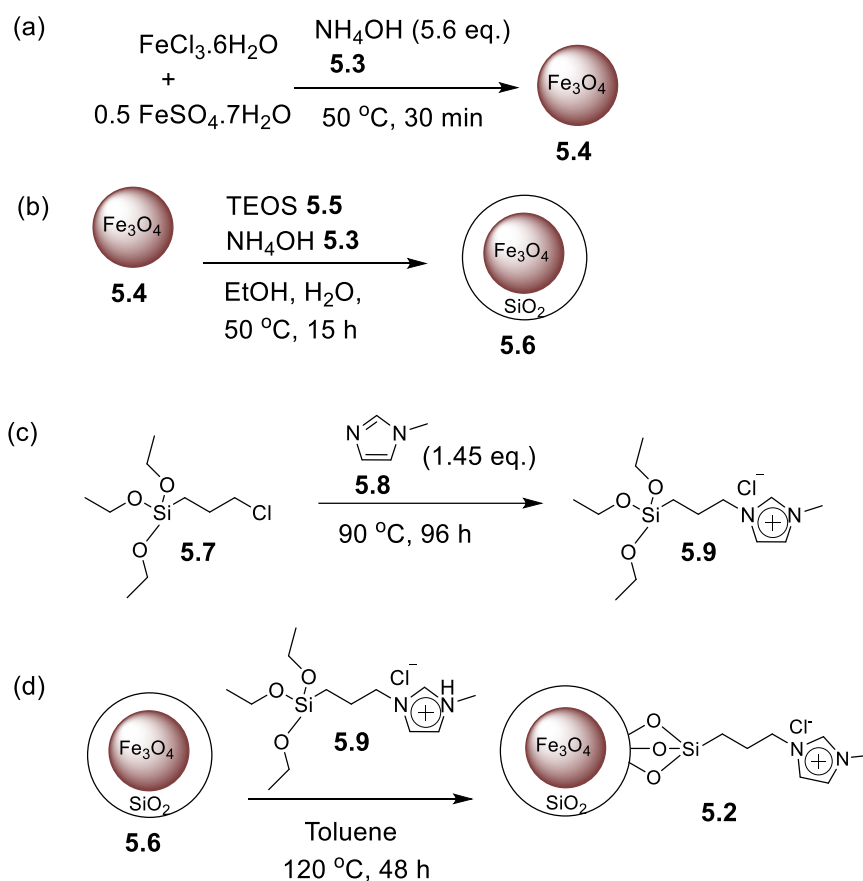


Figure 5.2: Core-shell iron oxide/imidazolium-based  $\text{Ag}^+$  extractant composite nanoparticle ( $\text{Fe}_3\text{O}_4@SiO_2@SIC$ ) 5.2

## 5.3 Results and discussion

### 5.3.1 Synthesis of core-shell iron oxide/imidazolium-based $\text{Ag}^+$ extractant nanoparticle ( $\text{Fe}_3\text{O}_4@SiO_2@SIC$ ) 5.2



Scheme 5.1: Synthesis of (a) bare  $\text{Fe}_3\text{O}_4$  (5.4) (b)  $\text{Fe}_3\text{O}_4@SiO_2$  (5.6) (c) Triethoxysilylpropylimidazolium chloride (5.9) and (d)  $\text{Fe}_3\text{O}_4@SiO_2@SIC$  (5.2)

The synthesis of the Fe<sub>3</sub>O<sub>4</sub>@SiO<sub>2</sub>@SIC **5.2** was achieved over four steps (see Scheme 5.1 above). In the first step, a mixture of FeSO<sub>4</sub> and FeCl<sub>3</sub> was treated with aqueous ammonia **5.3** at 50 °C for half an hour in water to give a black solid identified by XRD (Figure 5.3 below) as Fe<sub>3</sub>O<sub>4</sub> **5.4** particles (Scheme 5.1a).<sup>256</sup> The implication of this to this study is that the recovery of a nanoparticle with a Fe<sub>3</sub>O<sub>4</sub> core is easier than that with a Mn<sub>3</sub>O<sub>4</sub> core since the former has a higher magnetic response than the latter.<sup>248</sup> Subsequently, the Fe<sub>3</sub>O<sub>4</sub> **5.4** particles were coated with SiO<sub>2</sub> by warming a mixture of the former, tetraethoxysilane (TEOS) **5.5** and aqueous ammonia **5.3** in water and ethanol for 15 h to give Fe<sub>3</sub>O<sub>4</sub>@SiO<sub>2</sub> **5.6** (Scheme 5.1b).<sup>257</sup> Coating of the Fe<sub>3</sub>O<sub>4</sub> with SiO<sub>2</sub> was important for a number of reasons including; the protection of the Fe<sub>3</sub>O<sub>4</sub> **5.4** particles from degradation (for example in low pH media) and for provision of an appropriate surface chemistry for subsequent surface modification.<sup>125</sup> In a separate set-up, a mixture of triethoxysilylpropyl chloride **5.7** and 1-methyl imidazole **5.8** were heated (at 90 °C) for 4 days to give the triethoxysilylpropylimidazolium chloride **5.9** (Scheme 5.1c).<sup>164</sup> The synthesis of the **5.9** is important as it is the component of the nanoparticle **5.2** responsible for selective Ag<sup>+</sup> extraction.<sup>164</sup> Finally, a toluene solution of **5.9** was added to a sonicated toluene solution of the Fe<sub>3</sub>O<sub>4</sub>@SiO<sub>2</sub> **5.6** after which the resulting mixture was refluxed in toluene for 2 days to give Fe<sub>3</sub>O<sub>4</sub>@SiO<sub>2</sub>@SIC **5.2** (Scheme 5.1c).<sup>258</sup>

In addition to identification of the Fe<sub>3</sub>O<sub>4</sub> **5.4**, the x-ray diffractogram (using the peak with the highest intensity - 311) was employed alongside the Scherrer equation<sup>241</sup> to determine the particle size of the Fe<sub>3</sub>O<sub>4</sub> **5.4** as 10.0±0.3 nm (detailed calculation provided in experimental section).

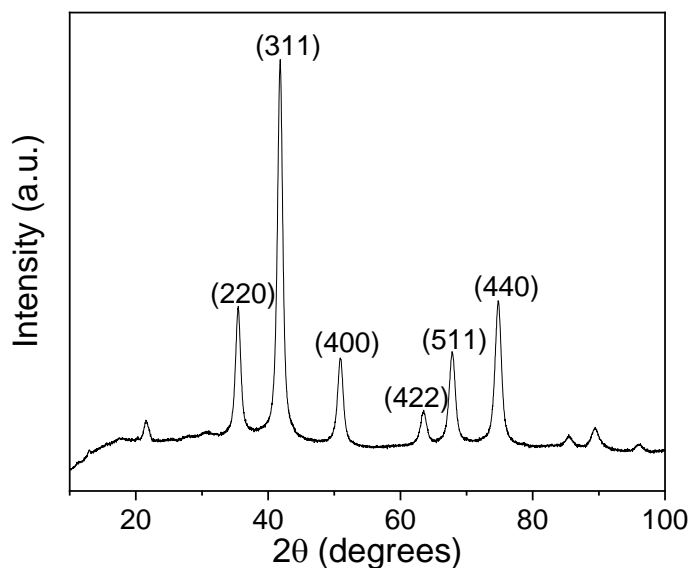


**Figure 5. 3: X-ray diffractogram of bare Fe<sub>3</sub>O<sub>4</sub> (Co K $\alpha$  source wavelength = 1.79 Å, voltage = 40 kV, current = 40 mA)**

The difference between the particle size of Fe<sub>3</sub>O<sub>4</sub> **5.4** (10.0±0.3 nm) obtained after XRD and that obtained after TEM analysis (13.5±2.8 nm, average of 100 particles) (see Figure 5.4b below) was attributed to error associated with manual sizing of the particles using the TEM micrograph, where the Fe<sub>3</sub>O<sub>4</sub> **5.4** appear as roughly spherical and aggregated particles (Figure 5.4a). Aggregation of bare Fe<sub>3</sub>O<sub>4</sub> nanoparticles is not uncommon and it has been explained that bare Fe<sub>3</sub>O<sub>4</sub> particles aggregate in order to reduce their surface energy.<sup>259</sup> As expected, the Fe<sub>3</sub>O<sub>4</sub>@SiO<sub>2</sub> **5.6** (Figure 5.4c) and Fe<sub>3</sub>O<sub>4</sub>@SiO<sub>2</sub>@SIC **5.2** particles (Figure 5.4e) are bigger than the Fe<sub>3</sub>O<sub>4</sub> **5.4** with average sizes of 19.3±3.0 (Figure 5.4d) and 18.5±3.1 nm (Figure 5.4f) respectively. Only about 50 particles of the nanoparticles **5.6** and **5.2** could be sized due to the high amounts of aggregation of these particles. The aggregation observed for the Fe<sub>3</sub>O<sub>4</sub>@SiO<sub>2</sub> **5.6** (Figure 5.4c) particles has been attributed to the increase in ionic strength of the reaction medium as a result of the hydrolysis and condensation of the TEOS **5.5** units.<sup>260</sup> On the other hand, aggregation observed for the Fe<sub>3</sub>O<sub>4</sub>@SiO<sub>2</sub>@SIC **5.2** particles (Figure 5.4e) may have been caused by intermolecular electrostatic attraction between surfaces bearing the ionic liquid **5.9**. Based on the sizes of the Fe<sub>3</sub>O<sub>4</sub> **5.4** and the Fe<sub>3</sub>O<sub>4</sub>@SiO<sub>2</sub> **5.6**, the average thickness

of the silica layer, which appear as grey fringes in the micrograph of the  $\text{Fe}_3\text{O}_4@ \text{SiO}_2$  5.6 (Figure 5.4c) will have been about 6 nm.

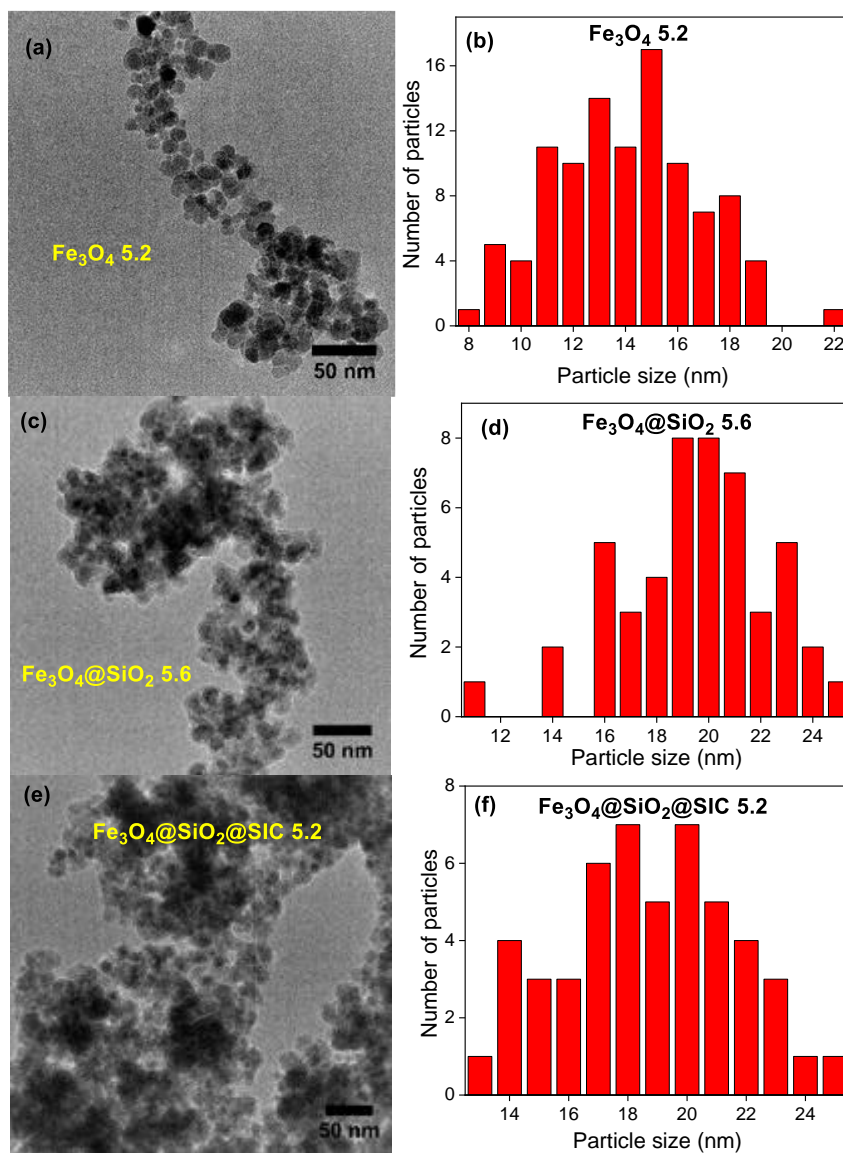


**Figure 5.4:** (a,c,e) Transmission electron micrographs of (a) Bare  $\text{Fe}_3\text{O}_4$  5.4 (b)  $\text{Fe}_3\text{O}_4@ \text{SiO}_2$  5.6 and (c)  $\text{Fe}_3\text{O}_4@ \text{SiO}_2@ \text{SIC}$  5.2, (b,d,f) Histograms showing size distribution of (b) Bare  $\text{Fe}_3\text{O}_4$  5.4 (d)  $\text{Fe}_3\text{O}_4@ \text{SiO}_2$  5.6 and (f)  $\text{Fe}_3\text{O}_4@ \text{SiO}_2@ \text{SIC}$  5.2.

The observed particle sizes indicated that all three nanoparticles are superparamagnetic (being less than 20 nm).<sup>261,262</sup> Indeed, this inference was confirmed from the magnetization curves (Figure 5.5a-c below) obtained after SQUID characterization, where all three nanoparticles had low coercivities<sup>263,243</sup> ( $\text{Fe}_3\text{O}_4$  = 18,  $\text{Fe}_3\text{O}_4@ \text{SiO}_2$  = 21 and  $\text{Fe}_3\text{O}_4@ \text{SiO}_2@ \text{SIC}$  = 22 Oe)

(Figure 5.5). Expectedly, the  $\text{Fe}_3\text{O}_4$  **5.4** had the highest magnetization saturation ( $M_s$ ) value of  $77.60 \pm 0.10$  emu/g. Pleasingly, the  $M_s$  of the  $\text{Fe}_3\text{O}_4@SiO_2$  **5.6** and  $\text{Fe}_3\text{O}_4@SiO_2@SiC$  **5.2** are not significantly different with values of  $50.99 \pm 0.01$  and  $50.30 \pm 0.10$  emu/g respectively, showing that the magnetic response of the  $\text{Fe}_3\text{O}_4@SiO_2$  **5.6** is not significantly reduced after the surface modification. The lower  $M_s$  for **5.6** and **5.2** is attributed to the surface modifications by non-magnetic materials –  $\text{SiO}_2$  and imidazolium **5.9** respectively.<sup>258</sup> In fact, particle **5.2** can be quickly separated from an aqueous solution in about 1 min (Figure 5.5 inset).

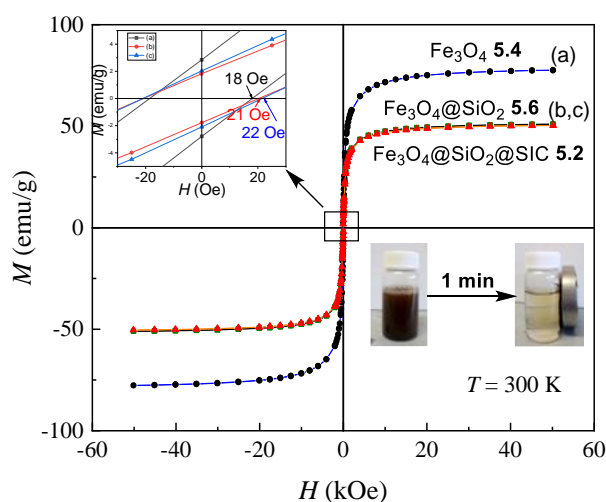


**Figure 5.5: Magnetization curves for (a) Bare  $\text{Fe}_3\text{O}_4$  **5.4** (b)  $\text{Fe}_3\text{O}_4@SiO_2$  **5.6** and (c)  $\text{Fe}_3\text{O}_4@SiO_2@SiC$  **5.2** (Inset: Expanded magnetization curve showing coercivities of bare  $\text{Fe}_3\text{O}_4$  **5.4** (black),  $\text{Fe}_3\text{O}_4@SiO_2$  **5.6** (red),  $\text{Fe}_3\text{O}_4@SiO_2@SiC$  **5.2** (blue), separation of **5.2** from an aqueous solution using a magnet).**

The chemical compositions of these nanoparticles were identified by means of FTIR and XPS. FTIR spectra of all three nanoparticles (Figure 5.6a-c below) contain a peak around  $554\text{ cm}^{-1}$  which was attributed to the Fe-O vibrations in  $\text{Fe}_3\text{O}_4$ .<sup>264</sup> As expected, the spectrum of the  $\text{Fe}_3\text{O}_4@SiO_2$  **5.6** (Figure 5.6b) contains an intense peak at  $1168$  and  $1069\text{ cm}^{-1}$  (attributed to the Si-O-Si stretching vibrations), clearly differentiating it from the spectrum of the bare  $\text{Fe}_3\text{O}_4$  (Figure 5.6a) and suggesting that  $\text{SiO}_2$  has been chemisorbed onto  $\text{Fe}_3\text{O}_4$ .<sup>250,264</sup> While the spectra of the  $\text{Fe}_3\text{O}_4@SiO_2$  **5.6** (Figure 5.6b) and the  $\text{Fe}_3\text{O}_4@SiO_2@SiC$  **5.2** (Figure 5.6c) may look identical, the very weak peak at  $1558\text{ cm}^{-1}$  (attributed to the -C=N stretching vibration)

slightly differentiates them, indicating that the imidazolium **5.9** may have been linked to the Fe<sub>3</sub>O<sub>4</sub>@SiO<sub>2</sub> **5.6**.<sup>265</sup>

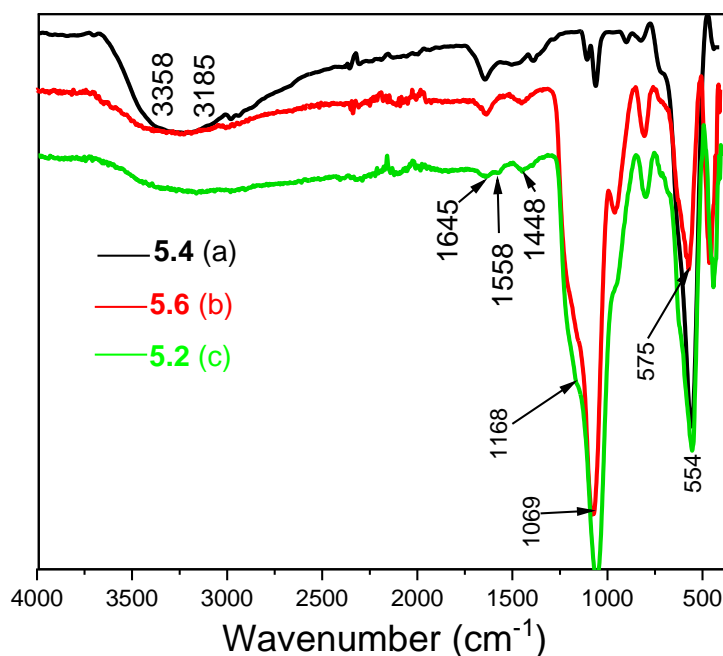


**Figure 5.6:** FTIR spectra of (a) Bare Fe<sub>3</sub>O<sub>4</sub> **5.4** (black) (b) Fe<sub>3</sub>O<sub>4</sub>@SiO<sub>2</sub> **5.6** (red) and (c) Fe<sub>3</sub>O<sub>4</sub>@SiO<sub>2</sub>@SIC **5.2** (green)

Pleasingly, the XPS data confirms the FTIR data about the chemical compositions of all three nanoparticles. For example, the photoelectron lines representing Fe 2p and O 1s at 725/710 and 533 eV respectively can be observed in the survey spectra of all three nanoparticles (see Figure 5.7a – c below).<sup>242</sup> Furthermore, the spectra of the Fe<sub>3</sub>O<sub>4</sub>@SiO<sub>2</sub> **5.6** (Figure 5.7b) is clearly different from that of the Fe<sub>3</sub>O<sub>4</sub> **5.4** (Figure 5.7a) with the presence of extra photoelectron line representing Si 2p at 106 eV, confirming that SiO<sub>2</sub> has been chemisorbed onto the Fe<sub>3</sub>O<sub>4</sub> **5.4**. Indeed, the spectra of the Fe<sub>3</sub>O<sub>4</sub>@SiO<sub>2</sub>@SIC **5.2** (Figure 5.7c) also contains the Si 2p photoelectron line in addition to those of the N 1s, C 1s and Cl 2p at 400, 284.8 and 199 eV respectively, confirming the linkage of the imidazolium **5.9** to the Fe<sub>3</sub>O<sub>4</sub>@SiO<sub>2</sub> **5.6**.<sup>242,266</sup> The photoelectron lines at 284.8 eV (characteristic of the C 1s) in the spectra of all nanoparticles; Fe<sub>3</sub>O<sub>4</sub> **5.4**, Fe<sub>3</sub>O<sub>4</sub>@SiO<sub>2</sub> **5.6** and the Fe<sub>3</sub>O<sub>4</sub>@SiO<sub>2</sub>@SIC **5.2**

nanoparticles is attributed to adventitious carbon.<sup>267</sup> Adventitious carbon refers to carbon impurity which may have entered the sample from the atmosphere for example.<sup>268</sup>

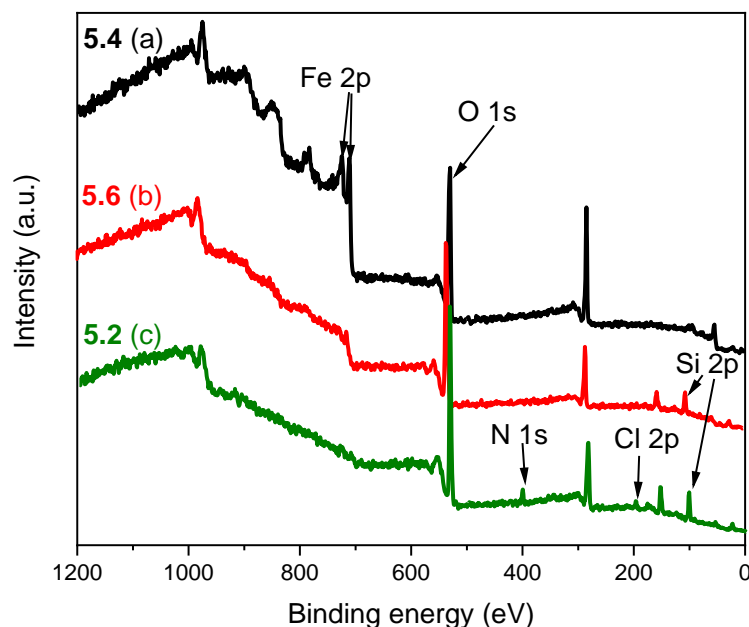


**Figure 5.7: XPS survey spectra of (a) Bare  $\text{Fe}_3\text{O}_4$  5.4 (black) (b)  $\text{Fe}_3\text{O}_4$ @ $\text{SiO}_2$  5.6 (red) and (c)  $\text{Fe}_3\text{O}_4$ @ $\text{SiO}_2$ @SIC 5.2 (green)**

The difference in surface compositions of the  $\text{Fe}_3\text{O}_4$ , **5.4**  $\text{Fe}_3\text{O}_4$ @ $\text{SiO}_2$  **5.6** and  $\text{Fe}_3\text{O}_4$ @ $\text{SiO}_2$ @SIC **5.2** was further highlighted by the different weight loss patterns exhibited by each nanoparticle in the TGA thermogram (see Figure 5.8 below). The weight loss of 4 % for  $\text{Fe}_3\text{O}_4$  **5.4** between 180 and 570 °C was attributed to the loss of trapped water molecules in the  $\text{Fe}_3\text{O}_4$  lattice and perhaps adventitious carbon as well.<sup>269</sup> As expected, the  $\text{Fe}_3\text{O}_4$ @ $\text{SiO}_2$  remained stable losing a meagre 3 % in the entire experimental temperature range. The  $\text{Fe}_3\text{O}_4$ @ $\text{SiO}_2$ @SIC **5.2** lost only 9 % of its weight attributed to the decomposition of the siloxyimidazolium chloride coating.<sup>270</sup> The surface coverage of the imidazolium **5.9** was found to be approximately 2 molecules/ $\text{nm}^2$ .

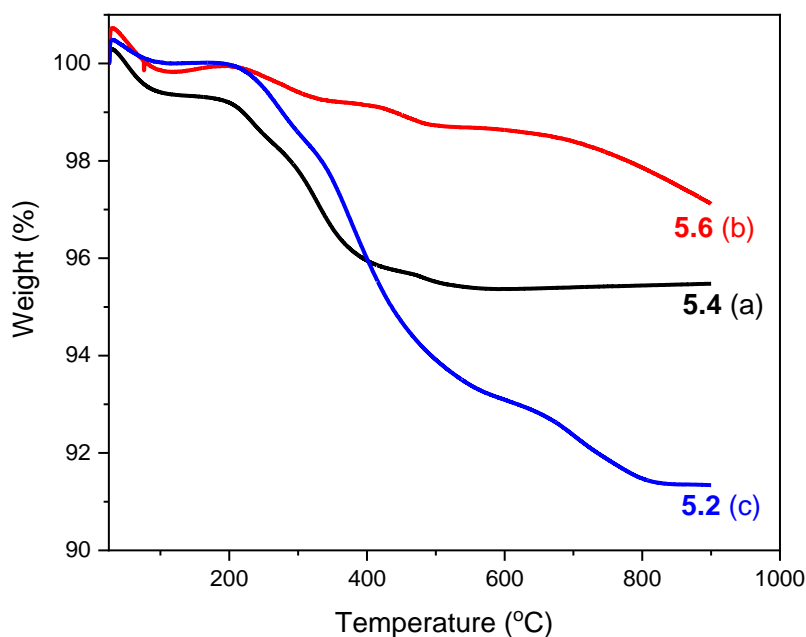


**Figure 5.8:** TGA thermograms for (a) Bare Fe<sub>3</sub>O<sub>4</sub> **5.4** (black) (b) Fe<sub>3</sub>O<sub>4</sub>@SiO<sub>2</sub> **5.6** (red) and (c) Fe<sub>3</sub>O<sub>4</sub>@SiO<sub>2</sub>@SIC **5.2** (blue) (Atmosphere: nitrogen, heating rate: 10 °C/min)

### 5.3.2 Ag<sup>+</sup> extraction studies

#### 5.3.2.1 Control experiment

Prior to the investigation of the optimum conditions for Ag<sup>+</sup> extraction by the Fe<sub>3</sub>O<sub>4</sub>@SiO<sub>2</sub>@SIC **5.2**, it was necessary to establish the imidazolium **5.9** as the molecule responsible for the Ag<sup>+</sup> extraction. Therefore, the Ag<sup>+</sup> extraction efficiencies of the nanoparticles Fe<sub>3</sub>O<sub>4</sub> **5.4**, Fe<sub>3</sub>O<sub>4</sub>@SiO<sub>2</sub> **5.6** and Fe<sub>3</sub>O<sub>4</sub>@SiO<sub>2</sub>@SIC **5.2** were measured by contacting 20 mg of each nanoparticle with 10 mL aqueous solution containing 1 ppm Ag<sup>+</sup> at pH 1 and at room temperature. The extraction efficiency was determined by the following equation;

$$\% EE = \frac{C_i - C_f}{C_i} \times 100 \quad 2.1$$

Where % *EE* is percentage extraction efficiency,  $C_i$  and  $C_f$  in ppm are initial and final Ag<sup>+</sup> concentration respectively.

As expected, the Ag<sup>+</sup> extraction of the three nanoparticles increased in the order; Fe<sub>3</sub>O<sub>4</sub> **5.4** (3.4±0.6 %) < Fe<sub>3</sub>O<sub>4</sub>@SiO<sub>2</sub> **5.6** (5.8±1.5 %) < Fe<sub>3</sub>O<sub>4</sub>@SiO<sub>2</sub>@SIC **5.2** (94.4±0.4 %), with **5.2** demonstrating the highest extraction efficiency (Figure 5.9). The quantitative recovery of Ag<sup>+</sup> by the Fe<sub>3</sub>O<sub>4</sub>@SiO<sub>2</sub>@SIC **5.2** was attributed to the preferential binding of the soft *N*- donor in imidazolium **5.9** to the soft Ag<sup>+</sup> acceptor.<sup>204</sup> Going forward, the nanoparticle Fe<sub>3</sub>O<sub>4</sub>@SiO<sub>2</sub>@SIC **5.2** was employed for the investigation of the optimum conditions for the extraction of Ag<sup>+</sup>.

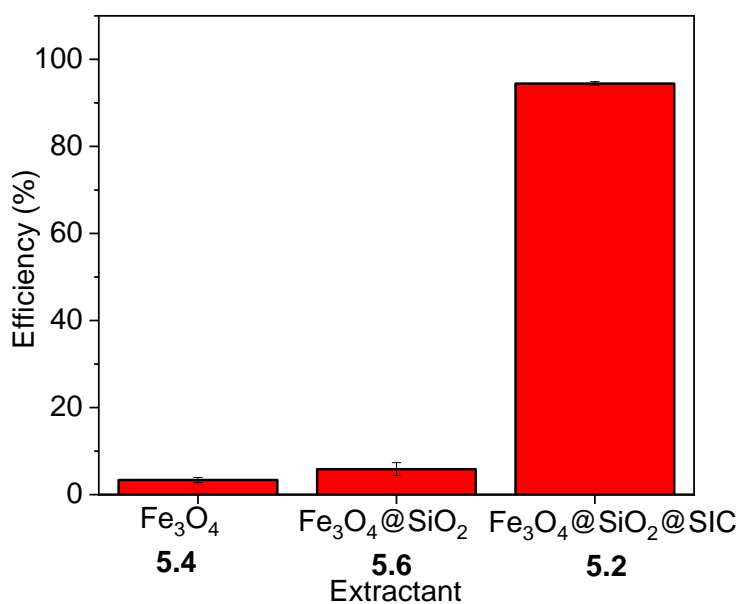


**Figure 5.9:** Extraction efficiencies of bare Fe<sub>3</sub>O<sub>4</sub> **5.4**, Fe<sub>3</sub>O<sub>4</sub>@SiO<sub>2</sub> **5.6** and Fe<sub>3</sub>O<sub>4</sub>@SiO<sub>2</sub>@SIC **5.2** for Ag<sup>+</sup> extraction from aqueous solution. (conditions: [Ag<sup>+</sup>]<sub>0</sub> = 1 ppm, volume = 10 mL, pH = 1.30, contact time = 45 min, temperature = RT, extractant dose = 20 mg).

### 5.3.3 Optimization studies for the selective extraction of Ag<sup>+</sup> by the Fe<sub>3</sub>O<sub>4</sub>@SiO<sub>2</sub>@SIC 5.2 (pH, contact time, nanoparticle extractant dose)

The effect of some conditions (including pH, contact time and extractant dose) on the extraction efficiency and selectivity of the Fe<sub>3</sub>O<sub>4</sub>@SiO<sub>2</sub>@SIC 5.2 for Ag<sup>+</sup> recovery from aqueous solutions also containing competing ions (Cu<sup>2+</sup> and Pb<sup>2+</sup>) were investigated by contacting the extractant 5.2 with 10 mL of aqueous solutions containing *ca.* 2 ppm each of Cu<sup>2+</sup>, Ag<sup>+</sup> and Pb<sup>2+</sup>. As stated in chapter 2, the choice of Cu<sup>2+</sup> and Pb<sup>2+</sup> as competing ions was informed by the knowledge that Ag<sup>+</sup>, usually coexists with Cu<sup>2+</sup> and Pb<sup>2+</sup> in ores and mine tailings, for example.<sup>209</sup> Also, it was stated that very low concentrations of Ag<sup>+</sup>, Cu<sup>2+</sup> and Pb<sup>2+</sup> was employed in this study because Ag<sup>+</sup>, typically exists in very low concentrations in potential Ag<sup>+</sup> repositories of interest.

In a typical extraction study, the Fe<sub>3</sub>O<sub>4</sub>@SiO<sub>2</sub>@SIC 5.2 was introduced into a 10 mL aqueous solution containing 2 ppm each of Cu<sup>2+</sup>, Ag<sup>+</sup> and Pb<sup>2+</sup> inside a screw-capped 30 mL plastic vial. After addition of the nanoparticle to the aqueous solution, the suspension inside the plastic vial was vigorously shaken manually and left for the required duration after which the nanoparticle is magnetically separated (using a magnet) and the supernatant (or raffinate) is collected using a plastic syringe and prepared for metal content determination by means of ICP-OES. The extraction experiments were undertaken in triplicates. The extraction efficiency was determined by the equation 5.1 in section 5.3.2 above. The selectivity factor was determined by the following equation<sup>208</sup>;

$$K_{Ag^+/M^{n+}} = \frac{K_d^{Ag^+}}{K_d^{M^{n+}}} \quad 4.3$$

$$K_d = \frac{(C_i - C_f)v}{mC_f} \quad 4.4$$

K<sub>d</sub> is distribution ratio, C<sub>i</sub> and C<sub>f</sub> are initial and final metal ion concentration respectively (in ppb), v is the volume of aqueous solution in mL, m is the mass of extractant (in mg).

### 5.3.3.1 Effect of pH

The pH is an important parameter usually investigated in metal recovery studies since metal extraction efficiencies have usually been found to be dependent upon pH. In this study, the effect of selectivity for and extraction efficiency of Ag<sup>+</sup> was investigated by varying the pH of the mixed metal aqueous solution from 1 to 5. This pH range was chosen since the efficiency of the extractant low pH was of particular interest because to low pH environments the extractant may be applied to. Interestingly, it was observed that the extraction efficiency of Ag<sup>+</sup> by the Fe<sub>3</sub>O<sub>4</sub>@SiO<sub>2</sub>@SIC **5.2** was dependent on pH. The highest extraction efficiency for Ag<sup>+</sup> (99.2±0.8 %) by **5.2** was obtained at pH 3 (see Figure 5.10 below). Similar studies have reported excellent extraction efficiencies at this pH.<sup>164,203</sup> The quantitative recovery of Ag<sup>+</sup> at this pH (pH 3) can be explained by the HSAB rule with the soft N- donors on the surface of **5.2** preferentially binding to the soft acceptor Ag<sup>+</sup>, despite the competition for binding sites with Ag<sup>+</sup> by H<sub>3</sub>O<sup>+</sup>, Pb<sup>2+</sup> and Cu<sup>2+</sup>.<sup>204</sup> This explanation also helps to understand the quantitative recoveries of Ag<sup>+</sup> at lower pH (pH 1 = 95.5±0.7 %, pH 2 = 97.7±0.7 %) (Figure 5.10). Furthermore, observation of quantitative extraction efficiencies of Ag<sup>+</sup> at very low pH indicates that the extractant **5.2** may be stable at low pH.

The selectivity for Ag<sup>+</sup> over Cu<sup>2+</sup> and Pb<sup>2+</sup> by Fe<sub>3</sub>O<sub>4</sub>@SiO<sub>2</sub>@SIC **5.2** was also observed to be pH dependent. The highest selectivity for Ag<sup>+</sup> over both Cu<sup>2+</sup> and Pb<sup>2+</sup> was observed at pH 3 ( $K_{Ag^+/Cu^{2+}} = 2272.3$  and  $K_{Ag^+/Pb^{2+}} = 928.7$ ) (see Table 5.1 below). It can be observed that the selectivity factor of the adsorbent for Cu<sup>2+</sup> was higher than that for Pb<sup>2+</sup> over the pH range investigated. It is unclear why this was observed. In hard/soft terms Cu<sup>2+</sup> is softer than Pb<sup>2+</sup>, therefore the selectivity for Ag<sup>+</sup> over Pb<sup>2+</sup> should be higher than over Cu<sup>2+</sup> and not the other way around as observed. Other factors such as differential removal by precipitation as Pb and Cu chlorides or electrostatic attraction of the aqua ions; Pb<sub>4</sub>(OH)<sub>4</sub><sup>4+</sup> and Cu(H<sub>2</sub>O)<sub>6</sub><sup>2+</sup> to the Cl<sup>-</sup> in the nanoparticle are unlikely explanations as they both form chlorides and aqua ions readily. It might be related to the average pore size of the nanoparticles (the ionic radius of Pb<sup>2+</sup> is bigger than Cu<sup>2+</sup> (1.27 vs 0.72 Å), but this couldn't be verified as the pore size of the

nanoparticles were not measured. Summarily, the highest extraction efficiency and highest selectivity of Ag<sup>+</sup> were obtained using extractant Fe<sub>3</sub>O<sub>4</sub>@SiO<sub>2</sub>@SIC 5.2 at pH 3.

**Table 5.1: Effect of pH on selectivity of the Fe<sub>3</sub>O<sub>4</sub>@SiO<sub>2</sub>@SIC 5.2 for Ag<sup>+</sup> over Cu<sup>2+</sup> and Pb<sup>2+</sup>**

pH	Ag <sup>+</sup> extraction efficiency	$K_{Ag^+/Cu^{2+}}$	$K_{Ag^+/Pb^{2+}}$
1	95.5±0.7	833.3	240.4
2	97.7±0.7	1428	441.3
3	99.2±0.8	2272.3	928.7
4	95.8±0.7	416.3	142.4
5	96.3±0.7	283.3	61.8

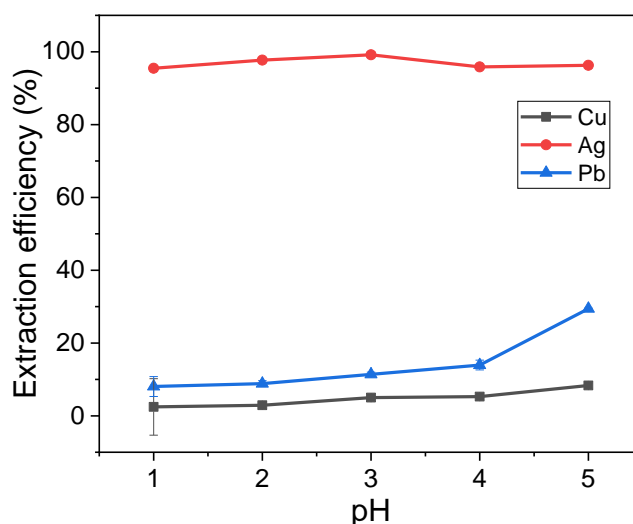


**Figure 5.10: Effect of pH in the selective extraction of Ag<sup>+</sup> from simulated mixed metal aqueous solution by the Fe<sub>3</sub>O<sub>4</sub>@SiO<sub>2</sub>@SIC 5.2 (Conditions: [M<sup>n+</sup>] = 2 ppm, volume = 10 mL, contact time = 2 h, temperature = RT, extractant dose = 10 mg)**

### 5.3.3.2 Effect of contact time

The optimum contact time for the extraction of Ag<sup>+</sup> by the Fe<sub>3</sub>O<sub>4</sub>@SiO<sub>2</sub>@SIC 5.2 was investigated by varying the contact time from 0 to 90 min. A duration of 0 min refers to the situation where the nanoparticle is separated immediately after the extractant had been contacted with the mixed metal aqueous solution. Usually, the magnetic separation of the extractant occurs in less than 2 min.

The extraction efficiency showed no significant difference across the contact time (15-90 min) investigated (Figure 5.11), with the highest and lowest extraction efficiencies being  $96.1 \pm 0.7$  % (75 min) and  $94.9 \pm 0.7$  % (0 min) respectively (Figure 5.11). This observation was attributed to the availability of enough sites on the surface of the  $\text{Fe}_3\text{O}_4@\text{SiO}_2@\text{SIC } 5.2$  for the extraction of  $\text{Ag}^+$  with a rapid reactivity (noting even at 0 minutes 94.9% of  $\text{Ag}^+$  was extracted)<sup>271,272</sup>

The selectivity factor of  $\text{Ag}^+$  over the interfering ions ( $\text{Cu}^{2+}$  and  $\text{Pb}^{2+}$ ) worsens over an increase in the contact time. The highest selectivity factor for  $\text{Ag}^+$  over  $\text{Cu}^{2+}$  and  $\text{Pb}^{2+}$  were observed at 0 and 15 min respectively (Table 5.2 below), with the implication that selective  $\text{Ag}^+$  recovery is favourable for the least duration possible suggesting a kinetically controlled selectivity. The lowest selectivity factor of  $\text{Ag}^+$  over  $\text{Cu}^{2+}$  and  $\text{Pb}^{2+}$  were observed at 90 min, indicating that exchange of metals may be occurring in line with a thermodynamic equilibrium being reached, thus allowance for a lengthy contact time reduces the selective extraction of  $\text{Ag}^+$ .

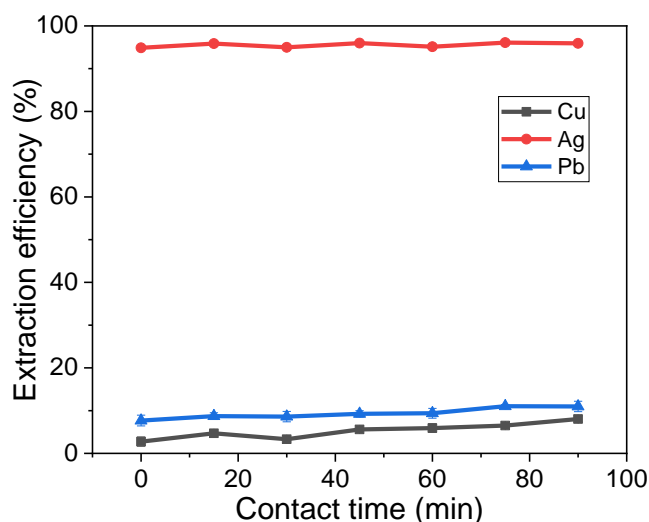


**Figure 5.11:** Effect of contact time in the selective extraction of  $\text{Ag}^+$  from simulated mixed metal aqueous solution by the  $\text{Fe}_3\text{O}_4@\text{SiO}_2@\text{SIC } 5.2$  (Conditions:  $[\text{M}^{n+}] = 2$  ppm, volume = 10 mL, pH = 1.30, temperature = RT, extractant dose = 10 mg).

**Table 5.2: Effect of contact time on selectivity of the Fe<sub>3</sub>O<sub>4</sub>@SiO<sub>2</sub>@SIC 5.2 for Ag<sup>+</sup> over Cu<sup>2+</sup> & Pb<sup>2+</sup>**

Contact time (min)	Ag <sup>+</sup> extraction efficiency	$K_{Ag^+/Cu^{2+}}$	$K_{Ag^+/Pb^{2+}}$
0	94.9±0.7	652.9	223.4
15	95.9±0.7	469.2	241.8
30	95.0±0.7	558.8	201.9
45	96.0±0.7	404.9	235.5
60	95.1±0.7	311.8	190.4
75	96.1±0.7	354.4	196.1
90	96.0±0.7	264.3	186.4

### 5.3.3.3 Effect of Extractant dose

In order to develop an efficient and cost-effective metal extraction system, determination of the optimum dose of the extractant needed is important. Therefore, the effect of extractant (Fe<sub>3</sub>O<sub>4</sub>@SiO<sub>2</sub>@SIC 5.2) dose on efficiency and selectivity of Ag<sup>+</sup> was investigated by varying the amount of the extractant contacted with the mixed metal solution from 5 to 80 mg for 45 min. As expected, extraction efficiency for Ag<sup>+</sup> extraction increased with increasing extractant dose (see Figure 4.12 below). The lowest and highest extraction efficiencies for Ag<sup>+</sup> were observed at the lowest and highest amounts of extractant used (87.0±0.3 % at 5 mg and 99.5±0.1 % for 80 mg of nanoparticle 5.2). The increase of Ag<sup>+</sup> extraction efficiency with increasing extractant 5.2 dosage used is of course due to the increase in the number of sites on nanoparticle 5.2 available for binding Ag<sup>+</sup>. The lowest efficiency observed (87.0±0.3 %) is better than the 85 % extraction efficiency reported by Abdolmohammad-Zadeh and Javan's<sup>164</sup> where a greater amount of a similar extractant (320 mg) was used. This difference was attributed to the higher surface area of the extractant in contact with the aqueous solution in this study compared with that in Abdolmohammad-Zadeh and Javan's<sup>164</sup>, as they confined their extractant in a syringe while in this study, the extractant was dispersed in the mixed metal aqueous solution.

The selectivity factor of Ag<sup>+</sup> over the interfering ions (Cu<sup>2+</sup> and Pb<sup>2+</sup>) was also found to be dependent on extractant dose. From the results presented in Table 5.3 below, the highest

selectivity for  $\text{Ag}^+$  over the interfering ions ( $K_{\text{Ag}^+/\text{Cu}^{2+}} = 4119.9$  and  $K_{\text{Ag}^+/\text{Pb}^{2+}} = 2250.9$ ) was obtained with the highest extractant dose used (80 mg). Conversely, the least selectivity factor for  $\text{Ag}^+$  over the interfering ions ( $K_{\text{Ag}^+/\text{Cu}^{2+}} = 266.6$  and  $K_{\text{Ag}^+/\text{Pb}^{2+}} = 239.1$ ) was obtained with the least adsorbent dose used (5 mg) (Table 5.3). The rationale for this observation was not certain. Kinetics was ruled out as an explanation since the study was undertaken for 45 min which is outside the kinetic range (0 – 15 min) observed from contact time study.

Therefore, in practical terms, the highest purity of  $\text{Ag}^+$  can be extracted from a mixed metal solution containing the ion alongside  $\text{Cu}^{2+}$  and  $\text{Pb}^{2+}$  by using as much  $\text{Fe}_3\text{O}_4@\text{SiO}_2@\text{SIC } 5.2$  as would be commercially possible.

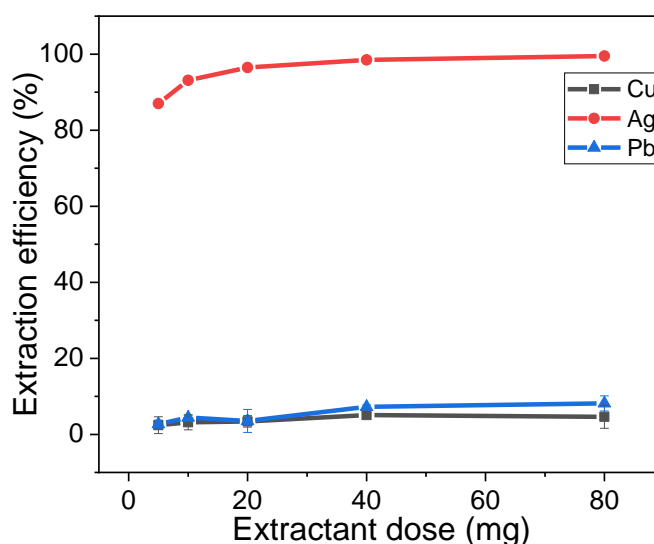


**Figure 5.12:** Effect of extractant dose in the selective extraction of  $\text{Ag}^+$  from simulated mixed metal aqueous solution by the  $\text{Fe}_3\text{O}_4@\text{SiO}_2@\text{SIC } 5.2$  (conditions:  $[\text{M}^{\text{n}+}] = 2$  ppm, volume = 10 mL, pH = 1.30, contact time = 45 min, temperature = RT)

**Table 5.3: Effect of extractant dose on selectivity by the Fe<sub>3</sub>O<sub>4</sub>@SiO<sub>2</sub>@SIC 5.2 for Ag<sup>+</sup> over Cu<sup>2+</sup> and Pb<sup>2+</sup>**

Extractant dose (mg)	Ag <sup>+</sup> extraction efficiency	$K_{Ag^+/Cu^{2+}}$	$K_{Ag^+/Cu^{2+}}$
5	87.0±0.3	266.6	239.1
10	93.1±0.1	410.9	291.9
20	96.5±0.2	776.3	743.1
40	98.5±0.0	1236.7	845.8
80	99.5±0.1	4119.9	2250.9

### 5.3.4 Effect of type of stripping agents

Recovery of the extracted metal ion is an important factor in studies on metal recycling. Furthermore, the choice of an efficient metal recovery (or stripping) agent and establishment of optimum recovery conditions is important in metal recycling studies. Therefore, the effect of the type of the stripping agent on the efficiency of Ag<sup>+</sup> recovery was investigated by contacting aqueous solutions of three different types of stripping agents – HCl (0.6 and 3 M), HNO<sub>3</sub> (0.6 and 3 M) and thiourea (0.6 M) with Ag<sup>+</sup> loaded extractant - Fe<sub>3</sub>O<sub>4</sub>@SiO<sub>2</sub>@SIC 5.2, noting that 3 M thiourea could not be prepared due to the limited solubility in water. The choice of HCl and thiourea for this study was informed by previous work which reported excellent stripping efficiencies of Ag<sup>+</sup> by these stripping agents.<sup>164,200,273,274</sup> The Ag<sup>+</sup> stripping experiment was undertaken by contacting 5 mL of each stripping agent with Ag<sup>+</sup>-laden extractant 5.2 for 1 h without stirring at room temperature inside screw capped plastic vials. At the end of the experiment, the nanoparticles were separated using a magnet and the supernatant (aqueous solution of stripping agent) was collected using a plastic syringe and prepared for ICP-OES analysis. Each stripping experiment was undertaken in triplicates. The % stripping efficiency (SE) of Ag<sup>+</sup> by the stripping agents was determined as follows;

$$\%SE = \frac{C_e}{C_i} \times 100 \quad 5.3$$

Where % SE is percentage stripping efficiency,  $C_e$  represents the concentration of Ag<sup>+</sup> extracted by the stripping agent (Ag<sup>+</sup> concentration in the stripping agent solution) and  $C_i$

represents the initial  $\text{Ag}^+$  concentration respectively (concentration of  $\text{Ag}^+$  in extractant prior to stripping).

Stripping of  $\text{Ag}^+$  from the  $\text{Ag}^+$ -impregnated extractant **5.2** was found to be dependent on the type of stripping agent. As expected, the highest % SE ( $85.4 \pm 1.3$  %) was observed for 0.6 M thiourea and this was attributed to the preference of the soft S- donor atom in thiourea for the soft  $\text{Ag}^+$  acceptor (see Figure 5.13 below).<sup>204</sup> Presumably, a higher % SE could be observed at higher thiourea concentration. Interestingly, 3 M, HCl as found to strip more  $\text{Ag}^+$  than  $\text{HNO}_3$  of the same concentration ( $\text{HCl} = 59.5 \pm 5.5$  % vs  $\text{HNO}_3 = 30.9 \pm 3.4$  %). This could be attributed to the formation of the anionic complex –  $\text{AgCl}_2^-$  at high  $\text{Cl}^-$  concentrations.<sup>164</sup> The % SE observed for both acids at 0.6 M are identical considering their errors.

Generally, an increase in the concentration of the stripping agent (excluding thiourea) resulted in an increase in % SE, but thiourea was the agent of choice.

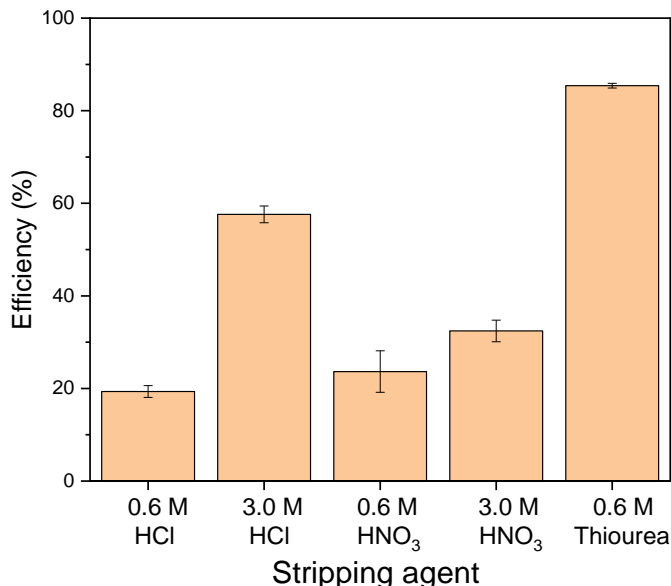
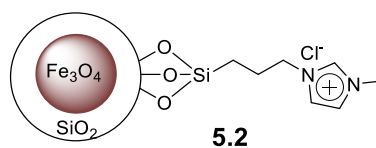


**Figure 5.13:** Effect of stripping agent type and concentration in the stripping of  $\text{Ag}^+$  from impregnated  $\text{Fe}_3\text{O}_4@\text{SiO}_2@\text{SIC 5.2}$  (volume of acid = 5 mL, contact time = 1 h, temperature = RT).

## 5.4 Summary of results

- The extractant Fe<sub>3</sub>O<sub>4</sub>@SiO<sub>2</sub>@SIC **5.2** has been prepared.



- The efficient and selective extraction of Ag<sup>+</sup> from aqueous solution (also containing Cu<sup>2+</sup> and Pb<sup>2+</sup>) by extractant nanoparticle **5.2** was found to be dependent on pH and extractant dose, but independent of contact time after 15 minutes. The most acceptable conditions for efficiency and selectivity were found to occur at pH 3 with a contact time of between 0-15 minutes with the highest loading of extractant nanoparticle **5.2** that would be commercially appropriate (cost implications).
- The highest percentage recovery of Ag<sup>+</sup> from extractant nanoparticle **5.2** was obtained using thiourea (0.6 M) as a stripping agent.

## **Chapter 6: Conclusions and Future work**

## 6.1 Conclusions

In this work, a range of novel Ag<sup>+</sup> ligands including derivatives of **2.10** (a previously reported malonamide derivative), gem diethyl substituted malonamide derivatives and a styrylamide were synthesized and tested for selective Ag<sup>+</sup> recovery. Access to analogues of the malonamide derivative **2.10** was achieved (yields ranging from 12 – 89 %), by a novel route involving the use two equivalents of the precursor amine in order for it to serve as the base catalyst for the amidation reaction. After failed attempts to access a derivative of malonamide **2.10** with only one vinyl tether, the novel styrylamide **2.38**, which could also be potentially linked to a magnetic nanoparticle was accessed over two steps with a yield of 76 %. All Ag<sup>+</sup> ligands synthesized were tested and observed to be selective for Ag<sup>+</sup> as measured by their selectivity coefficients with the methoxy analogue of **2.10** (**2.15**) exhibiting the highest selectivity for Ag<sup>+</sup>. The highest and lowest efficiencies (98.4 and 36.1 %) of Ag<sup>+</sup> recovered were afforded by the divinyl analogue of **2.10** (**2.14**) and the styrylamide **2.38** respectively.

The binding stoichiometries of the Ag<sup>+</sup> complexes separately formed by the malonamide derivative **2.10** and the styrylamide **2.38** were investigated by means of mass spectrometry and <sup>1</sup>H NMR titration (leading to Job's and mole ratio plots). It was observed that the malonamide derivative **2.10** formed a 1:1 complex with Ag<sup>+</sup>. The styrylamide **2.38** was observed to form both 1:1 and 1:2 (Ag<sup>+</sup>:**2.38**) complexes with Ag<sup>+</sup>. The observed stoichiometries of the Ag<sup>+</sup> complexes formed by **2.10** and **2.38** and magnitude of the chemical shifts from the <sup>1</sup>H NMR titrations of the interaction of these ligands with Ag<sup>+</sup> indicated that the malonamide derivative **2.10** may form a tetrahedral complex with Ag<sup>+</sup>, while the styrylamide **2.38** may form both bent linear (for the 1:1 stoichiometry) and tetrahedral (for the 1:2 stoichiometry) complexes with Ag<sup>+</sup>.

The styrylamide **2.38** was successfully linked to a magnetic nanoparticle (Fe<sub>3</sub>O<sub>4</sub>@initiator **4.7**) by the free radical process initiated by AIBN to give Fe<sub>3</sub>O<sub>4</sub>@initiator@amide **2.38** (**4.8**). Interestingly, the precursor nanoparticle **4.7** was observed to demonstrate equal efficiency (100 %) but better selectivity for Ag<sup>+</sup> recovery than the nanoparticle **4.8**.

Finally, optimization studies for  $\text{Ag}^+$  recovery from aqueous solution using a previously reported extractant nanoparticle –  $\text{Fe}_3\text{O}_4@\text{SiO}_2@\text{siloxymidazolium}$  chloride **5.2** and stripping of the  $\text{Ag}^+$  from the impregnated extractant were undertaken. It was observed that the highest amounts of  $\text{Ag}^+$  were recovered when the pH of the ternary aqueous metal solution was 3, the contact time between the extractant and the ternary solution was 75 min and when 80 mg of the extractant nanoparticle was used. The highest amount of  $\text{Ag}^+$  was stripped from an impregnated extractant by 5 mL of a 0.6 M thiourea solution.

## 6.2 Future work

Future work could consider the utilization of micro-sized particles of  $\text{Fe}_3\text{O}_4@\text{initiator}@amide$  **2.38 (4.8)** and the previously reported  $\text{Fe}_3\text{O}_4@\text{SiO}_2@\text{siloxymidazolium}$  chloride **5.2** for  $\text{Ag}^+$  recovery from other  $\text{Ag}^+$  repositories such as mine tailings and metallurgical slag heaps.

## **Chapter 7 : Experimental**

## 7.1 Materials and Instrumentation

Unless otherwise stated, all chemicals and solvents (including anhydrous solvents) employed in the syntheses were purchased from commercial sources and used without further purification. In relevant sections, petroleum ether (40 – 60 °C) was used. Deionized water produced on site was used in all the procedures. Some reactions were monitored by means of TLC, performed on Merck silica gel 60F-254 TLC sheets and visualized either under UV fluorescence (254 nm) or developed by dipping in potassium permanganate solution. Flash chromatography was undertaken using Sigma Aldrich silica gel 60 – 43  $\mu\text{m}$  as the stationary phase.

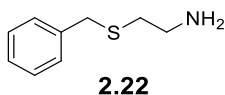
$^1\text{H}$  and  $^{13}\text{C}$  NMR were recorded at room temperature on Bruker<sup>®</sup> Advance av300, hd300 and hd400 spectrometers and all chemical shift values were referenced to TMS in deuterated chloroform ( $\delta = 0$  ppm) unless otherwise stated. Fourier transform infra-red (FTIR) spectra were recorded on Bruker<sup>®</sup> Alpha Platinum-Attenuated Total Reflectance IR spectrometer. Measurements were taken at the mid-IR region. Melting points were recorded on a Stuart<sup>®</sup> SMP10 instrument. All accurate mass spectra were run on a Bruker<sup>®</sup> MaXis mass spectrometer. X-ray diffraction (XRD) data were collected on a Panalytical Empyrean X-ray diffractometer employing a Co  $K\alpha$  radiation at 40 kV and 40 mA. Transmission electron microscopy (TEM) was undertaken on JEOL 2100+ machine operating an acceleration voltage of 200 kV from samples prepared on a copper EM grid. X-ray photoelectron spectroscopy (XPS) data were collected on the Kratos<sup>®</sup> AXIS Ultra DLD spectrometer and take off angle of 90° was used with Al(mono) x-ray source. Metal concentrations were measured by means of a PerkinElmer 5300DV Inductively Coupled Plasma Optical Emission spectrophotometer (ICP-OES). Thermogravimetry analyses (TGA) were undertaken by means of a Metler Toledo<sup>®</sup> DSC1 – STAR at a scan rate of 10 °C/min on samples placed inside 70  $\mu\text{L}$  alumina pans under a nitrogen atmosphere from 25 – 900 °C. Magnetization data were recorded on a quantum design MPM S5S SQUID magnetometer at 300 K.

## 7.2 Experimental for chapter two

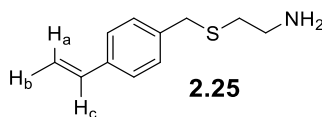
### 7.2.1 General method for synthesis of benzyl cysteamines (2.20 and 2.25 – 2.28)

The benzyl cysteamines **2.22** and **2.25 – 2.28** were synthesized following the method reported by Ghosh and Tochtrop<sup>214</sup>. Briefly, to a stirred water/ethanol (1:3) solution of LiOH (2 eq.) and 2-aminoethanethiolhydrochloride **2.17** (1 eq.) was added dropwise for 5 min, the appropriate benzyl chlorides (1 eq.) and the reaction was left to stir at 35 °C for 20 min (for **2.20**) or 40 min (for **2.25 – 2.28**) after which the solvent was removed *in vacuo*. The crude mixture was extracted with DCM after it had been solubilized with water. The DCM extract was then dried with anhydrous Na<sub>2</sub>SO<sub>4</sub> or MgSO<sub>4</sub>, filtered and concentrated *in vacuo*. All amines except for **2.27** (the fluoro example) were obtained as colourless oils needing no purification. The amine **2.27** was purified from its crude by column chromatography using a mobile phase gradient of 100 % EtOAc to 50 % v/v EtOAc/MeOH.

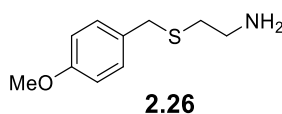
#### 2-(Benzylthio)ethan-1-amine (2.22)



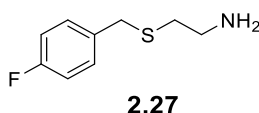
Viscous colourless oil. Yield: 5.76 g (86 %),  $\nu(\text{cm}^{-1})$  3363, 3279 (N-H stretch), 1600 (N-H bend), <sup>1</sup>H NMR (400 MHz, CDCl<sub>3</sub>)  $\delta$  7.39 – 7.18 (m, 5H, ArH), 3.70 (s, 2H, PhCH<sub>2</sub>S), 2.81 (t, *J* = 6.5 Hz, 2H, SCH<sub>2</sub>CH<sub>2</sub>), 2.51 (t, *J* = 6.5 Hz, 2H, SCH<sub>2</sub>CH<sub>2</sub>), 1.29 (s, 2H, CH<sub>2</sub>CH<sub>2</sub>NH<sub>2</sub>)  
<sup>13</sup>C NMR (100 MHz, CDCl<sub>3</sub>) 138.5, 128.9, 128.6 and 127.1 (ArC), 40.9 (CH<sub>2</sub>CH<sub>2</sub>NH<sub>2</sub>), 36.0 (PhCH<sub>2</sub>S), 35.7 (SCH<sub>2</sub>CH<sub>2</sub>); *m/z* (ESI) [M+H]<sup>+</sup> 168.

**2-((4-Vinylbenzyl)thio)ethan-1-amine (2.25)**

Viscous yellow oil. Yield: 5.87 g (77 %),  $\nu(\text{cm}^{-1})$  3365, (N-H stretch), 1627, 1567 (N-H bend),  $^1\text{H NMR}$  (300 MHz,  $\text{CDCl}_3$ )  $\delta$  7.36 (d,  $J = 8.0$  Hz, 2H, ArH), 7.27 (d,  $J = 8.0$  Hz, 2H, ArH), 6.70 (dd,  $J = 17.5, 11.0$  Hz, 1H,  $\text{CH}_2\text{CHPh}$ ), 5.73 (d,  $J = 17.5$  Hz, 1H,  $\text{CH}_a\text{H}_b\text{CHPh}$ ), 5.23 (d,  $J = 11.0$  Hz, 1H,  $\text{CH}_a\text{H}_b\text{CHPh}$ ), 3.69 (s, 2H,  $\text{PhCH}_2\text{S}$ ), 2.82 (t,  $J = 6.0$  Hz, 2H,  $\text{CH}_2\text{CH}_2\text{NH}_2$ ), 2.51 (t,  $J = 6.0$  Hz, 2H,  $\text{SCH}_2\text{CH}_2$ ), 1.29 (s, 2H,  $\text{CH}_2\text{CH}_2\text{NH}_2$ ),  $^{13}\text{C NMR}$  (75 MHz,  $\text{CDCl}_3$ )  $\delta$  138.1 and 136.5 (ArC), 136.4 ( $\text{CH}_2\text{CHPh}$ ), 129.1 and 126.5 (ArC), 113.9 ( $\text{CH}_2\text{CHPh}$ ), 41.0 ( $\text{CH}_2\text{CH}_2\text{NH}_2$ ), 35.8 ( $\text{PhCH}_2\text{S}$ ), 35.7 ( $\text{SCH}_2\text{CH}_2$ ),  $m/z$  (ESI) for  $[\text{C}_{11}\text{H}_{16}\text{NS}]^+$  calculated; 194.1003, found 194.0998.

**2-((4-Methoxybenzyl)thio)ethan-1-amine (2.26)**

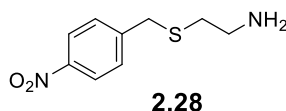
Viscous colourless oil. Yield: 4.37 g (88 %),  $\nu(\text{cm}^{-1})$ : 3261 (N-H stretch), 1663 (N-H bend),  $^1\text{H NMR}$  (400 MHz,  $\text{CDCl}_3$ )  $\delta$  7.23 (d,  $J = 8.5$  Hz, 2H and 6.84 (d,  $J = 8.5$  Hz, 2H) (ArH), 3.79 (s, 3H,  $\text{CH}_3\text{OPh}$ ), 3.67 (s, 2H,  $\text{PhCH}_2\text{S}$ ), 2.85 (t,  $J = 6.5$  Hz, 2H,  $\text{CH}_2\text{CH}_2\text{NH}_2$ ), 2.71 (s, 2H,  $\text{CH}_2\text{CH}_2\text{NH}_2$ ), 2.55 (t,  $J = 6.5$  Hz, 2H,  $\text{SCH}_2\text{CH}_2$ ).  $^{13}\text{C NMR}$  (100 MHz,  $\text{CDCl}_3$ )  $\delta$  159.0, 130.2, 130.0 and 114.1 (ArC), 55.4 ( $\text{CH}_3\text{OPh}$ ), 40.5 ( $\text{CH}_2\text{CH}_2\text{NH}_2$ ), 35.4 ( $\text{PhCH}_2\text{S}$ ), 34.5 ( $\text{SCH}_2\text{CH}_2$ ),  $m/z$  (ESI)  $[\text{M}+\text{H}]^+$  198.

**2-((4-Fluorobenzyl)thio)ethan-1-amine (2.27)**

Viscous colourless oil. Yield: 4.27 g (85 %),  $\nu(\text{cm}^{-1})$ : 3365 (N-H stretch), 1599 (N-H bend),  $^1\text{H NMR}$  (400 MHz,  $\text{CDCl}_3$ )  $\delta$  7.35 – 7.23 (dd, 2H,  $J_{\text{HCCH}} = 9$  Hz,  $J_{\text{HCCCH}} = 3$  Hz, ArH), 7.06 –

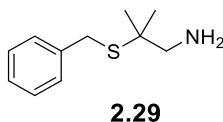
6.96 (t, 2H,  $J_{\text{HCCF}} = 15$  Hz, ArH), 3.68 (s, 2H, PhCH<sub>2</sub>S), 2.82 (t,  $J = 6.5$  Hz, 2H, CH<sub>2</sub>CH<sub>2</sub>NH<sub>2</sub>), 2.51 (t,  $J = 6.5$  Hz, 2H, SCH<sub>2</sub>CH<sub>2</sub>), 1.33 (s, 2H, CH<sub>2</sub>CH<sub>2</sub>NH<sub>2</sub>), <sup>13</sup>C NMR (100 MHz, CDCl<sub>3</sub>) δ 162 (d,  $J_{\text{CF}}=244$  Hz), 134.2 (d,  $J_{\text{CCCCF}}=3$  Hz), 130.4 (d,  $J_{\text{CCF}}= 8$  Hz) and 115.4 (d,  $J_{\text{CCF}}=21$  Hz) (ArC), 40.9 (CH<sub>2</sub>CH<sub>2</sub>NH<sub>2</sub>), 35.6 (PhCH<sub>2</sub>S), 35.2 (SCH<sub>2</sub>CH<sub>2</sub>),  $m/z$  (ESI): [M+H]<sup>+</sup> 186.

### 2-((4-Nitrobenzyl)thio)ethan-1-amine (2.28)



Yellow oil. Yield: 3.23 g (85 %),  $\nu(\text{cm}^{-1})$ : 3365 (N-H stretch), 1599 (N-H bend), 1367 (N-O stretch), <sup>1</sup>H NMR (300 MHz, CDCl<sub>3</sub>) δ 8.18 (d,  $J = 8.5$  Hz, 2H, ArH), 7.50 (d,  $J = 8.5$  Hz, 2H, ArH), 3.79 (s, 2H, PhCH<sub>2</sub>S), 2.85 (t,  $J = 6.5$  Hz, 2H, CH<sub>2</sub>CH<sub>2</sub>NH<sub>2</sub>), 2.53 (t,  $J = 6.5$  Hz, 2H, SCH<sub>2</sub>CH<sub>2</sub>), 1.38 (s, 2H, CH<sub>2</sub>CH<sub>2</sub>NH<sub>2</sub>), <sup>13</sup>C NMR (75 MHz, CDCl<sub>3</sub>) δ 147.1 (ArC), 146.4 (ArC), 129.7 (ArC), 123.9 (ArC), 40.9 (CH<sub>2</sub>CH<sub>2</sub>NH<sub>2</sub>), 35.8 (PhCH<sub>2</sub>S), 35.6 (SCH<sub>2</sub>CH<sub>2</sub>),  $m/z$  (ESI) [M+H]<sup>+</sup> 213.

### 7.2.2 Synthesis of 2,2-dimethyl-2-benzylthioethyl amine (2.29)



Access to 2,2-dimethyl-2-benzylthioethyl amine **2.29** was achieved by following the method reported by Carroll and coworkers<sup>215</sup> in two steps. In the first step, a mixture of acetone (3.67 mL, 0.05 mol), benzylmearptan (5.90 mL, 0.05 mol), nitromethane (2.71 mL, 0.05 mol) and benzene (18.75 mL) were heated at 100 °C inside a flask fitted with a Dean Stark apparatus (filled with benzene). After 22 h, the crude mixture was left to cool and was washed with 2.0 M HCl and then with water. It was then dried with anhydrous MgSO<sub>4</sub>, concentrated *in vacuo* and purified by flash chromatography using *n*-hexane as eluent to yield 1-(benzylthio)-1,1-dimethylnitroethane **2.30** (2.60 g, 23 %). In the second step, dry ether solution of 1-(Benzylthio)-1,1-dimethylnitroethane **2.30** (1 g, 4.4 mmol) was added to a cold ether solution of LiAlH<sub>4</sub> (4 M, 3.25 mL) inside a 2-necked flask. The mixture was left to stir for another 3

min after which it was transferred to a heating block in order to heat under reflux. The reaction was monitored using TLC (and a mobile phase of; MeOH:EtOAc = 1:1). The reaction now under reflux took place for 100 min. Crude mixture was transferred to a 250 mL flask and a stir bar added. Water and subsequently potassium sodium tartarate (25 mL, 20 %) was added. The mixture was left to stir until all solids dissolved. It was then extracted with ether (20 mL x 3). Purification by flash chromatography (16 – 50 % ethyl acetate: *n*-hexane, ethyl acetate and finally methanol). The solvent was removed *in vacuo* to give 2-(Benzylthio)-2,2-dimethylmethanamine **2.29** as a yellow oil. Yield: (0.60 g, 70%),  $\nu$  (cm<sup>-1</sup>) 3376 (NH), <sup>1</sup>H (300 MHz CDCl<sub>3</sub>) 7.40 – 7.19 (m, 5H, ArH), 3.68 (s, 2H, PhCH<sub>2</sub>S), 2.61 (s, 2H, CH<sub>2</sub>NH<sub>2</sub>), 1.44 (s, 2H, NH<sub>2</sub>), 1.28 (s, 6H, SC(CH<sub>3</sub>)<sub>2</sub>); <sup>13</sup>C (75 MHz, CDCl<sub>3</sub>) 138.5, 129.0, 128.7 and 127.1 (ArC), 51.8 (C(CH<sub>3</sub>)<sub>2</sub>CH<sub>2</sub>NH<sub>2</sub>), 48.9 (C(CH<sub>3</sub>)<sub>2</sub>CH<sub>2</sub>NH<sub>2</sub>), 32.8 (PhCH<sub>2</sub>S), 26.6 (C(CH<sub>3</sub>)<sub>2</sub>CH<sub>2</sub>NO<sub>2</sub>), *m/z* (ESI) [M+H]<sup>+</sup> 196.

### 7.2.3 Attempted syntheses of *N*<sup>1</sup>,*N*<sup>3</sup>-bis(2(benzylthio)ethyl)malonamide derivative **2.10**

#### 7.2.3.1 By microwave irradiation

The synthesis of *N*<sup>1</sup>,*N*<sup>3</sup>-bis(2-(benzylthio)ethyl)malonamide derivative **2.10** was attempted following the method reported by Daubinet and Kaye<sup>203</sup> with the only modification being the use of a laboratory microwave reactor instead of a kitchen microwave. Briefly, a mixture of amine **2.20** (2 eq.) and diethylmalonate **2.21** (1 eq.) was measured into a 10 mL Schlenk-like tube and placed into a laboratory microwave reactor (Emrys Optimizer) and the reaction mixture was heated at varying temperatures (100 – 250 °C) and durations (3.5 to 10 min). At the end of each reaction, the crude mixture was left to cool and a 0.5 mL sample of the crude product was withdrawn for <sup>1</sup>H NMR characterization.

#### 7.2.3.2 Base catalysed route

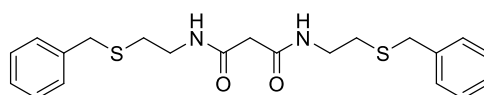
To a stirred solution of amine **2.20** (1.0 g, 5.99 mmol) and pyridine (0.48 mL, 5.99 mmol) in anhydrous THF (51 mL) was added, dropwise, a solution of malonyl chloride (0.29 mL, 2.99 mmol) in anhydrous THF (10 mL) at room temperature. Stirring was stopped after 15 h.

Solvent was removed from the resulting mixture and it was diluted with EtOAc (80 mL) and water (70 mL). This was followed by successive washing with saturated NaHCO<sub>3</sub> (50 mL x 2), 2 M HCl (50 mL x 2), water (50 mL) and brine (50 mL). Finally, the EtOAc extract was dried over anhydrous MgSO<sub>4</sub>, filtered and dried *in vacuo*. Isolation of target malonamide derivative **2.10** was attempted by means of flash chromatography. However, this attempt was unsuccessful.

### 7.2.4 General method for synthesis of malonamide derivatives (2.10 and 2.14 – 2.18)

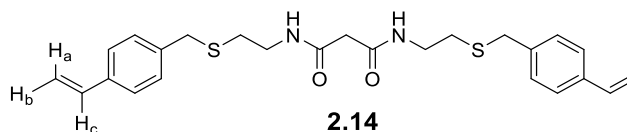
To a stirred solution of an amine (e.g.; **2.20**) (1 eq) in dry THF, malonyl chloride (0.25 eq) solution in dry THF was added dropwise for between 15 – 90 min and the crude mixture was left to stir overnight. The THF solvent was removed from the crude product *in vacuo*, after which water was added. The crude product was extracted with EtOAc, washed successively with HCl (2 M), NaHCO<sub>3</sub>, water and finally brine. It was then dried over Na<sub>2</sub>SO<sub>4</sub> and concentrated *in vacuo* and finally purified by flash chromatography (20% EtOAc/Hexane to 100% EtOAc) to give the desired malonamide derivatives **2.10** and **2.14 – 2.18**.

#### *N*<sup>1</sup>,*N*<sup>3</sup>-Bis(2-(benzylthio)ethyl)malonamide (**2.10**)

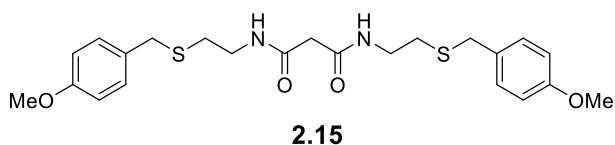


**2.10**

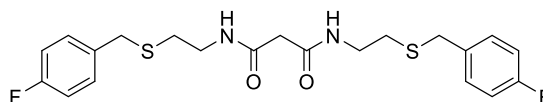
Yellow powder. Yield: 0.21 g (33 %), m.p.: 108 – 112 °C (from Daubinet and Kaye:<sup>203</sup> 105 – 106 °C),  $\nu(\text{cm}^{-1})$ : 3296 (amide N-H stretch), 1647 (amide C=O bend), <sup>1</sup>H NMR (400 MHz, CDCl<sub>3</sub>)  $\delta$  7.40 – 7.19 (m, 10H, ArH), 7.05 (s, 2H, CONHCH<sub>2</sub>), 3.71 (s, 4H, PhCH<sub>2</sub>S), 3.39 (m, 4H, NHCH<sub>2</sub>CH<sub>2</sub>), 3.10 (s, 2H, COCH<sub>2</sub>CO), 2.56 (t, *J* = 6.5 Hz, 4H, CH<sub>2</sub>CH<sub>2</sub>S), <sup>13</sup>C NMR (100 MHz, CDCl<sub>3</sub>)  $\delta$  167.3 (COCH<sub>2</sub>CO), 138.2, 129.0, 128.8 and 127.3 (ArC), 43.1 (COCH<sub>2</sub>CO), 38.5 (NHCH<sub>2</sub>CH<sub>2</sub>), 36.0 (PhCH<sub>2</sub>S), 30.9 (CH<sub>2</sub>CH<sub>2</sub>S), *m/z* (ESI) [M+Na]<sup>+</sup> 425.

***N*<sup>1</sup>,*N*<sup>3</sup>-Bis(2-((4-vinylbenzyl)thio)ethyl)malonamide (2.14)**

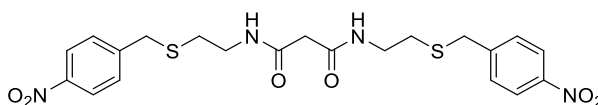
Yellow powder. Yield: 0.09 g (33%), m.p.: 151 – 156 °C,  $\nu(\text{cm}^{-1})$ : 3292 (amide N-H stretch), 1648 (amide C=O bend),  $^1\text{H NMR}$  (400 MHz,  $\text{CDCl}_3$ )  $\delta$  7.36 (d,  $J = 7.5$  Hz, 4H) and 7.27 (d,  $J = 7.5$  Hz, 4H) (ArH), 6.94 (s, 2H,  $\text{CONHCH}_2$ ), 6.69 (dd,  $J = 17.5, 11.0$  Hz, 2H,  $\text{PhCH}_c\text{CH}_a\text{H}_b$ ), 5.73 (d,  $J = 17.5$  Hz, 2H,  $\text{PhCHCH}_a\text{H}_b$ ), 5.24 (d,  $J = 11.0$  Hz, 2H,  $\text{PhCH}_c\text{CH}_a\text{H}_b$ ), 3.70 (s, 4H,  $\text{PhCH}_2\text{S}$ ), 3.40 (m,  $\text{CH}_2\text{CH}_2\text{NH}$ ), 3.11 (s, 2H,  $\text{COCH}_2\text{CO}$ ), 2.56 (t,  $J = 6.5$  Hz, 4H,  $\text{SCH}_2\text{CH}_2$ ),  $^{13}\text{C NMR}$  (100 MHz,  $\text{CDCl}_3$ )  $\delta$  167.2 ( $\text{COCH}_2\text{CO}$ ), 137.7 and 136.8 (ArC), 136.5 ( $\text{CH}_2\text{CHPh}$ ), 129.2 and 126.6 (ArC), 114.1 ( $\text{PhCHCH}_2$ ), 43.1 ( $\text{COCH}_2\text{CO}$ ), 38.4 ( $\text{CH}_2\text{CH}_2\text{NH}$ ), 35.7 ( $\text{CH}_2\text{SCH}_2$ ), 30.8 ( $\text{SCH}_2\text{CH}_2$ ),  $m/z$  (ESI) for  $[\text{C}_{25}\text{H}_{27}\text{N}_2\text{NaO}_2\text{S}_2]^+$  calculated: 477.1646, found: 477.1643.

***N*<sup>1</sup>,*N*<sup>3</sup>-Bis(2-((4-methoxybenzyl)thio)ethyl)malonamide (2.15)**

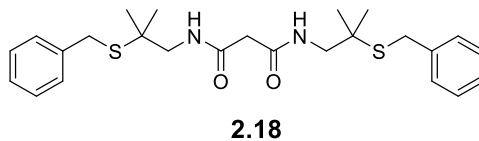
Yellow solid. Yield: 0.43 g (12%), m.p.: 146 – 149 °C,  $\nu(\text{cm}^{-1})$ : 3337 (NH), 1650 (C=O; amide), 1240 (C-O; aromatic ether),  $^1\text{H NMR}$  (300 MHz,  $\text{CDCl}_3$ )  $\delta$  7.24 (d,  $J = 8.5$  Hz, 4H, ArH), 6.97 (s, 2H,  $\text{CH}_2\text{CH}_2\text{NH}$ ), 6.85 (d,  $J = 8.5$  Hz, 4H, ArH), 3.79 (s, 6H,  $\text{CH}_3\text{OPh}$ ), 3.67 (s, 4H,  $\text{PhCH}_2\text{S}$ ), 3.40 (m, 4H,  $\text{CH}_2\text{CH}_2\text{NH}$ ), 3.11 (s, 2H,  $\text{COCH}_2\text{CO}$ ), 2.55 (t,  $J = 6.5$  Hz, 4H,  $\text{SCH}_2\text{CH}_2$ ),  $^{13}\text{C NMR}$  (75 MHz,  $\text{CDCl}_3$ )  $\delta$  167.2 ( $\text{COCH}_2\text{CO}$ ), 158.6 (ArC), 130.1 (ArC), 130.0 (ArC), 114.2 (ArC), 55.4 ( $\text{CH}_3\text{O}$ ), 43.1 ( $\text{COCH}_2$ ), 38.5 ( $\text{CH}_2\text{CH}_2\text{NH}$ ), 35.4 ( $\text{PhCH}_2\text{S}$ ), 30.8 ( $\text{SCH}_2\text{CH}_2$ ),  $m/z$  (ESI) for  $[\text{C}_{23}\text{H}_{30}\text{N}_2\text{NaO}_4\text{S}_2]^+$  calculated: 485.1545, found: 485.1539.

***N*<sup>1</sup>,*N*<sup>3</sup>-Bis(2-((4-fluorobenzyl)thio)ethyl)malonamide (2.16)****2.16**

Yellow powder. Yield: 0.55 g (31%), m.p.: 121 – 123 °C,  $\nu(\text{cm}^{-1})$ : 3296 (amide N-H), 1647 (amide C=O bend),  $^1\text{H NMR}$  (400 MHz,  $\text{CDCl}_3$ )  $\delta$  7.28 (d,  $J_{\text{HCCF}} = 13.5$  Hz, 4H, ArH), 7.18 (s, 2H,  $\text{CH}_2\text{NHCO}$ ), 6.99 (t,  $J = 8.5$  Hz, 4H, ArH), 3.69 (s, 4H,  $\text{PhCH}_2\text{S}$ ), 3.41 (m, 4H,  $\text{CH}_2\text{CH}_2\text{NH}$ ), 3.15 (s, 2H,  $\text{COCH}_2\text{CO}$ ), 2.55 (t,  $J = 6.5$  Hz, 4H,  $\text{SCH}_2\text{CH}_2$ ),  $^{13}\text{C NMR}$  (100 MHz,  $\text{CDCl}_3$ ) 167.3 ( $\underline{\text{COCH}_2\text{CO}}$ ), 165.3 and 160.86 ( $J_{\text{CF}} = 242$ , FArC), 133.8 ( $J_{\text{CCCCF}} = 3$  Hz, ArC), 130.6 and 130.5 (d,  $J_{\text{CCCF}} = 8$  Hz), 115.7 and 115.5 (d,  $J_{\text{CCF}} = 21$  Hz), 43.1 ( $\text{COCH}_2\text{CO}$ ), 38.5 ( $\text{CH}_2\text{CH}_2\text{NH}$ ), 35.2 ( $\text{FPhCH}_2\text{S}$ ), 30.8 ( $\text{CH}_2\text{CH}_2\text{S}$ ),  $m/z$  (ESI) for  $[\text{C}_{21}\text{H}_{24}\text{F}_2\text{N}_2\text{NaO}_2\text{S}_2]^+$  calculated: 461.1145 found: 461.1143.

***N*<sup>1</sup>,*N*<sup>3</sup>-Bis(2-((4-nitrobenzyl)thio)ethyl)malonamide (2.17)****2.17**

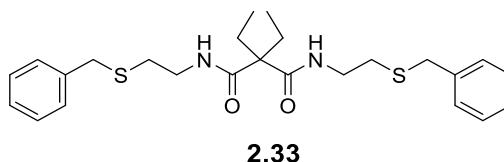
Yellow solid. Yield: 1.22 g (34%), m.p.: 82 – 85 °C,  $\nu(\text{cm}^{-1})$ : 3294 (N-H stretch), 1647 (C=O bend), 1544 and 1367 (N-O stretch),  $^1\text{H NMR}$  (300 MHz,  $\text{CDCl}_3$ )  $\delta$  8.17 (d,  $J = 8.5$  Hz, 4H, ArH), 7.50 (d,  $J = 8.5$  Hz, 4H, ArH), 7.19 (s, 2H,  $\text{CH}_2\text{CH}_2\text{NH}$ ), 3.80 (s, 4H,  $\text{PhCH}_2\text{S}$ ), 3.43 (m, 4H,  $\text{CH}_2\text{CH}_2\text{NH}$ ), 3.16 (s, 2H,  $\text{COCH}_2\text{CO}$ ), 2.58 (t,  $J = 6.5$  Hz, 4H,  $\text{SCH}_2\text{CH}_2$ ).  $^{13}\text{C NMR}$  (75 MHz,  $\text{CDCl}_3$ )  $\delta$  167.3, ( $\underline{\text{COCH}_2}$ ), 147.2 (ArC), 145.9 (ArC), 129.9 (ArC), 124.0 (ArC), 42.9 ( $\text{COCH}_2$ ), 38.4 ( $\text{CH}_2\text{CH}_2\text{NH}$ ), 35.4 ( $\text{PhCH}_2\text{S}$ ), 31.0 ( $\text{SCH}_2\text{CH}_2$ ),  $m/z$  (ESI) for  $[\text{C}_{21}\text{H}_{24}\text{N}_4\text{NaO}_6\text{S}_2]^+$  calculated: 515.1035, found: 515.1029.

***N*<sup>1</sup>,*N*<sup>3</sup>-Bis(2-(benzylthio)-2-methylpropyl)malonamide (2.18)**

Cream solid. Yield: 0.68 g (89 %), m.p.: 71 – 74 °C,  $\nu(\text{cm}^{-1})$ : 3260 (amide N-H stretch), 1663 (amide C=O bend), <sup>1</sup>H NMR (300 MHz, CDCl<sub>3</sub>)  $\delta$  7.40 – 7.20 (m, 10H, ArH), 7.01 (s, 2H, CH<sub>2</sub>NHCO), 3.71 (s, 4H, PhCH<sub>2</sub>S), 3.32 (d, *J* = 6.0 Hz, 4H, C(CH<sub>3</sub>)<sub>2</sub>CH<sub>2</sub>NH), 3.11 (s, 2H, COCH<sub>2</sub>CO), 1.29 (s, 12H, SC(CH<sub>3</sub>)<sub>2</sub>CH<sub>2</sub>), <sup>13</sup>C NMR (75 MHz, CDCl<sub>3</sub>)  $\delta$  167.3 (NHCOCH<sub>2</sub>), 138.3 129.0, 128.8 and 127.2 (ArC), 48.0 (CH<sub>2</sub>NHCO), 46.6 (PhCH<sub>2</sub>S), 43.2 (COCH<sub>2</sub>CO), 33.1 (SC(CH<sub>3</sub>)<sub>2</sub>), 26.8 (SC(CH<sub>3</sub>)<sub>2</sub>), *m/z* (ESI) for [C<sub>25</sub>H<sub>34</sub>N<sub>2</sub>NaO<sub>2</sub>S<sub>2</sub>]<sup>+</sup> calculated: 481.1959 found: 481.1959.

**7.2.5 General method for synthesis of gem-diethyl malonamide (2.33 – 2.37)**

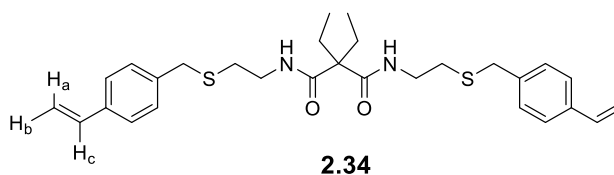
To a stirred solution of amines (e.g.; **2.20**) (1 eq.) and triethylamine (1 eq.) in dry diethyl ether was added diethyl malonyl chloride (0.5 eq) dropwise for between 30 – 90 min and the crude mixture was left to stir overnight. Next, water was added, and the crude product was extracted using diethyl ether. The organic extract was washed successively with HCl (2 M), NaHCO<sub>3</sub>, water and brine and later dried over Na<sub>2</sub>SO<sub>4</sub> and concentrated *in vacuo*. Finally, the crude product was purified by flash chromatography (20% EtOAc/Hexane to 100% EtOAc) to give the desired diethylmalonamides **2.33 – 2.37**.

***N*<sup>1</sup>,*N*<sup>3</sup>-Bis(2-(benzylthio)ethyl)-2,2-diethylmalonamide (2.33)**

Viscous colourless oil. Yield: 1.1 g (54%),  $\nu(\text{cm}^{-1})$ : 3326 (amide N-H stretch), 1630 (amide C=O bend), <sup>1</sup>H NMR (300 MHz, CDCl<sub>3</sub>)  $\delta$  7.42 (s, 2H, CONHCH<sub>2</sub>), 7.38 – 7.12 (m, 10H,

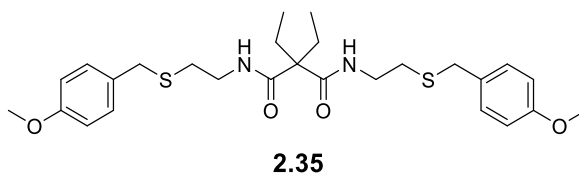
ArH), 3.72 (s, 4H,  $\text{SCH}_2\text{Ph}$ ), 3.41 (m, 4H,  $\text{NHCH}_2\text{CH}_2$ ), 2.57 (t,  $J = 6.5$  Hz, 4H,  $\text{CH}_2\text{CH}_2\text{S}$ ), 1.85 (q,  $J = 7.0$  Hz, 4H,  $\text{CCH}_2\text{CH}_3$ ), 0.82 (t,  $J = 7.0$  Hz, 6H,  $\text{CCH}_2\text{CH}_3$ ),  $^{13}\text{C}$  NMR (75 MHz,  $\text{CDCl}_3$ )  $\delta$  173.2 ( $\text{COC}(\text{CH}_2\text{CH}_3)_2\text{CO}$ ), 138.2, 129.0, 128.7 and 127.3 (ArC), 58.3 ( $\text{COC}(\text{C}_2\text{H}_5)\text{CO}$ ), 38.2 ( $\text{NHCH}_2\text{CH}_2\text{S}$ ), 35.9 ( $\text{CH}_2\text{CH}_2\text{S}$ ), 31.1 ( $\text{SCH}_2\text{Ph}$ ), 30.3 ( $\text{CCH}_2\text{CH}_3$ ), 9.6 ( $\text{CCH}_2\text{CH}_3$ ).  $m/z$  (ESI) for  $[\text{C}_{29}\text{H}_{35}\text{N}_2\text{O}_2\text{S}_2]^+$  calculated: 459.2140 found: 459.2138.

**$N^1, N^3$ -Bis(2-((4-vinylbenzyl)thio)ethyl)-2,2-diethylmalonamide (2.34)**



Colourless gel. Yield: 0.12 g, (83%),  $\nu_{\text{max}}(\text{cm}^{-1})$ : 3323 (amide N-H stretch), 1655 (amide C=O bend),  $^1\text{H}$  NMR (300 MHz,  $\text{CDCl}_3$ )  $\delta$  7.36 (d,  $J = 7.5$  Hz, 4H, ArH and  $\text{CH}_2\text{NHCO}$ ), 7.27 (d,  $J = 7.5$  Hz, 4H, ArH), 6.69 (dd,  $J = 17.5, 11$  Hz, 2H,  $\text{CH}_2\text{CH}_c\text{Ph}$ ), 5.73 (d,  $J = 17.5$  Hz, 2H,  $\text{CH}_a\text{H}_b\text{CHPh}$ ), 5.23 (d,  $J = 11.0$  Hz, 2H,  $\text{CH}_a\text{H}_b\text{CHPh}$ ), 3.71 (s, 4H,  $\text{CH}_2\text{CHPhCH}_2\text{S}$ ), 3.43 (m, 4H,  $\text{CH}_2\text{CH}_2\text{NH}$ ), 2.57 (t,  $J = 6.5$  Hz, 4H,  $\text{SCH}_2\text{CH}_2$ ), 1.85 (q,  $J = 7.5$  Hz, 4H,  $\text{COC}(\text{CH}_2\text{CH}_3)_2$ ), 0.82 (t,  $J = 7.5$  Hz, 6H,  $\text{COC}(\text{CH}_2\text{CH}_3)_2$ ),  $^{13}\text{C}$  NMR (75 MHz,  $\text{CDCl}_3$ )  $\delta$  173.2 ( $\text{COC}(\text{CH}_2\text{CH}_3)_2\text{CO}$ ), 137.8 and 136.7 (ArC), 136.5 ( $\text{CH}_2\text{CHPh}$ ), 129.2 and 126.6 (ArC), 114.0 ( $\text{CH}_2\text{CHPh}$ ), 58.3 ( $\text{COC}(\text{CH}_2\text{CH}_3)_2$ ), 38.2 ( $\text{CONHCH}_2$ ), 35.6 ( $\text{CH}_2\text{CHPhCH}_2\text{S}$ ), 31.1 ( $\text{C}(\text{CH}_2\text{CH}_3)_2$ ), 30.3 ( $\text{SCH}_2\text{CH}_2$ ), 9.6 ( $\text{C}(\text{CH}_2\text{CH}_3)_2$ ),  $m/z$  (ESI) for  $[\text{C}_{29}\text{H}_{36}\text{N}_2\text{O}_2\text{S}_2]^+$  calculated: 511.2453 found: 511.2450.

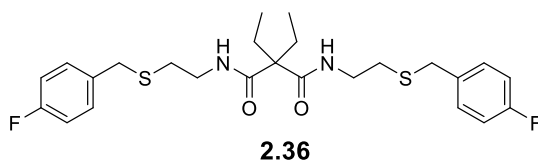
**$N^1, N^3$ -Bis(2-((4-methoxybenzyl)thio)ethyl)-2,2-diethylmalonamide(2.35)**



Viscous colourless oil. Yield: 1.27g (45%),  $\nu$  ( $\text{cm}^{-1}$ ): 3337 (NH), 1650 (C=O; amide), 1240 (C-O; aromatic ether),  $^1\text{H}$  NMR (300 MHz,  $\text{CDCl}_3$ )  $\delta$  7.44 (s, 2H,  $\text{CH}_2\text{CH}_2\text{NH}$ ), 7.23 (d,  $J =$

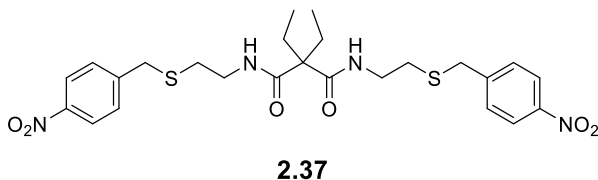
8.5 Hz, 4H, ArH), 6.84 (d,  $J = 8.5$  Hz, 4H, ArH), 3.79 (s, 6H,  $\text{CH}_3\text{O}$ ), 3.68 (s, 4H,  $\text{PhCH}_2\text{S}$ ), 3.42 (m, 4H,  $\text{CH}_2\text{CH}_2\text{NH}$ ), 2.56 (t,  $J = 6.5$  Hz, 4H,  $\text{SCH}_2\text{CH}_2$ ), 1.86 (q,  $J = 7.5$  Hz, 4H,  $\text{CCH}_2\text{CH}_3$ ), 0.83 (t,  $J = 7.5$  Hz, 6H,  $\text{CCH}_2\text{CH}_3$ ),  $^{13}\text{C}$  NMR (75 MHz,  $\text{CDCl}_3$ )  $\delta$  173.2 ( $\text{NHCO}$ ), 158.8 (ArC), 130.1 (ArC), 130.0 (ArC), 114.1 (ArC), 58.3 ( $\text{COCCO}$ ), 55.4 ( $\text{OCH}_3$ ), 38.2 ( $\text{NHCH}_2\text{CH}_2$ ), 35.3 ( $\text{SCH}_2\text{Ph}$ ), 31.0 ( $\text{CCH}_2\text{CH}_3$ ), 30.2 ( $\text{CH}_2\text{CH}_2\text{S}$ ), 9.5 ( $\text{CCH}_2\text{CH}_3$ ),  $m/z$  (ESI) for  $[\text{C}_{27}\text{H}_{38}\text{N}_2\text{NaO}_4\text{S}_2]^+$  calculated: 518.2171, found: 541.2165.

**$N^1, N^3$ -Bis(2-((4-fluorobenzyl)thio)ethyl)-2,2-diethylmalonamide (2.36)**



Viscous yellow oil. Yield: 0.91 g (46%),  $\nu(\text{cm}^{-1})$ : 3296 (amide N-H), 1647 (amide C=O bend),  $^1\text{H}$  NMR (300 MHz,  $\text{CDCl}_3$ )  $\delta$  7.42 (s, 2H,  $\text{CH}_2\text{NHCO}$ ), 7.29 (t,  $J = 8.0$  Hz, 4H, ArH), 7.00 (t,  $J = 8.0$  Hz, 4H, ArH), 3.70 (s, 4H,  $\text{SCH}_2\text{Ph}$ ), 3.44 (m, 4H,  $\text{NHCH}_2\text{CH}_2$ ), 2.56 (t,  $J = 6.0$  Hz, 4H,  $\text{CH}_2\text{CH}_2\text{S}$ ), 1.87 (q,  $J = 7.0$  Hz, 4H,  $\text{CCH}_2\text{CH}_3$ ), 0.83 (t,  $J = 7.0$  Hz, 6H,  $\text{CCH}_2\text{CH}_3$ ).  $^{13}\text{C}$  NMR (75 MHz,  $\text{CDCl}_3$ )  $\delta$  173.2 ( $\text{COCCO}$ ), 162.1 (d,  $J_{\text{CF}} = 242$ , ArC), 133.9 (d,  $J_{\text{CCCCF}} = 3$  Hz, ArC), 130.5 (d,  $J_{\text{CCCF}} = 8$  Hz), 115.6 (d,  $J_{\text{CCF}} = 21$  Hz), 58.3 ( $\text{COCCO}$ ), 38.2 ( $\text{NHCH}_2\text{CH}_2$ ), 35.1 ( $\text{SCH}_2\text{ArC}$ ), 31.1 ( $\text{CCH}_2\text{CH}_3$ ), 30.3 ( $\text{CH}_2\text{CH}_2\text{S}$ ), 9.6 ( $\text{CCH}_2\text{CH}_3$ ).  $m/z$  (ESI) for  $[\text{C}_{25}\text{H}_{32}\text{F}_2\text{N}_2\text{NaO}_2\text{S}_2]^+$  calculated; 517.1771 found; 517.1765.

**$N^1, N^3$ -2,2-Diethyl-bis(2-((4-nitrobenzyl)thio)ethyl)malonamide(2.37)**



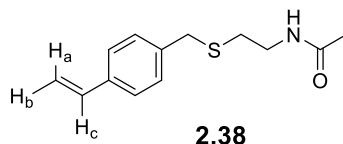
Viscous yellow oil. Yield: 2.836 g (76%),  $\nu(\text{cm}^{-1})$ : 3294 (N-H stretch), 1647 (C=O bend), 1544 and 1367 (N-O stretch),  $^1\text{H}$  NMR (300 MHz,  $\text{CDCl}_3$ )  $\delta$  8.18 (d,  $J = 8.5$  Hz, 4H, ArH), 7.51 (d,  $J = 8.5$  Hz, 4H, ArH), 7.45 (s, 2H,  $\text{CH}_2\text{CH}_2\text{NH}$ ), 3.81 (s, 4H,  $\text{PhCH}_2\text{S}$ ), 3.46 (m, 4H,  $\text{SCH}_2\text{CH}_2$ ), 2.57 (t,  $J = 6.5$  Hz, 4H,  $\text{SCH}_2\text{CH}_2$ ), 1.87 (q,  $J = 7.5$  Hz, 4H,  $\text{CCH}_2\text{CH}_3$ ), 0.83 (t,  $J$

= 7.5 Hz, 6H, CCH<sub>2</sub>CH<sub>3</sub>), <sup>13</sup>C NMR (75 MHz, CDCl<sub>3</sub>) δ 173.3 (NH<sub>2</sub>COC), 147.2 (ArC), 146.0 (ArC), 130.0 (ArC), 124.0 (ArC), 58.3 (COCCO), 38.2 (CH<sub>2</sub>CH<sub>2</sub>NH), 35.3 (PhCH<sub>2</sub>S), 31.3 (CCH<sub>2</sub>CH<sub>3</sub>), 30.5 (SCH<sub>2</sub>CH<sub>2</sub>), 9.6 (CCH<sub>2</sub>CH<sub>3</sub>), *m/z* (ESI) for [C<sub>25</sub>H<sub>32</sub>N<sub>4</sub>NaO<sub>6</sub>S<sub>2</sub>]<sup>+</sup> calculated: 571.1661, found 571.1605.

### 7.2.6 Attempted synthesis of *N*<sup>1</sup>-(2-benzylthio)ethyl)-*N*<sup>3</sup>-(2-((4-vinylbenzyl)thio)ethyl)malonamide (2.13)

To a stirred solution of amine **2.20** (1.30 g, 7.77 mmol) and amine **2.25** (1.50 g, 7.77 mmol) in anhydrous diethyl ether (20 mL) was added, dropwise, malonyl chloride solution (0.38 mL, 3.89 mmol) in anhydrous diethyl ether (40 mL). After 16 h reaction time, the resulting crude mixture was diluted with diethyl ether (150 mL) and water (150 mL). This solution was washed successively with 2 M HCl (50 mL), saturated NaHCO<sub>3</sub> (50 mL), water (50 mL) and brine (50 mL). The ether extract was then dried over anhydrous MgSO<sub>4</sub> and filtered. The crude product left was concentrated *in vacuo*. Isolation of target compound was attempted by means of flash chromatography; however, it was unsuccessful. Yield (of mixture): 0.77 g.

### 7.2.7 Synthesis of *N*-(2-((4-Vinylbenzyl)thio)ethyl)acetamide (2.38)



Amine **2.25** (13.69 g, 0.071 mol, 2 eq.) was dissolved in dry diethyl ether (150 mL) in a one necked flask. Acetyl chloride (2.53 mL, 0.035 mol, 1 eq.) was dissolved in dry diethyl ether (50 mL) and added dropwise into the amine **2.25** solution using a syringe pump for 90 min at 0° C. The reaction was left to stir and warm up to room temperature overnight. At the end of the reaction time, it was quenched with 2 M HCl (75 mL x 2) and extracted with ether (50 mL). The organic layer was then washed with saturated NaHCO<sub>3</sub> (75 mL x 2), water (150 mL x 2) and finally brine (150 mL). The organic layer was then dried over anhydrous MgSO<sub>4</sub>, filtered and concentrated *in vacuo* to give a white solid. It was observed from <sup>1</sup>H NMR analysis of the crude product that it was pure, needing no purification. Yield: 6.28 (76 %), m.p. = 73 –

75 °C, found: 258.0925,  $\nu(\text{cm}^{-1})$ : 3292 (N-H stretch), 1632 (C=O bend),  $^1\text{H NMR}$  (300 MHz,  $\text{CD}_3\text{CN}$ ) 7.40 (d,  $J = 7.5$  Hz, 2H, ArH), 7.29 (d,  $J = 7.5$  Hz, 2H, ArH), 6.73 (dd,  $J = 17.5, 11.0$  Hz, 1H,  $\text{CH}_a\text{H}_b\text{CH}_c$ ), 6.53 (s, 1H,  $\text{CH}_2\text{NHCO}$ ), 5.78 (d,  $J = 17.5$  Hz, 1H,  $\text{CH}_a\text{H}_b\text{CH}_c$ ), 5.23 (d,  $J = 11.0$  Hz, 1H,  $\text{CH}_a\text{H}_b\text{CH}_c$ ), 3.72 (s, 2H,  $\text{PhCH}_2\text{S}$ ), 3.27 (m, 2H,  $\text{CH}_2\text{CH}_2\text{NH}$ ), 2.48 (t,  $J = 7.0$  Hz, 2H,  $\text{SCH}_2\text{CH}_2$ ), 1.83 (s, 3H,  $\text{NHCOCH}_3$ ).  $^{13}\text{C NMR}$  (75 MHz,  $\text{CD}_3\text{CN}$ ) 170.7 ( $\text{NHCOCH}_3$ ), 139.7 (ArC), 137.4 (ArC), 137.3 ( $\text{CH}_2=\text{CHArC}$ ), 130.2 (ArC), 127.2 (ArC), 114.4 ( $\text{CH}_2=\text{CHArC}$ ), 39.3 ( $\text{CH}_2\text{CH}_2\text{NH}_2$ ), 35.8 ( $\text{ArCCH}_2\text{S}$ ), 31.5 ( $\text{SCH}_2\text{CH}_2$ ), 23.0 ( $\text{NHCOCH}_3$ ).  $m/z$  (ESI) for  $[\text{C}_{13}\text{H}_{14}\text{NNaOS}]^+$  calculated, 258.0929, found, 258.0923.

## 7.2.8 Competitive metal extraction

This was undertaken following reported protocols.<sup>203,205</sup> A solution of equal concentrations of  $\text{Cu}^{2+}$ ,  $\text{Ag}^+$  and  $\text{Pb}^{2+}$  (4000 ppb each) in 0.023 M  $\text{Na}_2\text{SO}_4$  in 0.476 M  $\text{HNO}_3$  was prepared. Chloroform was presaturated with twice its volume of 0.5 M  $\text{H}_2\text{SO}_4$  by constant shaking in a separatory funnel for 5 min. This chloroform was used to prepare ligand solutions. Ligand solution with molarity equal to 250 times that of  $\text{Ag}^+$  were prepared. For each metal extraction experiment, equal volumes (10 mL) of metal solution and ligand solution were contacted by rapid and vigorous stirring (using a stir bar) in capped plastic vials for 15 min in an oil bath set at 25 °C. Each experiment was undertaken in duplicates. After stirring, the immiscible solutions were transferred to a separatory funnel, allowed to separate and collected separately. The aqueous layer was collected into a beaker and residual chloroform was removed over a steam bath in about 15 min. Then the aqueous layer was made back up to 10 mL and prepared for ICP-OES analysis. Metal extraction efficiencies were determined by;

$$\% EE = \frac{C_i - C_f}{C} \times 100$$

Where % *EE* is percentage extraction efficiency,  $C_i$  and  $C_f$  are the initial metal ion concentrations respectively.

**Table 7.1: Calibration data for the ICP-OES analysis**

	<b>Cu<sup>2+</sup> (324 nm)</b>	<b>Ag<sup>+</sup> (338 nm)</b>	<b>Pb<sup>2+</sup> (217 nm)</b>
<b>Concentration (ppb)</b>	<b>Mean intensities (n = 3)</b>		
0	2995	-152	60
25	5391	2370	25
50	12543	5453	72
100	26555	11770	186
250	65870	29984	474
500	134726	63073	985
1000	265809	127199	1990
2500	623331	305490	4679
5000	1279856	624613	9548
<b>R<sup>2</sup></b>	0.9998	0.9999	0.9999
<b>Coefficient of x</b>	1528	-500	14

**Table 7.2: ICP-OES extraction analysis data for neat chloroform (control)**

<b>Time (min)</b>	<b>Cu<sup>2+</sup></b>	<b>Ag<sup>+</sup></b>	<b>Pb<sup>2+</sup></b>
<b>Concentration (ppb)</b>			
0	3915±7	4067±9	3713±7
15	3792±34	3522±147	3644±15
<b>Extraction efficiency (%)</b>			
	3.1±1.0	13.4±3.8	1.9±0.6

**Table 7.3: ICP-OES extraction analysis data for 2.10**

<b>Time (min)</b>	<b>Cu<sup>2+</sup></b>	<b>Ag<sup>+</sup></b>	<b>Pb<sup>2+</sup></b>
<b>Concentration (ppb)</b>			
0	3915±7	4067±9	3713±7
15	3590±303	116±40	3703±30
<b>Extraction efficiency (%)</b>			
	8.3±7.9	96.3±1.2	0.3±1.0
<b>Selectivity coefficient</b>			
	11.6	-	321

**Table 7.4: ICP-OES extraction analysis data for 2.38**

<b>Time (min)</b>	<b>Cu<sup>2+</sup></b>	<b>Ag<sup>+</sup></b>	<b>Pb<sup>2+</sup></b>
<b>Concentration (ppb)</b>			
0	4042±12	4222±2	3797±22
15	4043±30	2696±78	3836±13
<b>Extraction efficiency (%)</b>			
	-0.0±1.0	36.1±1.9	-1.0±0.9
<b>Selectivity coefficient</b>			
	36.1	-	36.1

**Table 7.5: ICP-OES extraction analysis data for 2.14**

<b>Time (min)</b>	<b>Cu<sup>2+</sup></b>	<b>Ag<sup>+</sup></b>	<b>Pb<sup>2+</sup></b>
<b>Concentration (ppb)</b>			
0	3857±3	3990±3	3671±2
15	3128±93	64±12	2976±60
<b>Extraction efficiency (%)</b>			
	18.9±2.4	98.4±0.4	18.9±1.7
<b>Selectivity coefficient</b>			
	5.2	-	5.2

**Table 7.6: ICP-OES extraction analysis data for 2.15**

<b>Time (min)</b>	<b>Cu<sup>2+</sup></b>	<b>Ag<sup>+</sup></b>	<b>Pb<sup>2+</sup></b>
<b>Concentration (ppb)</b>			
0	3915±7	4067±9	3713±7
15	3957±41	239±55	3729±24
<b>Extraction efficiency (%)</b>			
	-1.1±1.2	94.1±1.6	-0.4±0.8
<b>Selectivity coefficient</b>			
	85.5	-	235.3

**Table 7.7: ICP-OES extraction analysis data for 2.16**

<b>Time (min)</b>	<b>Cu<sup>2+</sup></b>	<b>Ag<sup>+</sup></b>	<b>Pb<sup>2+</sup></b>
<b>Concentration (ppb)</b>			
0	3857±3	3990±3	3671±2
15	3180±59	357±38	3021±49
<b>Extraction efficiency (%)</b>			
	17.6±1.6	91.4±1.0	17.5±1.4
<b>Selectivity coefficient</b>			
	5.2	-	5.2

**Table 7.8: ICP-OES extraction analysis data for 2.17**

<b>Time (min)</b>	<b>Cu<sup>2+</sup></b>	<b>Ag<sup>+</sup></b>	<b>Pb<sup>2+</sup></b>
<b>Concentration (ppb)</b>			
0	3857±3	3990±3	3671±2
15	3154±1	354±106	3053±27
<b>Extraction efficiency (%)</b>			
	18.2±0.1	91.1±2.7	16.8±0.8
<b>Selectivity coefficient</b>			
	5.0	-	5.4

**Table 7.9: ICP-OES extraction analysis data for 2.18**

<b>Time (min)</b>	<b>Cu<sup>2+</sup></b>	<b>Ag<sup>+</sup></b>	<b>Pb<sup>2+</sup></b>
<b>Concentration (ppb)</b>			
0	3857±3	3990±3	3671±2
15	3876±11	317±7	3667±14
<b>Extraction efficiency (%)</b>			
	-1.4±0.4	92.2±0.2	20.6±0.9
<b>Selectivity coefficient</b>			
	65.9	-	4.5

**Table 7.10: ICP-OES extraction analysis data for 2.33**

Time (min)	Cu <sup>2+</sup>	Ag <sup>+</sup>	Pb <sup>2+</sup>
<b>Concentration (ppb)</b>			
0	3933±3	4075±2	3762±18
15	3623±170	45±5	3429±179
<b>Extraction efficiency (%)</b>			
	7.9±4.4	98.9±0.2	8.9±4.8
<b>Selectivity coefficient</b>			
	12.5	-	11.1

## 7.3 Experimental for chapter three

### 7.3.1 Synthesis of Ag<sup>+</sup> complexes of 2.10 and 2.38 and attempted crystal growth

The silver salt AgNO<sub>3</sub> or AgClO<sub>4</sub> (1 eq.) was dissolved in acetonitrile, added to a dichloroethane solution of **2.10** or **2.38** and the mixture was stirred in the dark at room temperature for 2 h. Crystal growth was attempted by vapour diffusion and slow evaporation of solvent. For the vapour diffusion method, an acetonitrile/dichloromethane solution of either Ag<sup>+</sup>-**2.10** or **2.38** complex inside a vial was placed inside a beaker containing ether, covered and left overnight. For the slow evaporation method, a solution of either Ag<sup>+</sup>-**2.10** or **2.38** complex inside a vial was left to slowly dry for 1 week.

#### [Ag(**2.10**)]NO<sub>3</sub> (**3.21**)

Golden yellow paste. Yield: 40 mg (70 %),  $\nu(\text{cm}^{-1})$ : 3282 (NH), 1636 (CO), 1294 (NO), *Anal calc.*, found: C, 42.73; H, 4.25; N, 7.00; C<sub>21</sub>H<sub>26</sub>AgN<sub>3</sub>O<sub>5</sub>S<sub>2</sub> requires C, 44.06; H, 4.58; N, 7.34 %,  $m/z$  (ESI) calculated for [C<sub>21</sub>H<sub>26</sub><sup>107</sup>AgN<sub>2</sub>O<sub>2</sub>S<sub>2</sub>]<sup>+</sup>: 509.0487, found 509.0481.

#### [Ag(**2.10**)]ClO<sub>4</sub> (**3.22**)

Golden yellow paste. Yield: 40 mg (66%),  $\nu(\text{cm}^{-1})$ : 3342 (NH), 1637 (C=O), 1065 (Cl-O), *Anal calc.*, found: C, 41.55; H, 4.40; N, 6.57; C<sub>21</sub>H<sub>26</sub>AgClN<sub>2</sub>O<sub>6</sub>S<sub>2</sub> requires C, 41.35; H, 4.30; N, 4.60%,  $m/z$  (ESI) calculated for [C<sub>21</sub>H<sub>26</sub><sup>107</sup>AgN<sub>2</sub>O<sub>2</sub>S<sub>2</sub>]<sup>+</sup>: 509.0487, found 509.0481.

[Ag(**2.38**)]NO<sub>3</sub> (**3.23**)

Brown paste. Yield: 62 mg (77%),  $\nu(\text{cm}^{-1})$ : 3293 (NH), 1627 (CO), 1362 or 1282 (NO), *Anal calc.* found: C, 38.43; H, 3.95; N, 6.81; C<sub>13</sub>H<sub>17</sub>AgN<sub>2</sub>O<sub>4</sub>S requires C, 38.52; H, 4.23; N, 6.92%, *m/z* (ESI) calculated for [C<sub>13</sub>H<sub>17</sub>AgNOS]<sup>+</sup>; 342.0082, found 342.0076 and calculated for [C<sub>26</sub>H<sub>34</sub><sup>107</sup>AgN<sub>2</sub>O<sub>2</sub>S<sub>2</sub>]<sup>+</sup> 577.1113, found 577.1107.

[Ag(**2.38**)]ClO<sub>4</sub> (**3.24**)

Colourless paste. Yield: 43 mg (98%),  $\nu(\text{cm}^{-1})$ : 3364 (NH), 1629 (CO), 1068 (Cl-O), *Anal calc.* found: C, 37.07; H, 4.05; N, 3.63; C<sub>13</sub>H<sub>17</sub>AgClNO<sub>5</sub>S requires C, 35.26; H, 3.87; N, 3.17 %, *m/z* (ESI) calculated for [C<sub>13</sub>H<sub>17</sub>AgNOS]<sup>+</sup>; 342.0082, found 342.0076 and calculated for [C<sub>26</sub>H<sub>34</sub><sup>107</sup>AgN<sub>2</sub>O<sub>2</sub>S<sub>2</sub>]<sup>+</sup> 577.1113, found 577.1107.

### 7.3.2 Mass spectrometry studies of Ag<sup>+</sup>-**2.10** and Ag<sup>+</sup>-**2.38** complexes

Typically, **2.10** or **2.38** (1 eq.) was dissolved in EtOAc (5 mL) and added to AgOSO<sub>2</sub>CF<sub>3</sub> (1 – 3 eq.) also in EtOAc (5 mL). The mixture was refluxed for 15 min after which the product was concentrated *in vacuo*. Finally, samples were prepared for mass spectrometry analysis.

[Ag(**2.10**)]OSO<sub>2</sub>CF<sub>3</sub> (**3.25** – **3.27**)

**3.25**: Brown paste. Yield: 30 mg (91 %), **3.26**: Brown solid. Yield: 30 mg (65 %), **3.27**: Yellow paste, Yield: 50 mg (85 %), *m/z* (ESI) calculated for [C<sub>21</sub>H<sub>26</sub><sup>107</sup>AgN<sub>2</sub>O<sub>2</sub>S<sub>2</sub>]<sup>+</sup> 509.0487 found; 509.0481.

[Ag(**2.38**)<sub>2</sub>]OSO<sub>2</sub>CF<sub>3</sub> (**3.28** – **3.30**)

**3.28**: Colourless paste. Yield: 60 mg (94 %), **3.29**: Colourless paste. Yield: 50 mg (75 %), **3.30**: Colourless paste. Yield: 50 mg (85 %). *m/z* (ESI) calculated for [C<sub>13</sub>H<sub>17</sub><sup>107</sup>AgNOS]<sup>+</sup>; 342.0082, found 342.0076 and calculated for [C<sub>26</sub>H<sub>34</sub><sup>107</sup>AgN<sub>2</sub>O<sub>2</sub>S<sub>2</sub>]<sup>+</sup>: 577.1113, found; 577.1107.

### 7.3.3 Job's plot for the interaction of AgClO<sub>4</sub> with **2.10** or **2.38**.

Standard solutions of **2.10** or **2.38** (0.005 M) in d<sub>6</sub>-DMSO (for **2.10**) or CD<sub>3</sub>OD (for **2.38**) and AgClO<sub>4</sub> (0.005 M) in d<sub>6</sub>-DMSO (for **2.10**) or CD<sub>3</sub>OD (**2.38**) were prepared. Varying ratios of each solution (**2.10** or **2.38** and AgClO<sub>4</sub>) were then taken and mixed together (with the overall concentration remaining the same) to get different Ag<sup>+</sup> mole fractions ( $\chi_{\text{Ag}^+}$ ). For example, to get a  $\chi_{\text{Ag}^+} = 0.1$ , 0.45 mL **2.10** or **2.38** solution was mixed with 0.05 mL AgClO<sub>4</sub> solution inside an NMR tube. Also, to get a  $\chi_{\text{Ag}^+} = 0.2$ , 0.40 mL **2.10** or **2.38** solution was mixed with 0.10 mL AgClO<sub>4</sub> solution and so on until a  $\chi_{\text{Ag}^+} = 0.9$  prepared by mixing 0.05 mL **2.10** or **2.38** solution with 0.45 mL AgClO<sub>4</sub> solution. The <sup>1</sup>H NMR experiments of all mixtures and the free ligand (**2.10** or **2.38**) were recorded. The plot of  $\chi_{\text{L}} \cdot \Delta\delta$  (where  $\chi_{\text{L}}$  = mole fraction of **2.10** or **2.38** and  $\Delta\delta$  = chemical shift of Ag<sup>+</sup>-**2.10** or **2.38** complex minus chemical shift of free **2.10** or **2.38**) against  $\chi_{\text{Ag}^+}$  was constructed from the data generated.

**Table 7.11: <sup>1</sup>H NMR titration data for the Job's plot of the interaction of **2.10** and AgClO<sub>4</sub>**

	Protons					
	a,b,c	d	e	F	g	h
$\chi_{\text{Ag}^+}$	$\chi_{\text{2.10}} \cdot \Delta\delta$ (ppm)					
0.1	0.001	0.003	0.003	0.003	0.002	0.001
0.2	0.002	0.005	0.006	0.003	0.003	0.002
0.3	0.001	0.006	0.007	0.004	0.004	0.002
0.4	0.002	0.007	0.008	0.005	0.005	0.002
0.5	0.002	0.008	0.009	0.005	0.006	0.003
0.6	0.002	0.007	0.008	0.004	0.006	0.002
0.7	0.002	0.006	0.008	0.004	0.005	0.002
0.8	0.001	0.005	0.006	0.003	0.004	0.002
0.9	0.001	0.003	0.003	0.002	0.002	0.001

**Table 7.12: <sup>1</sup>H NMR titration data for the Job's plot of the interaction of 2.38 and AgClO<sub>4</sub>**

	Protons								
	1	3	4	5	6	7	8	9	10
$\chi_{\text{Ag}^+}$	$\chi_{2.38} \cdot \Delta\delta$ (ppm)								
0.1	0.005	0.020	0.029	0.032	0.014	0.010	0.007	0.009	0.009
0.2	0.010	0.034	0.078	0.064	0.022	0.018	0.011	0.016	0.015
0.3	0.013	0.046	0.104	0.085	0.028	0.025	0.012	0.021	0.018
0.4	0.015	0.052	0.116	0.096	0.031	0.030	0.012	0.025	0.020
0.5	0.015	0.053	0.120	0.099	0.033	0.033	0.014	0.024	0.020
0.6	0.013	0.048	0.108	0.090	0.029	0.031	0.011	0.021	0.018
0.7	0.011	0.038	0.089	0.075	0.024	0.026	-	0.018	0.015
0.8	0.008	0.028	0.063	0.053	0.017	0.019	-	0.012	-

### 7.3.4 Mole ratio plot for the interaction of AgClO<sub>4</sub> with 2.10 or 2.38.

The malonamide derivative **2.10** (13 mg, 0.03 mmol) or the amide **2.38** (13.8 mg, 0.059 mmol) was dissolved in 0.5 mL d<sub>6</sub>-DMSO (for **2.10**) or CD<sub>3</sub>OD (for **2.38**) and transferred to into ambered NMR tube. Standard solutions of AgClO<sub>4</sub> (0.539 M) was made up in d<sub>6</sub>-DMSO (for **2.10**) or 0.419 M in CD<sub>3</sub>OD (for **2.38**). A constant volume of AgClO<sub>4</sub> solution (30 μL for **2.10** and 25 μL for **2.38**) was added to **2.10** or **2.38** in the NMR tube to obtain varying Ag<sup>+</sup>/**2.10** or **2.38** mole ratios ( $n_{\text{Ag}^+}/n_{2.10 \text{ or } 2.38}$ ). For example, to target a  $n_{\text{Ag}^+}/n_{2.10 \text{ or } 2.38} = 0.5$ , 30 or 25 μL of AgClO<sub>4</sub> was added using a glass syringe to the neat **2.10** or **2.38** solution respectively and the <sup>1</sup>H NMR spectrum was recorded. Also, to target a  $n_{\text{Ag}^+}/n_{2.10 \text{ or } 2.38} = 1.0$ , 30 or 25 μL of AgClO<sub>4</sub> was added using a glass syringe to the  $n_{\text{Ag}^+}/n_{2.10 \text{ or } 2.38} = 0.5$  solution and the <sup>1</sup>H NMR spectrum was recorded. The constant addition of the AgClO<sub>4</sub> solution was continued until a  $n_{\text{Ag}^+}/n_{2.10 \text{ or } 2.38} = 4.0$  was achieved. The plot of  $\Delta\delta$  (where  $\Delta\delta$  = chemical shift of Ag<sup>+</sup>-**2.10** or **2.38** complex minus chemical shift of free **2.10** or **2.38**) against  $n_{\text{Ag}^+}/n_{2.10 \text{ or } 2.38}$  was constructed using the data generated.

**Table 7.13:**  $^1\text{H}$  NMR titration data for the mole ratio plot of the interaction of 2.10 and  $\text{AgClO}_4$ 

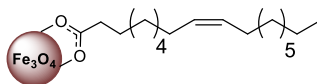
	Protons				
	a,b,c	d	e	g	h
$n_{\text{Ag}^+}/n_{2.10}$	$\Delta\delta$ (ppm)				
0.5	0.017	0.056	0.071	0.046	0.021
1	0.028	0.095	0.122	0.074	0.034
1.5	0.036	0.123	0.155	0.091	0.042
2	0.043	0.144	0.178	0.104	0.047
2.5	0.046	0.158	0.194	0.110	0.050
3	0.048	0.170	0.205	0.116	0.052
3.5	0.050	0.178	0.215	0.119	0.054
4	0.052	0.185	0.221	0.122	0.055

**Table 7.14:**  $^1\text{H}$  NMR titration data for the mole ratio plot of the interaction of 2.38 and  $\text{AgClO}_4$ 

	Protons								
	1	3	4	5	6	7	8	9	10
$n_{\text{Ag}^+}/n_{2.38}$	$\Delta\delta$ (ppm)								
0.5	0.020	0.040	0.140	0.090	0.010	0.025	0.010	0.030	0.030
1	0.050	0.150	0.370	0.280	0.080	0.085	0.045	0.070	0.060
1.5	0.050	0.160	0.390	0.320	0.115	0.105	0.085	0.070	0.070
2	0.060	0.180	0.420	0.350	0.145	0.135	0.135	0.090	0.090
2.5	0.070	0.190	0.430	0.370	0.165	0.155	0.170	0.100	0.100
3	0.080	0.190	0.440	0.380	0.180	0.170	0.205	0.110	0.115
3.5	0.080	0.200	0.450	0.390	0.190	0.185	0.235	0.120	0.125
4	0.090	0.210	0.460	0.400	0.200	0.200	0.255	0.130	0.135

## 7.4 Experimental for chapter four

### 7.4.1 Synthesis of $\text{Fe}_3\text{O}_4@$ oleate (4.9)

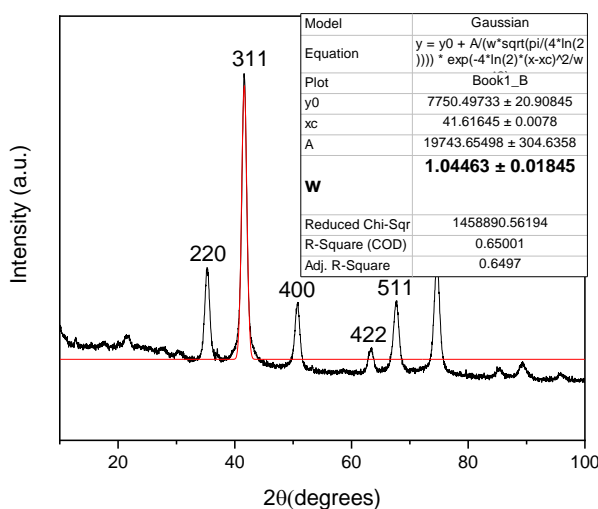
**4.9**

The  $\text{Fe}_3\text{O}_4@$ oleate **4.9** was synthesized by the method reported by Puig and coworkers.<sup>241</sup>

Briefly, to a stirred aqueous solution of  $\text{FeSO}_4 \cdot 7\text{H}_2\text{O}$  (8.34 g, 0.03 mol) and  $\text{FeCl}_3 \cdot 6\text{H}_2\text{O}$  (12.16 g, 0.045 mol) under a nitrogen atmosphere and set at  $90^\circ\text{C}$  was added  $\text{NH}_3 \cdot \text{H}_2\text{O}$  (30 mL, 25%)

and oleic acid (2.23 mL) successively and rapidly. After 3 h, the resulting solids were magnetically separated and washed with water until a neutral pH was observed from the supernatant. Finally, the solids were dispersed in toluene to give a 26 mg/mL solution.  $\nu(\text{cm}^{-1})$ : 2907 and 2844 (C-H stretch), 1515 (C-O asymmetric stretch), 1411 (C-O symmetric stretch) and 557 (Fe-O).

#### 7.4.1.1 Determination of particle size of $\text{Fe}_3\text{O}_4@$ oleate 4.9 using the Scherrer equation<sup>241</sup>.



$$\tau = \frac{K\lambda}{\beta \cos\theta}$$

Where  $\tau$  = particle diameter,  $K$  = Scherrer constant for spherical particles (0.94),  $\lambda$  = X-ray source wavelength,  $\theta$  = Bragg (diffraction) angle of the most intense peak and  $\beta$  = broadening at half the maximum intensity (FWHM) of the most intense peak.

$K = 0.94$ ,  $\lambda = 0.179$  nm,  $\beta$  (FWHM in radians) = 0.0179 rad (lower limit) and 0.01855 rad (lower limit) (which is  $w$  from XRD spectrum, after it has been converted to radians from degrees),  $\theta$  (half of the angle of peak with highest intensity) = 20.8°.

For  $\beta = 0.0179$  rad (lower limit)

$$\tau = \frac{0.94 \times 0.179}{0.0179 \cos 20.8} = 9.7 \text{ nm}$$

For  $\beta = 0.0186$  rad (upper limit)

$$\tau = \frac{0.94 \times 0.179}{0.0179 \cos 20.8} = 10.1 \text{ nm}$$

Therefore, particle size of Fe<sub>3</sub>O<sub>4</sub>@oleate ranges from 9.7 to 10.1 nm or 9.9±0.2 nm

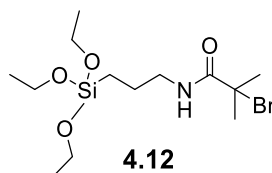
#### 7.4.1.2 Determination of surface coverage of oleic acid

$$\text{No of molecules per nm}^2 = \frac{W \times d_{\text{Fe}_3\text{O}_4} \times r \times N_A}{M(1-W) \times 3 \times 10^{21}}$$

Where  $W$  is the weight loss of sample = 19.1 %,  $d_{\text{Fe}_3\text{O}_4}$  is the density of the Fe<sub>3</sub>O<sub>4</sub> = 5.17 g/cm<sup>3</sup>,  $N_A$  is the Avogadro's constant = 6.022 x 10<sup>23</sup>,  $M$  is the molecular weight of oleic acid = 282.47 g/mol,  $r$  is the radius of the Fe<sub>3</sub>O<sub>4</sub>@oleate **4.9** = 9.9 nm.

$$\text{No of molecules per nm}^2 = 4.29$$

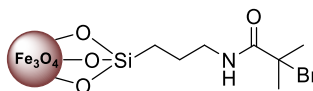
#### 7.4.2 Synthesis of 2-Bromo-2-methyl-*N*-(3-(triethoxysilyl)propyl)propanamide (BMTP) (4.12)



BMTP **4.12** was accessed by the method reported by Sun and coworkers.<sup>242</sup> Concisely, to a stirred solution of 3-aminopropyltriethoxysilane **4.10** (0.99 mL, 8 mmol) and triethylamine (1.12 mL, 8 mmol) in dry toluene (90 mL), 2-bromoisobutyrylbromide **4.11** (0.99 mL, 8 mmol) was added dropwise for 90 min under nitrogen at 0°C. The reaction was left to warm up to room temperature overnight. Subsequently, the crude mixture was filtered and concentrated *in vacuo* to yield as a yellow oil 2-bromo-2-methyl-*N*-(3-(triethoxysilyl)propyl)propanamide **4.12**. Yield: 2.58 g (87%),  $\nu$  (cm<sup>-1</sup>) 3350 (N-H stretch), 2972 (C-H – alkyl stretch), 1653 (C=O – amide stretch), <sup>1</sup>H NMR (300 MHz, CDCl<sub>3</sub>)  $\delta$  6.85 (s, 1H, NHCO), 3.81 (q,  $J = 6.5$  Hz, 6H, CH<sub>3</sub>CH<sub>2</sub>OSi), 3.26 (m, 2H, CH<sub>2</sub>NHCO), 1.94 (s, 6H, (CH<sub>3</sub>)<sub>2</sub>CBr), 1.64 (m, 2H, CH<sub>2</sub>CH<sub>2</sub>CH<sub>2</sub>), 1.22 (t,  $J = 6.5$  Hz, 9H, CH<sub>3</sub>CH<sub>2</sub>OSi), 0.63 (t,  $J = 6.0$  Hz, 2H, OSiCH<sub>2</sub>CH<sub>2</sub>); <sup>13</sup>C NMR (75 MHz, CDCl<sub>3</sub>)  $\delta$  172.0 (NHCOC(CH<sub>3</sub>)<sub>2</sub>Br), 63.4 (COC(CH<sub>3</sub>)Br),

58.6 ((CH<sub>3</sub>CH<sub>2</sub>O)<sub>3</sub>Si), 42.7 (CH<sub>2</sub>CH<sub>2</sub>NH), 32.7 (COC(CH<sub>3</sub>)<sub>2</sub>Br), 22.8 (SiCH<sub>2</sub>CH<sub>2</sub>CH<sub>2</sub>), 18.4 ((CH<sub>3</sub>CH<sub>2</sub>O)<sub>3</sub>Si), 7.6 (SiCH<sub>2</sub>CH<sub>2</sub>); (ESI) *m/z* (ESI) [M+Na]<sup>+</sup> 391.9.

### 7.4.3 Synthesis of Fe<sub>3</sub>O<sub>4</sub>@initiator **4.12** (**4.7**)



**4.7**

The Fe<sub>3</sub>O<sub>4</sub>@initiator **4.12** (**4.7**) was accessed by modification of the method reported by Sun and coworkers.<sup>242</sup> Hence, to a stirred solution of BTMP **4.12** (3.5 mL) and triethylamine (2 M, 6.5 mL) in toluene (35 mL) was added Fe<sub>3</sub>O<sub>4</sub>@oleate **4.9** (80 mL, 4 mg/mL) under a nitrogen atmosphere. After 48 h., petroleum ether (250 mL) was added to the crude product to precipitate a brown solid that was redispersed in toluene (100 mL) and again precipitated by the addition of petroleum ether (100 mL). The redispersion and precipitation continued for four more times after which the solids were dried in vacuo to give **4.7** as a brown solid.  $\nu(\text{cm}^{-1})$ : 2919 (C-H stretch), 1641 (C-O asymmetric stretch), 1530 (C-O symmetric stretch), 1107 (Si-O-Si symmetric stretch), 552 (Fe-O).

#### 7.4.3.1 Determination of surface coverage of initiator **4.12**<sup>242</sup>

$$\text{No of molecules per nm}^2 = \frac{W \times d_{\text{Fe}_3\text{O}_4} \times r \times N_A}{M(1-W) \times 3 \times 10^{21}}$$

Where *W* is the weight loss of sample = 14.9 %,  $d_{\text{Fe}_3\text{O}_4}$  is the density of the Fe<sub>3</sub>O<sub>4</sub> = 5.17 g/cm<sup>3</sup>,  $N_A$  is the Avogadro's constant = 6.022 × 10<sup>23</sup>, *M* is the molecular weight of oleic acid = 369 g/mol, *r* is the radius of the Fe<sub>3</sub>O<sub>4</sub>@oleate **4.9** = 10 nm.

$$\text{No of molecules per nm}^2 = 2.46$$

### 7.4.4 Attempted linkage of amide **2.38** to Fe<sub>3</sub>O<sub>4</sub>@initiator **4.12** (**4.7**)

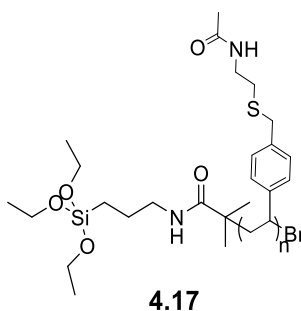
Attempt at linking amide **2.38** to Fe<sub>3</sub>O<sub>4</sub>@initiator **4.12** (**4.7**) was undertaken by the modification of the method reported by Sun and coworkers<sup>242</sup>. Briefly, to a stirred solution of CuBr (29 mg, 0.2 mmol) in DMF (0.5 mL) in a Schlenk tube was charged PMDETA (42 μL,

0.2 mmol). After observing the CuBr solution turn greenish-blue, a mixture of **4.7** (40 mg) and amide **2.38** (400 mg, 1.7 mmol) in DMF (0.5 mL) were charged into the Schlenk followed by degassing by three freeze-pump-thaw cycles. Subsequently, the reaction mixture was left to warm up to room temperature after which it was immersed in an oil bath set at 110°C. After 16 h, THF was added to the crude mixture and the whole crude reaction was emptied into a beaker containing petroleum ether to precipitate out any solids present. The brown solid obtained (**4.15**) was dried *in vacuo*.

#### 7.4.5 Synthesis of Cu- *N*-(2-(4-vinylbenzylthio)ethyl)-acetamide (**4.16**)

A mixture of amide **2.38** (25 mg, 0.106 mmol) and CuBr (15 mg, 0.104 mmol) in EtOAc (8 mL) were refluxed for 1 h. The resulting solution was concentrated *in vacuo* to give a pale green solid. Yield: 30 mg (53%). <sup>1</sup>H NMR (300 MHz, CDCl<sub>3</sub>) δ 7.36 (d, ArH, 2H), 7.28 (d, ArH, 2H), 6.69 (dd, 1H), 5.92 (s, 1H), 5.73 (d, 1H), 5.25 (d, 1H), 3.75 (s, 2H), 3.41 (q, 2H), 2.62 (t, 2H), 1.95 (s, 3H); <sup>13</sup>C NMR (75 MHz, CDCl<sub>3</sub>) 139.7 (ArC), 137.4 (ArC), 137.3 (CH<sub>2</sub>CHArC), 130.2 (ArC), 127.2 (ArC), 114.4 (CH<sub>2</sub>CHArC), 39.3 (CH<sub>2</sub>CH<sub>2</sub>NH<sub>2</sub>), 35.8 (ArCCH<sub>2</sub>S), 31.5 (SCH<sub>2</sub>CH<sub>2</sub>), 23.0 (NHCOCH<sub>3</sub>), *m/z* (ESI) calculated for [C<sub>26</sub>H<sub>34</sub>CuN<sub>2</sub>O<sub>2</sub>S<sub>2</sub>]<sup>+</sup> 533.1358, found: 533.1352.

#### 7.4.6 Synthesis of poly(amide **2.38**) (**4.17**) by the solution ATRP of amide **2.38**



Synthesis of poly(amide **2.38**) by ATRP was attempted following the protocol employed for the attempted linkage of the amide **2.38** to the Fe<sub>3</sub>O<sub>4</sub>@initiator **4.12** (**4.7**) where **4.7** was substituted for initiator **4.12**. Briefly, to a stirred solution of CuBr (10 mg, 0.07 mmol, 1 eq.)

in DMF (0.5 mL) in a Schlenk tube was charged PMDETA (15  $\mu$ L, 0.07 mmol, 1 eq.). After observing the CuBr solution turn greenish-blue, a mixture of initiator **4.12** (413 mg, 1.76 mmol, 25 eq.) and amide **2.38** (26 mg, 0.07 mmol, 1 eq.) in DMF (0.5 mL) were charged into the Schlenk followed by degassing by three freeze-pump-thaw cycles. At this point, a 0.5 mL sample was withdrawn in order to measure conversion. Subsequently, the remaining reaction mixture was left to warm up to room temperature after which it was immersed in an oil bath set at 110°C. After 16 h, A 0.5 mL sample of the crude was withdrawn for  $^1\text{H}$  NMR characterization in order to measure conversion.

#### 7.4.7 Synthesis of poly(amide **2.38**) (**4.17**) by free radical polymerization

A degassed AIBN (4 mg, 0.24 mmol) solution in THF (1 mL) was added to another degassed solution of **2.38** (250 mg, 1.06 mmol) in THF (1 mL) and the mixture was left to stir at 65 °C for 17 h. The conversion was monitored by means of  $^1\text{H}$  NMR by taking samples of the reaction mixture at the start and end of the reaction. The resulting crude mixture was introduced into stirred MeOH (10 mL) inside a 25 mL vial. The stirring continued for 20 min after which solids precipitated. Solvent was removed *in-vacuo* to give as a colourless solid poly(amide **2.38**) or **4.17**.

#### 7.4.8 Free radical-mediated linkage of amide **2.38** to $\text{Fe}_3\text{O}_4$ @initiator **4.12** (**4.7**)

A mixture of the  $\text{Fe}_3\text{O}_4$ @initiator (**4.7**) (40 mg), amide **2.38** (160 mg, 0.68 mmol) and AIBN (8 mg, 0.05 mmol) in toluene (4 mL) inside a 20 mL glass vial were sonicated at room temperature for 30 min and subsequently degassed for another 30 min. AIBN (24 mg, 0.146 mmol) was dissolved in toluene (3 mL) and degassed for 30 min. The AIBN solution was then added dropwise to the stirred mixture of the  $\text{Fe}_3\text{O}_4$ @initiator (**4.7**) and amide **2.38** for 15 h. Subsequently, the resulting brown solid was magnetically separated and the supernatant decanted. Finally, the solids were washed with THF, magnetically separated and dried *in vacuo* to give  $\text{Fe}_3\text{O}_4$ @initiator **4.12**@amide **2.38** (**4.8**).  $\nu$  ( $\text{cm}^{-1}$ ): 3268 (N-H stretch), 2919 (C-

H stretch), 1641 (C-O asymmetric stretch), 1544 (C-O symmetric stretch), 1104 and 1020 (Si-O-Si stretch), 552 (Fe-O).

### 7.4.9 Competitive metal extraction

A 1 L test aqueous solution containing 4.6, 5.5 and 5.0 ppm Cu<sup>2+</sup>, Ag<sup>+</sup> and Pb<sup>2+</sup> respectively in 0.023 M NaNO<sub>3</sub> and 0.476 M HNO<sub>3</sub>, was prepared from a 500 ppm stock solution. Subsequently, 10 mL of the test solution was measured into a screw-cap plastic vial and 10 mg of extractant (Fe<sub>3</sub>O<sub>4</sub>@OA **4.9** or Fe<sub>3</sub>O<sub>4</sub>@initiator **4.12 (4.7)** or Fe<sub>3</sub>O<sub>4</sub>@initiator **4.12@amide 2.38 (4.8)**) was added. The vial was capped and shook after which was placed on the bench to sit. After 15 mins, the extractant was magnetically separated and the supernatant was carefully collected and prepared for ICP-OES analyses. The extraction experiments were undertaken in triplicates. The extraction efficiency of the extractants for Ag<sup>+</sup> was determined by the equation below;

$$\% EE = \frac{C_i - C_f}{C} \times 100$$

Where % *EE* is percentage extraction efficiency, *C<sub>i</sub>* and *C<sub>f</sub>* are the initial metal ion concentrations respectively.

**Table 7.15: ICP-OES calibration data for the metal extraction experiment by Fe<sub>3</sub>O<sub>4</sub>@oleate (4.9), Fe<sub>3</sub>O<sub>4</sub>@initiator 4.12 (4.7) and Fe<sub>3</sub>O<sub>4</sub>@initiator@amide 2.38 (4.8)**

	<b>Cu<sup>2+</sup> (324 nm)</b>	<b>Ag<sup>+</sup> (338 nm)</b>	<b>Pb<sup>2+</sup> (217 nm)</b>
<b>Concentration (ppb)</b>	<b>Mean intensities (n = 3)</b>		
0	2437	-14	53
25	9157	4644	65
50	15960	8362	118
100	33244	16734	255
250	76254	38604	564
500	143423	72847	1047
1000	253282	126520	1851
2500	572239	282995	4042
5000	1154788	560847	8022
<b>R<sup>2</sup></b>	0.9996	0.9995	0.9993
<b>Coefficient of x</b>	229	111	6

**Table 7.16: ICP-OES extraction analysis data for Fe<sub>3</sub>O<sub>4</sub>@oleate (4.9)**

<b>Time (min)</b>	<b>Cu<sup>2+</sup></b>	<b>Ag<sup>+</sup></b>	<b>Pb<sup>2+</sup></b>
	<b>Concentration (ppb)</b>		
0	4593±31	5546±37	4968±18
15	4569±14	5494±36	4942±31
	<b>Extraction efficiency (%)</b>		
	0.5±1.0	0.9±1.3	0.5±1.0
	<b>Selectivity coefficient</b>		
	1.8	-	1.8

**Table 7.17: ICP-OES extraction analysis data for Fe<sub>3</sub>O<sub>4</sub>@initiator 4.12 (4.7)**

<b>Time (min)</b>	<b>Cu<sup>2+</sup></b>	<b>Ag<sup>+</sup></b>	<b>Pb<sup>2+</sup></b>
	<b>Concentration (ppb)</b>		
0	4593±31	5546±37	4968±18
15	4609±39	0±0	4967±38
	<b>Extraction efficiency (%)</b>		
	-0.3±1.5	100±0	0.0±1.1
	<b>Selectivity coefficient</b>		
	333.3	-	625

**Table 7.18: ICP-OES extraction analysis data for Fe<sub>3</sub>O<sub>4</sub>@initiator@amide 2.38 (4.8)**

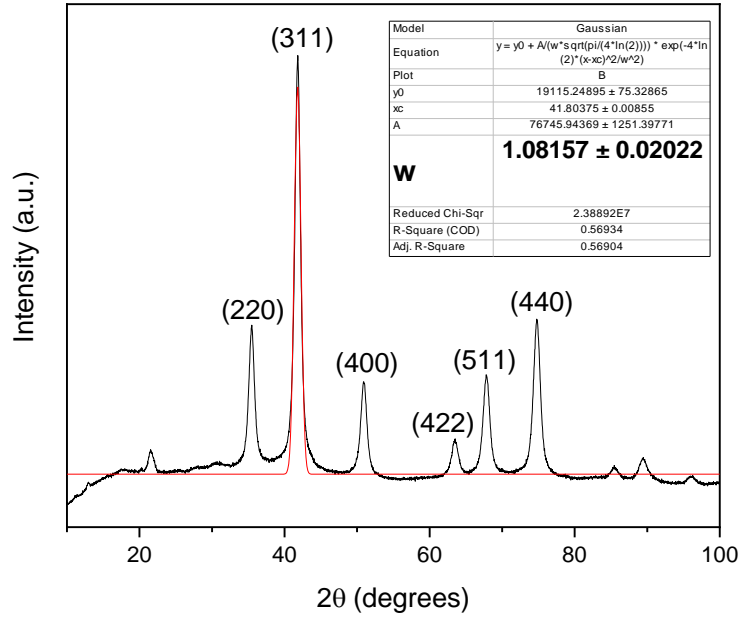
Time (min)	Cu <sup>2+</sup>	Ag <sup>+</sup>	Pb <sup>2+</sup>
	<b>Concentration (ppb)</b>		
0	4593±31	5546±37	4968±18
15	4667±33	0±0	5008±31
	<b>Extraction efficiency (%)</b>		
	-1.6±1.4	100±0	-0.8±1.0
	<b>Selectivity coefficient</b>		
	62.5	-	125

## 7.5 Experimental for chapter five

### 7.5.1 Synthesis of Fe<sub>3</sub>O<sub>4</sub> 5.4

The Fe<sub>3</sub>O<sub>4</sub> **5.4** was prepared following the method reported by Naka *et al.*<sup>256</sup> Summarily, FeCl<sub>3</sub>·6H<sub>2</sub>O (5.41 g, 0.02 mole) and FeSO<sub>4</sub>·7H<sub>2</sub>O (2.78 g, 0.01 mole) were dissolved by stirring in water (300 mL) at 50 °C. Then, aqueous ammonia (8.52 mL, 13.2 M, 0.11 mol) was added to the iron oxide solution and vigorously stirred for 30 minutes, after which the black solids obtained were separated using a magnet. The solids were washed with water (100 mL x 3) and EtOH (50 mL x 3). Finally, the solids were dried *in vacuo* at 70 °C to give the black solid Fe<sub>3</sub>O<sub>4</sub>.  $\nu(\text{cm}^{-1})$ : 554 (Fe-O).

### 7.5.1.1 Determination of particle size of Fe<sub>3</sub>O<sub>4</sub> 5.4 using the Scherrer equation<sup>241</sup>



$$\tau = \frac{K\lambda}{\beta \cos\theta}$$

Where  $\tau$  = particle diameter,  $K$  = Scherrer constant for spherical particles (0.94),  $\lambda$  = X-ray source wavelength,  $\theta$  = Bragg (diffraction) angle of the most intense peak and  $\beta$  = broadening at half the maximum intensity (FWHM) of the most intense peak.

$K = 0.94$  (ref),  $\lambda = 0.179$  nm,  $\beta$  (FWHM in radians) = 0.0176 rad (lower limit) and 0.0185 rad (lower limit) (which is  $w$  from XRD spectrum, after it has been converted to radians from degrees),  $\theta$  (half of the angle of peak with highest intensity) = 21°.

For  $\beta = 0.0176$  rad (lower limit of FWHM),

$$\tau = \frac{0.94 \times 0.179}{(0.0176) \times \cos 21} = 10.2 \text{ nm}$$

For  $\beta = 0.0185$  rad (upper limit of FWHM)

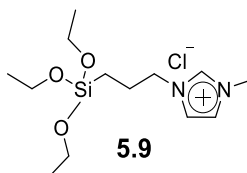
$$\tau = \frac{0.94 \times 0.179}{(0.0185) \times \cos 21} = 9.7 \text{ nm}$$

Therefore, the size of Fe<sub>3</sub>O<sub>4</sub> **5.4** ranges from 9.7 – 10.2 nm or 10.0±0.3 nm

### 7.5.2 Synthesis of Fe<sub>3</sub>O<sub>4</sub>@SiO<sub>2</sub> **5.6**

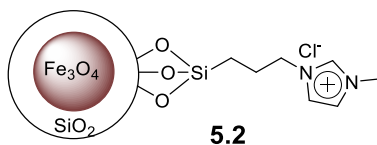
The Fe<sub>3</sub>O<sub>4</sub>@SiO<sub>2</sub> **5.6** was prepared following the method reported by Fan *et al*<sup>257</sup>. In brief, to a stirred suspension of Fe<sub>3</sub>O<sub>4</sub> **5.4** (0.4 g) and TEOS **5.5** (0.36 g) in dry EtOH (3 mL) at 50 °C was added a mixture of NH<sub>4</sub>OH **5.3** (0.66 mL, 13.2 M), EtOH (1.2 mL) and water (0.58 mL). The reaction was set to stir for 8 h at 50 °C and at the end of which the product suspension was left to cool to room temperature. The solids obtained were separated with a magnet, washed with water (25 mL x 3) and finally dried *in vacuo* at 70 °C to give **5.6** as a black solid.  $\nu(\text{cm}^{-1})$ : 1168 and 1069 (Si-O-Si stretch), 575 (Si-O-Fe).

### 7.5.3 Synthesis of Triethoxysilylpropylimidazolium chloride **5.9**



The siloxyimidazolium chloride **5.9** was accessed following a protocol reported by Abdolmohammad-Zadeh and Javan.<sup>164</sup> Hence, a mixture of *N*-methylimidazole **5.8** (4.8 mL, 0.06 mol) and 3-chloropropyltriethoxysilane **5.7** (9 mL, 0.04 mol) was refluxed at 90°C for 96 h, after which the crude product was left to cool to room temperature. This crude product was washed with dry diethyl ether (200 mL x 3) and dried *in-vacuo* at room temperature to give **5.9** as a brown oil. Yield: 10.27 g (53 %),  $\nu(\text{cm}^{-1})$ : 2976 – 2885 (C-H stretch), 1648 (C=C stretch), 1572 (C=N stretch), 1450 and 1387 (C-H bend), 1167 and 1066 (Si-O-Si stretch), <sup>1</sup>H NMR (300 MHz, DMSO-d<sub>6</sub>)  $\delta$  9.35 (s, 1H, NCHN), 7.80 (d, *J* = 6.0 Hz, 2H, NCHCHN), 4.16 (t, *J* = 6.5 Hz, 2H, CH<sub>2</sub>CH<sub>2</sub>N), 3.87 (s, 3H, CHNCH<sub>3</sub>), 3.74 (q, *J* = 6.5 Hz, 6H, CH<sub>3</sub>CH<sub>2</sub>O), 1.81 (m, 2H, CH<sub>2</sub>CH<sub>2</sub>CH<sub>2</sub>), 1.14 (t, *J* = 6.5 Hz, 9H, CH<sub>3</sub>CH<sub>2</sub>O), 0.51 (t, *J* = 6.5 Hz, 2H, SiCH<sub>2</sub>CH<sub>2</sub>CH<sub>2</sub>). <sup>13</sup>C NMR (75 MHz, DMSO-d<sub>6</sub>)  $\delta$  136.7 (NCHN) 123.6 (NCHCHN), 122.2 (NCHCHN), 57.8 (CH<sub>2</sub>CH<sub>2</sub>O), 51.0 (CH<sub>3</sub>CH<sub>2</sub>N), 35.7 (CHNCH<sub>3</sub>), 23.7 (CH<sub>2</sub>CH<sub>2</sub>CH<sub>2</sub>), 18.2 (CH<sub>3</sub>CH<sub>2</sub>O), 6.7 (SiCH<sub>3</sub>CH<sub>3</sub>), *m/z* (ESI) [M+Na]<sup>+</sup> 348.

## 7.5.4 Synthesis of Fe<sub>3</sub>O<sub>4</sub>@SiO<sub>2</sub>@siloxymidazolium chloride 5.2



The Fe<sub>3</sub>O<sub>4</sub>@SiO<sub>2</sub>@siloxymidazolium chloride **5.2** was prepared by the method reported by Chen *et al.*<sup>258</sup> In summary, Fe<sub>3</sub>O<sub>4</sub>@SiO<sub>2</sub> **5.6** (1.5 g) was dissolved in toluene (300 mL) and sonicated at room temperature for 10 min. Also, siloxymidazolium chloride **5.9** (15.40 g) was dissolved in toluene (100 mL) and sonicated at room temperature for 10 min. The siloxymidazolium chloride **5.9** solution was then added to the **5.6** and the mixture was refluxed at 120° C for 48 h. After 48 h, reaction mixture was left to cool to room temperature and supernatant was decanted. The solid left behind was then washed with deionized water (250 mL x 2) and EtOH (250 mL x 3) and finally dried *in vacuo* at 70°C to give **5.2** as a black solid.  $\nu(\text{cm}^{-1})$ : 1645 (C=C stretch), 1558 (C=N stretch), 1448 (C-H bend), 1168 and 1069 (Si-O-Si stretch), 554 (Fe-O).

### 7.5.4.1 Determination of surface coverage by siloxymidazolium chloride 5.9 in 5.2<sup>242</sup>

$$\text{No of molecules per nm}^2 = \frac{W \times d_{\text{Fe}_3\text{O}_4} \times r \times N_A}{M(1-W) \times 3 \times 10^{21}}$$

Where  $W$  is the weight loss of sample = 7 %,  $d_{\text{Fe}_3\text{O}_4}$  is the density of the Fe<sub>3</sub>O<sub>4</sub> = 5.17 g/cm<sup>3</sup>,  $N_A$  is the avogadro's constant = 6.022 x 10<sup>23</sup>,  $M$  is the molecular weight of oleic acid = 325 g/mol,  $r$  is the radius of the Fe<sub>3</sub>O<sub>4</sub>@SiO<sub>2</sub> = 18.5 nm.

$$\text{No of molecules per nm}^2 = 2.22$$

## 7.5.5 Competitive metal extraction

### 7.5.5.1 Control study

For the control study, a 500 mL, aqueous solution containing 1 ppm Ag<sup>+</sup> in 0.023 M NaNO<sub>3</sub> was prepared from a 500 ppm stock solution. Afterwards, 20 mg of extractants (Fe<sub>3</sub>O<sub>4</sub> **5.4**, Fe<sub>3</sub>O<sub>4</sub>@SiO<sub>2</sub> **5.6** and Fe<sub>3</sub>O<sub>4</sub>@SiO<sub>2</sub>@siloxymidazolium chloride **5.2**) were separately

contacted with 10 mL, 1 ppm Ag<sup>+</sup> aqueous metal solution at pH 1 inside a 30 mL plastic screw cap vial. After 45 min. The solids were magnetically separated in about 2 min and the supernatant was carefully removed using a 12 mL plastic syringe and prepared for metal content determination by ICP-OES.

#### 7.5.5.2 Optimization of Ag<sup>+</sup> extraction (pH, time and dosage)

For the effect of pH study, 10 mg of Fe<sub>3</sub>O<sub>4</sub>@SiO<sub>2</sub>@siloxymidazolium chloride **5.2** was contacted with 10 mL aqueous solution containing equal concentrations of Cu<sup>2+</sup>, Ag<sup>+</sup> and Pb<sup>2+</sup> (2 ppm) in 0.023 M NaNO<sub>3</sub> in the pH range of 1 – 5, for 45 min. The solution pH was adjusted to the desired value using HNO<sub>3</sub> or NaOH solutions. Contact time study was undertaken by contacting 10 mg of **5.2** with 10 mL aqueous solution containing equal concentrations of Cu<sup>2+</sup>, Ag<sup>+</sup> and Pb<sup>2+</sup> (2 ppm) in 0.023 M NaNO<sub>3</sub> at pH 1 from 0 to 90 mins. Effect of extractant dose was undertaken by contacting increasing amounts of **5.2** (5 – 80 mg) with 10 mL aqueous solution containing equal concentrations of Cu<sup>2+</sup>, Ag<sup>+</sup> and Pb<sup>2+</sup> (2 ppm) in 0.023 M NaNO<sub>3</sub> at pH 1 for 45 min. All studies were undertaken in triplicates.

The extraction efficiency of the extractants for Ag<sup>+</sup> was determined by the equation below;

$$\% EE = \frac{C_i - C_f}{C} \times 100$$

Where % EE is percentage extraction efficiency, C<sub>i</sub> and C<sub>f</sub> are the initial and final metal ion concentrations respectively.

#### 7.5.5.3 Stripping efficiency

For the stripping efficiency study, Ag<sup>+</sup>-impregnated Fe<sub>3</sub>O<sub>4</sub>@SiO<sub>2</sub>@siloxymidazolium chloride **5.2** (from the contact time study) were washed with de-ionized water and magnetically separated after which it was contacted with 5 mL of stripping agent (HCl, HNO<sub>3</sub> or thiourea) inside screw-capped plastic vials for 1 h. Thereafter, the extractant were magnetically separated and the supernatant stripping agent solution was carefully removed using a plastic syringe. The stripping agent solution was made up to 10 mL by adding deionized water and the content was determined again by ICP-OES. The experiments were

undertaken in triplicates. The stripping efficiency of  $\text{Ag}^+$  by a stripping agent was determined following the equation;

$$\%SE = \frac{C_e}{C_i} \times 100$$

Where  $\% SE$  is percentage stripping efficiency,  $C_e$  represents the concentration of  $\text{Ag}^+$  extracted by the stripping agent ( $\text{Ag}^+$  concentration in the stripping agent solution) and  $C_i$  represents the initial  $\text{Ag}^+$  concentration respectively (concentration of  $\text{Ag}^+$  in extractant prior to stripping).

**Table 7.19: ICP-OES calibration data for the metal extraction experiment by  $\text{Fe}_3\text{O}_4@\text{SiO}_2$ @siloxymidazolium chloride 5.2 and  $\text{Ag}^+$  stripping studies different stripping agents**

	<b><math>\text{Cu}^{2+}</math> (324 nm)</b>	<b><math>\text{Ag}^+</math> (338 nm)</b>	<b><math>\text{Pb}^{2+}</math> (217 nm)</b>
<b>Concentration (ppb)</b>	<b>Mean intensities (n = 3)</b>		
0	3185	232	66
25	4245	2097	30
50	8964	4833	68
100	19768	10714	149
250	45100	23751	335
500	89836	47366	686
1000	175292	90750	1350
2500	417593	213612	3185
5000	867714	436300	6544
<b><math>R^2</math></b>	0.9998	0.9999	0.9999
<b>Coefficient of x</b>	172	87	5

**Table 7.20 (a-e): ICP-OES extraction analysis data by Fe<sub>3</sub>O<sub>4</sub>@SiO<sub>2</sub>@siloxymidazolium chloride 5.2 at pH 1.03 – 4.97****Table 7.20a: pH 1.30**

	<b>Cu<sup>2+</sup></b>	<b>Ag<sup>+</sup></b>	<b>Pb<sup>2+</sup></b>
<b>Concentration (ppb)</b>			
Initial	2304±11	1926±10	2388±20
Final	2247±55	87±1	2195±57
<b>Efficiency (%)</b>			
	2.5±2.9	95.5±0.7	8.1±3.2
<b>Selectivity coefficient</b>			
	833.3	-	240.4

**Table 7.20b: pH 2.04**

	<b>Cu<sup>2+</sup></b>	<b>Ag<sup>+</sup></b>	<b>Pb<sup>2+</sup></b>
<b>Concentration (ppb)</b>			
Initial	2304±11	1926±10	2388±20
Final	2237±9	44±0	2177±15
<b>Efficiency (%)</b>			
	2.5±0.9	97.7±0.7	8.9±1.5
<b>Selectivity coefficient</b>			
	1428	-	441.3

**Table 7.20c: pH 3.04**

	<b>Cu<sup>2+</sup></b>	<b>Ag<sup>+</sup></b>	<b>Pb<sup>2+</sup></b>
<b>Concentration (ppb)</b>			
Initial	2304±11	1926±10	2388±20
Final	2189±22	16±4	2116±5
<b>Efficiency (%)</b>			
	5.0±1.4	99.2±0.8	11.4±1.1
<b>Selectivity coefficient</b>			
	2272.3	-	928.7

**Table 7.20d: pH 4.11**

	<b>Cu<sup>2+</sup></b>	<b>Ag<sup>+</sup></b>	<b>Pb<sup>2+</sup></b>
<b>Concentration (ppb)</b>			
Initial	2304±11	1926±10	2388±20
Final	2183±13	80±3	2055±20
<b>Efficiency (%)</b>			
	5.3±1.0	95.8±0.7	13.9±1.7
<b>Selectivity coefficient</b>			
	416.3	-	142.4

**Table 7.20e: pH 4.97**

	<b>Cu<sup>2+</sup></b>	<b>Ag<sup>+</sup></b>	<b>Pb<sup>2+</sup></b>
<b>Concentration (ppb)</b>			
Initial	2304±11	1926±10	2388±20
Final	2112±12	72±2	1686±18
<b>Efficiency (%)</b>			
	8.3±1.0	96.3±0.7	29.4±1.6
<b>Selectivity coefficient</b>			
	283.3	-	61.8

**Table 7.21 (a-g): ICP-OES extraction analysis data by Fe<sub>3</sub>O<sub>4</sub>@SiO<sub>2</sub>@siloxymidazolium chloride 5.2 from 0 to 90 min****Table 7.21a: 0 min**

	<b>Cu<sup>2+</sup></b>	<b>Ag<sup>+</sup></b>	<b>Pb<sup>2+</sup></b>
<b>Concentration (ppb)</b>			
Initial	2304±11	1926±10	2388±20
Final	2240±15	98±2	2204±12
<b>Efficiency (%)</b>			
	2.8±1.1	94.9±0.7	7.7±1.3
<b>Selectivity coefficient</b>			
	652.9	-	223.4

Table 7.21b: 15 min

	<b>Cu<sup>2+</sup></b>	<b>Ag<sup>+</sup></b>	<b>Pb<sup>2+</sup></b>
<b>Concentration (ppb)</b>			
Initial	2304±11	1926±10	2388±20
Final	2196±	80±2	2180±3
<b>Efficiency (%)</b>			
	4.7±1.0	95.8±0.7	8.7±0.8
<b>Selectivity coefficient</b>			
	469.2	-	241.8

Table 7.21c: 30 min

	<b>Cu<sup>2+</sup></b>	<b>Ag<sup>+</sup></b>	<b>Pb<sup>2+</sup></b>
<b>Concentration (ppb)</b>			
Initial	2304±11	1926±10	2388±20
Final	2228±18	96±3	2182±20
<b>Efficiency (%)</b>			
	3.3±1.3	95.0±0.7	8.6±1.7
<b>Selectivity coefficient</b>			
	558.8	-	201.9

Table 7.21d: 45 min

	<b>Cu<sup>2+</sup></b>	<b>Ag<sup>+</sup></b>	<b>Pb<sup>2+</sup></b>
<b>Concentration (ppb)</b>			
Initial	2304±11	1926±10	2388±20
Final	2175±6	77±2	2167±17
<b>Efficiency (%)</b>			
	5.6±0.7	96.0±0.7	9.3±1.6
<b>Selectivity coefficient</b>			
	404.9	-	235.5

Table 7.21e: 60 min

	<b>Cu<sup>2+</sup></b>	<b>Ag<sup>+</sup></b>	<b>Pb<sup>2+</sup></b>
<b>Concentration (ppb)</b>			
Initial	2304±11	1926±10	2388±20
Final	2167±13	93±3	2164±9
<b>Efficiency (%)</b>			
	5.9±1.0	95.2±0.7	9.4±1.2
<b>Selectivity coefficient</b>			
	311.8	-	190.4

Table 7.21f: 75 min

	<b>Cu<sup>2+</sup></b>	<b>Ag<sup>+</sup></b>	<b>Pb<sup>2+</sup></b>
<b>Concentration (ppb)</b>			
Initial	2304±11	1926±10	2388±20
Final	2154±7	75±1	2121±9
<b>Efficiency (%)</b>			
	6.5±0.8	96.1±0.7	11.2±1.2
<b>Selectivity coefficient</b>			
	354.4	-	196.1

Table 7.21g: 90 min

	<b>Cu<sup>2+</sup></b>	<b>Ag<sup>+</sup></b>	<b>Pb<sup>2+</sup></b>
<b>Concentration (ppb)</b>			
Initial	2304±11	1926±10	2388±20
Final	2119±18	80±3	2125±11
<b>Efficiency (%)</b>			
	8.0±1.3	95.8±0.7	11.0±0.1
<b>Selectivity coefficient</b>			
	264.3	-	186.4

**Table 7.22 (a-e): ICP-OES extraction analysis data by Fe<sub>3</sub>O<sub>4</sub>@SiO<sub>2</sub>@siloxymidazolium chloride 5.2 using 5 – 80 mg**

**Table 7.22a: 5 mg**

	<b>Cu<sup>2+</sup></b>	<b>Ag<sup>+</sup></b>	<b>Pb<sup>2+</sup></b>
<b>Concentration (ppb)</b>			
Initial	2285±9	2417±7	2275±3
Final	2229±43	314±6	2213±22
<b>Efficiency (%)</b>			
	2.6±2.3	87.0±0.6	2.7±1.1
<b>Selectivity coefficient</b>			
	35.8	-	32.1

**Table 7.22b: 10 mg**

	<b>Cu<sup>2+</sup></b>	<b>Ag<sup>+</sup></b>	<b>Pb<sup>2+</sup></b>
<b>Concentration (ppb)</b>			
Initial	2285±9	2417±7	2275±3
Final	2212±43	166±2	2174±12
<b>Efficiency (%)</b>			
	3.3±2.4	93.1±0.5	4.4±0.7
<b>Selectivity coefficient</b>			
	29.3	-	21.0

**Table 7.22c: 20 mg**

	<b>Cu<sup>2+</sup></b>	<b>Ag<sup>+</sup></b>	<b>Pb<sup>2+</sup></b>
<b>Concentration (ppb)</b>			
Initial	2285±9	2417±7	2275±3
Final	2207±40	85±4	2194±71
<b>Efficiency (%)</b>			
	3.4±2.1	96.5±5.3	3.6±3.3
<b>Selectivity coefficient</b>			
	28.3	-	27.2

**Table 7.22d: 40 mg**

	<b>Cu<sup>2+</sup></b>	<b>Ag<sup>+</sup></b>	<b>Pb<sup>2+</sup></b>
<b>Concentration (ppb)</b>			
Initial	2285±9	2417±7	2275±3
Final	2169±10	36±1	2110±10
<b>Efficiency (%)</b>			
	5.1±0.8	98.5±0.4	7.3±0.6
<b>Selectivity coefficient</b>			
	19.5	-	13.6

**Table 7.22e: 80 mg**

	<b>Cu<sup>2+</sup></b>	<b>Ag<sup>+</sup></b>	<b>Pb<sup>2+</sup></b>
<b>Concentration (ppb)</b>			
Initial	2285±9	2417±7	2275±3
Final	2176±61	12±2	2089±43
<b>Efficiency (%)</b>			
	4.6±3.1	99.5±0.5	8.3±2.0
<b>Selectivity coefficient</b>			
	21.5	-	12.2

**Table 7.23: ICP-OES extraction analysis data of the stripping of Ag<sup>+</sup> by different stripping agents**

	<b>Stripping agent</b>				
	0.6 M HCl	3.0 M HCl	0.6 M HNO <sub>3</sub>	3.0 M HNO <sub>3</sub>	0.6 M thiourea
<b>Concentration (ppb)</b>					
Initial	1828±104	1846±104	1830±105	1849±104	5468±44
Final	306±65	1098±81	429±65	572±55	4669±58
<b>Stripping efficiency (%)</b>					
	16.7±3.7	59.5±5.5	23.4±3.8	30.9±3.4	85.4±1.3

## References

- 1 M. Grimwade, *Introduction to precious metals : metallurgy for jewelers & silversmiths*, Brynmorgen Press, 2009.
- 2 A. Kędziora, M. Speruda, E. Krzyżewska, J. Rybka, A. Łukowiak and G. Bugła-Płoskońska, *Int. J. Mol. Sci.*, 2018, **19**, 444.
- 3 J. Emsley, *Nature's building blocks, An A-Z guide to the elements*, Oxford University Press, Oxford, New Editio., 2011.
- 4 M. Sahan, M. A. Kucuker, B. Demirel, K. Kuchta and A. Hursthouse, *Int. J. Environ. Res. Public Health*, 2019, **16**, 887.
- 5 G. Taillades and J. Sarradin, *J. Power Sources*, 2004, **125**, 199–205.
- 6 B. W. C. Buttermann and H. E. Hilliard, *Mineral Commodity Profiles: Silver*, Virginia, 2005.
- 7 B. Boonkaew, M. Kempf, R. Kimble, P. Supaphol and L. Cuttle, *Burns*, 2014, **40**, 89–96.
- 8 N. Kolpakova, Z. Sabitova, V. Sachkov, R. Medvedev, R. Nefedov and V. Orlov, *Minerals*, 2019, **9**, 78.
- 9 K. Avarmaa, L. Klemettinen, H. O'Brien and P. Taskinen, *Miner. Eng.*, 2019, **133**, 95–102.
- 10 M. Zhao, Y. Xu, C. Zhang, H. Rong and G. Zeng, *Appl. Microbiol. Biotechnol.*, 2016, **100**, 6509–6518.
- 11 F. Fu and Q. Wang, *J. Environ. Manage.*, 2011, **92**, 407–18.
- 12 C. F. Carolin, P. S. Kumar, A. Saravanan, G. J. Joshiba and M. Naushad, *J. Environ. Chem. Eng.*, 2017, **5**, 2782–2799.
- 13 F. Ahlatcı, E. Koç, E. Y. Yazıcı, O. Celep and H. Deveci, *XV. Int. Miner. Process. Symp. Exhib.*, 2016, 750–760.
- 14 P. Ratanamskul, C., Lertviriyaprapa, K. and Saiyasitpanich, in *Ninth International Conference of Greening of Industry Network*, Bangkok, 2001, vol. 2, pp. 2–8.
- 15 N. Chitpong and S. M. Husson, *J. Memb. Sci.*, 2017, **523**, 418–429.
- 16 T. A. Kurniawan, G. Y. S. Chan, W. H. Lo and S. Babel, *Chem. Eng. J.*, 2006, **118**, 83–98.
- 17 M. A. Barakat and E. Schmidt, *Desalination*, 2010, **256**, 90–93.
- 18 M. Zanain and R. Lovitt, *E3S Web Conf.*, 2013, **1**, 25005.
- 19 W. H. Holl, *Encycl. Sep. Sci.*, 2000, 4477–4484.
- 20 S. Virolainen, M. Tyster, M. Haapalainen and T. Sainio, *Hydrometallurgy*, 2015, **152**, 100–106.
- 21 S. Y. Kang, J. U. Lee, S. H. Moon and K. W. Kim, *Chemosphere*, 2004, **56**, 141–147.
- 22 M. Bilal, J. A. Shah, T. Ashfaq, S. M. H. Gardazi, A. A. Tahir, A. Pervez, H. Haroon and Q. Mahmood, *J. Hazard. Mater.*, 2013, **263**, 322–333.

References

- 23 C. An, G. Huang, Y. Yao and S. Zhao, *Sci. Total Environ.*, 2017, **579**, 537–556.
- 24 G. Chen, *Sep. Purif. Technol.*, 2004, **38**, 11–41.
- 25 Z. Al-Qodah and M. Al-Shannag, *Sep. Sci. Technol.*, 2017, **52**, 2649–2676.
- 26 I. Heidmann and W. Calmano, *J. Hazard. Mater.*, 2008, **152**, 934–941.
- 27 T. Ölmez, *J. Hazard. Mater.*, 2009, **162**, 1371–1378.
- 28 J. R. Parga, D. L. Cocke, J. L. Valenzuela, J. A. Gomes, M. Kesmez, G. Irwin, H. Moreno and M. Weir, *J. Hazard. Mater.*, 2005, **124**, 247–254.
- 29 A. Shafaei, M. Rezayee, M. Arami and M. Nikazar, *Desalination*, 2010, **260**, 23–28.
- 30 I. Kabdaşli, T. Arslan, T. Ölmez-Hanci, I. Arslan-Alaton and O. Tünay, *J. Hazard. Mater.*, 2009, **165**, 838–845.
- 31 A. V. Kolesnikov, V. V. Kuznetsov, V. A. Kolesnikov and Y. I. Kapustin, *Theor. Found. Chem. Eng.*, 2015, **49**, 1–9.
- 32 K. A. Selim, F. I. El Hosiny, M. A. A. Khalek and I. Osama, *Colloid Surf. Sci.*, 2017, **2**, 47–53.
- 33 I. De Oliveira Da Mota, J. A. De Castro, R. De Góes Casqueira and A. G. De Oliveira Junior, *J. Mater. Res. Technol.*, 2015, **4**, 109–113.
- 34 A. Lambert, P. Drogui, R. Daghrir, F. Zaviska and M. Benzaazoua, *J. Environ. Manage.*, 2014, **133**, 78–85.
- 35 J. H. Chang, A. V. Ellis, C. T. Yan and C. H. Tung, *Sep. Purif. Technol.*, 2009, **68**, 216–221.
- 36 J. Paul Chen and L. L. Lim, *Chemosphere*, 2005, **60**, 1384–1392.
- 37 I. C. Agarwal, A. M. Rochon, H. D. Gesser and A. B. Sparling, *Water Res.*, 1984, **18**, 227–232.
- 38 A. T. Ojedokun and O. S. Bello, *Water Resour. Ind.*, 2016, **13**, 7–13.
- 39 A. Ewecharoen, P. Thiravetyan, E. Wendel and H. Bertagnolli, *J. Hazard. Mater.*, 2009, **171**, 335–339.
- 40 A. Demirbas, *J. Hazard. Mater.*, 2008, **157**, 220–229.
- 41 M. Pettinato, S. Chakraborty, H. A. Arafat and V. Calabro', *Ecotoxicol. Environ. Saf.*, 2015, **121**, 57–62.
- 42 P. SenthilKumar, S. Ramalingam, V. Sathyaselvabala, S. D. Kirupha and S. Sivanesan, *Desalination*, 2011, **266**, 63–71.
- 43 M. A. Hossain, H. H. Ngo, W. S. Guo and T. V. Nguyen, *Bioresour. Technol.*, 2012, **113**, 97–101.
- 44 A. A.D, O. O.U, O. O.O and A. I.A, *IOSR J. Appl. Chem.*, 2017, **10**, 30–39.
- 45 E. Pehlivan, T. Altun and S. Parlayici, *Food Chem.*, 2012, **135**, 2229–2234.
- 46 N. C. Feng and X. Y. Guo, *Trans. Nonferrous Met. Soc. China (English Ed.)*, 2012, **22**, 1224–1231.
- 47 R. Apiratikul and P. Pavasant, *Bioresour. Technol.*, 2008, **99**, 2766–2777.
- 48 M. Rajfur, A. Kłos and M. Waclawek, *Bioelectrochemistry*, 2012, **87**, 65–70.

References

- 49 V. J. P. Vilar, C. M. S. Botelho and R. A. R. Boaventura, *Bioresour. Technol.*, 2008, **99**, 750–762.
- 50 L. C. Ajjabi and L. Chouba, *J. Environ. Manage.*, 2009, **90**, 3485–3489.
- 51 A. Singh, D. Kumar and J. P. Gaur, *J. Hazard. Mater.*, 2008, **152**, 1011–1019.
- 52 G. M. Zeng, M. H. Zhao, D. L. Huang, C. Lai, C. Huang, Z. Wei, P. Xu, N. J. Li, C. Zhang, F. L. Li and M. Cheng, *Int. Biodeterior. Biodegrad.*, 2013, **85**, 166–172.
- 53 M. Zhao, Z. Zeng, G. Zeng, D. Huang, C. Feng, C. Lai, C. Huang, Z. Wei, N. Li, P. Xu, C. Zhang, Z. Liu and G. Xie, *Biochem. Eng. J.*, 2012, **67**, 132–139.
- 54 C. Chen and J. Wang, *J. Hazard. Mater.*, 2008, **151**, 65–70.
- 55 T. Şahan, H. Ceylan, N. Şahiner and N. Aktaş, *Bioresour. Technol.*, 2010, **101**, 4520–4526.
- 56 H. Huo, H. Su and T. Tan, *Chem. Eng. J.*, 2009, **150**, 139–144.
- 57 K. Z. Elwakeel, G. O. El-Sayed and R. S. Darweesh, *Int. J. Miner. Process.*, 2013, **120**, 26–34.
- 58 L. Zhang, S. Yang, T. Han, L. Zhong, C. Ma, Y. Zhou and X. Han, *Appl. Surf. Sci.*, 2012, **263**, 696–703.
- 59 A. Kongsuwan, P. Patnukao and P. Pavasant, *J. Ind. Eng. Chem.*, 2009, **15**, 465–470.
- 60 Y. Sudaryanto, S. B. Hartono, W. Irawaty, H. Hindarso and S. Ismadji, *Bioresour. Technol.*, 2006, **97**, 734–739.
- 61 R. Baccar, J. Bouzid, M. Feki and A. Montiel, *J. Hazard. Mater.*, 2009, **162**, 1522–1529.
- 62 M. Momčilović, M. Purenović, A. Bojić, A. Zarubica and M. Randelovid, *Desalination*, 2011, **276**, 53–59.
- 63 E. S. I. El-Shafey and S. M. Z. Al-Kindy, *Environ. Technol. (United Kingdom)*, 2013, **34**, 395–406.
- 64 K. M. Mena Aguilar, Y. Amano and M. Machida, *J. Environ. Chem. Eng.*, 2016, **4**, 4644–4652.
- 65 H. Tounsadi, A. Khalidi, A. Machrouhi, M. Farnane, R. Elmoubarki, A. Elhalil, M. Sadiq and N. Barka, *J. Environ. Chem. Eng.*, 2016, **4**, 4549–4564.
- 66 S. Iijima, *Nature*, 1991, **354**, 56–58.
- 67 B. Hayati, A. Maleki, F. Najafi, H. Daraei, F. Gharibi and G. McKay, *J. Mol. Liq.*, 2016, **224**, 1032–1040.
- 68 H. Wang, A. Zhou, F. Peng, H. Yu and J. Yang, *J. Colloid Interface Sci.*, 2007, **316**, 277–283.
- 69 Ihsanullah, F. A. Al-Khalidi, B. Abu-Sharkh, A. M. Abulkibash, M. I. Qureshi, T. Laoui and M. A. Atieh, *Desalin. Water Treat.*, 2016, **57**, 7232–7244.
- 70 Y. Li, F. Liu, B. Xia, Q. Du, P. Zhang, D. Wang, Z. Wang and Y. Xia, *J. Hazard. Mater.*, 2010, **177**, 876–880.
- 71 Y. Xue, S. Wu and M. Zhou, *Chem. Eng. J.*, 2013, **231**, 355–364.
- 72 T. K. Naiya, A. K. Bhattacharya and S. K. Das, *J. Hazard. Mater.*, 2009, **170**, 252–

- 262.
- 73 J. K. Bediako, W. Wei and Y. S. Yun, *J. Ind. Eng. Chem.*, 2016, **43**, 61–68.
- 74 M. S. Al-Harashseh, K. Al Zboon, L. Al-Makhadmeh, M. Hararah and M. Mahasneh, *J. Environ. Chem. Eng.*, 2015, **3**, 1669–1677.
- 75 E. P. Kuncoro and M. Z. Fahmi, *Procedia Earth Planet. Sci.*, 2013, **6**, 377–382.
- 76 A. Bhatnagar and A. K. Minocha, *Chem. Eng. J.*, 2009, **150**, 145–151.
- 77 A. Agrawal and K. K. Sahu, *J. Hazard. Mater.*, 2006, **137**, 915–924.
- 78 R. Taman, M. E. Ossman, M. S. Mansour and H. A. Farag, *J. Adv. Chem. Eng.*, 2015, **5**, 1–8.
- 79 P. Xu, G. M. Zeng, D. L. Huang, C. L. Feng, S. Hu, M. H. Zhao, C. Lai, Z. Wei, C. Huang, G. X. Xie and Z. F. Liu, *Sci. Total Environ.*, 2012, **424**, 1–10.
- 80 G. A. Seisenbaeva, G. Daniel, J. M. Nedelec, Y. K. Gun'Ko and V. G. Kessler, *J. Mater. Chem.*, 2012, **22**, 20374–20380.
- 81 J. Mukherjee, J. Ramkumar, S. Chandramouleeswaran, R. Shukla and A. K. Tyagi, *J. Radioanal. Nucl. Chem.*, 2013, **297**, 49–57.
- 82 Y. Cai, C. Li, D. Wu, W. Wang, F. Tan, X. Wang, P. K. Wong and X. Qiao, *Chem. Eng. J.*, 2017, **312**, 158–166.
- 83 P. K. Stoimenov, R. L. Klinger, G. L. Marchin and K. J. Klabunde, *Langmuir*, 2002, **18**, 6679–6686.
- 84 S. Mahdavi, M. Jalali and A. Afkhami, *Chem. Eng. Commun.*, 2013, **200**, 448–470.
- 85 T. C. Madzokere and A. Karthigeyan, *Mater. Today Proc.*, 2017, **4**, 9–18.
- 86 C. Xiong, W. Wang, F. Tan, F. Luo, J. Chen and X. Qiao, *J. Hazard. Mater.*, 2015, **299**, 664–674.
- 87 J. Feng, L. Zou, Y. Wang, B. Li, X. He, Z. Fan, Y. Ren, Y. Lv, M. Zhang and D. Chen, *J. Colloid Interface Sci.*, 2015, **438**, 259–267.
- 88 S. Anandan, K. Kathiravan, V. Murugesan and Y. Ikuma, *Catal. Commun.*, 2009, **10**, 1014–1019.
- 89 A. M. Youssef and F. M. Malhat, *Macromol. Symp.*, 2014, **337**, 96–101.
- 90 D. NABI, I. ASLAM and I. A. QAZI, *J. Environ. Sci.*, 2009, **21**, 402–408.
- 91 G. A. Seisenbaeva, G. Daniel, V. G. Kessler and J. M. Nedelec, *Chem. - A Eur. J.*, 2014, **20**, 10732–10736.
- 92 H. Hao, M. Stoller, Y. Bao, T. Wang, J. Wang and H. Lu, *Adv. Mater. Sci. Eng.*, 2016, **2016**, 1–10.
- 93 D. E. Giles, M. Mohapatra, T. B. Issa, S. Anand and P. Singh, *J. Environ. Manage.*, 2011, **92**, 3011–3022.
- 94 Z. Saadi, R. Saadi and R. Fazaeli, *J. Nanostructure Chem.*, 2013, **3**, 48.
- 95 S. Tabesh, F. Davar and M. R. Loghman-Estarki, *J. Alloys Compd.*, 2018, **730**, 441–449.
- 96 J. Yang, B. Hou, J. Wang, B. Tian, J. Bi, N. Wang, X. Li and X. Huang,

- Nanomaterials*, 2019, **9**, 424.
- 97 J. Ayawanna, W. T. Teoh, S. Niratisairak and K. Sato, *Mater. Sci. Semicond. Process.*, 2015, **40**, 136–139.
- 98 S. Recillas, J. Colón, E. Casals, E. González, V. Puentes, A. Sánchez and X. Font, *J. Hazard. Mater.*, 2010, **184**, 425–431.
- 99 P. K. Mishra, A. Saxena, A. S. Rawat, P. K. Dixit, R. Kumar and P. K. Rai, *Environ. Prog. Sustain. Energy*, 2018, **37**, 221–231.
- 100 K. Y. Kumar, H. B. Muralidhara, Y. A. Nayaka, J. Balasubramanyam and H. Hanumanthappa, *Powder Technol.*, 2013, **246**, 125–136.
- 101 X. Huangfu, J. Jiang, X. Lu, Y. Wang, Y. Liu, S. Y. Pang, H. Cheng, X. Zhang and J. Ma, *Water. Air. Soil Pollut.*, 2015, **226**, 1–9.
- 102 T. Sheela, Y. A. Nayaka, R. Viswanatha, S. Basavanna and T. G. Venkatesha, *Powder Technol.*, 2012, **217**, 163–170.
- 103 M. Hemmati, M. Rajabi and A. Asghari, *Microchim. Acta*, 2018, **185**, 1–32.
- 104 J. Wang, S. Zheng, Y. Shao, J. Liu, Z. Xu and D. Zhu, *J. Colloid Interface Sci.*, 2010, **349**, 293–299.
- 105 Y. Jeong, M. Fan, S. Singh, C. L. Chuang, B. Saha and J. Hans van Leeuwen, *Chem. Eng. Process. Process Intensif.*, 2007, **46**, 1030–1039.
- 106 T. K. Jain, M. A. Morales, S. K. Sahoo, D. L. Leslie-Pelecky and V. Labhsetwar, *Mol. Pharm.*, 2005, **2**, 194–205.
- 107 I. Chourpa, L. Douziech-Eyrolles, L. Ngaboni-Okassa, J. F. Fouquenot, S. Cohen-Jonathan, M. Soucé, H. Marchais and P. Dubois, *Analyst*, 2005, **130**, 1395–1403.
- 108 N. D. Cuong, N. D. Hoa, T. T. Hoa, D. Q. Khieu, D. T. Quang, V. Van Quang and N. Van Hieu, *J. Alloys Compd.*, 2014, **582**, 83–87.
- 109 C. Corot, P. Robert, J. M. Idée and M. Port, *Adv. Drug Deliv. Rev.*, 2006, **58**, 1471–1504.
- 110 J. W. M. Bulte, *Magn. Reson. Imaging*, 2006, **124**, 419–439.
- 111 M. Mahmoudi, S. Sant, B. Wang, S. Laurent and T. Sen, *Adv. Drug Deliv. Rev.*, 2011, **63**, 24–46.
- 112 L. Mohammed, H. G. Gomaa, D. Ragab and J. Zhu, *Particuology*, 2017, **30**, 1–14.
- 113 D. Horák, M. Babič, H. Macková and M. J. Beneš, *J. Sep. Sci.*, 2007, **30**, 1751–1772.
- 114 Y. Amemiya, A. Arakaki, S. S. Staniland, T. Tanaka and T. Matsunaga, *Biomaterials*, 2007, **28**, 5381–5389.
- 115 S. A. M. K. Ansari, E. Ficiarà, F. A. Ruffinatti, I. Stura, M. Argenziano, O. Abollino, R. Cavalli, C. Guiot and F. D’Agata, *Materials (Basel)*, 2019, **12**, 1–24.
- 116 N. A. Frey, S. Peng, K. Cheng and S. Sun, *Chem. Soc. Rev.*, 2009, **38**, 2532–2542.
- 117 W. Glasgow, B. Fellows, B. Qi, T. Darroudi, C. Kitchens, L. Ye, T. M. Crawford and O. T. Mefford, *Particuology*, 2016, **26**, 47–53.
- 118 T. Hyeon, Su Seong Lee, J. Park, Y. Chung and Hyon Bin Na, *J. Am. Chem. Soc.*, 2001, **123**, 12798–12801.

References

- 119 R. Hufschmid, H. Arami, R. M. Ferguson, M. Gonzales, E. Teeman, L. N. Brush, N. D. Browning and K. M. Krishnan, *Nanoscale*, 2015, **7**, 11142–11154.
- 120 X. Sun, C. Zheng, F. Zhang, Y. Yang, G. Wu, A. Yu and N. Guan, *J. Phys. Chem. C*, 2009, **113**, 16002–16008.
- 121 G. Gao, R. Shi, W. Qin, Y. Shi, G. Xu, G. Qiu and X. Liu, *J. Mater. Sci.*, 2010, **45**, 3483–3489.
- 122 K. Kekalo, K. Koo, E. Zeitchick and I. Baker, *Mater. Res. Soc. Symp. Proc.*, 2012, **1416**, 61–66.
- 123 M. Darbandi, F. Stromberg, J. Landers, N. Reckers, B. Sanyal, W. Keune and H. Wende, *J. Phys. D. Appl. Phys.*, 2012, **45**, 1–11.
- 124 C. Okoli, M. Boutonnet, L. Mariey, S. Järås and G. Rajarao, *J. Chem. Technol. Biotechnol.*, 2011, **86**, 1386–1393.
- 125 W. Wu, Z. Wu, T. Yu, C. Jiang and W.-S. Kim, *Sci. Technol. Adv. Mater.*, 2015, **16**, 023501.
- 126 W. Guangshuo, M. Yingying, T. Yu and D. Xufeng, *Smart Mater. Struct.*, 2016, **25**, 35028.
- 127 S. Laurent, D. Forge, M. Port, A. Roch, C. Robic, L. Vander Elst and R. N. Muller, *Chem. Rev.*, 2008, **108**, 2064–2110.
- 128 A. H. M. Yusoff, M. N. Salimi and M. F. JamLos, *AIP Conf. Proc.*, 2017, **1835**, 1–5.
- 129 R. Ahmadi, E. Ranjarnodeh and N. Gu, *Mater. Sci. Pol.*, 2012, **30**, 382–389.
- 130 T. Saragi, B. L. Depi, S. Butarbutar, B. Permana and Risdiana, in *4th International seminar of Mathematics, Science and Computer Science Education*, 2018, vol. 1013, pp. 1–4.
- 131 C. H. Chia, S. Zakaria, R. Farahiyah and S. Ahmad, *Sains Malaysiana*, 2008, **37**, 389–394.
- 132 J. M. Niu and Z. G. Zheng, *Adv. Mater. Res.*, 2014, **900**, 172–176.
- 133 I. N. Bhattacharya, J. K. Pradhan, P. K. Gochhayat and S. C. Das, *Int. J. Miner. Process.*, 2002, **65**, 109–124.
- 134 L. Babes, B. Denizot, G. Tanguy, J. J. Le Jeune and P. Jallet, *J. Colloid Interface Sci.*, 1999, **212**, 474–482.
- 135 J. P. Jolivet, P. Belleville, E. Tronc and J. Livage, *Clays Clay Miner.*, 1992, **40**, 531–539.
- 136 M. Mahdavi, M. B. Ahmad, M. J. Haron, F. Namvar, B. Nadi and J. Ab Rahman, M.Z. and Amin, *Molecules*, 2013, **18**, 7533–7548.
- 137 Sunaryono, A. Taufiq, Mashuri, S. Pratapa, M. Zainuri, Triwikantoro and Darminto, *Mater. Sci. Forum*, 2015, **827**, 229–234.
- 138 M. Sun, J.; Zhou, S.; Hou, P.; Yang, Y.; Weng, J.; Li, X.; Li, *J. Biomed. Mater. Res. Part. A*, 2006, **10**, 333–341.
- 139 A. P. A. Faiyas, E. M. Vinod, J. Joseph, R. Ganesan and R. K. Pandey, *J. Magn. Magn. Mater.*, 2010, **322**, 400–404.
- 140 W. L. Tan and M. Abu Bakar, *J. Phys. Sci.*, 2006, **17**, 37–50.

## References

- 141 Y. B. Sun, Q. Wang, S. T. Yang, G. D. Sheng and Z. Q. Guo, *J. Radioanal. Nucl. Chem.*, 2011, **290**, 643–648.
- 142 Y. H. Chen and F. A. Li, *J. Colloid Interface Sci.*, 2010, **347**, 277–281.
- 143 H. I. Adegoke, F. AmooAdekola, O. S. Fatoki and B. J. Ximba, *Korean J. Chem. Eng.*, 2014, **31**, 142–154.
- 144 H. J. Shipley, K. E. Engates and V. A. Grover, *Environ. Sci. Pollut. Res.*, 2013, **20**, 1727–1736.
- 145 M. Hemmati, M. Rajabi and A. Asghari, *Microchim. Acta*, 2018, **185**, 1–32.
- 146 M. Amjadi, A. Samadi and J. L. Manzoori, *Microchim. Acta*, 2015, **182**, 1627–1633.
- 147 M. R. Sohrabi, Z. Matbouie, A. A. Asgharinezhad and A. Dehghani, *Microchim. Acta*, 2013, **180**, 589–597.
- 148 M. Taghizadeh, A. A. Asgharinezhad, M. Pooladi, M. Barzin, A. Abbaszadeh and A. Tadjarodi, *Microchim. Acta*, 2013, **180**, 1073–1084.
- 149 Y. Wang, J. Xie, Y. Wu and X. Hu, *Microchim. Acta*, 2014, **181**, 949–956.
- 150 S. E. Moradi, A. M. H. Shabani, S. Dadfarnia and S. Emami, *Anal. Methods*, 2016, **8**, 6337–6346.
- 151 J. F. Liu, Z. S. Zhao and G. Bin Jiang, *Environ. Sci. Technol.*, 2008, **42**, 6949–6954.
- 152 F. J. Stevenson, *Humus chemistry: genesis, composition, reactions.*, John Wiley and Sons Inc., New York, 2nd edn., 1994.
- 153 S. R. Chowdhury and E. K. Yanful, *J. Environ. Manage.*, 2010, **91**, 2238–2247.
- 154 L. Feng, M. Cao, X. Ma, Y. Zhu and C. Hu, *J. Hazard. Mater.*, 2012, **217–218**, 439–446.
- 155 M. Behbahani, A. A. Akbari, M. M. Amini and A. Bagheri, *Anal. Methods*, 2014, **6**, 8785–8792.
- 156 M. Taghizadeh, A. A. Asgharinezhad, N. Samkhaniyany, A. Tadjarodi, A. Abbaszadeh and M. Pooladi, *Microchim. Acta*, 2014, **181**, 597–605.
- 157 M. Manoochehri and L. Naghibzadeh, *Food Anal. Methods*, 2017, **10**, 1777–1786.
- 158 S. Bahar and F. Karami, *J. Iran. Chem. Soc.*, 2015, **12**, 2213–2220.
- 159 E. Aliyari, M. Alvand and F. Shemirani, *Anal. Methods*, 2015, **7**, 7582–7589.
- 160 S. Zhang, Y. Zhang, J. Liu, Q. Xu, H. Xiao, X. Wang, H. Xu and J. Zhou, *Chem. Eng. J.*, 2013, **226**, 30–38.
- 161 R. Roto, Y. Yusran and A. Kuncaka, *Appl. Surf. Sci.*, 2016, **377**, 30–36.
- 162 X. Peng, W. Zhang, L. Gai, H. Jiang and Y. Tian, *Russ. J. Phys. Chem. A*, 2016, **90**, 1656–1664.
- 163 N. Schaeffer, H. Passos, I. Billard, N. Papaiconomou and J. A. P. Coutinho, *Crit. Rev. Environ. Sci. Technol.*, 2018, **48**, 859–922.
- 164 H. Abdolmohammad-Zadeh and Z. Javan, *Microchim. Acta*, 2015, **182**, 1447–1456.
- 165 W. Qian, J. Texter and F. Yan, *Chem. Soc. Rev.*, 2017, **46**, 1124–1159.
- 166 B. E. Gurkan, J. C. De Fuente, E. M. Mindrup, L. E. Ficke, B. F. Goodrich, A. Price,

References

- W. F. Schneider and J. F. Brennecke, *J. Am. Chem. Soc.*, 2010, **132**, 2116–7.
- 167 J. E. Bara, T. K. Carlisle, C. J. Gabriel, D. Camper, A. Finotello, D. L. Gin and R. D. Noble, *Ind. Eng. Chem. Res.*, 2009, **48**, 2739–2751.
- 168 G. Chatel and D. R. Macfarlane, *Chem. Soc. Rev.*, 2014, **43**, 8132–8149.
- 169 P. Scovazzo, D. Havard, M. McShea, S. Mixon and D. Morgan, *J. Memb. Sci.*, 2009, **327**, 41–48.
- 170 S. Wickramanayake, D. Hopkinson, C. Myers, L. Hong, J. Feng, Y. Seol, D. Plasynski, M. Zeh and D. Luebke, *J. Memb. Sci.*, 2014, **470**, 52–59.
- 171 Z. Lei, B. Chen, Y.-M. Koo and D. R. MacFarlane, *Chem. Rev.*, 2017, **117**, 6633–6635.
- 172 R. A. van Rantwijk, Fred and Sheldon, *Chem. Rev.*, 2007, **107**, 2757–2785.
- 173 A. Mehdinia, S. Shegefti and F. Shemirani, *Talanta*, 2015, **144**, 1266–1272.
- 174 S. Edmondson, V. L. Osborne and W. T. S. Huck, *Chem. Soc. Rev.*, 2004, **33**, 14–22.
- 175 S. Kalia, S. Kango, A. Kumar, Y. Haldorai, B. Kumari and R. Kumar, *Colloid Polym. Sci.*, 2014, **292**, 2025–2052.
- 176 S. Edmondson, V. L. Osborne and W. T. S. Huck, *Chem. Soc. Rev.*, 2004, **33**, 14–22.
- 177 Z. Dahaghin, H. Z. Mousavi and S. M. Sajjadi, *Food Chem.*, 2017, **237**, 275–281.
- 178 A. Mehdinia, Z. Shoormeij and A. Jabbari, *Microchim. Acta*, 2017, **184**, 1529–1537.
- 179 J. Abolhasani, R. Hosseinzadeh Khanmiri, M. Babazadeh, E. Ghorbani-Kalhor, L. Edjlali and A. Hassanpour, *Environ. Monit. Assess.*, 2015, **187**, 1–11.
- 180 C. Huang, K. G. Neoh and E. T. Kang, *Langmuir*, 2012, **28**, 563–571.
- 181 X. He, X. Wu, X. Cai, S. Lin, M. Xie, X. Zhu and D. Yan, *Langmuir*, 2012, **28**, 11929–11938.
- 182 O. Sayar, N. Akbarzadeh Torbati, H. Saravani, K. Mehrani, A. Behbahani and H. R. Moghadam Zadeh, *J. Ind. Eng. Chem.*, 2014, **20**, 2657–2662.
- 183 L. Fan, C. Luo, M. Sun, X. Li and H. Qiu, *Colloids Surfaces B Biointerfaces*, 2013, **103**, 523–529.
- 184 X. Sun, L. Yang, Q. Li, J. Zhao, X. Li, X. Wang and H. Liu, *Chem. Eng. J.*, 2014, **241**, 175–183.
- 185 N. Ballav, H. J. Choi, S. B. Mishra and A. Maity, *J. Ind. Eng. Chem.*, 2014, **20**, 4085–4093.
- 186 Y. Pang, G. Zeng, L. Tang, Y. Zhang, Y. Liu, X. Lei, Z. Li, J. Zhang and G. Xie, *Desalination*, 2011, **281**, 278–284.
- 187 E. Tahmasebi and Y. Yamini, *Microchim. Acta*, 2014, **181**, 543–551.
- 188 A. Z. M. Badruddoza, Z. B. Z. Shawon, W. J. D. Tay, K. Hidajat and M. S. Uddin, *Carbohydr. Polym.*, 2013, **91**, 322–332.
- 189 K. M. Gregorio-Jauregui, M. G. Pineda, J. E. Rivera-Salinas, G. Hurtado, H. Saade, J. L. Martinez, A. Ilyina and R. G. López, *J. Nanomater.*, 2012, **2012**, 1–8.
- 190 C. Cui, M. He, B. Chen and B. Hu, *Anal. Methods*, 2014, **6**, 8577–8583.

References

- 191 A. P. Paiva, *Sep. Sci. Technol.*, 1993, **28**, 947–1008.
- 192 A. P. Paiva, *Solvent Extr. Ion Exch.*, 2000, **18**, 223–271.
- 193 P. T. Kaye, *S Afr J Sci*, 2011, **107**, 1–8.
- 194 B. S. Fox, M. K. Beyer and V. E. Bondybey, *J. Am. Chem. Soc.*, 2002, **124**, 13613–13623.
- 195 K. Inoue, Y. Ooshita, T. Itaya and H. Nakahara, *Macromol. Chem. Phys.*, 1997, **198**, 3173–3184.
- 196 R. Saha, S. Guha, A. Sahana and D. Das, *J. Anal. Chem.*, 2013, **68**, 398–402.
- 197 D. J. Bray, J. K. Clegg, M. Wenzel, K. Gloe, J. C. McMurtrie, K. A. Jolliffe, K. Gloe and L. F. Lindoy, *Aust. J. Chem.*, 2015, **68**, 549–554.
- 198 A. S. Mohamad Ali, N. A. Razak and I. Ab Rahman, *World Appl. Sci. J.*, 2012, **16**, 1040–1047.
- 199 H. Refiker, M. Merdivan and R. S. Aygün, *Sep. Sci. Technol.*, 2008, **43**, 179–191.
- 200 E. Kazemi, A. M. Haji Shabani and S. Dadfarnia, *Microchim. Acta*, 2015, **182**, 1025–1033.
- 201 M. Ahamed, X. Y. Mbianda, A. F. Mulaba-Bafubiandi and L. Marjanovic, *React. Funct. Polym.*, 2013, **73**, 474–483.
- 202 K. Ohto, E. Murakami, T. Shinohara, K. Shiratsuchi, K. Inoue and M. Iwasaki, *Anal. Chim. Acta*, 1997, **341**, 275–283.
- 203 A. Daubinet and P. T. Kaye, *Synth. Commun.*, 2002, **32**, 3207.
- 204 R. G. Pearson, *J. Chem. Educ.*, 1968, **45**, 581.
- 205 K. C. Sole and J. B. Hiskey, *Hydrometallurgy*, 1992, **30**, 345–365.
- 206 A. Ikeda and S. Shinkai, *Chem. Rev.*, 2002, **97**, 1713–1734.
- 207 Ü. Ocak, H. Alp, P. Gökçe and M. Ocak, *Sep. Sci. Technol.*, 2006, **41**, 391–401.
- 208 M. Shamsipur, B. Hashemi, S. Dehdashtian, M. Mohammadi, M. B. Gholivand, A. Garau and V. Lippolis, *Anal. Chim. Acta*, 2014, **852**, 223–235.
- 209 R. A. Crane, D. E. Sinnett, P. J. Cleall and D. J. Sapsford, *Resour. Conserv. Recycl.*, 2017, **123**, 117–134.
- 210 F. I. Carroll, H. M. Dickson and M. E. Wall, *J. Org. Chem.*, 1965, **30**, 33–38.
- 211 S. H. Chu and H. G. Mautner, *J. Org. Chem.*, 1961, **26**, 4498–4501.
- 212 T. P. Johnston and A. Gallagher, *J. Org. Chem.*, 1963, **28**, 1305–1308.
- 213 A. L. Smith, C. S. Day, L. Que, Y. Zhou and U. Bierbach, *Inorganica Chim. Acta*, 2007, **360**, 2824–2828.
- 214 S. Ghosh and G. P. Tochtrop, *Tetrahedron Lett.*, 2009, **50**, 1723–1726.
- 215 F. I. Carroll, J. D. White and M. E. Wall, *J. Org. Chem.*, 1963, **28**, 1236–1239.
- 216 M. S. Islam, A. Barakat, A. M. Al-Majid, H. A. Ghabbour, A. F. M. M. Rahman, K. Javaid, R. Imad, S. Yousuf and M. I. Choudhary, *Bioorganic Med. Chem.*, 2016, **24**, 1675–1682.

References

- 217 V. K. Manchanda and P. N. Pathak, *Sep. Purif. Technol.*, 2004, **35**, 85–103.
- 218 A. B. Patil, P. N. Pathak, V. S. Shinde and P. K. Mohapatra, *Sep. Sci. Technol.*, 2014, **49**, 2927–2932.
- 219 D. Jańczewski, D. N. Reinhoudt, W. Verboom, E. Malinowska, M. Pietrzak, C. Hill and C. Allignol, *New J. Chem.*, 2007, **31**, 109–120.
- 220 M. Toure, G. Arrachart, J. Duhamet and S. Pellet-Rostaing, *Metals (Basel)*, 2018, **8**, 654.
- 221 Y. Hiruta, T. Watanabe, E. Nakamura, N. Iwasawa, H. Sato, K. Hamada, D. Citterio and K. Suzuki, *RSC Adv.*, 2014, **4**, 9791–9798.
- 222 L. Ortego, J. Gonzalo-Asensio, A. Laguna, M. D. Villacampa and M. C. Gimeno, *J. Inorg. Biochem.*, 2015, **146**, 19–27.
- 223 J. M. S. Cardoso, S. I. Guerreiro, A. Lourenço, M. M. Alves, M. F. Montemor, N. P. Mira, J. H. Leitão and M. F. N. N. Carvalho, *PLoS One*, 2017, **12**, 1–15.
- 224 K. Potgieter, Z. Engelbrecht, G. Naganagowda, M. J. Cronjé and R. Meijboom, *J. Coord. Chem.*, 2017, **70**, 2644–2658.
- 225 D. S. Rosser, M., Parker, D., Ferguson, G. Gallagher, J. F., Howard J.A.K, and Yufita, *J. Chem. Soc., Chem. Commun*, 1993, 1267–1269.
- 226 M. Poyraz, H. Berber, C. N. Banti, N. Kourkoumelis, M. J. Manos and S. K. Hadjikakou, *Polyhedron*, 2017, **128**, 95–103.
- 227 K. Potgieter, M. J. Cronjé and R. Meijboom, *Inorganica Chim. Acta*, 2016, **453**, 443–451.
- 228 A. José, J. Romero, García-Vázquez, A. Sousa-Pedrares, A. Sousa and M. Carabel, *Polyhedron*, 2005, **24**, 2043–2054.
- 229 K. Khoo, *Compr. Nat. Prod. II Chem. Biol.*, 2010, **6**, 123–156.
- 230 S. Inokuma, M. Kuramami, S. Otsuki, T. Shirakawa, S. ichi Kondo, Y. Nakamura and J. Nishimura, *Tetrahedron*, 2006, **62**, 10005–10010.
- 231 I. Starke, A. Koch, S. Kammer, H. J. Holdt and H. M. Möller, *J. Mass Spectrom.*, 2018, **53**, 408–418.
- 232 S. N. Podyachev, V. E. Semenov, V. V. Syakaev, N. E. Kashapova, S. N. Sudakova, J. K. Voronina, A. S. Mikhailov, A. D. Voloshina, V. S. Reznik and A. I. Konovalov, *RSC Adv.*, 2014, **4**, 10228–10239.
- 233 K. Akhbari and A. Morsali, *Cryst. Growth Des.*, 2007, **7**, 2024–2030.
- 234 A. Daubinet, Rhodes University, 2001.
- 235 S. M. Soliman, A. Barakat, M. S. Islam and H. A. Ghabbour, *Molecules*, 2018, **23**, 888.
- 236 J. S. Renny, L. L. Tomasevich, E. H. Tallmadge and D. B. Collum, *Angew. Chemie - Int. Ed.*, 2013, **52**, 11998–12013.
- 237 X. Yin, J. Long, Y. Xi and X. Luo, *ACS Sustain. Chem. Eng.*, 2017, **5**, 2090–2097.
- 238 M. A. Karimi, A. Hatefi-Mehrjardi, S. Z. Mohammadi, A. Mohadesi, M. Mazloum-Ardakani, A. A. Kabir, M. Kazemipour and N. Afsahi, *Int. J. Environ. Anal. Chem.*, 2012, **92**, 1325–1340.

References

- 239 R. Jalilian and A. Taheri, *E-Polymers*, 2018, **18**, 123–134.
- 240 A. Banaei, H. Vojoudi, S. Karimi, S. Bahar and E. Pourbasheer, *RSC Adv.*, 2015, **5**, 83304–83313.
- 241 J. Puig, C. E. Hoppe, L. A. Fasce, C. J. Pérez, Y. Piñeiro-Redondo, M. Bañobre-López, M. A. López-Quintela, J. Rivas and R. J. J. Williams, *J. Phys. Chem. C*, 2012, **116**, 13421–13428.
- 242 Y. Sun, X. Ding, Z. Zheng, X. Cheng, X. Hu and Y. Peng, *Eur. Polym. J.*, 2007, **43**, 762–772.
- 243 L. B. Salviano, T. M. da S. Cardoso, G. C. Silva, M. S. S. Dantas and A. de M. Ferreira, *Mater. Res.*, 2018, **21**, 2–8.
- 244 A. R. Mahdavian and M. A. S. Mirrahimi, *Chem. Eng. J.*, 2010, **159**, 264–271.
- 245 T. Tofaz, D. C. Mahanto, S. Akhter, M. Rahman and M. A. Latif, *Am. J. Polym. Sci. Technol.*, 2019, **5**, 1–8.
- 246 J. Safaei-Ghomi, H. Shahbazi-Alavi and P. Babaei, *Zeitschrift fur Naturforsch. - Sect. B J. Chem. Sci.*, 2016, **71**, 849–856.
- 247 O. Colombani, O. Langelier and E. Martwong, *J. Chem. Educ.*, 2011, **88**, 116–121.
- 248 H. Rahaman, A. Nath, R. Paul, M. Sengupta and S. K. Ghosh, *RSC Adv.*, 2016, **6**, 83146–83153.
- 249 L. Qian, J. Sun, C. Hou, J. Yang, Y. Li, D. Lei, M. Yang and S. Zhang, *Talanta*, 2017, **168**, 174–182.
- 250 S. Sajjadifar, M. A. Zolfigol and F. Tami, *J. Chinese Chem. Soc.*, 2019, **66**, 307–315.
- 251 H. Zhou, L. Yang, W. Li, Q. Shou, P. Xu, W. Li, F. Wang, P. Yu and H. Liu, *Ind. Eng. Chem. Res.*, 2012, **51**, 4582–4590.
- 252 F. Yang, R. Shen, Y. Long, X. Sun, F. Tang, Q. Cai and S. Yao, *J. Environ. Monit.*, 2011, **13**, 440–445.
- 253 Y. Wei, Y. Li, A. Tian, Y. Fan and X. Wang, *J. Mater. Chem. B*, 2013, **1**, 2066–2071.
- 254 N. Azgomi and M. Mokhtary, *J. Mol. Catal. A Chem.*, 2015, **398**, 58–64.
- 255 C. Garkoti, J. Shabir and S. Mozumdar, *New J. Chem.*, 2017, **41**, 9291–9298.
- 256 K. Naka, A. Narita, H. Tanaka, Y. Chujo, M. Morita, T. Inubushi, I. Nishimura, J. Hiruta, H. Shibayama, M. Koga, S. Ishibashi, J. Seki and S. Kizaka-Kondoh, *Polym. Adv. Technol.*, 2008, **19**, 1421–1429.
- 257 L. Fan, J. Song, W. Bai, S. Wang, M. Zeng, X. Li, Y. Zhou, H. Li and H. Lu, *Sci. Rep.*, 2016, **6**, 1–9.
- 258 J. Chen, Y. Wang, X. Ding, Y. Huang and K. Xu, *Anal. Methods*, 2014, **6**, 8358–8367.
- 259 A. Ditsch, P. E. Laibinis, D. I. C. Wang and T. A. Hatton, *Langmuir*, 2005, **21**, 6006–6018.
- 260 A. P. Philipse, M. P. B. Van Bruggen and C. Pathmamanoharan, *Langmuir*, 1994, **10**, 92–99.
- 261 S. Wahajuddin, A. and Arora, *Int. J. Med.*, 2012, **7**, 3445–3471.

References

- 262 J. Neamtu and N. Verga, *Dig. J. Nanomater. Biostructures*, 2011, **6**, 969–978.
- 263 A. R. Mahdavian and M. A. S. Mirrahimi, *Chem. Eng. J.*, 2010, **159**, 264–271.
- 264 M. Abbas, B. Parvatheeswara Rao, M. Nazrul Islam, S. M. Naga, M. Takahashi and C. Kim, *Ceram. Int.*, 2014, **40**, 1379–1385.
- 265 M. Kim, S. Hwang and J. S. Yu, *J. Mater. Chem.*, 2007, **17**, 1656–1659.
- 266 E. Korin, N. Froumin and S. Cohen, *ACS Biomater. Sci. Eng.*, 2017, **3**, 882–889.
- 267 M. Kim, J. H. Seo, D. Zhao, S. C. Liu, K. Kim, K. Lim, W. Zhou, E. Waks and Z. Ma, *J. Mater. Chem. C*, 2017, **5**, 264–268.
- 268 D. J. Miller, M. C. Biesinger and N. S. McIntyre, *Surf. Interface Anal.*, 2002, **33**, 299–305.
- 269 M. Khoobi, T. M. Delshad, M. Vosooghi, M. Alipour, H. Hamadi, E. Alipour, M. P. Hamedani, S. E. Sadat Ebrahimi, Z. Safaei, A. Foroumadi and A. Shafiee, *J. Magn. Magn. Mater.*, 2015, **375**, 217–226.
- 270 J. Xu, C. Ju, J. Sheng, F. Wang, Q. Zhang, G. Sun and M. Sun, *Bull. Korean Chem. Soc.*, 2013, **34**, 2408–2412.
- 271 M. R. Lasheen, I. Y. El-Sherif, D. Y. Sabry, S. T. El-Wakeel and M. F. El-Shahat, *Desalin. Water Treat.*, 2014, **52**, 6464–6473.
- 272 P. Beigzadeh and F. Moeinpour, *Trans. Nonferrous Met. Soc. China (English Ed.)*, 2016, **26**, 2238–2246.
- 273 H. Vojoudi, A. Badiei, A. Banaei, S. Bahar, S. Karimi, G. Mohammadi Ziarani and M. R. Ganjali, *Microchim. Acta*, 2017, **184**, 3859–3866.
- 274 K. Shimojo and M. Goto, *Anal. Chem.*, 2004, **76**, 5039–5044.